



NAM

Shake-table tests up to collapse of a Roof Structure of a Dutch Terraced House

A. A. Correia, A. I. Marques, V. Bernardo, L. Grottoli, U. Tomassetti and F. Graziotti

Eucentre

(European Centre for Training and Research in Earthquake Engineering)

Date October 2017

Editors Jan van Elk & Dirk Doornhof

General Introduction

Many of the buildings in the Groningen field area are terraced unreinforced masonry buildings. A program to assess the response of these building to earthquakes was therefore initiated. This program built on the experimental and modelling program into the properties of URM building materials, wall elements and wall units.

A typical Groningen terraced house built using materials from the Groningen area by builders from the Groningen area, was tested at the shake-table of Eucentre in Pavia, Italy (Ref. 1). Although the building was at the end of this test program seriously damaged, the building had not collapsed. This left questions on the remaining capacity of the structure and its ability to resist larger seismic movements before (partially) collapsing. The test in Eucentre was therefore followed-up with further tests at the laboratory of LNEC in Lisbon, Portugal (Ref. 2 to 5). Here the upper floors of the building tested in Eucentre were re-built in the LNEC laboratory and subjected to movements measured at the base of the upper floors in Eucentre.

Additionally, the roof structure was tested individually. This report shows the results of modelling of these shake-table experiments of the roof structure obtained by Mosayk using Extreme Loading for Structures (ELS), a commercial structural analysis software based on the Applied Element Method (AEM) after such tests, describing also the calibration process of the AEM numerical model.

References

1. Eucentre Shake-table Test of Terraced House Modelling Predictions and Analysis Cross Validation, staff from ARUP, Eucentre (Pavia) and TU Delft, November 2015 [this document also includes; (1) Instruments full-scale test-house Eucentre Laboratory, (2) Protocol for Shaking Table Test on Full Scale Building (Eucentre) V_1, and (3) Selection of Acceleration Time-Series for Shake Table Testing of Groningen Masonry Building at the EUCENTRE, Pavia, all three by staff from Eucentre (Pavia)],
2. Collapse shake-table testing of terraced house (LNEC-BUILD1), Eucentre and LNEC (U. Tomassetti, A. A. Correia, F. Graziotti, A.I. Marques, M. Mandirola, P.X. Candeias), 1st September 2017.
3. LNEC-BUILD1: Modelling predictions and analysis cross-validation, ARUP, TU Delft, Eucentre and Mosayk (several staff members from all four institutions), 8th September 2017.
4. Using the Applied Element Method to model the collapse shake-table testing of a URM cavity wall structure (LNEC-BUILD1), Mosayk (D. Malomo, R. Pinho), 31st October 2017.
5. Using the Applied Element Method to model the collapse shake-table testing of a terraced house roof substructure (LNEC-BUILD2), Mosayk (D. Malomo, R. Pinho), 31st October 2017.
6. Experimental campaign on a clay URM full-scale specimen representative of the Groningen building stock (EUC-BUILD2), Eucentre (F. Graziotti, U. Tomassetti, A. Rossi, B. Marchesi, S. Kallioras, M. Mandirola, A. Fragomeli, E. Mellia, S. Peloso, F. Cuppari, G. Guerrini, A. Penna, G. Magenes, G), 20th July 2016.
7. EUC-BUILD2: Modelling predictions and analysis cross-validation of detached single-storey URM Building, ARUP, TU Delft, Eucentre and Arcadis (several staff members from all four institutions), 30th September 2016



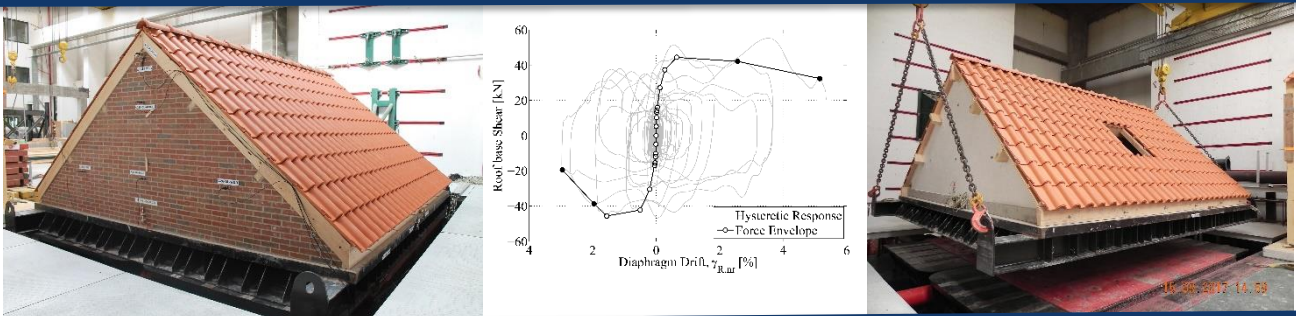
NAM

Title	Shake-table tests up to collapse of a Roof Structure of a Dutch Terraced House		Date	October 2017
			Initiator	NAM
Autor(s)	A. A. Correia, A. I. Marques, V. Bernardo, L. Grottoli, U. Tomassetti and F. Graziotti	Editors	Jan van Elk and Dirk Doornhof	
Organisation	Eucentre in Pavia (Italy) (European Centre for Training and Research in Earthquake Engineering)	Organisation	NAM	
Place in the Study and Data Acquisition Plan	<p><u>Study Theme:</u> Seismic Response of Buildings (URM)</p> <p><u>Comment:</u> Many of the buildings in the Groningen field area are terraced unreinforced masonry buildings. A program to assess the response of these building to earthquakes was therefore initiated. This program built on the experimental and modelling program into the properties of URM building materials, wall elements and wall units. A typical Groningen terraced house built using materials from the Groningen area by builders from the Groningen area, was tested at the shake-table of Eucentre in Pavia, Italy (Ref. 1). Although the building was at the end of this test program seriously damaged, the building had not collapsed. This left questions on the remaining capacity of the structure and its ability to resist larger seismic movements before (partially) collapsing. The test in Eucentre was therefore followed-up with further tests at the laboratory of LNEC in Lisbon, Portugal (Ref. 2 to 5). Here the upper floors of the building tested in Eucentre were re-built in the LNEC laboratory and subjected to movements measured at the base of the upper floors in Eucentre. Additionally, the roof structure was testes individually. This report shows the results of modelling of these shake-table experiments of the roof structure obtained by Mosayk using Extreme Loading for Structures (ELS), a commercial structural analysis software based on the Applied Element Method (AEM) after such tests, describing also the calibration process of the AEM numerical model.</p>			
Directly linked research	(1) Shake table tests (2) Fragility curves for building typologies (URM) (3) Risk Assessment			
Used data	Experiments			
Associated organisation	NAM			
Assurance	Eucentre			

SHAKE TABLE TEST UP TO COLLAPSE ON A ROOF SUBSTRUCTURE OF A DUTCH TERRACED HOUSE

Document authors

A. A. Correia, A. I. Marques, V. Bernardo, L. Grottolì, U. Tomassetti, F. Graziotti



SHAKE TABLE TEST UP TO COLLAPSE ON A ROOF SUBSTRUCTURE OF A DUTCH TERRACED HOUSE

A. A. Correia, A. I. Marques, V. Bernardo, L. Grottoli, U. Tomassetti, F. Graziotti

According to law, EUCENTRE Foundation trademark cannot be reproduced, copied or utilized, without the written permission of the EUCENTRE Foundation, which is the owner, except in accordance with established contract conditions pertaining to the production of this document.

31th October, 2017, Pavia

TABLE OF CONTENTS

TABLE OF CONTENTS	III
LIST OF TABLES	V
LIST OF FIGURES	VII
1 INTRODUCTION AND DESCRIPTION OF BUILDING PROTOTYPE	14
1.1 SCOPE AND MOTIVATION OF THE TEST	14
1.2 GEOMETRY OF THE SPECIMEN.....	16
1.3 BUILDING CONSTRUCTION DETAILS	18
2 MATERIALS CHARACTERISATION	23
2.1 MORTAR CHARACTERISATION TESTS	24
2.1.1 CHARACTERISATION AND IDENTIFICATION OF SAMPLES BEFORE HARDENING	24
2.1.2 TESTS FOR THE DETERMINATION OF THE BULK DENSITY OF FRESH MORTAR	27
2.1.3 TESTS FOR THE DETERMINATION OF THE CONSISTENCE OF FRESH MORTAR (BY FLOW TABLE) ..	28
2.1.4 CHARACTERISATION AND IDENTIFICATION OF SPECIMENS (HARDENED MORTAR)	29
2.1.5 TESTS FOR THE DETERMINATION OF DYNAMIC MODULUS OF ELASTICITY	31
2.1.6 TESTS FOR THE DETERMINATION OF FLEXURAL AND COMPRESSIVE STRENGTHS	35
2.2 BLOCK CHARACTERISATION TESTS	43
2.2.1 CHARACTERISATION AND IDENTIFICATION OF SPECIMENS.....	43
2.2.2 TESTS FOR THE DETERMINATION OF COMPRESSIVE STRENGTH.....	44
2.3 MASONRY CHARACTERISATION TESTS.....	49
2.3.1 CHARACTERISATION AND IDENTIFICATION OF SPECIMENS.....	49
2.3.2 -TEST FOR THE DETERMINATION OF COMPRESSIVE STRENGTH	52
2.3.3 TESTS FOR THE DETERMINATION OF BOND STRENGTH.....	66
2.4 ANALYSIS OF THE MATERIALS CHARACTERISATION RESULTS.....	73
3 INSTRUMENTATION OF THE SPECIMEN	74
4 SHAKE TABLE TEST PROCEDURE	81
4.1 SHAKE TABLE INPUT SEQUENCE.....	81
4.2 CHARACTERISATION OF THE INDUCED GROUND MOTION TESTS	83
5 SHAKE TABLE TEST RESULTS	85
5.1 DAMAGE EVOLUTION	85
5.2 DESCRIPTION OF THE COLLAPSE MECHANISM	86
5.3 SHAKE TABLE PERFORMANCE.....	89

5.4 SPECIMEN DYNAMIC IDENTIFICATION	90
5.4.1 INTRODUCTION AND METHODOLOGY	90
5.4.1.1 Frequency-Domain Decomposition method	92
5.4.1.2 Enhanced Frequency-Domain Decomposition method	93
5.4.2 DYNAMIC IDENTIFICATION RESULTS	94
5.4.2.1 Initial dynamic identification (CAT 00 – before any test).....	94
5.4.2.2 4 th dynamic identification (CAT 03 – after test FEQ2-100%)	97
5.4.2.3 7 th dynamic identification (CAT 06 – after test FEQ2-300%)	99
5.4.2.4 8 th dynamic identification (CAT 07 – after test FEQ2-400%)	100
5.4.2.5 9 th dynamic identification (CAT 08 – after test FEQ2-500%)	102
5.5 DISPLACEMENT AND ACCELERATION HISTORIES.....	105
5.6 DEFORMED SHAPE	113
5.7 HYSTERETIC RESPONSE	116
5.8 IDENTIFICATION OF SPECIMEN DAMAGE LIMIT STATES.....	121
5.9 DERIVATION OF EDP ACCORDING TO SPECIMEN PERFORMANCE	127
<u>6 QUASI-STATIC PUSHOVER TEST OF TIMBER ROOF SYSTEM</u>	<u>128</u>
<u>REFERENCES</u>	<u>136</u>

LIST OF TABLES

Table 1.1 Masses of the different structural elements characterising the specimen.	17
Table 1.2 Masses of the different elements characterising the roof of the specimen.	21
Table 2.1 Masonry mechanical properties.....	24
Table 2.2 Adopted amount of water for each type of mortar.....	25
Table 2.3 Determination of the water / product ratio for each corresponding mortar mix collection of samples.	27
Table 2.4 Results obtained for the determination of bulk density of all mortars.	28
Table 2.5 Results obtained in the determination of the consistency of fresh mortar for all samples collected.	29
Table 2.6 Summary of the average dynamic modulus of elasticity obtained for the two types of bedding mortar collected directly from the full-scale model for the different ages.....	34
Table 2.7 Summary of the average dynamic modulus of elasticity obtained for the two types of bedding mortar collected directly from the characterisation specimens for the different ages.	34
Table 2.8 Summary of the compressive and flexural strength averages obtained for the two types of bedding mortars collected directly from the full-scale model for different ages.	41
Table 2.9 .Summary of the compressive and flexural strength averages obtained for the two types of bedding mortars collected directly from characterisation specimens for different ages.....	42
Table 2.10 Characteristics of the two types of blocks selected for the tests.	44
Table 2.11 Bulk density for calcium silicate and clay blocks.....	44
Table 2.12 Compressive strength for calcium silicate blocks.....	47
Table 2.13 Compressive strength for clay bricks with both surfaces smoothed by wear.....	48
Table 2.14 Compressive strength for the clay bricks with different surface smoothing techniques.....	48
Table 2.15 Summary of the average compressive strength and average standard compressive strength in the two types of tested specimens.....	49
Table 2.16 Dimensions and masses of the two types of wallettes constructed for the compressive strength tests.	52
Table 2.17 Dimensions and masses of the two types of triplets built for the bond wrench tests.	52
Table 2.18 Summary of the results of the bulk density for the two types of specimens.	52
Table 2.19 Cyclic load values for calcium silicate wallettes.	56
Table 2.20 Summary of the compressive strength for the calcium silicate wallettes.....	58
Table 2.21 Summary of the modulus of elasticity for calcium silicate wallettes.....	61
Table 2.22 Cyclic load values for clay wallettes.	62
Table 2.23 Summary of the compressive strength for the clay wallettes.	63
Table 2.24 Summary of the modulus of elasticity for clay wallettes.	66
Table 2.25 Bond strength for the CS triplets.....	72
Table 2.26 Bond strength for the clay triplets performed with the device with a torque wrench.	72
Table 2.27 Bond strength for the clay triplets performed with the device used in the previous campaign.	73

Table 2.28 Summary of bond strength in the two types of tested specimens.	73
Table 3.1 Summary of the accelerometers and their location.	76
Table 3.2 Summary of the displacement transducers and their location.	77
Table 4.1 Applied testing sequence.	83
Table 4.2 Summary of the floor motion testing sequence dynamic characteristics.	84
Table 4.3 Summary of the floor motion dynamic characteristics.	84
Table 5.1 Summary of vibration modes' characteristics for 1 st dynamic identification (CAT 00 – before any test).	95
Table 5.2 MAC coefficients for 1 st dynamic identification (CAT 00 – before any test).	95
Table 5.3 Summary of vibration modes' characteristics for 4 th dynamic identification (CAT 03 – after test FEQ2-100%).	97
Table 5.4 MAC coefficients for 4 th dynamic identification (CAT 03 – after test FEQ2-100%).	97
Table 5.5 Summary of vibration modes' characteristics for 7 th dynamic identification (CAT 06 – after test FEQ2-300%).	99
Table 5.6 MAC coefficients for 7 th dynamic identification (CAT 06 – after test FEQ2-300%).	99
Table 5.7 Summary of vibration modes' characteristics for 8 th dynamic identification (CAT 07 – after test FEQ2-400%).	101
Table 5.8 MAC coefficients for 8 th dynamic identification (CAT 07 – after test FEQ2-400%).	101
Table 5.9 Summary of vibration modes' characteristics for 9 th dynamic identification (CAT 08 – after test FEQ2-500%).	103
Table 5.10 MAC coefficients for 9 th dynamic identification (CAT 08 – after test FEQ2-500%).	103
Table 5.11 Evolution of the fundamental mode of vibration of the model during the shaking table test.	105
Table 5.12 List of peak force and displacement values.	120

LIST OF FIGURES

Figure 1.1 A typical terraced house in Groningen: (a) illustration of the front façade; (b) plan view.	14
Figure 1.2 Views of the full-scale specimen built in Eucentre, Pavia, Italy.....	15
Figure 1.3 Views of the full-scale specimen built in LNEC, Lisbon, Portugal: (a) North-East elevation; (b) East elevation; (c) North elevation; (d) South-West elevation.	15
Figure 1.4 Views of the full-scale roof substructure built in LNEC, Lisbon, Portugal: (a) North-East elevation; (b) South-West elevation; (c) West elevation; (d) North elevation.	16
Figure 1.5 Plan view of the specimen's base. The arrow indicates the positive direction of the shake table motion.	17
Figure 1.6 Elevation views of the specimen's timber roof planks and CS walls (dimensions in cm).	18
Figure 1.7 Elevation views of the specimen's roof and clay outer leaf.	18
Figure 1.8 Construction of the specimen.	20
Figure 1.9 Construction details of the specimen's walls: (a) building phase of East CS wall; (b) building phase of outer leaf in West wall; (c) connection of timber roof beam to CS walls.	20
Figure 1.10 Details of the connections: (a,b) between the RC slab and the timber beam; (c) between timber beams and the walls; (d) between the two unreinforced masonry leaves.	21
Figure 1.11 Geometry and details of the timber roof diaphragms (dimensions in cm).	21
Figure 2.1 Types of product used in each bedding mortar.....	25
Figure 2.2 Construction of the full scale model at the time of collection of mortar samples.	25
Figure 2.3 Construction of characterisation specimens at the time of mortar sampling.....	26
Figure 2.4 Moulding of masonry specimens: (a) pestle and (b) mould.....	26
Figure 2.5 Carrying out the determination of bulk density of fresh mortar.....	28
Figure 2.6 Determination of consistence of fresh mortar by scattering: (a) schematic representation of equipment; (b) test run.	29
Figure 2.7 Part of mortar specimens.	30
Figure 2.8 Curing conditions of mortar specimens.	30
Figure 2.9 Carrying out the test to determine the dynamic modulus of elasticity and plot obtained.	31
Figure 2.10 Test results for the determination of the dynamic modulus of elasticity of bedding mortar for the calcium silicate blocks (MS) after 10 days of age.	32
Figure 2.11 Test results for the determination of the dynamic modulus of elasticity of bedding mortar for the calcium silicate blocks (MS) after 20 days of age.	32
Figure 2.12 Test results for the determination of the dynamic modulus of elasticity of bedding mortar for the calcium silicate blocks (MS) after 28 days of age.	32
Figure 2.13 Test results for the determination of the dynamic modulus of elasticity of bedding mortar for the clay bricks (MCL) after 10 days of age.	33

Figure 2.14 Test results for the determination of the dynamic modulus of elasticity of bedding mortar for the clay bricks (MCL) after 20 days of age.	33
Figure 2.15 Test results for the determination of the dynamic modulus of elasticity of bedding mortar for the clay bricks (MCL) after 28 days of age.	33
Figure 2.16 Relation between dynamic moduli of elasticity and maturation time for the two bedding mortars removed from the full scale model and the characterisation test specimens.	34
Figure 2.17 Test for determination of flexural strength: (a) scheme of positioning of the specimen and (b) specimen being tested.	35
Figure 2.18 Test for compressive strength: (a) test scheme and (b) specimen being tested.	36
Figure 2.19 Flexural strength test results for bedding mortar specimens used with calcium silicate blocks (MS) after 10 days of age.	36
Figure 2.20 Flexural strength test results for bedding mortar specimens used with calcium silicate blocks (MS) after 20 days of age.	37
Figure 2.21 Flexural strength test results for bedding mortar specimens used with calcium silicate blocks (MS) after 28 days of age.	37
Figure 2.22 Compressive strength and modulus of elasticity test results for bedding mortar specimens used with calcium silicate blocks (MS) after 10 days of age.	37
Figure 2.23 Compressive strength and modulus of elasticity test results for bedding mortar specimens used with calcium silicate blocks (MS) after 20 days of age.	38
Figure 2.24 Compressive strength and modulus of elasticity test results for bedding mortar specimens used with calcium silicate blocks (MS) after 28 days of age.	38
Figure 2.25 Distribution of the flexural and compressive strength of bedding mortars used with calcium silicate bricks (MS) after 28 days of age.	38
Figure 2.26 Flexural strength test results for bedding mortar specimens used with clay bricks (MCL) after 10 days of age.	39
Figure 2.27 Flexural strength test results for bedding mortar specimens used with clay bricks (MCL) after 20 days of age.	39
Figure 2.28 Flexural strength test results for bedding mortar specimens used with clay bricks (MCL) after 28 days of age.	40
Figure 2.29 Compressive strength and modulus of elasticity test results for bedding mortar specimens used with clay bricks (MCL) after 10 days of age.	40
Figure 2.30 Compressive strength and modulus of elasticity test results for bedding mortar specimens used with clay bricks (MCL) after 20 days of age.	40
Figure 2.31 Compressive strength and modulus of elasticity test results for bedding mortar specimens used with clay bricks (MCL) after 28 days of age.	41
Figure 2.32 Distribution of the flexural and compressive strengths of bedding mortars for the clay bricks (MCL) after 28 days of age.	41
Figure 2.33 Relation between flexural and compressive strengths and maturation time of bedding mortars for the calcium silicate blocks (MS) removed from the full-scale model and the characterisation test specimens.	42
Figure 2.34 Relation between flexural and compressive strength and maturation time of bedding mortars for the clay bricks (MCL) removed from the full-scale model and the characterisation test specimens.	42
Figure 2.35 Blocks used and indication of their dimensions.	43
Figure 2.36 Collection of test pieces.	43

Figure 2.37 Blocks units.....	44
Figure 2.38 Regularisation of clay specimens.....	45
Figure 2.39 Clay specimens smoothed by wear.....	45
Figure 2.40 Specimens subjected to compressive strength tests.....	46
Figure 2.41 Calcium silicate blocks during the compressive strength test and after failure.....	47
Figure 2.42 Clay bricks tested with different surface smoothing techniques.....	48
Figure 2.43 Clay bricks during the compressive strength test and after failure.....	49
Figure 2.44 Types of masonry specimens (wallettes and triplets) built for testing.....	50
Figure 2.45 Construction of wallettes and triplets.....	50
Figure 2.46 Example of characterisation (measure and weight) of all specimens.....	51
Figure 2.47 Schematic with the identification of the parameters measured in the various specimens.	51
Figure 2.48 Regularisation of the wallettes faces.....	53
Figure 2.49 Final regularisation of the wallettes' faces on top of the testing machine.....	54
Figure 2.50 Lack of verticality in wallettes.....	54
Figure 2.51 Scheme and numbering of the transducers placed on each face of the wallettes.....	54
Figure 2.52 Scheme with the location of the transducers placed on each face of the CS wallettes.	55
Figure 2.53 Scheme with the location of the transducers placed on each face of the clay wallettes.	55
Figure 2.54 Instrumentation placed on each face of the CS wallettes.....	55
Figure 2.55 Instrumentation placed on each face of the clay wallettes.....	56
Figure 2.56 Application of force as a function of time applied to calcium silicate wallettes.....	57
Figure 2.57 Calcium silicate block wallette (WS_00) during the test and after failure.....	57
Figure 2.58 Vertical stress vs. vertical and horizontal strains for wallette WS_00.....	58
Figure 2.59 Vertical stress vs. vertical and horizontal strains for wallette WS_0.....	59
Figure 2.60 Vertical stress vs. vertical and horizontal strains for wallette WS_1.....	59
Figure 2.61 Vertical stress vs. vertical and horizontal strains for wallette WS_3.....	59
Figure 2.62 Vertical stress vs. vertical and horizontal strains for wallette WS_4.....	59
Figure 2.63 Vertical stress vs. vertical and horizontal strains for wallette WS_5.....	59
Figure 2.64 Vertical stress vs. vertical and horizontal strains for wallette WS_6.....	59
Figure 2.65 Vertical stress vs. vertical strain and determination of the modulus of elasticity for wallette WS_00.....	60
Figure 2.66 Vertical stress vs. vertical strain and determination of the modulus of elasticity for wallette WS_0.....	60
Figure 2.67 Vertical stress vs. vertical strain and determination of the modulus of elasticity for wallette WS_1.....	60
Figure 2.68 Vertical stress vs. vertical strain and determination of the modulus of elasticity for wallette WS_2.....	61
Figure 2.69 Vertical stress vs. vertical strain and determination of the modulus of elasticity for wallette WS_3.....	61

Figure 2.70 Vertical stress vs. vertical strain and determination of the modulus of elasticity for wallette WS_4.....	61
Figure 2.71 Vertical stress vs. vertical strain and determination of the modulus of elasticity for wallette WS_5.....	61
Figure 2.72 Vertical stress vs. vertical strain and determination of the modulus of elasticity for wallette WS_6.....	61
Figure 2.73 Distribution of moduli of elasticity obtained for calcium silicate wallettes.	61
Figure 2.74 Application of force as a function of time applied to clay wallettes.....	62
Figure 2.75 Clay brick wallette (WCL_6) subjected to test and after failure.	63
Figure 2.76 Vertical stress vs. vertical and horizontal strains for wallette WCL_00.....	63
Figure 2.77 Vertical stress vs. vertical and horizontal strains for wallette WCL_0.....	64
Figure 2.78 Vertical stress vs. vertical and horizontal strains for wallette WCL_1.....	64
Figure 2.79 Vertical stress vs. vertical and horizontal strains for wallette WCL_2.....	64
Figure 2.80 Vertical stress vs. vertical and horizontal strains for wallette WCL_3.....	64
Figure 2.81 Vertical stress vs. vertical and horizontal strains for wallette WCL_4.....	64
Figure 2.82 Vertical stress vs. vertical and horizontal strains for wallette WCL_5.....	64
Figure 2.83 Vertical stress vs. vertical and horizontal strains for wallette WCL_6.....	64
Figure 2.84 Vertical stress vs. vertical strain and determination of the modulus of elasticity for wallette WCL_00.....	65
Figure 2.85 Vertical stress vs. vertical strain and determination of the modulus of elasticity for wallette WCL_0.....	65
Figure 2.86 Vertical stress vs. vertical strain and determination of the modulus of elasticity for wallette WCL_1.....	65
Figure 2.87 Vertical stress vs. vertical strain and determination of the modulus of elasticity for wallette WCL_2.....	66
Figure 2.88 Vertical stress vs. vertical strain and determination of the modulus of elasticity for wallette WCL_3.....	66
Figure 2.89 Vertical stress vs. vertical strain and determination of the modulus of elasticity for wallette WCL_4.....	66
Figure 2.90 Vertical stress vs. vertical strain and determination of the modulus of elasticity for wallette WCL_5.....	66
Figure 2.91 Vertical stress vs. vertical strain and determination of the modulus of elasticity for wallette WCL_6.....	66
Figure 2.92 Distribution of moduli of elasticity obtained for clay wallettes.....	66
Figure 2.93 Type of specimens subjected to bond strength test.....	67
Figure 2.94 Example of a possible device for the test in accordance with EN 1052-5 (CEN, 2005).	67
Figure 2.95 Test setups for bond-wrench test.	68
Figure 2.96 Test of the two connections in CS blocks using the same test device.	68
Figure 2.97 Test of the two connections in clay bricks using the same test device.....	69
Figure 2.98 Application of vertical force until bond failure.....	70
Figure 2.99 Measure of the weight of the top unit and adherent mortar.....	70

Figure 2.100 Admissible failure mechanisms for the bond wrench test.	71
Figure 2.101 Example of failure mechanisms obtained for each triplet type in the bond wrench test.	71
Figure 3.1 Locations of the instrumentation: (a) accelerometers and (b) displacement transducers (letters indicate the component at which the transducers is attached to: SL = slab, RF = reference frame, IL = inner leaf, OL = outer leaf, FB = foundation beam, ST = shaking table, TP = timber plate and RB = roof beam).	75
Figure 3.2 Pictures of the instrumentation.	78
Figure 4.1 Theoretical horizontal components of the adopted floor accelerograms.	82
Figure 4.2 Theoretical horizontal 5% damped acc. response spectra of the experimental inputs. .	82
Figure 5.1 Specimen transportation to the shake table.	85
Figure 5.2 Evolution of the crack pattern in the gable walls along the test stages.	86
Figure 5.3 Snapshots of the FEQ2-600% test.	87
Figure 5.4 Pictures of the specimen at the end of the test FEQ2-600%.	88
Figure 5.5 Theoretical-experimental 5% damped response spectra for all test stages.	89
Figure 5.6 Input acceleration history (above) and windowed average input (below).	91
Figure 5.7 Frequency response function from rectangular impulses in the horizontal direction.	91
Figure 5.8 Representation of the Singular Values matrix.	93
Figure 5.9 Frequency estimate (zero-crossings) and damping (logarithm decrement) of the impulse response estimate.	93
Figure 5.10 Test specimen fully instrumented on the shake table.	94
Figure 5.11 3D view of the accelerometers setup for dynamic identification.	94
Figure 5.12 FDD results for 1 st dynamic identification (CAT 00 – before any test).	95
Figure 5.13 Mode shapes for 1 st dynamic identification (CAT 00 – before any test).	96
Figure 5.14 FDD results for 4 th dynamic identification (CAT 03 – after test FEQ2-100%).	97
Figure 5.15 Mode shapes for 4 th dynamic identification (CAT 03 – after test FEQ2-100%).	98
Figure 5.16 FDD results for 7 th dynamic identification (CAT 06 – after test FEQ2-300%).	99
Figure 5.17 Mode shapes for 7 th dynamic identification (CAT 06 – after test FEQ2-300%).	100
Figure 5.18 FDD results for 8 th dynamic identification (CAT 07 – after test FEQ2-400%).	101
Figure 5.19 Mode shapes for 8 th dynamic identification (CAT 07 – after test FEQ2-400%).	102
Figure 5.20 FDD results for 9 th dynamic identification (CAT 08 – after test FEQ2-500%).	103
Figure 5.21 Mode shapes for 9 th dynamic identification (CAT 08 – after test FEQ2-500%).	104
Figure 5.22 FEQ1-50%: Displacement and acceleration histories.	105
Figure 5.23 FEQ1-100%: Displacement and acceleration histories.	106
Figure 5.24 FEQ1-150%: Displacement and acceleration histories.	106
Figure 5.25 FEQ2-50%: Displacement and acceleration histories.	107
Figure 5.26 FEQ2-100%: Displacement and acceleration histories.	107
Figure 5.27 FEQ2-150%: Displacement and acceleration histories.	108
Figure 5.28 FEQ2-200%: Displacement and acceleration histories.	108
Figure 5.29 FEQ2-300%: Displacement and acceleration histories.	109

Figure 5.30 FEQ2-400%: Displacement and acceleration histories.....	109
Figure 5.31 FEQ2-500%: Displacement and acceleration histories.....	110
Figure 5.32 FEQ2-100%-C: Displacement and acceleration histories.....	110
Figure 5.33 FEQ2-600%: Displacement and acceleration histories.....	111
Figure 5.34 FEQ2-100%: Rocking response at crack formation in East gable (above) and West gable (below).....	111
Figure 5.35 FEQ2-400%: Rocking response in East wall and West wall.....	112
Figure 5.36 FEQ2-400%: Sliding of roof timber plates with respect to the foundation beam.....	113
Figure 5.37 FEQ1-50%: Longitudinal cross section deflected shape.....	113
Figure 5.38 FEQ1-100%: Longitudinal cross section deflected shape.....	114
Figure 5.39 FEQ1-150%: Longitudinal cross section deflected shape.....	114
Figure 5.40 FEQ2-50%: Longitudinal cross section deflected shape.....	114
Figure 5.41 FEQ2-100%: Longitudinal cross section deflected shape.....	115
Figure 5.42 FEQ2-150%: Longitudinal cross section deflected shape.....	115
Figure 5.43 FEQ2-200%: Longitudinal cross section deflected shape.....	115
Figure 5.44 FEQ2-300%: Longitudinal cross section deflected shape.....	116
Figure 5.45 FEQ2-400%: Longitudinal cross section deflected shape.....	116
Figure 5.46 Evolution of specimen's hysteretic response.....	117
Figure 5.47 Comparison of specimen hysteretic response to previous tests.....	118
Figure 5.48 Comparison of specimen hysteretic response to previous tests – lumped case.....	119
Figure 5.49 Backbone capacity curve.....	120
Figure 5.50 Comparison of backbone capacity curve with previous tests.....	120
Figure 5.51 Identification of the DLs on the building backbone curve.....	122
Figure 5.52 Evolution of damage in the gable walls along DL0 to DL2.....	123
Figure 5.53 Evolution of damage in the gable walls up to DL3.....	124
Figure 5.54 Evolution of damage in the gable walls along DL4 to DL5.....	125
Figure 5.55 Evolution of the crack pattern in the gable walls along the DLs.....	126
Figure 5.56 Summary of the performance of the building specimen.....	127
Figure 6.1 Support and guidance system.....	128
Figure 6.2 Steel ties connecting the ridge beam to the reaction walls.....	129
Figure 6.3 Instrumentation for pushover test of timber roof system.....	129
Figure 6.4 Cyclic response of the roof structure.....	130
Figure 6.5 Evolution of displacements at the roof beams.....	130
Figure 6.6 Damage after the 220 mm pushover.....	131
Figure 6.7 Video images of the damage during the 350 mm pushover.....	132
Figure 6.8 Damage after the 350 mm pushover – West side.....	132
Figure 6.9 Damage after the 350 mm pushover – East side.....	133
Figure 6.10 Full response of the roof structure.....	133

Figure 6.11 Permanent drift after 350 mm pushover.	134
Figure 6.12 Damage in roof tiles.	134
Figure 6.13 Distortion of timber planks.	135

1 INTRODUCTION AND DESCRIPTION OF BUILDING PROTOTYPE

The main purpose of the present experimental campaign is to investigate the vulnerability of unreinforced masonry (URM) cavity-wall terraced houses of the late 1970s. This residential typology is characterised by wide openings on the front and back sides. The transverse walls, which separate units, are double-wythe cavity walls without any openings. Internal transverse walls are composed of a couple of load-bearing walls, carrying most of the vertical loads coming from the floors and roof and, therefore, capable of resisting significant in-plane lateral forces. Houses built with this common configuration are expected to be characterised by two very different seismic behaviours in the two principal directions, being generally more flexible and vulnerable in the longitudinal direction. Figure 1.1 shows the front view of a classic terraced house and its plan view.

Adjacent units are, in general, structurally detached, and the discontinuous slabs rest only on the load-bearing walls of the individual units. Each unit is therefore completely self-supported by transverse walls and structurally independent from the other units. The only common walls are the outer veneer walls, which do not play an important structural role. For this reason, it was possible to focus the present experimental campaign on shake table tests of a representative sub-volume (one end-unit) of a terraced house (as shown in Figure 1.1). The first floor is generally made of a reinforced concrete (RC) slab, while the second floor is either a RC or timber diaphragm; this test campaign dealt with cases where both slabs are in RC. On the other hand, the presence of a timber roof usually dominates over other typical roofing solutions for this building typology and was thus adopted in the tested models.

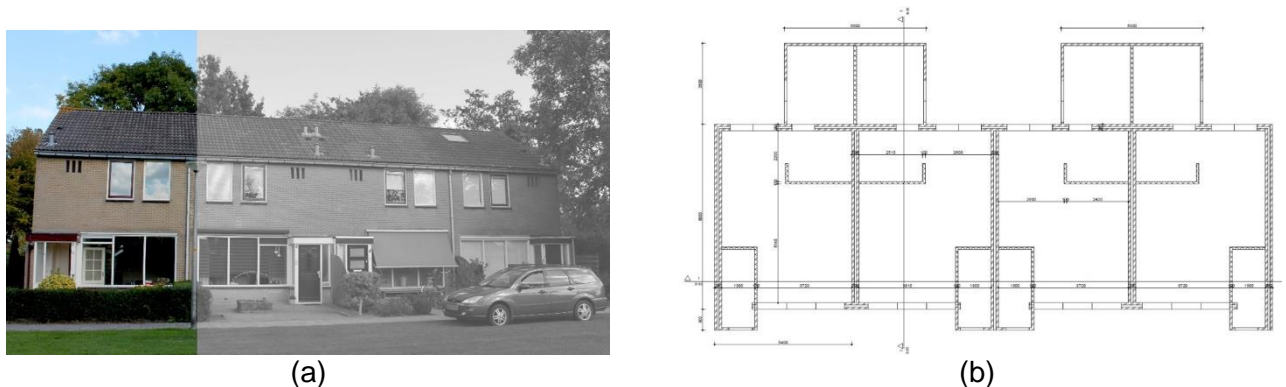


Figure 1.1 A typical terraced house in Groningen: (a) illustration of the front façade; (b) plan view.

1.1 Scope and motivation of the test

The test-house built in the EUCENTRE laboratory and tested in September 2015 (Graziotti et al. 2016a) was, according to the above reasoning, a full-scale two-storey building, with a timber roof and RC slabs, representing an end-unit of a typical terraced house. The testing campaign included in situ mechanical characterisation tests (Tondelli et al. 2015) and laboratory tests comprising: characterisation tests performed on brick units, mortar and small masonry assemblies; in-plane cyclic shear-compression and dynamic out-of-plane tests on full-scale masonry piers (Graziotti et al. 2016b). A uniaxial shake table test was carried out on a full-scale building representing a typical Dutch detached house, as shown in Figure 1.2.

Having not reached collapse in the shake table test performed in Pavia, in order to avoid damage to the laboratory facilities, a second shake table test was performed at the National Laboratory for Civil Engineering (LNEC), in Lisbon, Portugal (Tomassetti et al. 2017). This test was carried out on a full-scale sub-volume of the EUCENTRE specimen, corresponding to its second floor and roof, see Figure 1.3. This test was biaxial, also including a seismic excitation in the vertical direction and not just the horizontal one. The main goal of said test was, initially, to study large damage levels and assessing the failure mechanism leading to structural

collapse of these houses. In particular, the research team was interested in observing the influence of the vertical excitation and if the structural collapse would be led by a soft-storey mechanism or by the overturning of the gable walls and timber roof system.

The observed collapse of the second specimen was, contrarily to the numerical predictions, to an out-of-plane mechanism of the East load-bearing wall triggered by the vertical uplift of the RC slab due caused by the combined effect of the rocking motion of the masonry piers on the North and South façades and the vertical excitation. Nevertheless, the interest in characterising a failure of the gable walls and roof system remained and it was thus decided to make a third specimen related to a typical terraced house, now focusing only on its roof structure. Therefore, the subject of this report is the shake table test up to collapse of a replica of the roof substructure from both the first and second specimens. This model is depicted in Figure 1.4 and was tested in the horizontal direction only.



Figure 1.2 Views of the full-scale specimen built in Eucentre, Pavia, Italy.

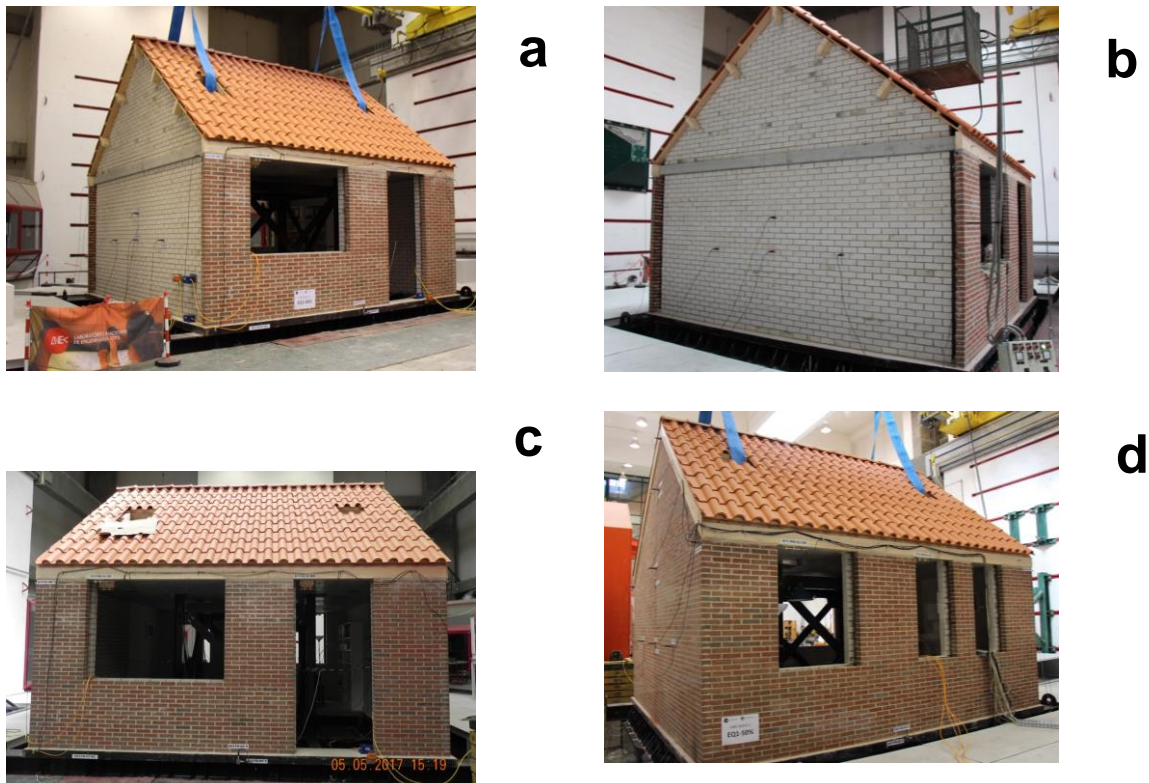


Figure 1.3 Views of the full-scale specimen built in LNEC, Lisbon, Portugal: (a) North-East elevation; (b) East elevation; (c) North elevation; (d) South-West elevation.

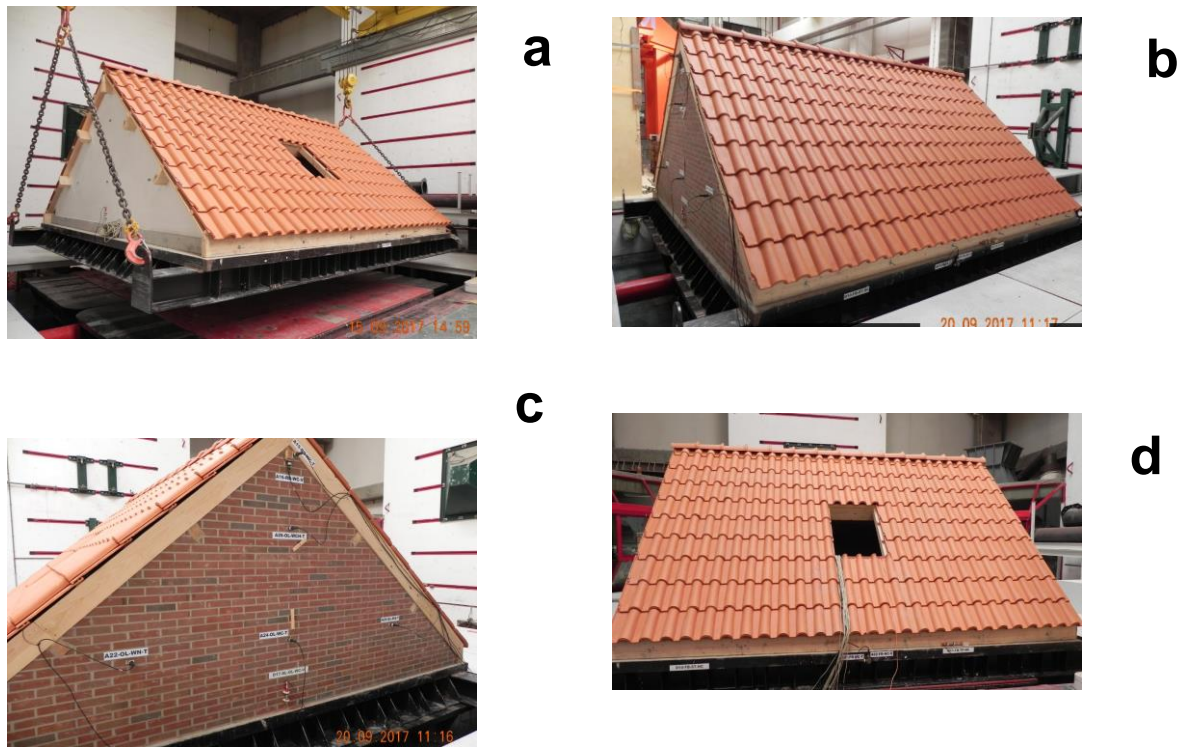


Figure 1.4 Views of the full-scale roof substructure built in LNEC, Lisbon, Portugal: (a) North-East elevation; (b) South-West elevation; (c) West elevation; (d) North elevation.

On the other hand, the experimental work carried out previously, supported by reliable numerical activities and risk models, suggested that the probability of structural collapse occurring in the Groningen region, according to the expected hazard, is rather low, representing only a limited fraction of the overall seismic risk. Therefore, while the construction and preparation of the LNEC test specimens was done, the focus of the overall study shifted to understanding and evaluating the different damage levels experienced by these structural typologies. Emphasis was then placed on the attainment of initial structural damage states and on the response of non-structural components, which in many cases govern the building performance in terms of economic losses and downtime.

Therefore, a plaster layer was applied on the East gable of the roof substructure in order to evaluate the specimen's response when subjected to low-intensity tests, with particular attention to the occurrence of the first damage states and their evolution, and to better characterise its seismic performance at different ground motion intensities. This information is most valuable for a refined characterisation of the overall seismic risk.

Finally, after the collapse of the gable walls, a quasi-static pushover test was performed on the timber roof system in order to complete the characterisation of the different structural components of the terraced house specimens.

1.2 Geometry of the specimen

The second test specimen built at the LNEC laboratory, in Lisbon, shown in Figure 1.4, was a full-scale timber roof with ceramic tiles, supported on URM gable walls and on a RC slab. The prototype was 5.82 m long, 5.46 m wide and 2.45 m high with a total mass M of 17.8 t. Table 1.1 specifies the masses associated to each structural element.

The East gable wall was made of load-bearing calcium silicate (CS) bricks, while the West gable wall was composed of two URM leaves: the inner load-bearing leaf was also made of CS bricks and the outer leaf was made of clay bricks without any load-bearing function. The

outer leaf was not present in the East façade, simply because the specimen was meant to represent the end-unit of a set of terraced houses.

Table 1.1 Masses of the different structural elements characterising the specimen.

Side	CS Wall [t]	Clay Wall [t]	RC Slab [t]	Roof [t]
North	-	-	11.40	2.83
South	-	-		
West	1.16	1.18		
East	1.16	-		

Figure 1.5 presents the plan view at the base of the specimen and the horizontal direction of shaking. The entire specimen was supported on the steel foundation built for the previous specimen, with the 0.16 m slab fixed to the steel foundation. Both CS gable walls were supported on the concrete slab, while the outer clay brick wall was built directly from the steel foundation (which has a U-shaped profile filled with reinforced mortar at the base of the wall), see Figure 1.4 and Figure 1.5.

An air gap of 80 mm was left between the two leaves, as usually seen in common practice. L-shaped steel ties with a diameter of 3.1 mm and a length of 200 mm were inserted in the 10 mm-thick mortar bed-joints during the laying of the bricks, ensuring the connection between the two masonry leaves. They were placed as shown at the elevation view of the CS inner leaf wall in Figure 1.6. In particular, the L-hook side was embedded into the inner CS wall for a length of 70 mm, while the “zigzag” extremity was embedded into the clay masonry for a length of 50 mm. Figure 1.6 shows the elevation views of the specimen’s timber roof planks and CS walls. The blue dots indicate the locations of the steel ties connecting the two leaves, with a density of about two per square meter. Figure 1.7 shows, instead, the elevation view of the specimen’s outer leaf.

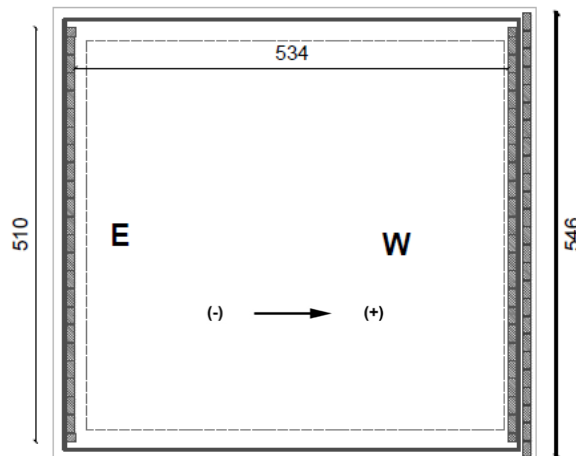


Figure 1.5 Plan view of the specimen's base. The arrow indicates the positive direction of the shake table motion.

North Elevation

South Elevation

West Elevation

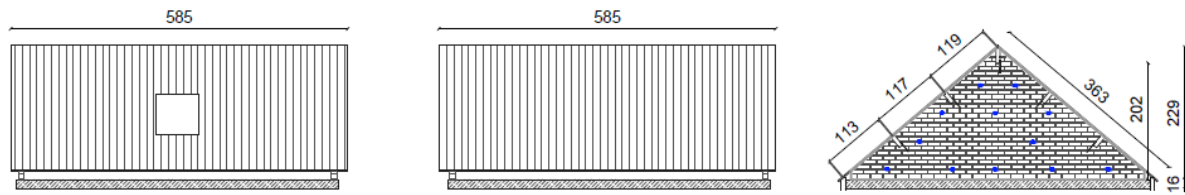


Figure 1.6 Elevation views of the specimen's timber roof planks and CS walls (dimensions in cm).

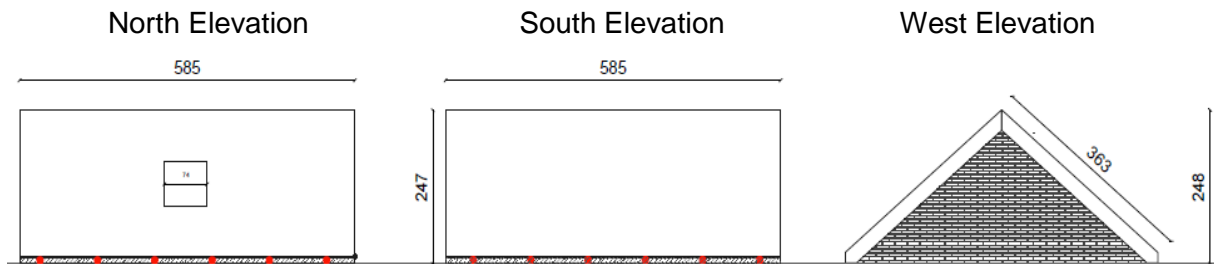


Figure 1.7 Elevation views of the specimen's roof and clay outer leaf.

The two gable walls in the transverse façades supported the roof beams of the 42° pitched timber roof. The timber beams at the slab level, instead, were attached directly on the longitudinal sides of the slab, where indicated by the red dots in Figure 1.7. A rectangular opening with 0.74 m x 0.70 m was left on the North side of the roof, granting access to the interior. On the other hand, a rigid steel-frame was installed in the interior of the specimen. This structure will be a rigid reference system for direct measurements of the floor, walls and roof displacements.

1.3 Building construction details

It is well known among the engineering community that construction details can significantly affect the seismic response of a structure, especially a URM building. Observation of damage caused by major earthquakes, as well as laboratory tests (Tomažević et al. 1991, Magenes et al. 2014) have shown that the role of the connections between horizontal and vertical structural elements is of primary importance for ensuring a good structural performance. The construction details of the specimen were representative of the Dutch common practice of the 1960s and 1970s.

Figure 1.8 shows pictures of the specimen's construction: the preparation of the steel base and the slab positioning; the attachment of timber plates to the slab, the reference frame for the instrumentation and the temporary supports for the timber roof beams; the walls as definitive support for the timber beams; the completed East and West walls; and views of the specimen with the laying of the tiles for roof completion.

Additionally, Figure 1.9 presents details of the construction of the specimen's walls and Figure 1.10 some details of the connections between structural elements. In Figure 1.9 (b), the steel ties connecting the two masonry leaves in the West wall are visible, although Figure 1.10 (d) shows that connection in more detail. The timber beams of the roof are supported by the transverse CS gable walls only, whereas this connection was further reinforced by the presence of L-shaped steel anchors, as shown in Figure 1.9 (c), as well as in Figure 1.10 (c).

The pitched timber roof, with 42° of inclination, is a simple structure consisting of one ridge beam, two timber plates on the sides of the RC slab and two girders per side between the ridge beam and the timber plates, at approximately 1.2 m of distance. As mentioned above, the timber plates, belonging to the roof but positioned at the slab level, are attached to the longitudinal sides of the slab by means of 100 cm-spaced 10 mm-diameter threaded bars cast

into the RC slab, as visible in Figure 1.10 (a) and (b). Figure 1.10 (a) illustrates the design detail of that connection, while (b) shows a picture of the same detail taken during the specimen's construction.

Tongue and groove planks, with a width equal to 182 mm and a thickness of 18 mm, were nailed on top by means of two 60×2 mm nails at each intersection, as foreseen in Figure 1.11. The in-plane stiffness of the timber roof diaphragms is essentially provided by the nailed connections between beams and planks, as well as by the effectiveness of the tongue and groove joints. The roof has been completed by the installation of clay tiles.

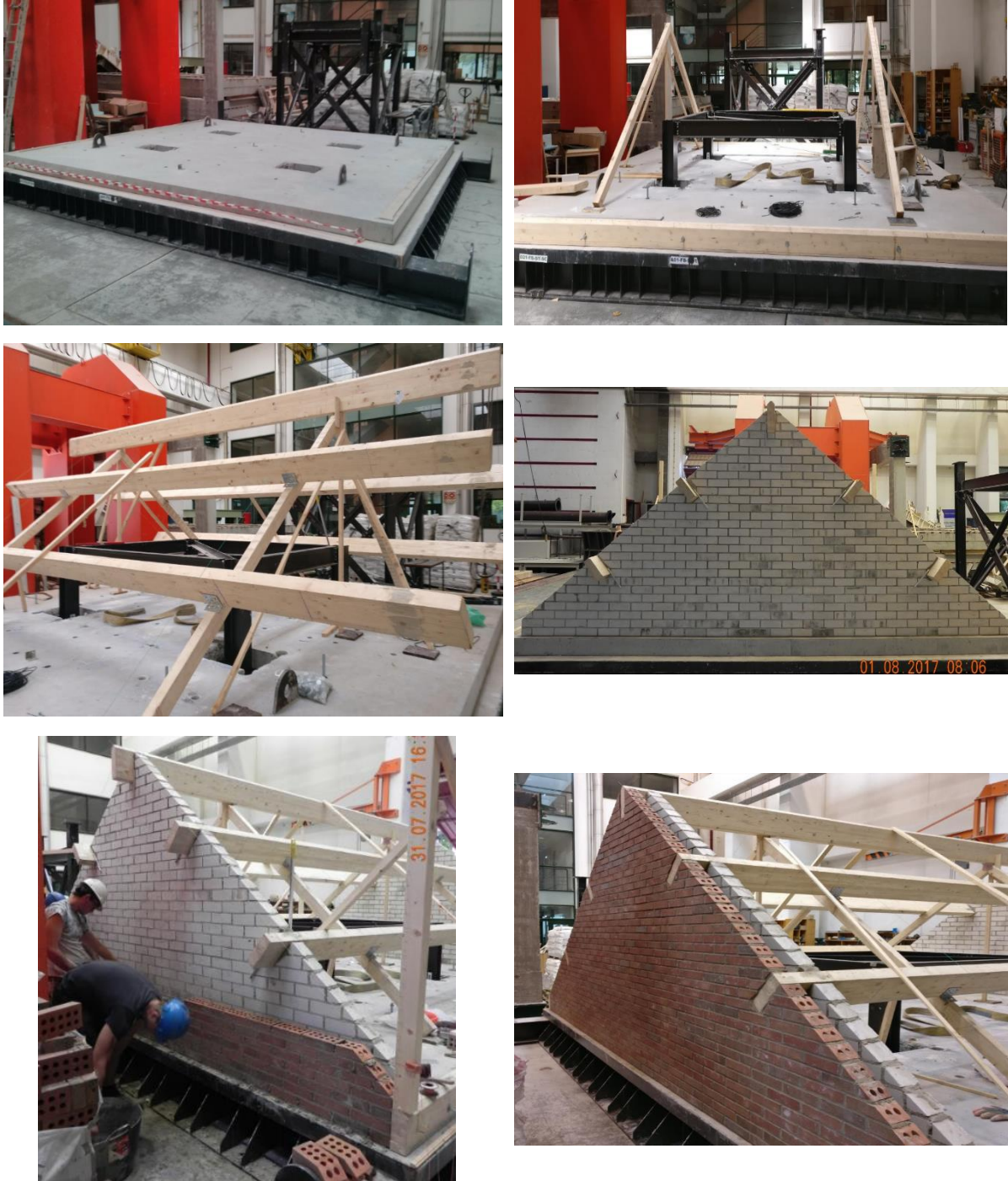




Figure 1.8 Construction of the specimen.

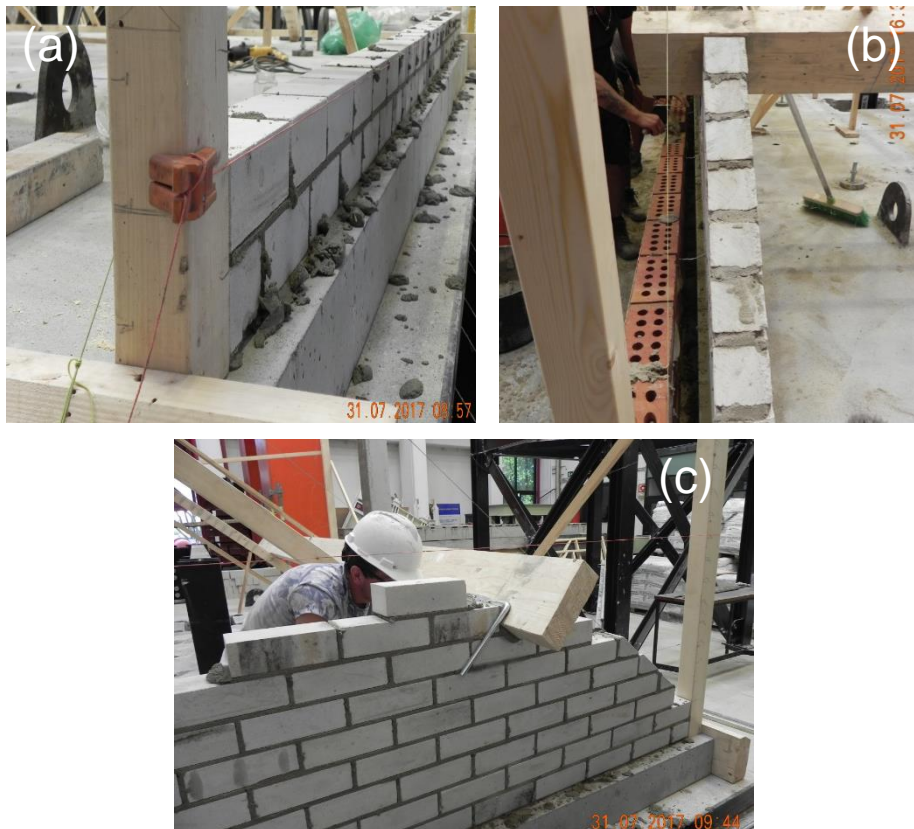
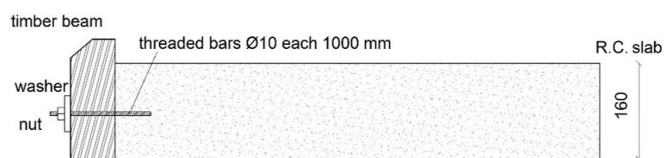
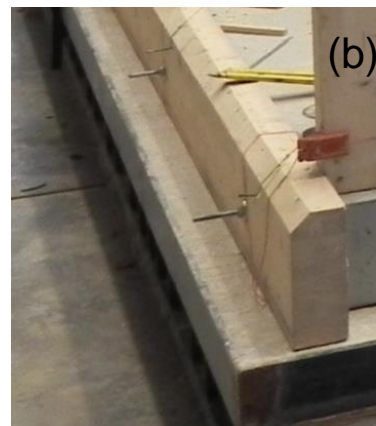


Figure 1.9 Construction details of the specimen's walls: (a) building phase of East CS wall; (b) building phase of outer leaf in West wall; (c) connection of timber roof beam to CS walls.

(a)



(b)



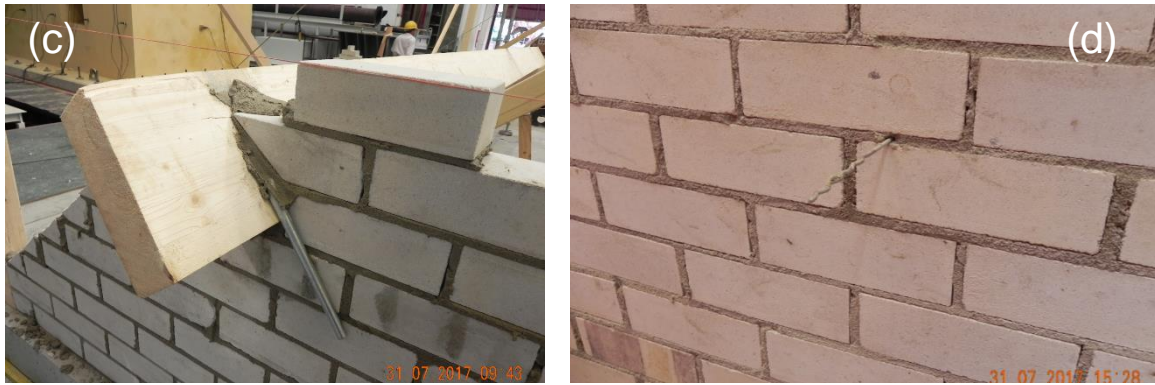


Figure 1.10 Details of the connections: (a,b) between the RC slab and the timber beam; (c) between timber beams and the walls; (d) between the two unreinforced masonry leaves.

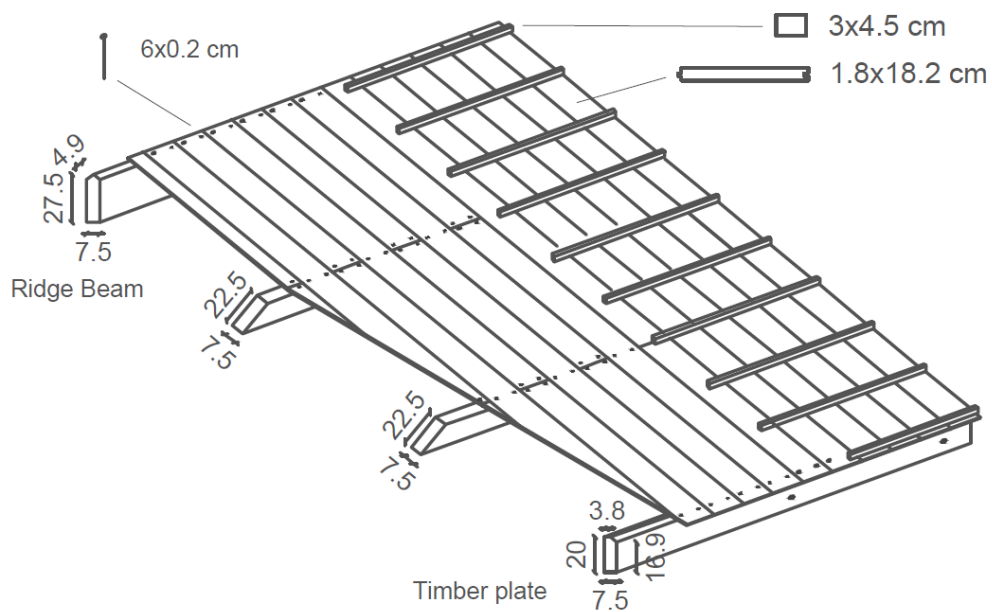


Figure 1.11 Geometry and details of the timber roof diaphragms (dimensions in cm).

Table 1.2 indicates the masses of the different elements characterising the roof structure, which, together with the information of Table 1.1 allows for the computation of inertia forces on the specimen during the shake table test.

Table 1.2 Masses of the different elements characterising the roof of the specimen.

Element	Mass [t]
Timber planks	0.442
Horizontal profiles (for the positioning of tiles)	0.096
Timber elements around the holes	0.008
Beams (including ridge beam and timber plates)	0.295
Tiles	1.970
Total	2.813

2 MATERIALS CHARACTERISATION

This part of the experimental campaign allowed the mechanical properties of the building materials employed for the construction of the specimen to be determined, similarly to the previous campaigns (Graziotti et al. 2015, Tomassetti et al. 2017). It comprised strength tests on mortar samples and on masonry blocks, as well as tests on small masonry assemblages, such as compression tests on *wallettes* and bond wrench tests on *triplets*. The dimensions of the CS units were 212 mm × 102 mm × 71 mm. The clay bricks, on the other hand, were perforated with ten vertical holes, having a void ratio of 17% and dimensions of 211 mm × 100 mm × 50 mm. The flexural and compressive strength of the mortar were determined according to the prescriptions of EN 1015-11 (CEN 1999b), while the compressive strength tests on the masonry blocks were performed according to EN 772-1 (CEN 2011). The masonry *wallettes* were tested in compression, in the direction perpendicular to the horizontal bed-joints, according to EN 1052-1 (CEN 1998b). These tests allowed the determination of the compressive strength of masonry (f_m), as well as the secant elastic modulus of masonry at 33% of the compressive strength (E_t). Bond wrench tests on CS and clay masonry *triplets* were performed in order to determine the bond strength of masonry, according to EN 1052-5 (CEN 2005).

Tests previously performed at the Delft University of Technology (TU Delft) allowed the determination of the tensile load capacity of the steel ties connecting the two masonry leaves (Messali et al. 2016). They found that the pull-in and pull-out strengths of the “zigzag” tie extremity embedded in clay masonry specimens, considering an overburden pressure of 0.3 MPa, was higher than the strengths associated with the hook extremity embedded in CS specimens and subjected to the same imposed pressure. The average pull-out and push-in strengths recorded for CS specimens were approximately 1.46 kN and 1.09 kN, respectively. Moreover, the tensile ultimate capacity of the steel anchors was approximately 4.3 kN. In Table 2.1 the green sections represent mechanical properties obtained from previously performed tests, while the remaining properties were determined during this experimental campaign.

Table 2.1 Masonry mechanical properties.

Material properties	Symbol	UM	Calcium Silicate		Clay	
			Average	C.o.V.	Average	C.o.V.
Density of mortar	ρ_{mortar}	[kg/m ³]	1617	0.034	1920	0.016
Elastic modulus of mortar (28 days)	E_{mortar}	[MPa]	7504 ^M 7997 ^C	0.105 ^M 0.022 ^C	11529 ^M 12245 ^C	0.023 ^M 0.009 ^C
Compressive strength of mortar (28 days)	f_c	[MPa]	3.70 ^M 4.84 ^C	0.259 ^M 0.223 ^C	6.28 ^M 8.18 ^C	0.239 ^M 0.017 ^C
Flexural strength of mortar (28 days)	f_t	[MPa]	2.50 ^M 2.57 ^C	0.143 ^M 0.133 ^C	3.67 ^M 3.45 ^C	0.104 ^M 0.014 ^C
Density of masonry units	ρ_b	[kg/m ³]	1887	0.019	1593	0.019
Standard compressive strength of masonry units	f_b	[MPa]	18.72	0.115	63.23	0.102
Tensile strength of masonry units	f_{bt}	[MPa]	2.74	0.06	4.78	0.20
Elastic modulus of masonry units	E_b	[MPa]	8990	0.36	7211	0.53
Density of masonry (<i>wallettes</i>)	ρ_{mw}	[kg/m ³]	1796	0.005	1833	0.009
Compressive strength of masonry in the direction perpendicular to bed joints	f_m	[MPa]	7.03	0.067	16.17	0.073
Elastic modulus of masonry in the direction perpendicular to bed joints (33% f_m)	E_m	[MPa]	6090	Preliminary results	12661	Preliminary results
Density of masonry (<i>triplets</i>)	ρ_{mt}	[kg/m ³]	1817	0.009	1815	0.011
Flexural bond strength	f_w	[MPa]	0.33	0.240	0.19	0.527

^M = referred to full scale model

^C = referred to characterisation tests specimens

2.1 Mortar characterisation tests

2.1.1 Characterisation and identification of samples before hardening

The bedding mortar used in the masonry with calcium silicate blocks is different from the one used in the masonry with clay bricks. Both mortars are pre-dosed with cement and hydraulic lime, with the references of the products used in the two bedding mortars shown in Figure 2.1.



Product used in bedding mortar
for calcium silicate blocks
ref.:150102 t.h.t.



Product used in bedding mortar
for clay bricks
ref.: 1401151030 t.h.t.

Figure 2.1 Types of product used in each bedding mortar.

Since there are two types of products for manufacturing the mortars, the amount of water used for each one is different. The amount of water was defined by construction professionals from the Netherlands and was measured by the LNEC technicians. Table 2.2 shows the adopted percentage of water for each mortar. These values were measured by Dutch construction professionals that prepared the mortars and are presented in Table 2.2.

Table 2.2 Adopted amount of water for each type of mortar.

Type of mortar	Water [kg]	Product [kg]	Water / product ratio [%]
Bedding mortar for calcium silicate blocks	2.6	25 (1 bag)	10.3
Bedding mortar for clay bricks	3.5	25 (1 bag)	14.2

The mortar samples were collected by LNEC technicians during the construction of the full-scale model and during the construction of the specimens for characterisation tests (*wallettes* and *triplets*). Figure 2.2 illustrates the construction of the full-scale model in one of the phases in which the mortar samples were collected. Figure 2.3 illustrates the construction of masonry characterisation specimens.



Figure 2.2 Construction of the full scale model at the time of collection of mortar samples.



Figure 2.3 Construction of characterisation specimens at the time of mortar sampling.

The mortar samples were collected directly from the *in situ* mortar mix and then moulded into standard moulds measuring 160 mm x 40 mm x 40 mm, as shown in Figure 2.4.

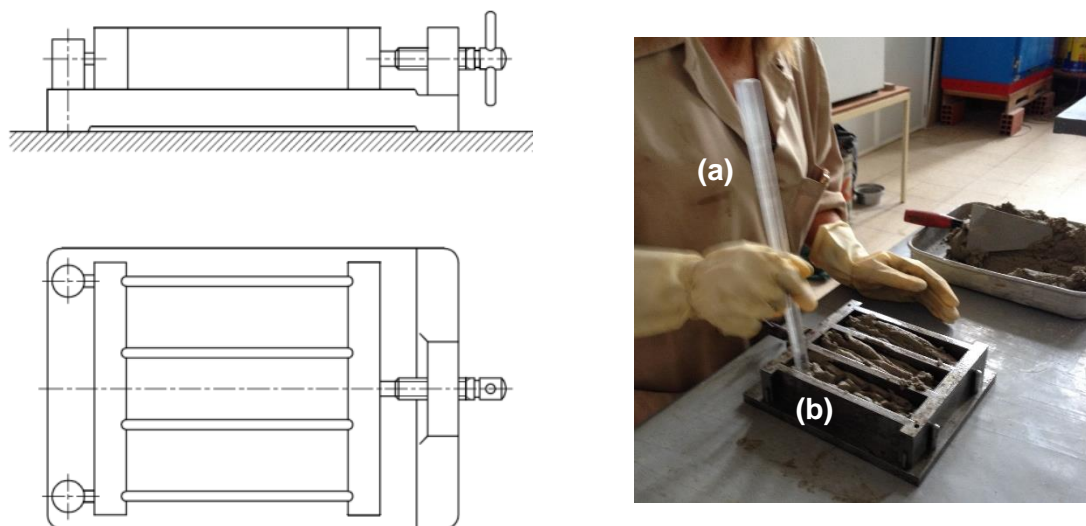


Figure 2.4 Moulding of masonry specimens: (a) pestle and (b) mould.

The designation of the mortar samples is conformant with the following description:

- | | |
|-------|--|
| MS_1 | First mortar collection for calcium silicate blocks removed from the walls of the model. |
| MS_2 | Second mortar collection for calcium silicate blocks removed from the walls of the model. |
| MS_C | Mortar collection for calcium silicate blocks removed from the characterisation specimens. |
| MCL_1 | Mortar collection for clay bricks removed from the walls of the model. |
| MCL_C | Mortar collection for clay bricks removed from the characterisation specimens. |

For each mortar collection the respective mortar mix was observed and all its constituents were measured. Table 2.3 shows the date and the water / product ratio for each batch corresponding to the collection of the respective samples.

Table 2.3 Determination of the water / product ratio for each corresponding mortar mix collection of samples.

Identification of the sample	Date of collection	Product [kg]	Water [kg]	Water / product ratio [%]
MS_1	2017-07-31	25	2.6	10.3
MS_2	2017-07-31	25	2.7	10.7
MS_C	2017-08-01	25	2.5	10.0
MCL_1	2017-07-31	25	3.6	14.3
MCL_C	2017-08-01	25	3.5	14.0

The tests considered adequate for characterising these samples were:

- Tests for the determination of the bulk density of fresh mortar;
- Tests for the determination of the consistence of fresh mortar (by flow table).

2.1.2 Tests for the determination of the bulk density of fresh mortar

The bulk density was determined by the quotient between the sample mass and its volume, for standard compaction conditions. The adopted methodology for this test is described in the standard EN 1015-6:1998 "Methods of test for mortar for masonry – Part 6: Determination of bulk density of fresh mortar" (CEN, 1998a). The test starts by the pre-determination of the mass of the container (cylindrical cup), thus obtaining m_1 . Then, using a spatula, the cylindrical cup is filled with a first layer up to approximately half of its capacity. The contents are then compacted with 10 strokes carried out from the oscillation of the container on alternate sides. The process continues by filling the container a little over its capacity, and repeating the same compaction process as described above. Finally, the surface is levelled with the aid of a spatula by removing the excess mortar so that the surface becomes flat and coincident with the upper edge of the container. The outer surface of the container is conveniently cleaned to remove any residual mortar and the assembly is weighed (thus obtaining m_2).

Considering that the mortar mass is given by the difference between the mass of the set m_2 and the mass of the empty container m_1 , the bulk density of the mortar can be determined by the following equation.

$$D = \frac{m_2 - m_1}{V} \quad (1)$$

where:

D is the bulk density [kg/m^3]

m_2 is the mass of the container with mortar [kg];

m_1 is the mass of the container [kg];

V is the volume of the container [m^3].

Figure 2.5 shows some phases of the test being performed, while the results obtained for the collected mortar are given in Table 2.4.



Figure 2.5 Carrying out the determination of bulk density of fresh mortar.

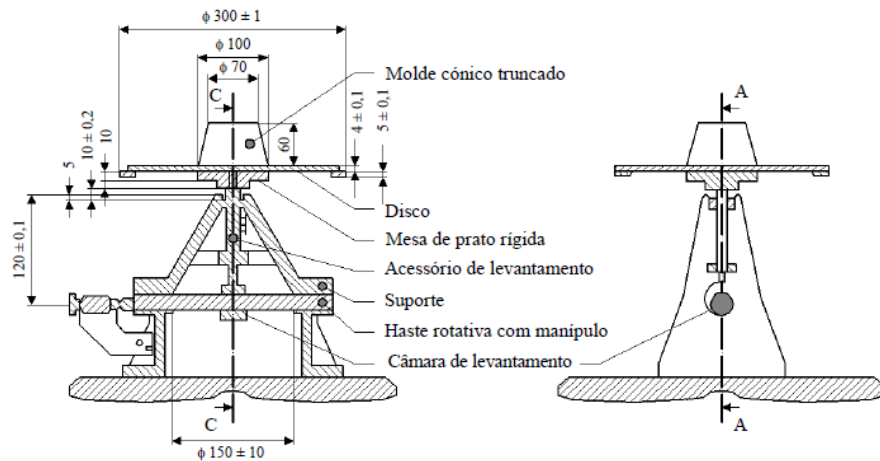
Table 2.4 Results obtained for the determination of bulk density of all mortars.

Identification of the sample	m_1 [kg]	m_2 [kg]	Bulk density [kg/m ³]
MS_1	0.463	2.002	1538
MS_2	0.463	2.105	1642
MS_C	0.463	2.130	1666
Average S			1617
Standard deviation S			55.58
Coefficient of variation [-]			0.034
MCL_1	0.463	2.350	1890
MCL_C	0.463	2.409	1950
Average CL			1920
Standard deviation CL			30.00
Coefficient of variation [-]			0.016

2.1.3 Tests for the determination of the consistence of fresh mortar (by flow table)

The purpose of this test is to determine the consistency of the mortar in its fresh state. The consistency is a measure of the fluidity of the fresh mortar, measuring the deformation of the mortar when subjected to external forces. The methodology adopted for this test is described in the standard EN 1015-3:1999 "Methods of test for mortar for masonry – Part 3: Determination of consistency of fresh mortar (by flow table)" (CEN, 1999a). The test begins by moistening the table and the mould after ensuring that they are properly cleaned, then the mould is placed centred on the table and the mortar is introduced in two equal layers. Both layers are compacted with 25 strokes with the compaction bar, making sure that each stroke reaches the full thickness of the layer to ensure uniform filling of the mould. The excess mortar is then extracted with the spatula, removing it and wiping with a cloth to leave the table dry and clean. Approximately 15 seconds later, the mould is raised slowly and 15 strokes are applied at a rate of 1 strokes per second in order to spread the mortar. The diameter (in millimetres) of the scattering is measured in two orthogonal directions (d_1 , and d_2). The mortar spreading is expressed in millimetres and is the result of the average values d_1 and d_2 .

Figure 2.6 (a) presents a schematic representation of the spreading table and in Figure 2.6 (b) some phases of the tests performed are illustrated. The results obtained for all mortar samples collected are given in Table 2.5.



(a)



(b)

Figure 2.6 Determination of consistence of fresh mortar by scattering: (a) schematic representation of equipment; (b) test run.

Table 2.5 Results obtained in the determination of the consistency of fresh mortar for all samples collected.

Identification of the sample	d ₁ [mm]	d ₂ [mm]	Consistency [mm]
MS_1	134	140	137
MS_2	143	137	140
MS_C	157	159	158
Average S			145
Standard deviation S			9.27
Coefficient of variation [-]			0.064
MCL_1	164	157	160
MCL_C	163	165	164
Average CL			162
Standard deviation CL			2.00
Coefficient of variation [-]			0.012

2.1.4 Characterisation and identification of specimens (hardened mortar)

After the samples were collected, they were used in the construction of the specimens to perform the physical and mechanical tests at three different ages: 10 days, 20 days and 28 days, as shown in Figure 2.7. These tests consist on determining the dynamic modulus of elasticity and determining the bending and compressive strengths. The storage of the specimens in a controlled environment followed the requirements of standard EN 1015-11:1999 "Methods of test for masonry – Part 11: Determination of flexural and compressive strength of hardened mortar" (CEN, 1999b) which correspond to placing the mould in a plastic

bag of polyethylene for 2 days, ensuring a relative humidity of $95 \pm 5\%$, in a room conditioned at 20 ± 2 °C and a relative humidity of $65 \pm 5\%$. Subsequently, the specimens were demoulded and kept under the aforementioned curing conditions for 5 days, after which the specimens were removed from the bag and remained in the same room (at 20 ± 2 °C and at a relative humidity of $65 \pm 5\%$) until the date of the test. Figure 2.8 illustrates the reported curing conditions of some of the specimens.



Figure 2.7 Part of mortar specimens.



Figure 2.8 Curing conditions of mortar specimens.

The designation of the specimens is the same used in the samples, but with an underscore and a number identifying each specimen. The characteristics of the various specimens of the two types of mortar are presented in Annex V.

Since the tests for the determination of the dynamic modulus of elasticity are non-destructive, the same specimens were also used for the bending and compression strength tests.

The selected tests for these samples were, thus:

- Tests to determine the dynamic modulus of elasticity;
- Tests for determination of flexural and compression strengths.

2.1.5 Tests for the determination of dynamic modulus of elasticity

The modulus of elasticity of a coating mortar is a property that translates its ability to absorb stresses and thus deformations. Thus, the quality and durability of a mortar coating are directly related to its modulus of elasticity. The dynamic modulus of elasticity was determined by the procedure described in standard NP EN 14146:2006 "Test methods for natural stone. Determination of dynamic modulus of elasticity (by measuring fundamental resonance frequency)" (CEN, 2006). This is a non-destructive test which consists in determining the resonance frequency of prismatic specimens through a vibration induced longitudinally to the test specimen. The specimen is attached to the measuring apparatus through its central part and is subsequently induced to vibrate at one of its extremities, with such vibration being received by a sensor placed at the other end of the specimen after having passed its entire length. In a frequency spectrum, we can observe the highest peak corresponding to the frequency of the specimen itself. Figure 2.9 shows one of the test specimens as well as the type of plot obtained.

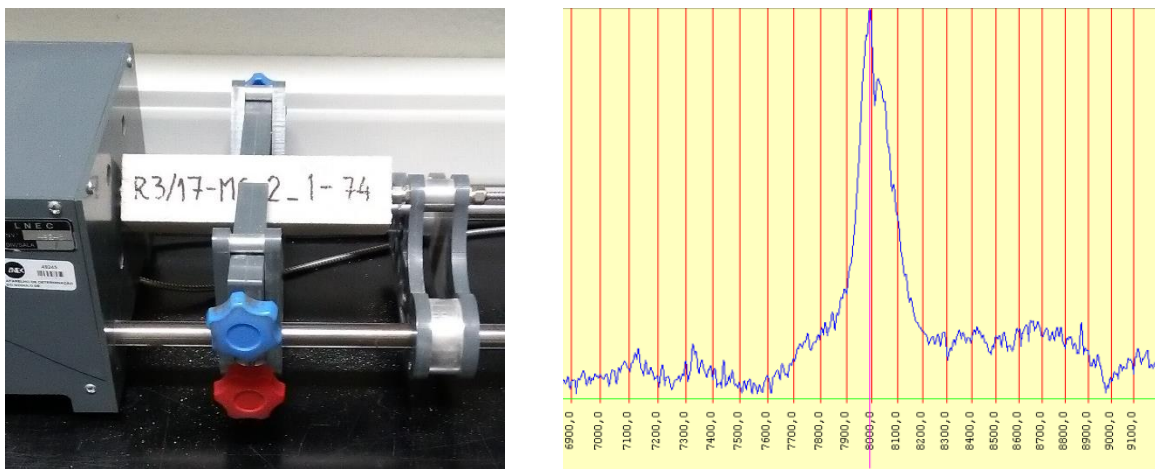


Figure 2.9 Carrying out the test to determine the dynamic modulus of elasticity and plot obtained.

From the observation of the frequency plot associated with each specimen it is possible to determine the fundamental resonance frequency (F) for each of them, which corresponds to the lowest frequency at which a maximum oscillation amplitude is obtained. After the specimens have been measured and weighed, and their resonance frequency determined, the dynamic modulus of elasticity was calculated using the following formula:

$$E_d = 4L^2 \times F^2 \times \rho \times 10^{-6} \quad (2)$$

where:

E_d is the dynamic modulus of elasticity [MPa];

L is the length of the specimen [m];

F is the longitudinal frequency of resonance [Hz];

ρ is the bulk density [kg/m^3].

In order to establish a relation between the days of maturation and the mechanical properties of the mortar, the results of the tests for the determination of the dynamic modulus of elasticity of the bedding mortar for calcium silicate blocks specimens (MS) for 10 days, 20 days and 28 days of age are presented in detail in Annex V and shown in Figure 2.10 to Figure 2.12.

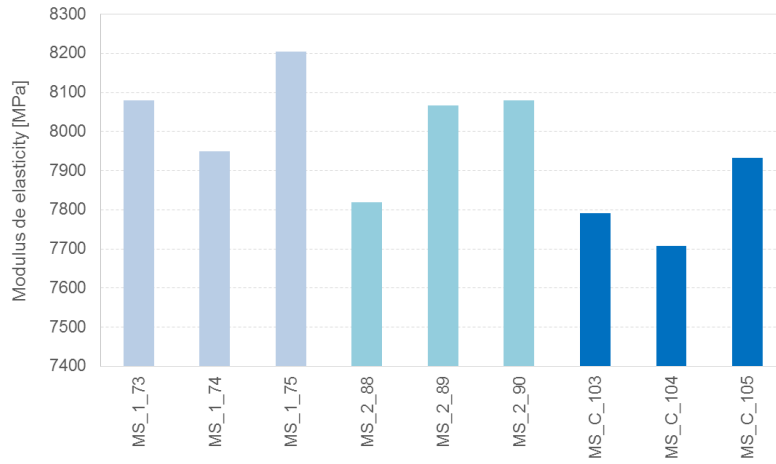


Figure 2.10 Test results for the determination of the dynamic modulus of elasticity of bedding mortar for the calcium silicate blocks (MS) after 10 days of age.

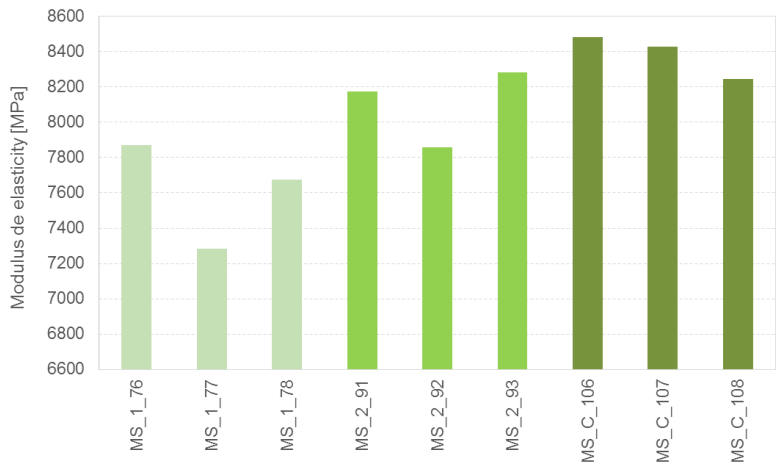


Figure 2.11 Test results for the determination of the dynamic modulus of elasticity of bedding mortar for the calcium silicate blocks (MS) after 20 days of age.

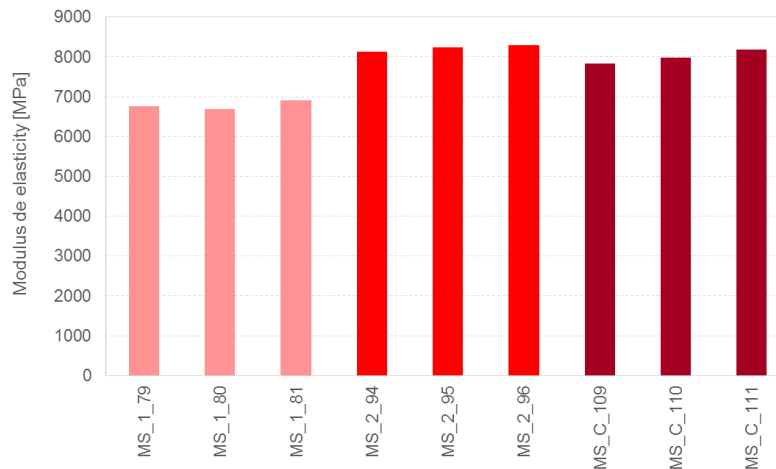


Figure 2.12 Test results for the determination of the dynamic modulus of elasticity of bedding mortar for the calcium silicate blocks (MS) after 28 days of age.

A similar analysis can be performed for the bedding mortar of clay bricks specimens (MCL). Results for 10 days, 20 days and 28 days of age are presented in detail in Annex V and shown in Figure 2.13 to Figure 2.15.

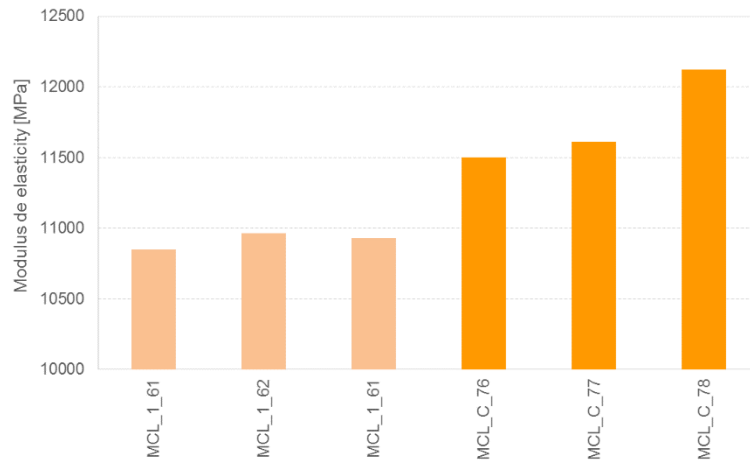


Figure 2.13 Test results for the determination of the dynamic modulus of elasticity of bedding mortar for the clay bricks (MCL) after 10 days of age.

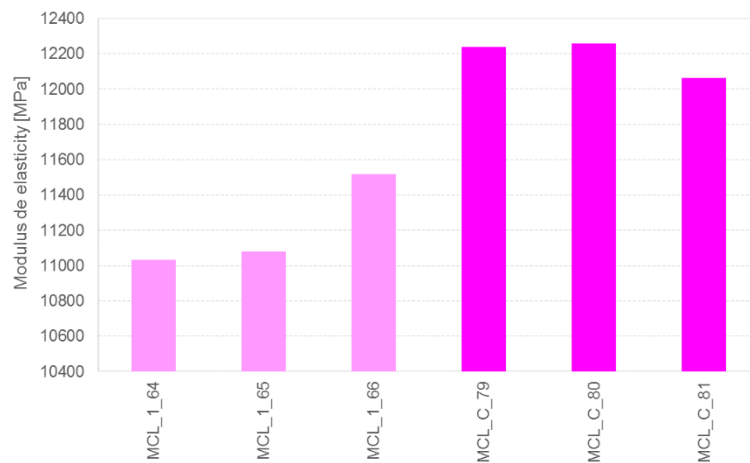


Figure 2.14 Test results for the determination of the dynamic modulus of elasticity of bedding mortar for the clay bricks (MCL) after 20 days of age.

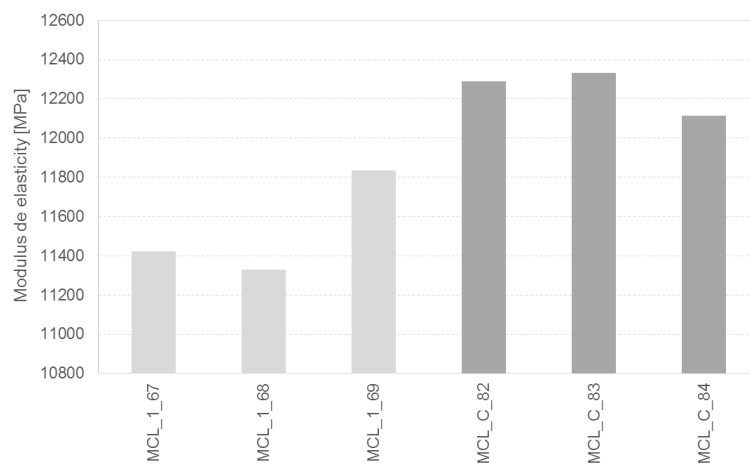


Figure 2.15 Test results for the determination of the dynamic modulus of elasticity of bedding mortar for the clay bricks (MCL) after 28 days of age.

Table 2.6 and Table 2.7 present a summary of the average dynamic modulus of elasticity obtained for the two types of bedding mortars collected directly from the full-scale model and the characterisation specimens, respectively.

Table 2.6 Summary of the average dynamic modulus of elasticity obtained for the two types of bedding mortar collected directly from the full-scale model for the different ages.

Specimens collected directly from the full scale	Age of mortar	Dynamic modulus of elasticity of bedding mortar specimens for calcium silicate blocks			Dynamic modulus of elasticity of bedding mortar specimens for clay bricks		
		Average [MPa]	Standard deviation [MPa]	C.o.V. [-]	Average [MPa]	Standard deviation [MPa]	C.o.V. [-]
	10 days	8033	132	0.016	10915	59	0.005
	20 days	7857	359	0.046	11210	269	0.024
	28 days	7504	788	0.105	11529	267	0.023

Table 2.7 Summary of the average dynamic modulus of elasticity obtained for the two types of bedding mortar collected directly from the characterisation specimens for the different ages.

Specimens collected directly from characterisation	Age of mortar	Dynamic modulus of elasticity of bedding mortar specimens for calcium silicate blocks			Dynamic modulus of elasticity of bedding mortar specimens for clay bricks		
		Average [MPa]	Standard deviation [MPa]	C.o.V. [-]	Average [MPa]	Standard deviation [MPa]	C.o.V. [-]
	10 days	7811	114	0.015	11746	332	0.028
	20 days	8384	124	0.015	12186	107	0.009
	28 days	7997	176	0.022	12245	115	0.009

The plot of Figure 2.16 shows the relation of the dynamic moduli of elasticity of the two types of bedding mortar as a function of maturation time. The dashed lines refer to the modulus of elasticity of the bedding mortars for the calcium silicate blocks and the clay bricks (MS and MCL) taken from the characterisation test specimens. The continuous lines refer to the dynamic moduli of elasticity of the bedding mortars for the calcium silicate blocks and the clay bricks taken from the real-scale model.

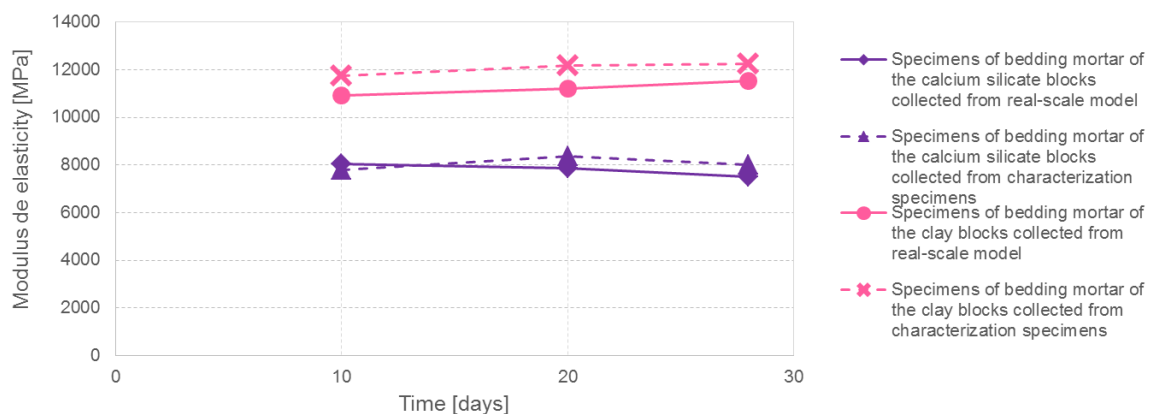


Figure 2.16 Relation between dynamic moduli of elasticity and maturation time for the two bedding mortars removed from the full scale model and the characterisation test specimens.

2.1.6 Tests for the determination of flexural and compressive strengths

Test for the determination of flexural strength

The test to determine the flexural strength was performed in accordance with the standard EN 1015-11:1999 "Methods of test for masonry – Part 11: Determination of flexural and compressive strength of hardened mortar" (CEN, 1999b). The purpose of this test is to obtain the flexural strength of the mortar (hardened mortar), by applying a half-span load to a simply supported prismatic specimen as depicted in Figure 2.17 (a). The specimen is placed on the test machine and is centred with the longitudinal axis perpendicular to the two supports, ensuring that one of the side moulding faces stays fixed on the supports. The load is applied at mid-span through an upper bearing point, and imposing a gradual force and increasing continuously, between 10 and 50 N/s, forcing the failure to occur in a range of time between 30 and 90 seconds. The maximum force supported by the specimen is recorded until failure and the flexural strength of the specimen then calculated. In Figure 2.17 (b) one of the test specimens is shown.

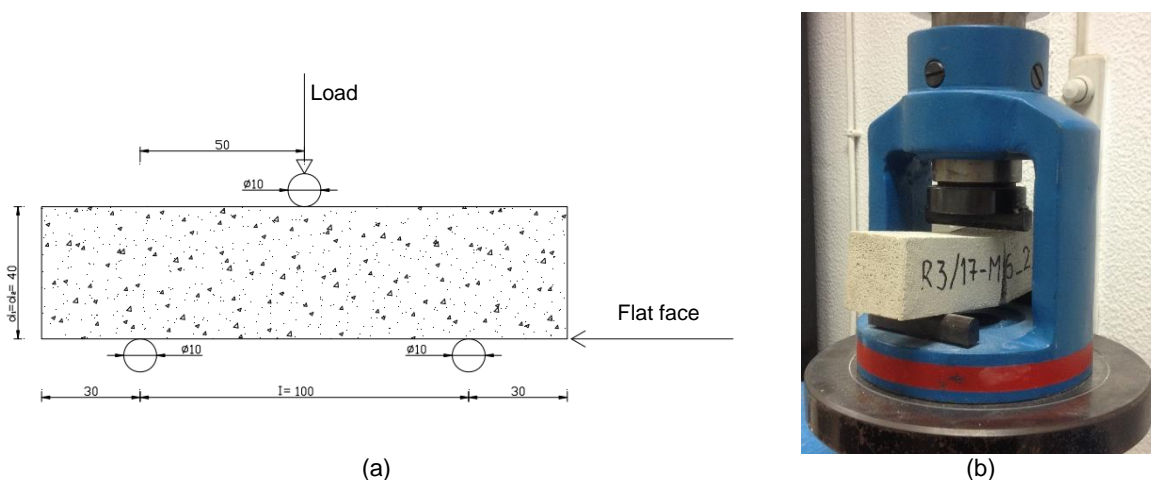


Figure 2.17 Test for determination of flexural strength: (a) scheme of positioning of the specimen and (b) specimen being tested.

The flexural strength is given by the following equation:

$$f_t = 1.5 \times \frac{F_f \times l^2}{b \times d} \quad (3)$$

where:

f_t is the flexural strength [MPa];

F_f is the maximum flexural force applied to the specimen at the moment of rupture [N];

l is the distance between the bottom rollers [mm];

b is the width of the test specimen [mm];

d is the height of the test specimen [mm].

Test for the determination of compressive strength

The test to determine the compressive strength was performed in accordance with the standard EN 1015-11:1999 "Methods of test for masonry – Part 11: Determination of flexural and compressive strength of hardened mortar" (CEN, 1999c). This test allows the determination of the compressive strength of mortar specimens (hardened mortar). This test is performed immediately after the flexural test, and on the prisms resulting therefrom, by applying a load until failure.

The specimen is placed centred on the lower plate of the machine test with the flat face in contact to the lower plate. The upper plate of the machine is lowered until it contacts the upper

face of the specimen, as shown in Figure 2.18 (a). An increasing force is then applied gradually and without shock, in order to obtain the failure between 30 and 90 seconds until the failure of the specimen. The compressive strength values determined by this method are designated by f_c . The calculation is to the following formula:

$$f_c = \frac{F_c}{A_c} \tag{4}$$

where:

f_c is the compressive strength [MPa];

F_c is the maximum compressive force applied to the specimen at the moment of failure [N];

A_c is the area of the specimen in contact with the plates of the machine test [mm²].

Figure 2.18 (b) depicts one of the specimens being tested.

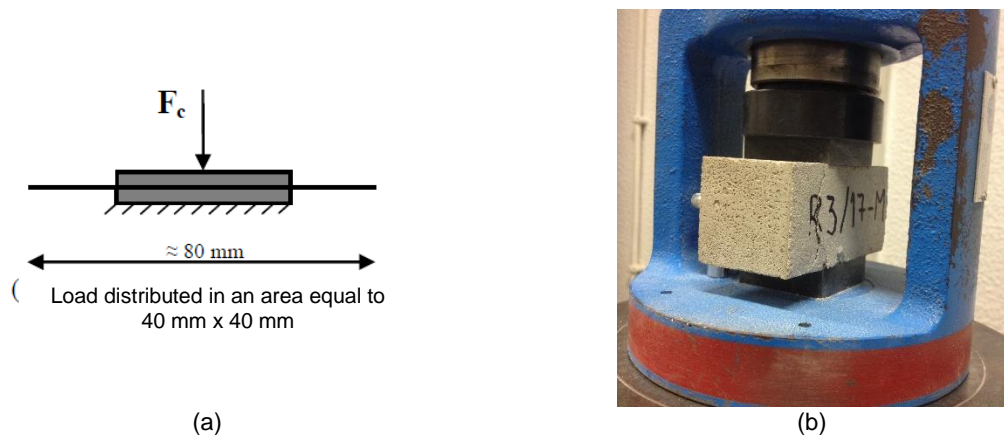


Figure 2.18 Test for compressive strength: (a) test scheme and (b) specimen being tested.

In order to obtain a relation between the maturation time and the mechanical properties of the mortars, Figure 2.19 to Figure 2.24 show the test results on flexural and compressive strengths of bedding mortar specimens for the calcium silicate blocks (MS) after 10 days, 20 days and 28 days of age. Additional results are given in Annex V. In the plots of Figure 2.22 to Figure 2.24, the compressive strength is represented with bars and the value of the modulus of elasticity for the corresponding specimens is represented by a line.

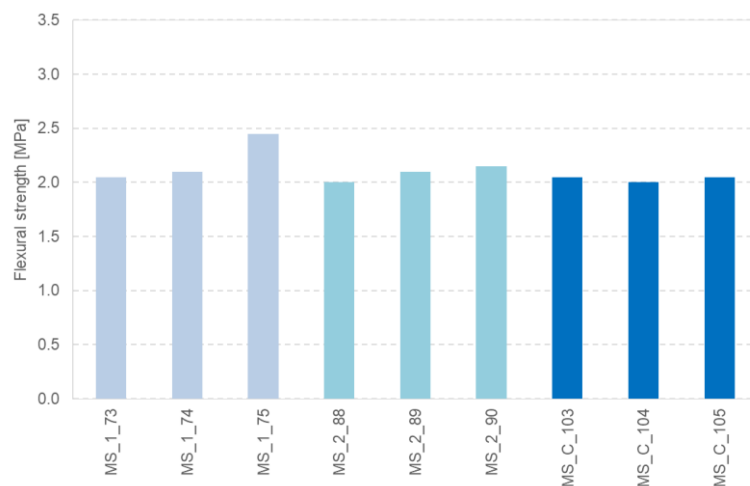


Figure 2.19 Flexural strength test results for bedding mortar specimens used with calcium silicate blocks (MS) after 10 days of age.

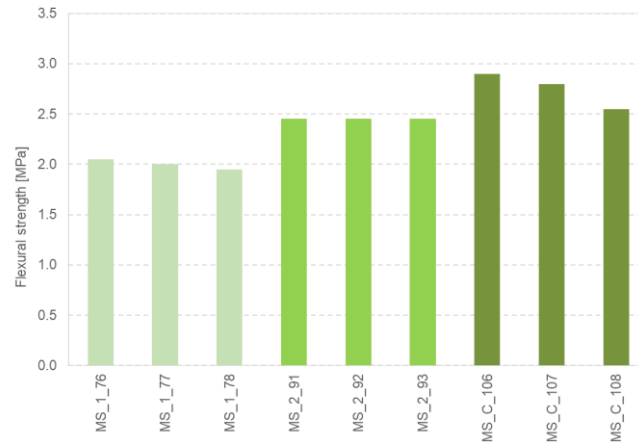


Figure 2.20 Flexural strength test results for bedding mortar specimens used with calcium silicate blocks (MS) after 20 days of age.

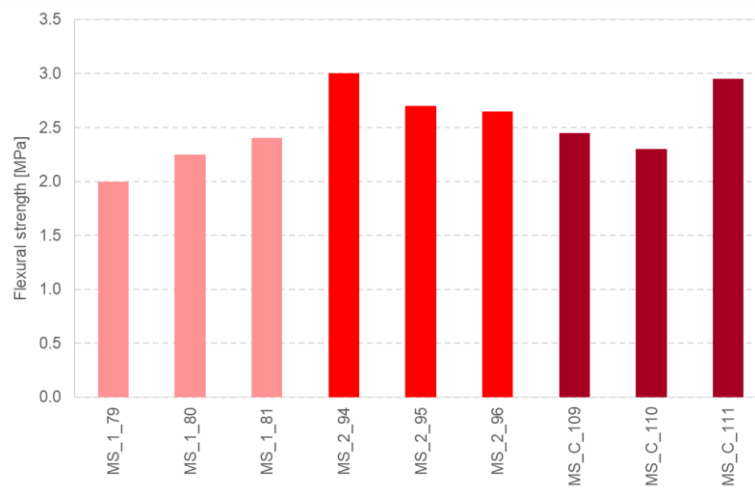


Figure 2.21 Flexural strength test results for bedding mortar specimens used with calcium silicate blocks (MS) after 28 days of age.

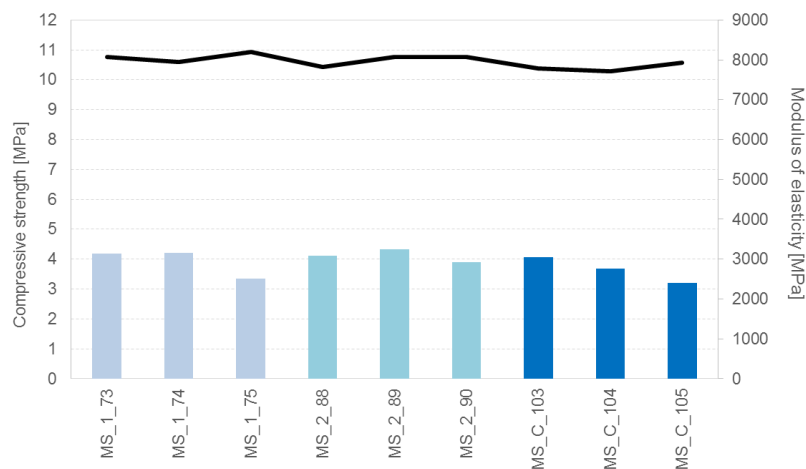


Figure 2.22 Compressive strength and modulus of elasticity test results for bedding mortar specimens used with calcium silicate blocks (MS) after 10 days of age.

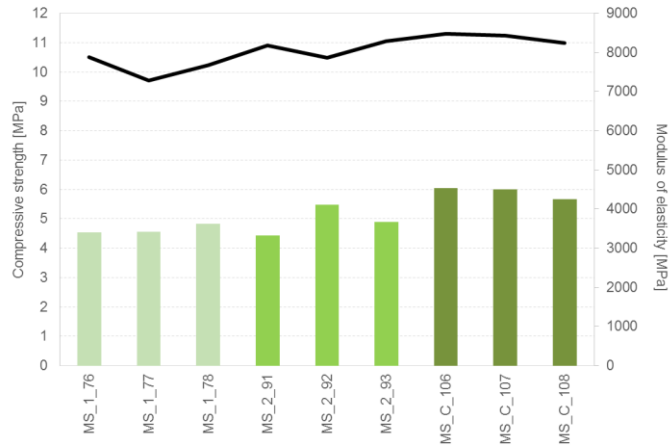


Figure 2.23 Compressive strength and modulus of elasticity test results for bedding mortar specimens used with calcium silicate blocks (MS) after 20 days of age.

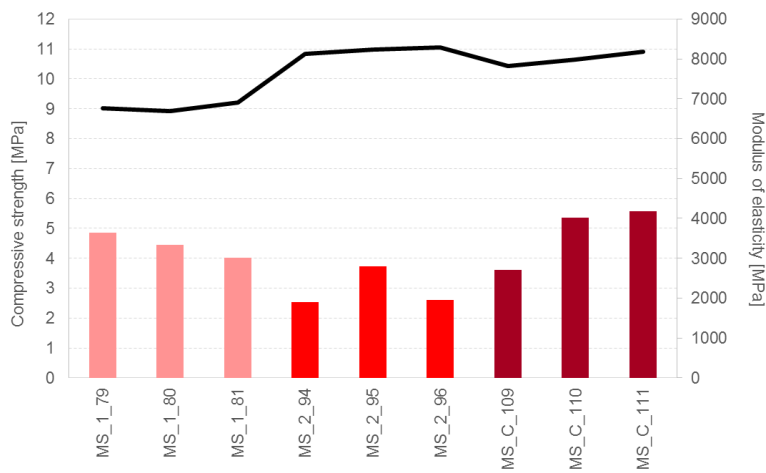


Figure 2.24 Compressive strength and modulus of elasticity test results for bedding mortar specimens used with calcium silicate blocks (MS) after 28 days of age.

Figure 2.25 presents the distribution of the flexural and compressive strengths of bedding mortars for the calcium silicate blocks (MS) after 28 days of age.

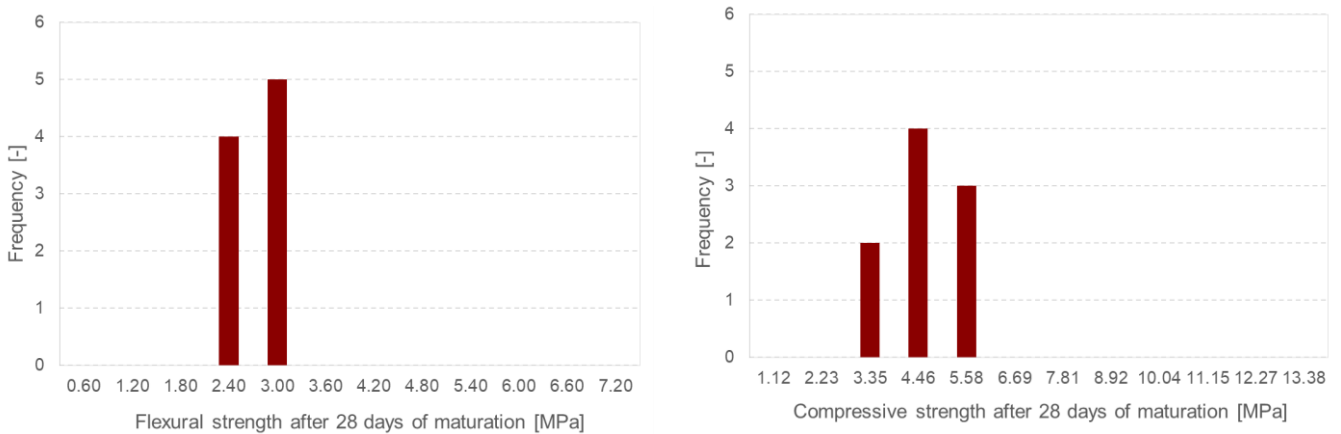


Figure 2.25 Distribution of the flexural and compressive strength of bedding mortars used with calcium silicate bricks (MS) after 28 days of age.

In order to obtain a relation between the maturation time and the mechanical properties of the mortars, Figure 2.26 to Figure 2.31 show the test results for the determination of flexural and compressive strengths of bedding mortar specimens for the clay bricks (MCL) after 10 days, 20 days and 28 days of age. Additional results are shown in Annex V. In the plots of Figure 2.29 to Figure 2.31, the compressive strength is represented with bars and the value of the modulus of elasticity for the corresponding specimens is represented by a line.

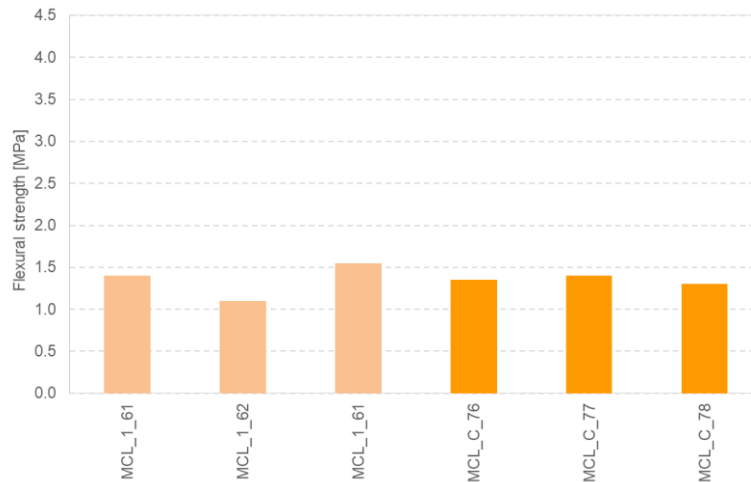


Figure 2.26 Flexural strength test results for bedding mortar specimens used with clay bricks (MCL) after 10 days of age.

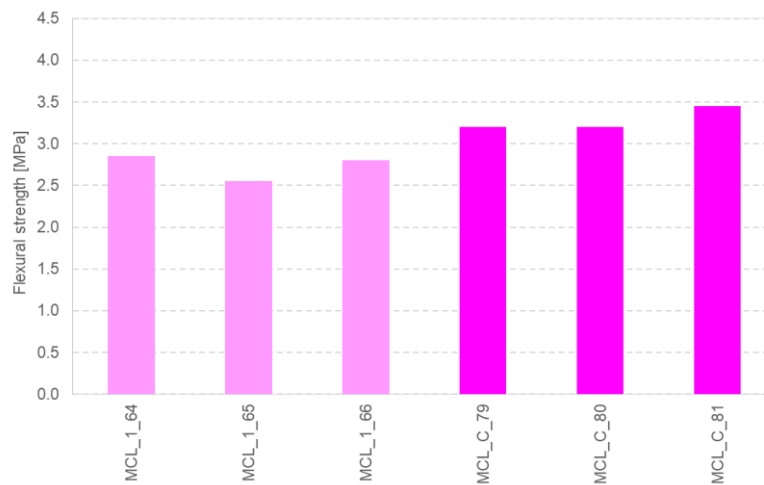


Figure 2.27 Flexural strength test results for bedding mortar specimens used with clay bricks (MCL) after 20 days of age.

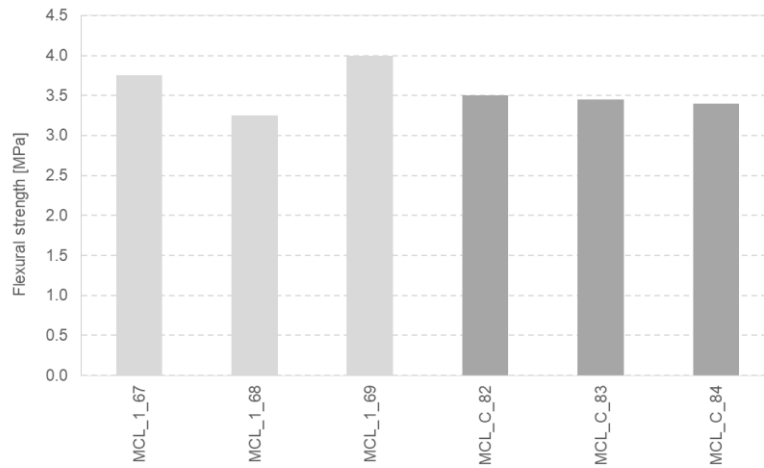


Figure 2.28 Flexural strength test results for bedding mortar specimens used with clay bricks (MCL) after 28 days of age.

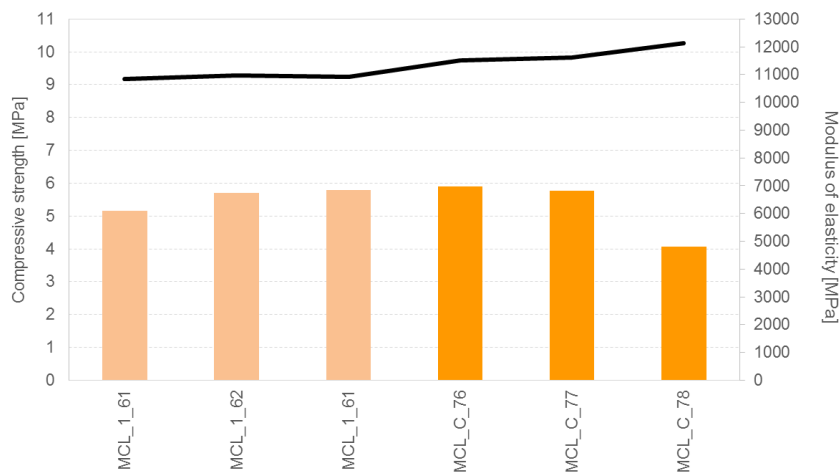


Figure 2.29 Compressive strength and modulus of elasticity test results for bedding mortar specimens used with clay bricks (MCL) after 10 days of age.

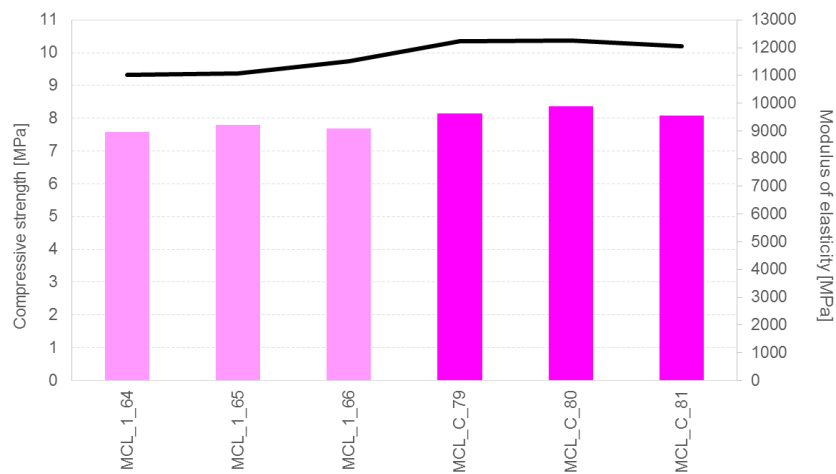


Figure 2.30 Compressive strength and modulus of elasticity test results for bedding mortar specimens used with clay bricks (MCL) after 20 days of age.

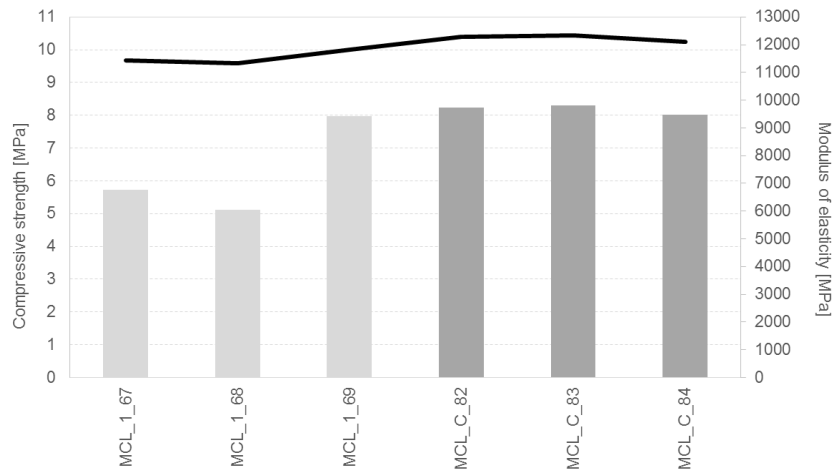


Figure 2.31 Compressive strength and modulus of elasticity test results for bedding mortar specimens used with clay bricks (MCL) after 28 days of age.

Figure 2.32 presents the distribution of the flexural and compressive strengths of bedding mortars for the clay bricks (MCL) after 28 days of age.

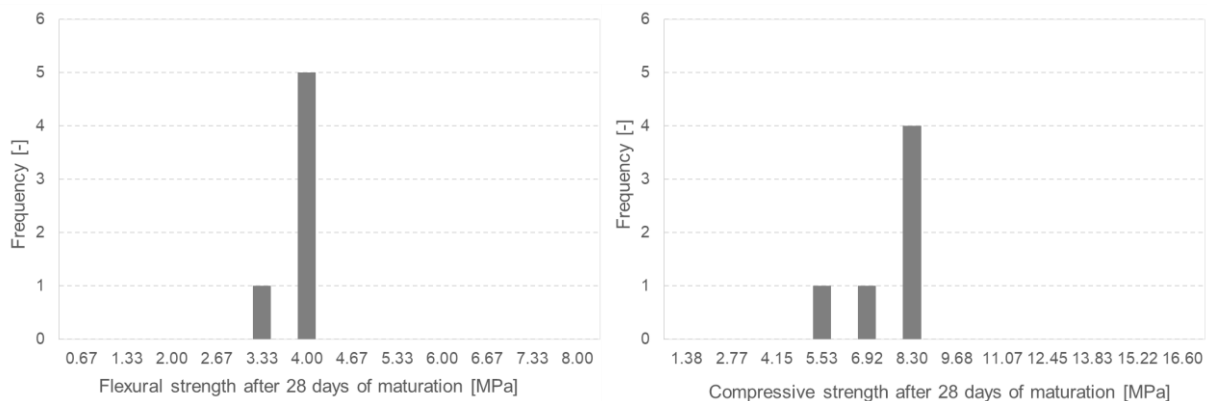


Figure 2.32 Distribution of the flexural and compressive strengths of bedding mortars for the clay bricks (MCL) after 28 days of age.

Table 2.8 and Table 2.9 show the summary of the averages of compressive and flexural strength obtained for the two types of bedding mortars collected directly from the full-scale model and the characterisation specimens, respectively.

Table 2.8 Summary of the compressive and flexural strength averages obtained for the two types of bedding mortars collected directly from the full-scale model for different ages.

Specimens collected directly from the full scale model	Type of mortar	Age of mortar	Compressive strength			Flexural strength		
			Average [MPa]	Standard deviation [MPa]	C.o.V. [-]	Average [MPa]	Standard deviation [MPa]	C.o.V. [-]
			MS	10 days	4.01	0.35	0.088	2.14
MCL	MS	20 days	4.78	0.38	0.080	2.23	0.25	0.112
		28 days	3.70	0.96	0.259	2.50	0.36	0.143
		10 days	5.55	0.35	0.063	1.35	0.23	0.170
	MCL	20 days	7.69	0.11	0.015	2.73	0.16	0.059
		28 days	6.28	1.50	0.239	3.67	0.38	0.104

Table 2.9 .Summary of the compressive and flexural strength averages obtained for the two types of bedding mortars collected directly from characterisation specimens for different ages.

Specimens collected directly from characterisation specimens	Type of mortar	Age of mortar	Compressive strength			Flexural strength		
			Average [MPa]	Standard deviation [MPa]	C.o.V. [-]	Average [MPa]	Standard deviation [MPa]	C.o.V. [-]
MS		10 days	4.12	0.44	0.106	2.03	0.03	0.014
		20 days	5.91	0.20	0.034	2.75	0.18	0.066
		28 days	4.84	1.08	0.223	2.57	0.34	0.133
MCL		10 days	5.25	1.02	0.194	1.35	0.05	0.037
		20 days	8.20	0.16	0.019	3.28	0.14	0.044
		28 days	8.18	0.14	0.017	3.45	0.05	0.014

The plots of Figure 2.33 and Figure 2.34 show the relation of the compressive and flexural strength as a function of maturation time for the two types of bedding mortar. The dashed line refers to the flexural and compressive strength of the bedding mortars taken from the characterisation test specimens. The continuous line refers to the flexural and compressive strengths of the bedding mortars taken from the full-scale model.

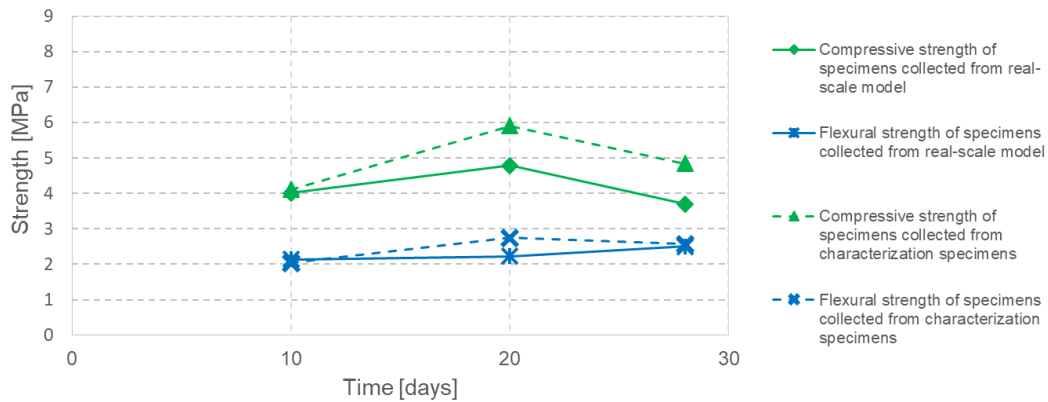


Figure 2.33 Relation between flexural and compressive strengths and maturation time of bedding mortars for the calcium silicate blocks (MS) removed from the full-scale model and the characterisation test specimens.

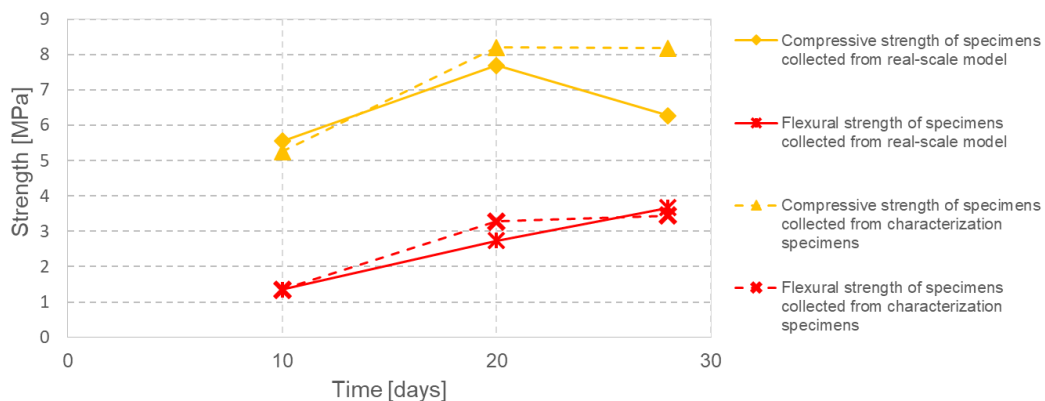


Figure 2.34 Relation between flexural and compressive strength and maturation time of bedding mortars for the clay bricks (MCL) removed from the full-scale model and the characterisation test specimens.

2.2 Block characterisation tests

2.2.1 Characterisation and identification of specimens

As previously mentioned, there are two types of masonry with corresponding two types of blocks. The inner load-bearing walls are composed of calcium silicate blocks and the outer walls are composed of perforated clay bricks. Figure 2.35 shows the two types of blocks that were tested.

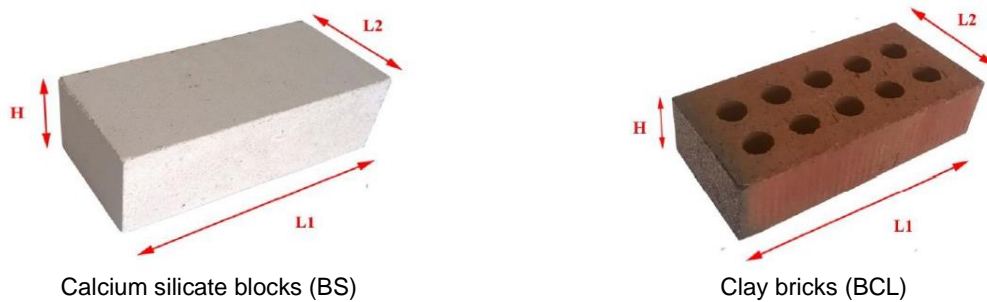


Figure 2.35 Blocks used and indication of their dimensions.

Several specimens of each type of block were collected and selected from the material used for the construction of the full-scale model and the characterisation samples (Figure 2.36 and Figure 2.37). The specimens collected were more than 30 days inside the premises of the laboratory units without specific packaging until the date of the test.

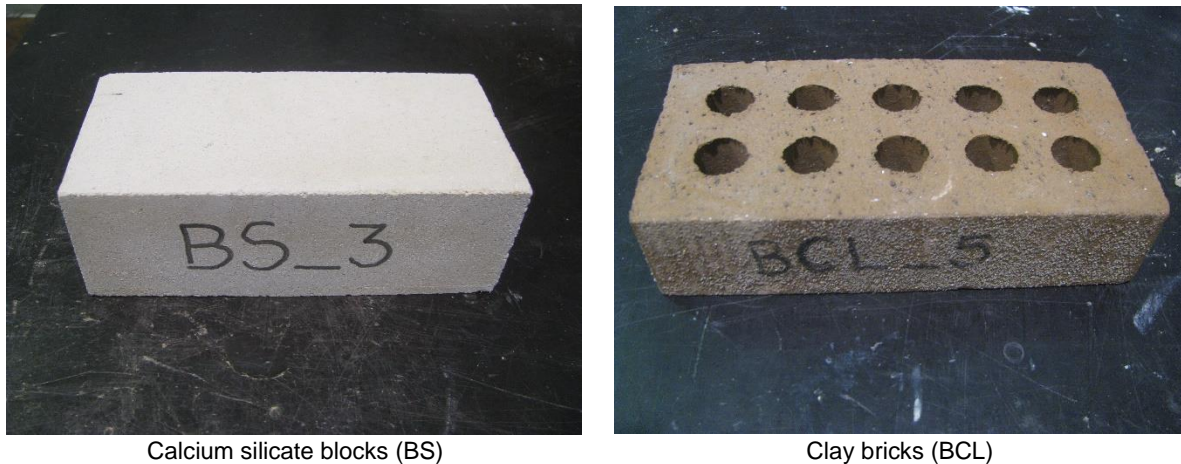


Calcium silicate blocks (BS)



Clay bricks (BCL)

Figure 2.36 Collection of test pieces.



Calcium silicate blocks (BS)

Clay bricks (BCL)

Figure 2.37 Blocks units.

The designation of the blocks is in accordance with the following:

- Calcium silicate blocks (BS);
- Clay bricks (BCL).

The drilling percentage of the perforated clay bricks is 17% (Graziotti F. et al.; 2015). In Table 2.10 the characteristics of the various specimens of the two types of blocks selected for the tests are presented, with additional details provided in Annex VI.

Table 2.10 Characteristics of the two types of blocks selected for the tests.

Type of specimen	Average Mass [kg]	Average Length (L1) [mm]	Average Width (L2) [mm]	Average Height (H) [mm]
BS	2.94	212.83	103.37	70.83
BCL	1.69	211.65	100.37	49.93

The bulk density average values for the calcium silicate and clay blocks are given in Table 2.11, with additional details provided in Annex VI.

Table 2.11 Bulk density for calcium silicate and clay blocks.

Specimen	Average bulk density	Standard deviation	C.o.V.
	[kg/m ³]	[kg/m ³]	[-]
BS	1887	36.29	0.019
BCL	1593	30.15	0.019

2.2.2 Tests for the determination of compressive strength

In order to quantify the compressive strength of the two types of blocks, the method described in EN 772-1 "Methods of test for masonry units; Part 1: Determination of compressive strength" (CEN, 2011) was used. It basically consists in placing the specimen in the test machine for the application of the load without shock, that is, in a gradual manner and with a controlled speed. The load was applied in the direction of the smallest dimension of the specimen, equal to the loading status to which the elements under analysis are subjected when inserted into the walls of the buildings. Finally, the breaking force is recorded.

The tests applied to the calcium silicate blocks were carried out on a 1000 kN-capacity test machine with a force control and a test speed of 3.2 kN/s, according to Table 2 of EN 772-1

(CEN, 2011), which presents the recommended values for the rate of application of the load according to the expected compressive strengths. Each test lasted approximately 180 s. For the clay bricks, the tests were carried out on a test machine with a capacity of 5000 kN, again with force control and a test speed of 6.4 kN/s. Each test lasted approximately 280 s.

The compressive strength values determined by this method are designated as f_b , calculated according to the following formula:

$$f_b = \frac{F_c}{A_c} \quad (5)$$

where:

f_b is the collapse compressive strength [MPa];

F_c is the maximum compressive force applied to the specimen at the time of collapse [N];

A_c is the area of the specimen in contact with the plates of the test machine [mm²].

Since the faces of the calcium silicate blocks are highly regular, it was decided to place the faces of the specimen directly in contact with the press. In the case of clay bricks, 14 specimens were tested with both surfaces smoothed by wear and 6 of the specimens were tested with a thin layer of gypsum on both sides, as shown in Figure 2.38.



Surfaces smoothed by wear



Surfaces smoothed with gypsum

Figure 2.38 Regularisation of clay specimens.

For the blocks smoothed by wear and considering that this process is carried out using a mechanical device cooled by water, the specimens were wetted. Afterwards they were heated in a ventilated oven at ± 105 °C until a constant mass was reached, as shown in Figure 2.39.



Drying of specimens



Weighing until constant mass is reached

Figure 2.39 Clay specimens smoothed by wear.

Figure 2.40 illustrates how the tests were performed to determine the compressive strength for the two types of bricks. The compressive strength was calculated considering the average

gross area of the two faces in contact with the press plates. To obtain the standard compressive strength, f_b , the compressive strength of each specimen is multiplied by a shape factor, d , which depends on the width and height of the block according to the aforementioned standard.

This test was carried out on the CS block specimens designated as BS_0 to BS_10 and on clay bricks specimens designated as BCL_0 to BCL_10 and BCL_17 to BCL_25. In Table 2.12 the compressive strength results for the calcium silicate blocks are presented.



Calcium silicate blocks (BSC)



Clay bricks (BCL)

Figure 2.40 Specimens subjected to compressive strength tests.

Table 2.12 Compressive strength for calcium silicate blocks.

Specimen	Date of test	Length (L1) [mm]	Width (L2) [mm]	Average gross area [mm ²]	Maximum force [kN]	Compressive strength [MPa]	Shape factor [-]	Standard compressive strength [MPa]
BS_0	25/07/2017	212.69	103.62	22038.94	484.7	22.0	0.87	19.1
BS_1	25/07/2017	212.84	103.39	22005.53	507.3	23.1	0.87	20.1
BS_2	25/07/2017	212.81	103.64	22055.63	452.0	20.5	0.87	17.8
BS_3	25/07/2017	213.10	103.19	21989.79	507.3	23.1	0.87	20.1
BS_4	25/07/2017	212.94	103.06	21945.60	522.7	23.8	0.87	20.7
BS_5	25/07/2017	212.66	102.12	21716.84	502.8	23.2	0.87	20.1
BS_6	25/07/2017	212.68	103.56	22025.14	505.4	22.9	0.87	20.0
BS_7	25/07/2017	212.81	103.39	22002.43	337.9	15.4	0.87	13.4
BS_8	25/07/2017	212.78	103.88	22103.59	486.0	22.0	0.87	19.1
BS_9	25/07/2017	212.70	103.73	22063.37	418.6	19.0	0.87	16.5
BS_10	25/07/2017	213.07	103.47	22046.35	481.2	21.8	0.87	19.0
Average		212.83	103.37	21999.38	473.26	21.52	0.87	18.72
Standard deviation		0.15	0.48	102.67	53.65	2.47	0.00	2.15
Coefficient of variation [-]		0.001	0.005	0.005	0.113	0.115	0.000	0.115

Figure 2.41 present two calcium silicate blocks after their failure, while in Annex VIII the figures with the obtained fractures are presented for all specimens.

In Table 2.13 the compressive strength results for the clay bricks with surfaces smoothed by wear are presented.

BS_

BS_

Figure 2.41 Calcium silicate blocks during the compressive strength test and after failure.

Table 2.13 Compressive strength for clay bricks with both surfaces smoothed by wear.

Specimen	Date of test	Length (L1) [mm]	Width (L2) [mm]	Average gross area [mm ²]	Maximum force [kN]	Compressive strength [MPa]	Shape factor [-]	Standard compressive strength [MPa]
BCL_0	28/07/2017	212.26	100.11	21249.35	1707	80.3	0.75	60.2
BCL_1	28/07/2017	209.90	101.42	21288.06	1934	90.8	0.75	68.1
BCL_2	28/07/2017	209.81	101.42	21278.93	1951	91.7	0.75	68.8
BCL_3	28/07/2017	209.88	99.56	20895.65	2068	99.0	0.75	74.2
BCL_4	28/07/2017	212.45	100.04	21253.50	1662	78.2	0.75	58.6
BCL_5	28/07/2017	213.50	102.17	21813.30	1588	72.8	0.75	54.6
BCL_6	28/07/2017	212.43	100.08	21259.99	1736	81.7	0.75	61.2
BCL_7	28/07/2017	209.89	101.38	21278.65	2036	95.7	0.75	71.8
BCL_8	28/07/2017	212.44	99.29	21093.17	1611	76.4	0.75	57.3
BCL_9	28/07/2017	213.89	98.46	21059.61	1739	82.6	0.75	61.9
BCL_10	28/07/2017	211.67	100.12	21192.40	1659	78.3	0.75	58.7
Average		211.65	100.37	21242.05	1790.09	84.31	-	63.23
Standard deviation		1.53	1.11	225.73	174.14	8.58	-	6.44
Coefficient of variation [-]		0.007	0.011	0.011	0.097	0.102	-	0.102

In order to evaluate the best type of smoothing to be made in clay bricks, tests were carried out on bricks smoothed by wear and smoothed with a thin layer of gypsum, as shown in Figure 2.42. The values of the compressive strength for the bricks tested are presented in Table 2.14.



Figure 2.42 Clay bricks tested with different surface smoothing techniques.

Table 2.14 Compressive strength for the clay bricks with different surface smoothing techniques.

Specimen	Date of test	Type of surface smoothing	Length (L1) [mm]	Width (L2) [mm]	Average gross area [mm ²]	Maximum force [kN]	Compressive strength [MPa]	Shape factor [-]	Standard compressive strength [MPa]
BCL_17	03/08/2017	wear	0.21089	0.10053	0.02119972	1771	83.5	0.75	62.7
BCL_18	03/08/2017	wear	0.21045	0.09860	0.02075037	1743	84.0	0.75	63.0
BCL_19	03/08/2017	wear	0.21196	0.09791	0.02075300	1419	68.4	0.75	51.3
BCL_20	03/08/2017	gypsum	0.21164	0.10181	0.02154707	1476	68.5	0.75	51.4
BCL_21	03/08/2017	gypsum	0.21175	0.10228	0.02165673	1406	64.9	0.75	48.7
BCL_22	03/08/2017	gypsum	0.21165	0.10029	0.02122532	1106	52.1	0.75	39.1
BCL_23	03/08/2017	gypsum	0.21226	0.09816	0.02083544	1217	58.4	0.75	43.8
BCL_24	03/08/2017	gypsum	0.21155	0.10189	0.02155483	1329	61.7	0.75	46.2
BCL_25	03/08/2017	gypsum	0.21145	0.10240	0.02165248	1402	64.8	0.75	48.6
Average			0.21	0.10	0.02	1429.89	67.36	-	50.52
Standard deviation			0.00	0.00	0.00	217.48	10.60	-	7.95
Coefficient of variation [-]			0.003	0.018	0.018	0.152	0.157	-	0.157

It was verified that, while bricks smoothed with gypsum failed in bending, the bricks smoothed by wear collapsed in compression. Figure 2.46 present two clay bricks after their failure, while in Annex VIII the figures with the obtained fractures are presented for all specimens.

BCL_

BCL_

Figure 2.43 Clay bricks during the compressive strength test and after failure.

In Table 2.15 present a summary of the average compressive strength and average standard compressive strength obtained for the two types of blocks.

Table 2.15 Summary of the average compressive strength and average standard compressive strength in the two types of tested specimens.

Type of specimen	Compressive strength			Standard compressive strength		
	Average [MPa]	Standard deviation [MPa]	Coefficient of variation [-]	Average [MPa]	Standard deviation [MPa]	Coefficient of variation [-]
Calcium silicate blocks	21.52	2.47	0.115	18.72	2.15	0.115
Clay bricks	84.31	8.58	0.102	63.23	6.44	0.102

2.3 Masonry characterisation tests

2.3.1 Characterisation and identification of specimens

For the two types of masonry, sixteen *wallettes* were built, with six layers for calcium silicate blocks *wallettes* with dimensions approximately 433 x 102 x 475 mm, and eight layers for clay brick *wallettes* with dimensions of approximately 430 x 100 x 475 mm. These dimensions are according to the provisions of norm NP EN 1052-1 (1998b). Twenty-two *triplets* specimens were tested, with approximately 236 x 212 x 101 mm for the calcium silicate *triplets* and 170 x 210 x 100 mm for the clay *triplets*. Figure 2.44 shows the two *wallettes* and *triplets* types that were constructed for the tests.



Calcium silicate *wallettes* (WS)



Clay *wallettes* (WCL)



Calcium silicate *triplets* (BWS)



Clay *triplets* (BWCL)

Figure 2.44 Types of masonry specimens (*wallettes* and *triplets*) built for testing.

The construction of the specimens for the characterisation tests (*wallettes* and *triplets*) took place in August 2017 during the construction of the full-scale model and was carried out by construction professionals from the Netherlands, as shown in Figure 2.45.



Wallettes



Triplets

Figure 2.45 Construction of *wallettes* and *triplets*.

The selected tests for these specimens were:

- Compressive strength tests (W##);
- Bond wrench tests (BW##).

The designation of the specimens is in accordance with the following descriptions: WS – Calcium silicate *wallettes* for the compressive strength tests; WCL – Clay *wallettes* for the

compressive strength tests; BWS – Calcium silicate *triplets* for the bond strength tests; BWCL – Clay *triplets* for the bond strength tests.

All of the specimens were measured with a calliper and weighed on a digital weighing-machine, as shown in Figure 2.46.



Figure 2.46 Example of characterisation (measure and weight) of all specimens.

Figure 2.47 presents a schematic view with the various parameters measured in the test specimens, while in Table 2.16 the dimensions and masses of the two types of *wallettes* constructed for the compressive strength tests are summarised, with additional details provided in Annex VII.

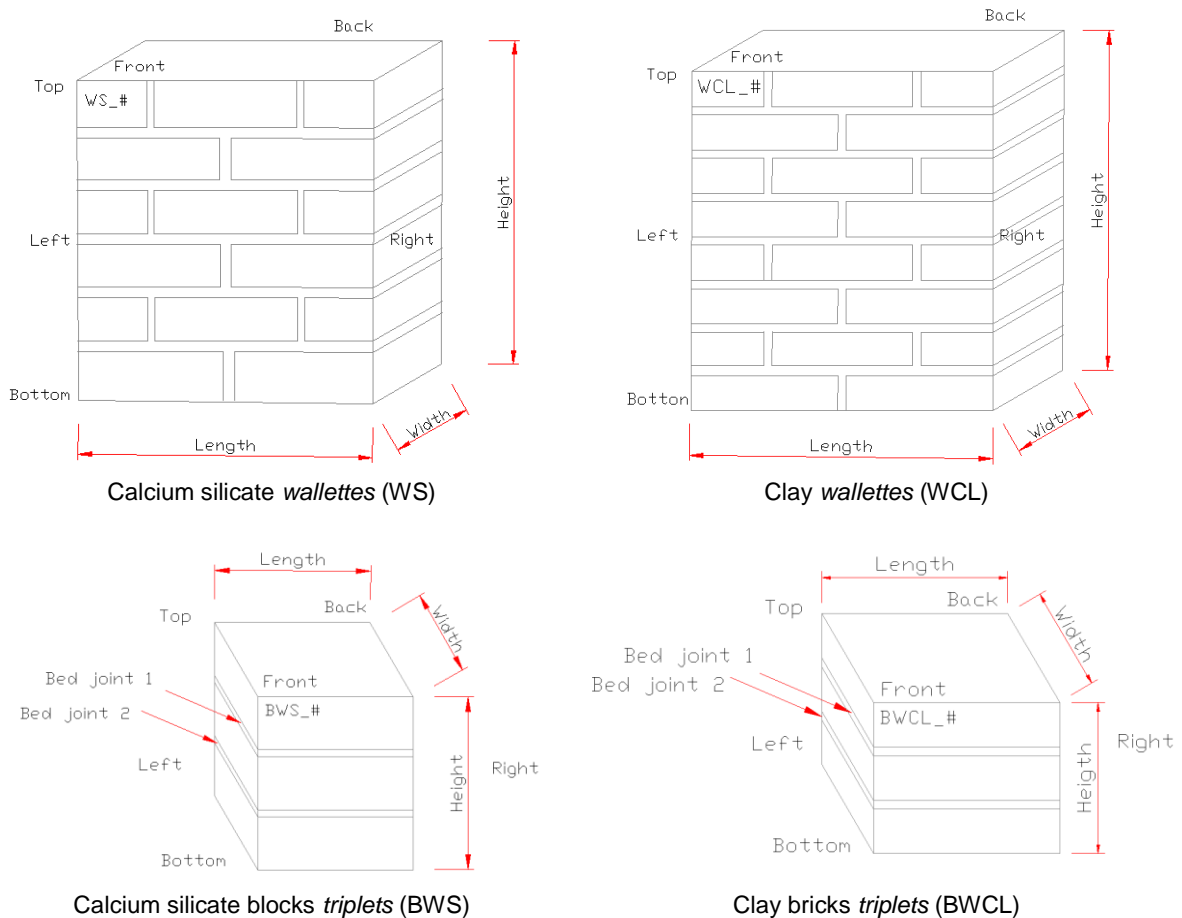


Figure 2.47 Schematic with the identification of the parameters measured in the various specimens.

Table 2.16 Dimensions and masses of the two types of *wallettes* constructed for the compressive strength tests.

Specimen	Average Length [mm]	Average Width [mm]	Average Height [mm]	Average Mass [kg]
WS	434.4	102.6	475.4	38.06
WCL	429.3	100.8	475.6	37.73

In Table 2.17, the dimensions and masses of the two types of *triplets* built for the bond strength tests are shown. Additional details are provided in Annex VII.

Table 2.17 Dimensions and masses of the two types of *triplets* built for the bond wrench tests.

Specimen	Average Height [mm]	Average Width [mm]	Average Length [mm]	Average Mass [kg]
BWS	235.92	102.63	212.17	9.32
BWCL	172.76	100.69	208.17	6.57

The bulk density values for the calcium silicate block and clay brick *wallettes* and *triplets* are summarised in Table 2.18, with additional results presented in Annex VII.

Table 2.18 Summary of the results of the bulk density for the two types of specimens.

Specimen type	Bulk density		
	Average [kg/m ³]	Standard deviation [kg/m ³]	Coefficient of variation [-]
Calcium silicate <i>wallettes</i>	1796	9.70	0.005
Clay <i>wallettes</i>	1833	16.45	0.009
Calcium silicate <i>triplets</i>	1817	15.79	0.009
Clay <i>triplets</i>	1815	19.48	0.011

2.3.2 -Test for the determination of compressive strength

The test to determine the compressive strength was performed according to an adaptation of the standard method described in the standard EN 1052-1:1998 "Methods of test for masonry – Part 1: Determination of compressive strength" (CEN, 1998b). The principle of this test is the determination of the compressive strength of masonry specimens and possible determination of the respective modulus of elasticity and *Poisson* coefficient.

This test was carried out in the abovementioned *wallettes*. Due to the small irregularities of the lower and upper faces of the clay *wallettes* (areas that would be in contact with the plates of the press), these faces were regularised with a thin layer of gypsum, as shown in Figure 2.48. After this regularisation a very fine layer of gypsum is placed on both sides already with the specimen on top of the testing machine, which are levelled by the plates of the press, as shown in Figure 2.49.

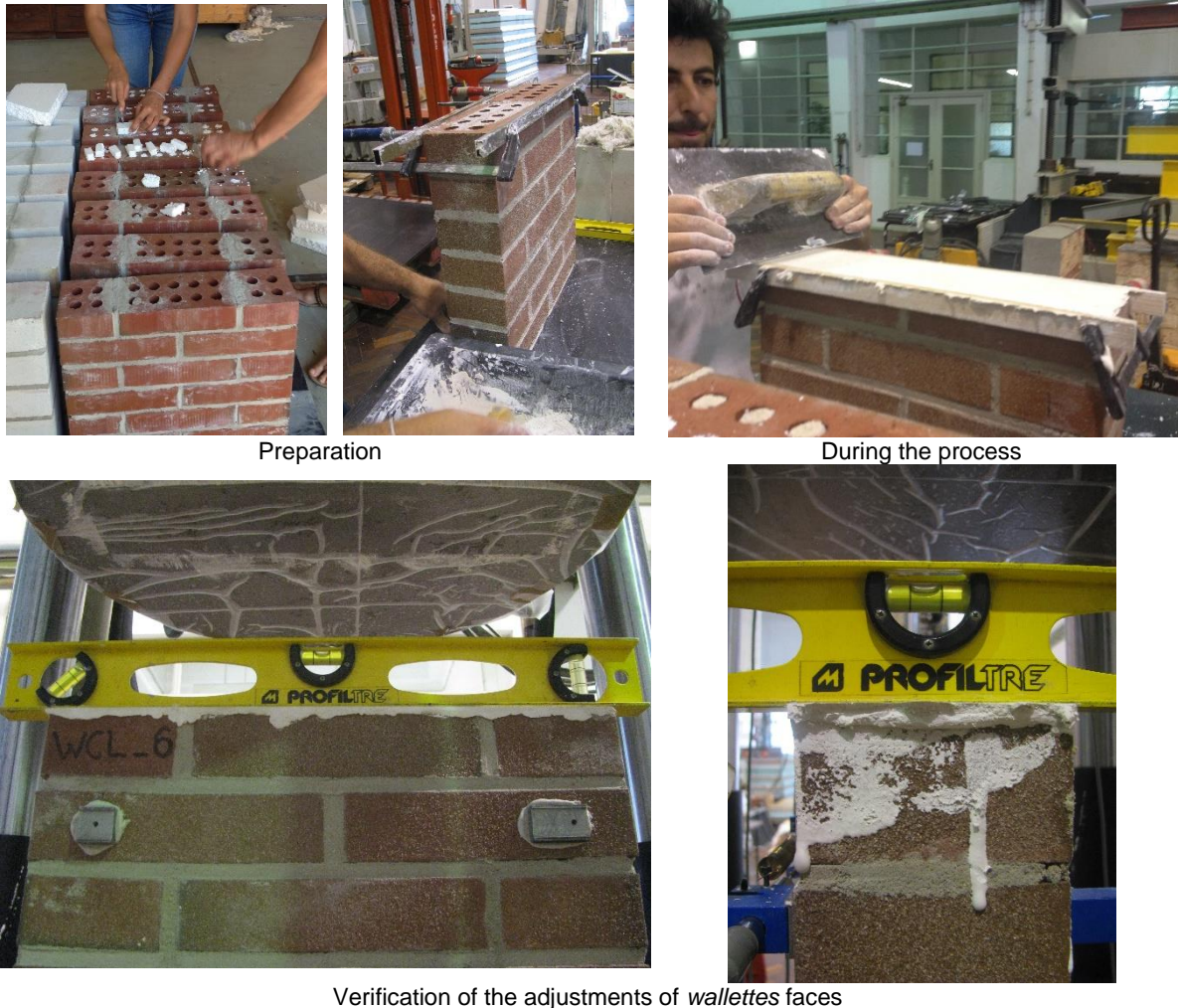


Figure 2.48 Regularisation of the *wallettes* faces.

Wallettes were not perfectly tiled at the time of construction, as shown in Figure 2.50. Subsequently, the specimens were instrumented with four displacement transducers on each face, as shown in Figure 2.51. The vertical displacement transducers are of type W20 (with a measuring range of ± 20 mm) and measure strains for the determination of the modulus of elasticity (1,2,5 and 6) and two horizontal displacement transducers of type W10 (with a measuring range of ± 10 mm, since smaller deformations are expected) which measure deformations in the direction perpendicular to the force in order to provide an evaluation of *Poisson's* coefficient (3, 4, 7 and 8).

The instrumentation was placed in the central area of the specimen so that the measurements are carried out in an area that is not affected by the boundary conditions, as illustrated in the schemes of Figure 2.52 and Figure 2.53 (the schematics with the instrumentation locations for all tested *wallettes* are shown in Annex VII). Additionally, two displacement transducers were placed that measure the deformation of the plates of the press so that the deformation of the specimen up to failure may be recorded. For example, Figure 2.54 and Figure 2.55 show the instrumentation performed on each face of the two types of *wallettes*. The displacement transducers and the testing machine were duly calibrated immediately prior to the start of the trials with the collaboration of the Metrological Quality Unit of LNEC's Scientific Instrumentation Centre.



Figure 2.49 Final regularisation of the wallettes' faces on top of the testing machine.



Figure 2.50 Lack of verticality in wallettes.

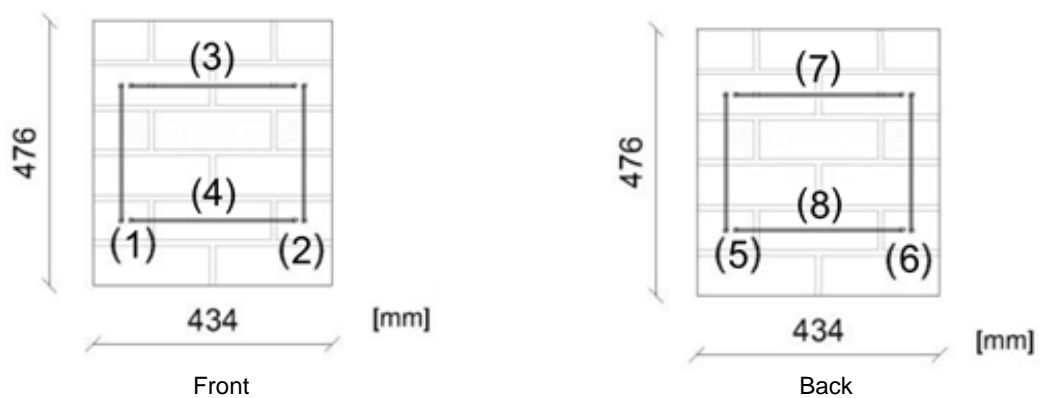


Figure 2.51 Scheme and numbering of the transducers placed on each face of the wallettes.

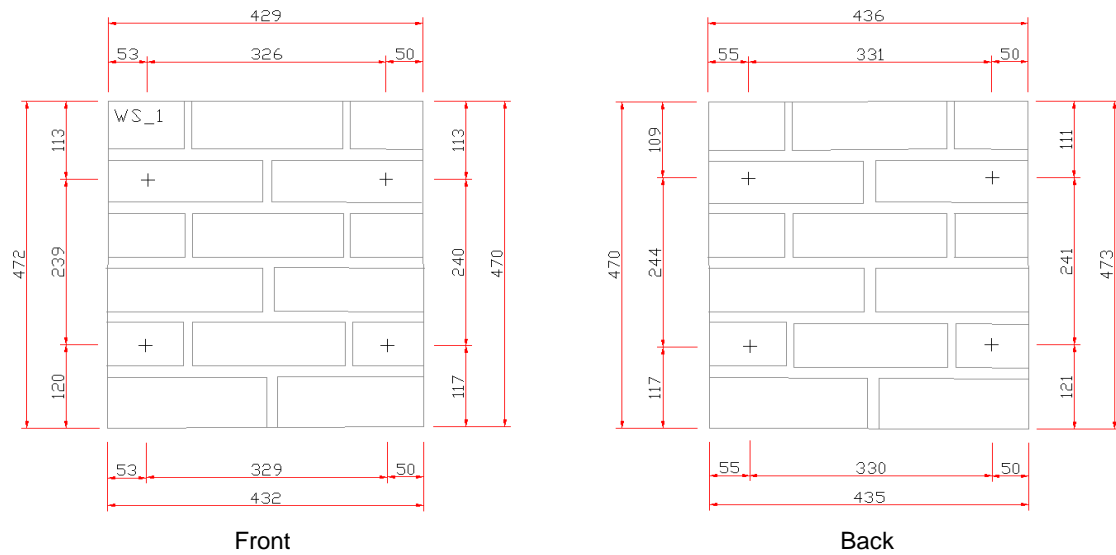


Figure 2.52 Scheme with the location of the transducers placed on each face of the CS wallettes.

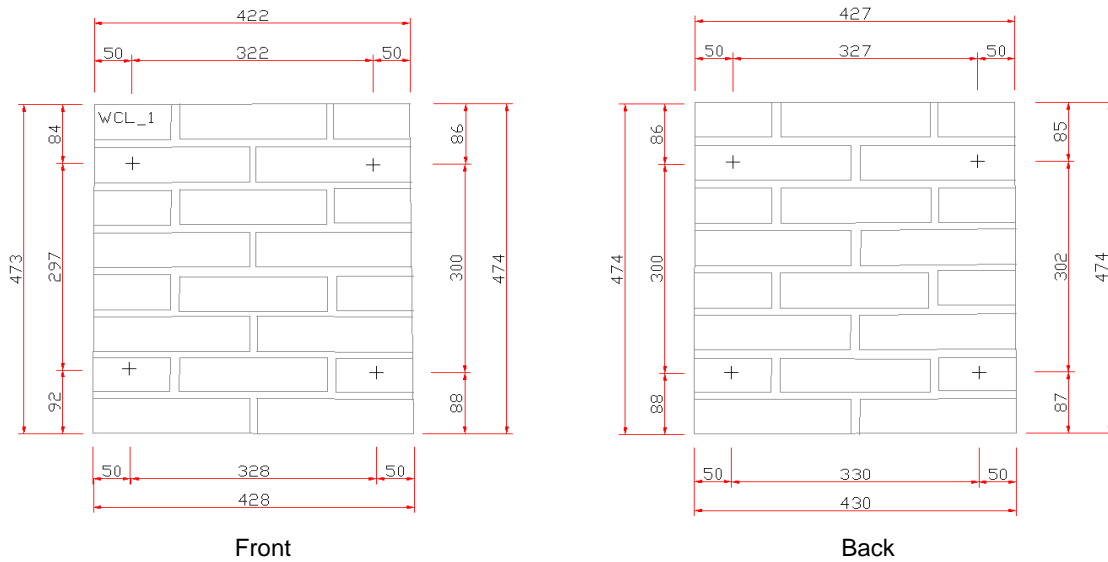


Figure 2.53 Scheme with the location of the transducers placed on each face of the clay wallettes.



Figure 2.54 Instrumentation placed on each face of the CS wallettes.

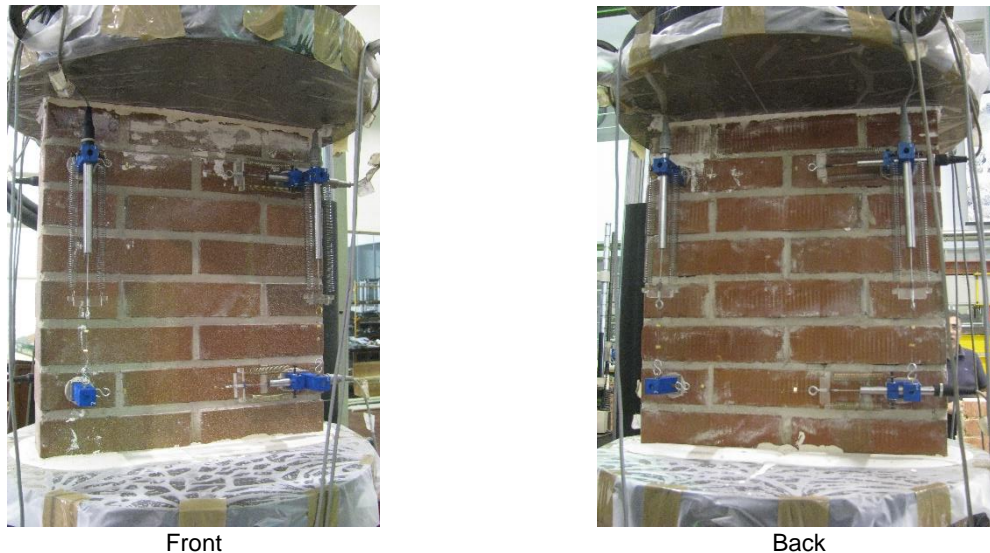


Figure 2.55 Instrumentation placed on each face of the clay wallettes.

The test procedure for the calcium silicate *wallettes* consists essentially in placing the specimen in the test machine for load application without shock, i.e. in a gradual way and at a controlled speed until the failure of the specimen. Several increasing cycles of loading and unloading were carried out, with equal increments (at each load level three cycles were performed). In Table 2.19 the load values of these cycles for calcium silicate *wallettes* are presented, while in Figure 2.56 an example of one of these tests is presented as a plot showing the force as a function of time.

The tests were performed on a machine with a capacity of 1000 kN, with a control in force and a test speed of 1.1 kN/s in the first four cycles. In the collapse cycle the test was performed with a control in displacement and a test speed of 0.01 mm/s. A sampling frequency of 5 Hz was used, each run lasting approximately 75 minutes. The load application was performed vertically to the specimen.

Table 2.19 Cyclic load values for calcium silicate wallettes.

Specimen	Load values of 1 st cycle [kN]	Load values of 2 nd cycle [kN]	Load values of 3 rd cycle [kN]	Load values of 4 th cycle [kN]
WS_00	74	148	222	296
WS_0	74	148	222	296
WS_1	74	148	222	296
WS_2	74	148	222	296
WS_3	74	148	222	296
WS_4	60	120	180	240
WS_5	60	120	180	240
WS_6	60	120	180	240

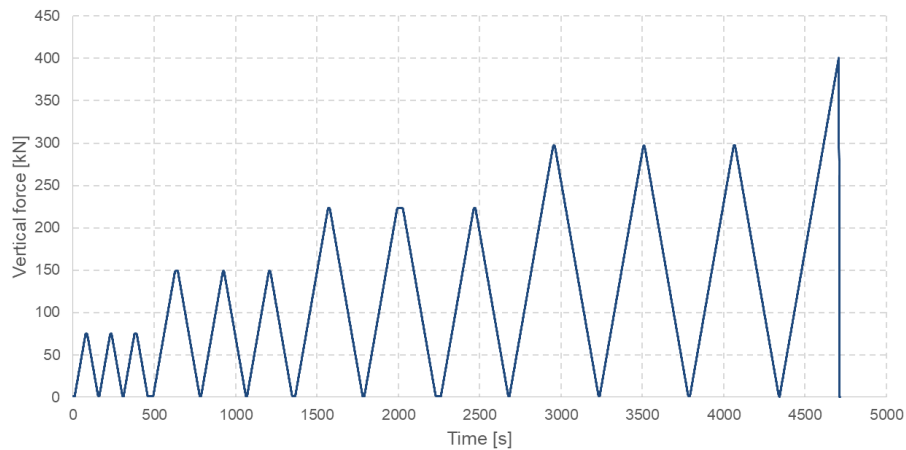


Figure 2.56 Application of force as a function of time applied to calcium silicate wallettes.

For the sake of safeguarding the equipment, the instrumentation was maintained up to the fourth load level, and after the last cycle at this load level the final loading was started until the specimen failure. For this final loading, the deformation until failure was measured using the transducers installed in the press plate. The WS_00 *wallette* was used to evaluate the compressive strength of the test specimens in order to define the loading threshold from which the instrumentation should be removed.

Figure 2.57 present two calcium silicate *wallettes* during the test and after their failure, while in Annex VIII the figures with the obtained fractures are presented for all specimens.

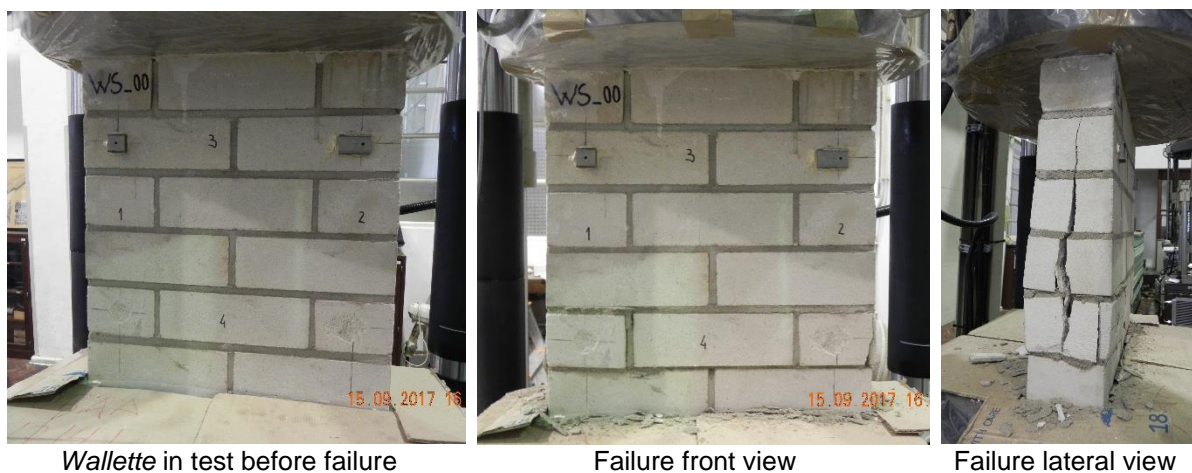


Figure 2.57 Calcium silicate block wallette (WS_00) during the test and after failure.

The results of the compressive strength obtained in the calcium silicate *wallettes* are summarised in Table 2.20. In order to determine the modulus of elasticity of the *wallettes*, the average of the vertical deformations recorded by the displacement transducers 1, 2, 5 and 6 was computed and the modulus of elasticity (E_t), given by the secant line from the origin up to 33% of the failure load, was derived.

Table 2.20 Summary of the compressive strength for the calcium silicate walleτες.

Specimen	Date of test	Average gross area [mm ²]	Maximum force [kN]	Compressive strength [MPa]
WS_00	15/09/2017	44585.36	329.39	7.39
WS_0	18/09/2017	44788.80	310.94	6.94
WS_1	20/09/2017	44574.45	333.80	7.49
WS_2	20/09/2017	44615.20	340.40	7.63
WS_3	21/09/2017	44352.19	297.00	6.70
WS_4	09/10/2017	44460.44	319.50	7.19
WS_5	28/09/2017	44600.55	279.70	6.27
WS_6	27/09/2017	44687.55	296.30	6.63
Average		44583.07	313.38	7.03
Standard deviation		132.56	21.18	0.47
Coefficient of variation [-]		0.003	0.068	0.067

Figure 2.60 to Figure 2.64 shows the plots that relate the vertical and horizontal deformations to the vertical load measured for each specimen.

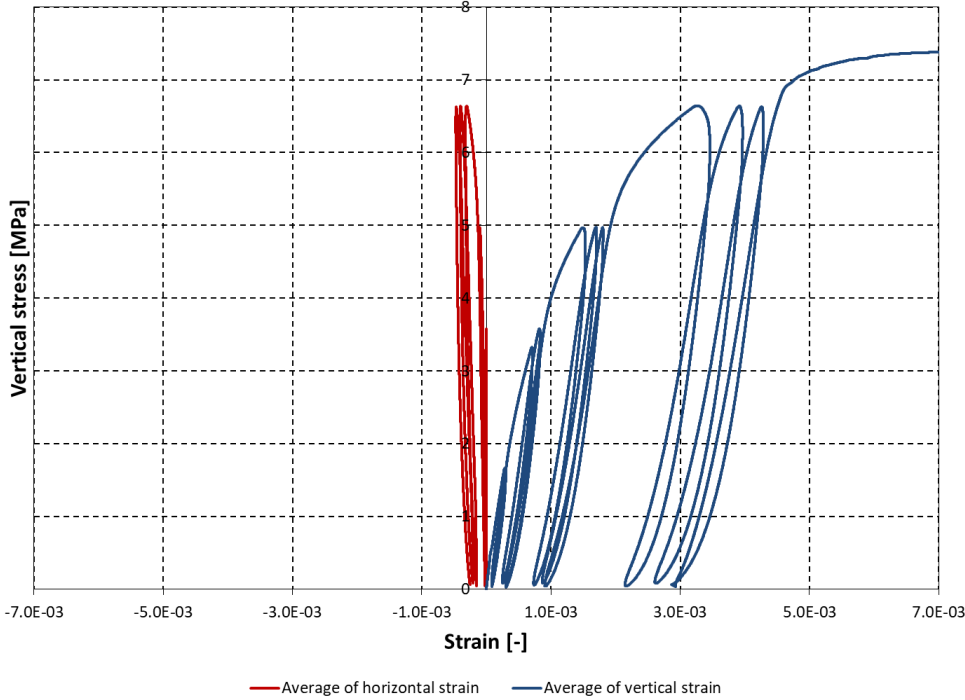


Figure 2.58 Vertical stress vs. vertical and horizontal strains for walette WS_00.

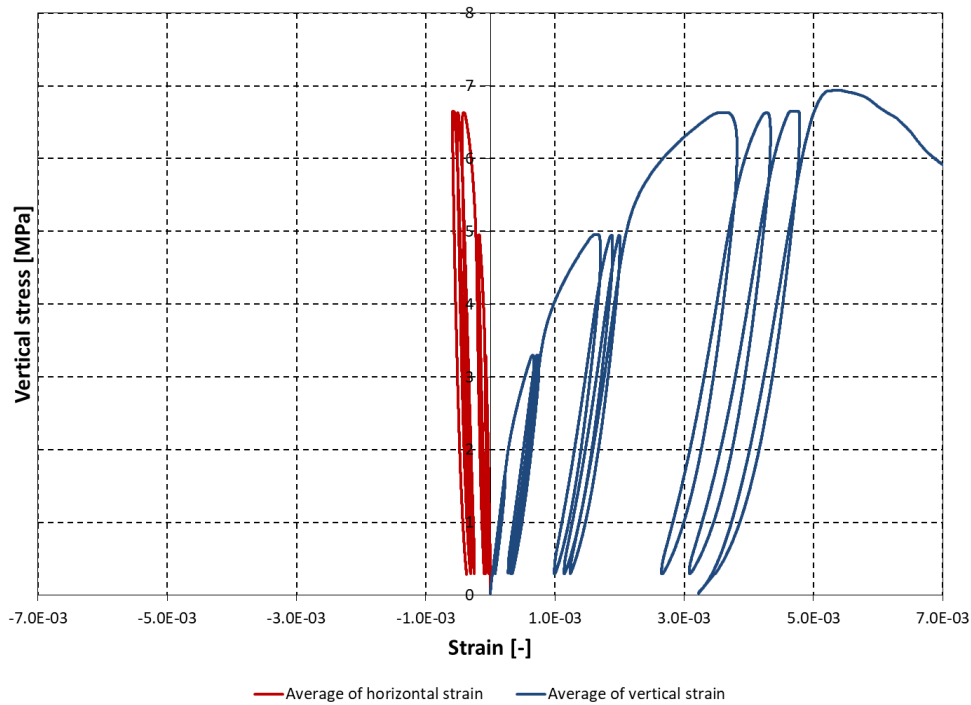


Figure 2.59 Vertical stress vs. vertical and horizontal strains for wallette WS_0.

Figure 2.60 Vertical stress vs. vertical and horizontal strains for wallette WS_1.

Figure 2.61 Vertical stress vs. vertical and horizontal strains for wallette WS_3.

Figure 2.62 Vertical stress vs. vertical and horizontal strains for wallette WS_4.

Figure 2.63 Vertical stress vs. vertical and horizontal strains for wallette WS_5.

Figure 2.64 Vertical stress vs. vertical and horizontal strains for wallette WS_6.

Figure 2.67 to Figure 2.72 show the plots relating the vertical stress with the vertical strain measured for the CS *wallettes*, as well as the corresponding modulus of elasticity.

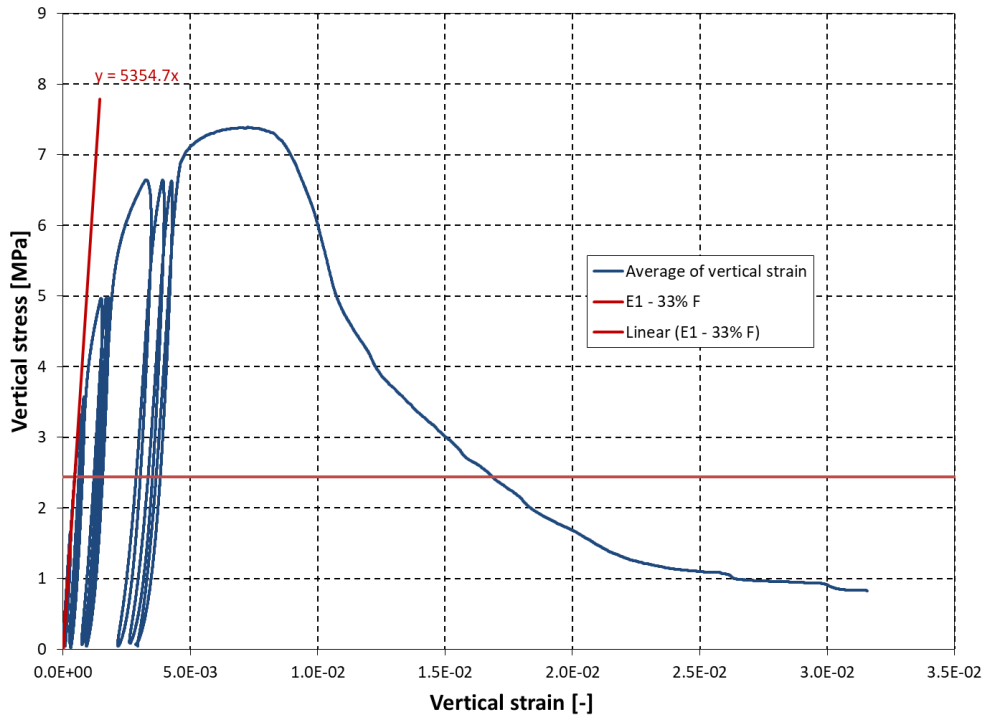


Figure 2.65 Vertical stress vs. vertical strain and determination of the modulus of elasticity for wallette WS_00.

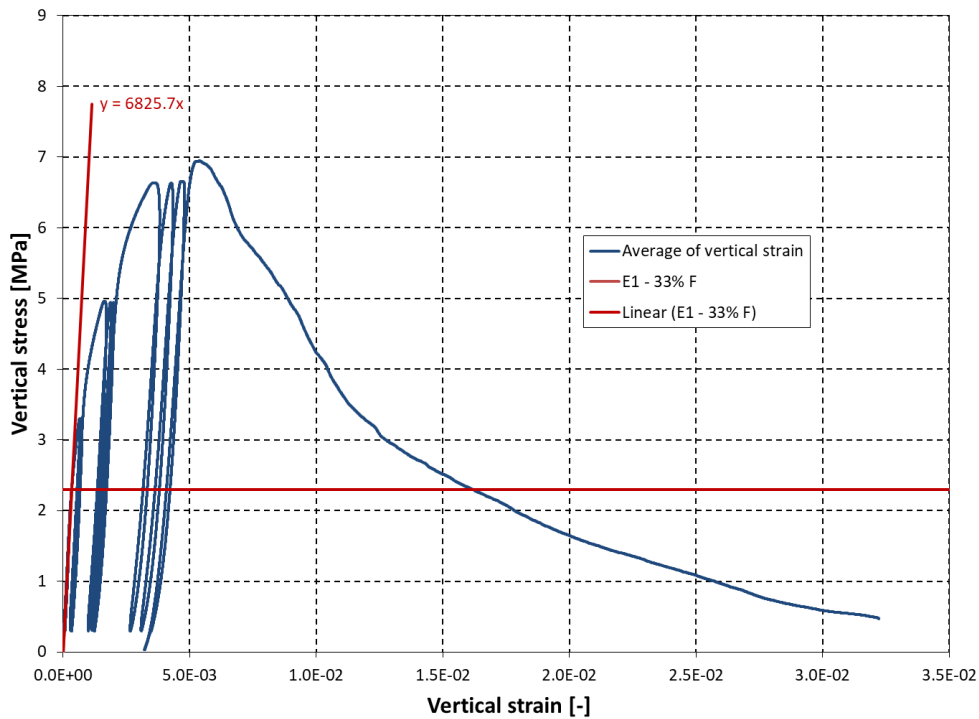


Figure 2.66 Vertical stress vs. vertical strain and determination of the modulus of elasticity for wallette WS_0.

Figure 2.67 Vertical stress vs. vertical strain and determination of the modulus of elasticity for wallette WS_1.

Figure 2.68 Vertical stress vs. vertical strain and determination of the modulus of elasticity for wallette WS_2.

Figure 2.69 Vertical stress vs. vertical strain and determination of the modulus of elasticity for wallette WS_3.

Figure 2.70 Vertical stress vs. vertical strain and determination of the modulus of elasticity for wallette WS_4.

Figure 2.71 Vertical stress vs. vertical strain and determination of the modulus of elasticity for wallette WS_5.

Figure 2.72 Vertical stress vs. vertical strain and determination of the modulus of elasticity for wallette WS_6.

The results obtained for the modulus of elasticity E_1 for each CS *wallette* are summarised in Table 2.21, while Figure 2.73 shows the distribution of the moduli of elasticity obtained.

Table 2.21 Summary of the modulus of elasticity for calcium silicate wallettes.

Specimen	Compressive strength [MPa]	E_1 (33% F_{max}) [MPa]
WS_00	7.39	5354.7
WS_0	6.94	6825.7
WS_1	7.49	
WS_2	7.63	
WS_3	6.70	
WS_4	7.19	
WS_5	6.27	
WS_6	6.63	
Average [MPa]	7.03	
Standard deviation [MPa]	0.47	
Coefficient of variation [-]	0.067	

Figure 2.73 Distribution of moduli of elasticity obtained for calcium silicate wallettes.

For the clay *wallettes*, several increasing cycles of loading and unloading were also carried out, with equal increments (at each load level three cycles were performed). In Table 2.22 the load values of these cycles for clay *wallettes* are presented, while in Figure 2.74 an example of one of these cycles is presented as a plot showing the force as a function of time. The test was performed on a machine with a capacity of 1000 kN, with a control in force in the cycles up to 500 kN of load level and a test speed of 3.5 kN/s. In the fourth cycle and in the collapse

cycle the test was performed with a control in displacement and a test speed of 0.01 mm/s. A sampling frequency of 5 Hz was used, each run lasting approximately 60 minutes. The load application was performed vertically to the specimen.

Similarly to what was done in the calcium silicate *wallettes*' tests, the WCL_00 *wallette* was used to evaluate the compressive strength of the test specimens in order to define the loading threshold from which the instrumentation should be removed. Figure 2.75 presents a clay *wallette* during the test and after its failure. In Annex VIII the figures with the obtained fractures are presented for all specimens.

Table 2.22 Cyclic load values for clay *wallettes*.

Specimen	Load values of 1 st cycle [kN]	Load values of 2 nd cycle [kN]	Load values of 3 rd cycle [kN]	Load values of 4 th cycle [kN]
WCL_00	150	300	450	600
WCL_0	150	300	450	600
WCL_1	130	260	390	520
WCL_2	130	260	390	520
WCL_3	130	260	390	520
WCL_4	130	260	390	520
WCL_5	130	260	390	520
WCL_6	130	260	390	520

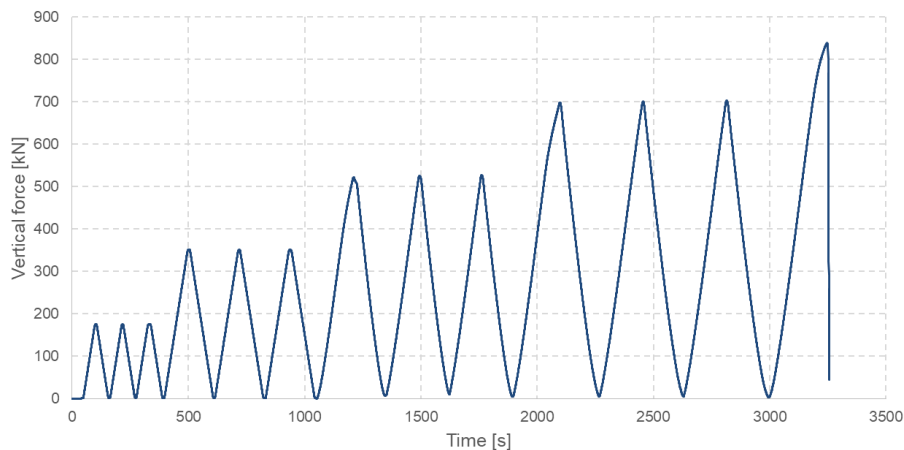


Figure 2.74 Application of force as a function of time applied to clay *wallettes*.



Wallette in test before failure

Failure front view

Failure lateral view

Figure 2.75 Clay brick walette (WCL_6) subjected to test and after failure.

The results of the compressive strength tests obtained for the clay *wallettes* are summarised in Table 2.23. Figure 2.76 to Figure 2.83 show the plots that relate the vertical and horizontal deformations to the vertical load measured for each specimen.

Table 2.23 Summary of the compressive strength for the clay *wallettes*.

Specimen	Date of test	Average gross area [mm ²]	Maximum force [kN]	Compressive strength [MPa]
WCL_00	28-09-2017	43111.20	687.73	15.95
WCL_0	29-09-2017	43729.26	643.61	14.72
WCL_1	02-10-2017	43799.80	692.30	15.81
WCL_2	02-10-2017	43238.91	723.00	16.72
WCL_3	04-10-2017	42987.10	754.70	17.56
WCL_4	10-10-2017	43043.00	778.00	18.07
WCL_5	10-10-2017	43037.28	659.50	15.32
WCL_6	11-10-2017	43243.20	657.90	15.21
Average		43273.72	699.59	16.17
Standard deviation		317.16	48.41	1.18
Coefficient of variation [-]		0.007	0.069	0.073

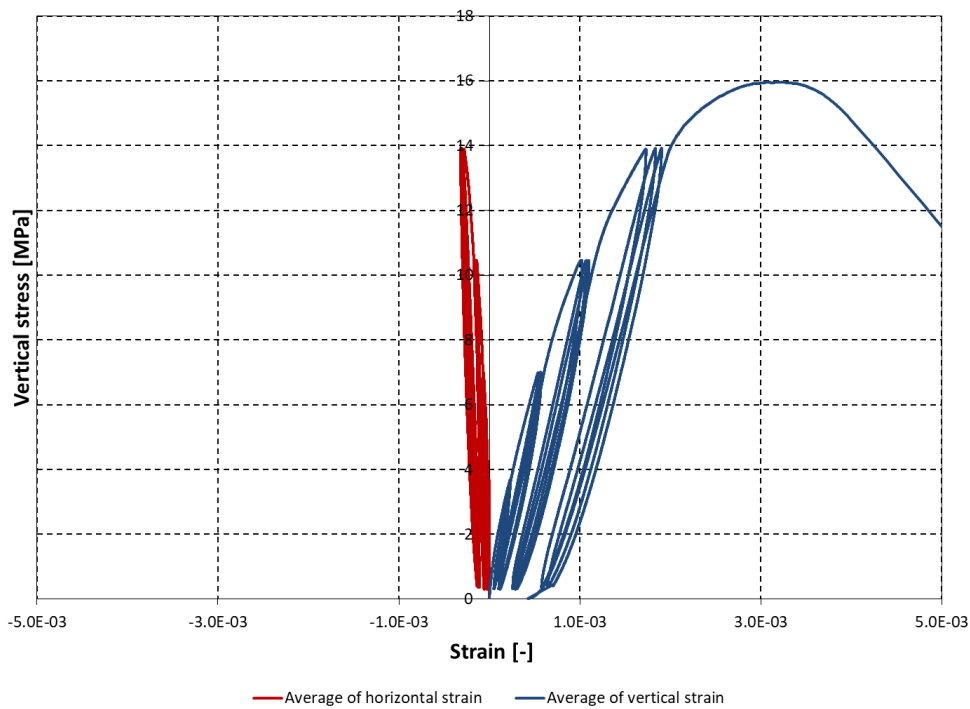


Figure 2.76 Vertical stress vs. vertical and horizontal strains for walette WCL_00.

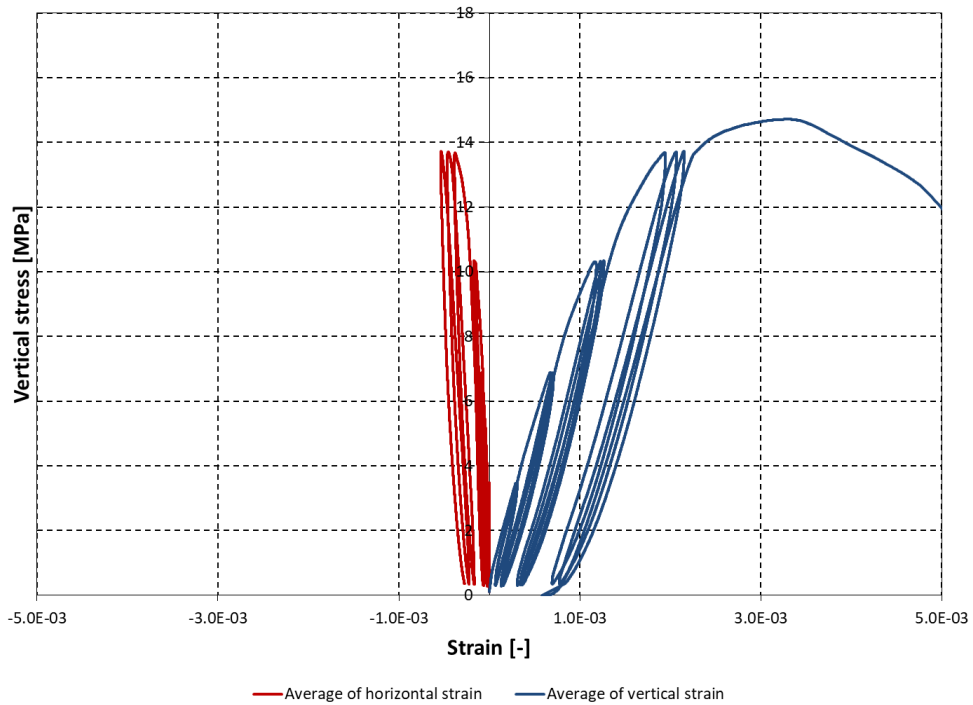


Figure 2.77 Vertical stress vs. vertical and horizontal strains for wallette WCL_0.

Figure 2.78 Vertical stress vs. vertical and horizontal strains for wallette WCL_1.

Figure 2.79 Vertical stress vs. vertical and horizontal strains for wallette WCL_2.

Figure 2.80 Vertical stress vs. vertical and horizontal strains for wallette WCL_3.

Figure 2.81 Vertical stress vs. vertical and horizontal strains for wallette WCL_4.

Figure 2.82 Vertical stress vs. vertical and horizontal strains for wallette WCL_5.

Figure 2.83 Vertical stress vs. vertical and horizontal strains for wallette WCL_6.

Figure 2.84 to Figure 2.91 show the plots relating the vertical stress with the vertical strain measured for the clay *wallettes*, as well as the corresponding moduli of elasticity.

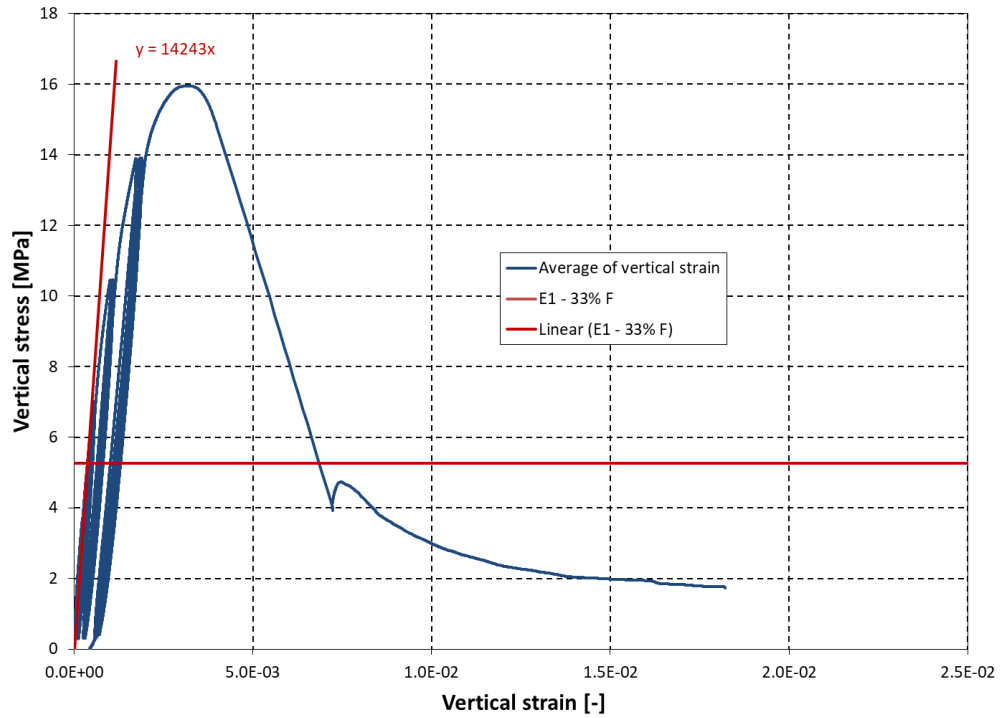


Figure 2.84 Vertical stress vs. vertical strain and determination of the modulus of elasticity for wallette WCL_00.

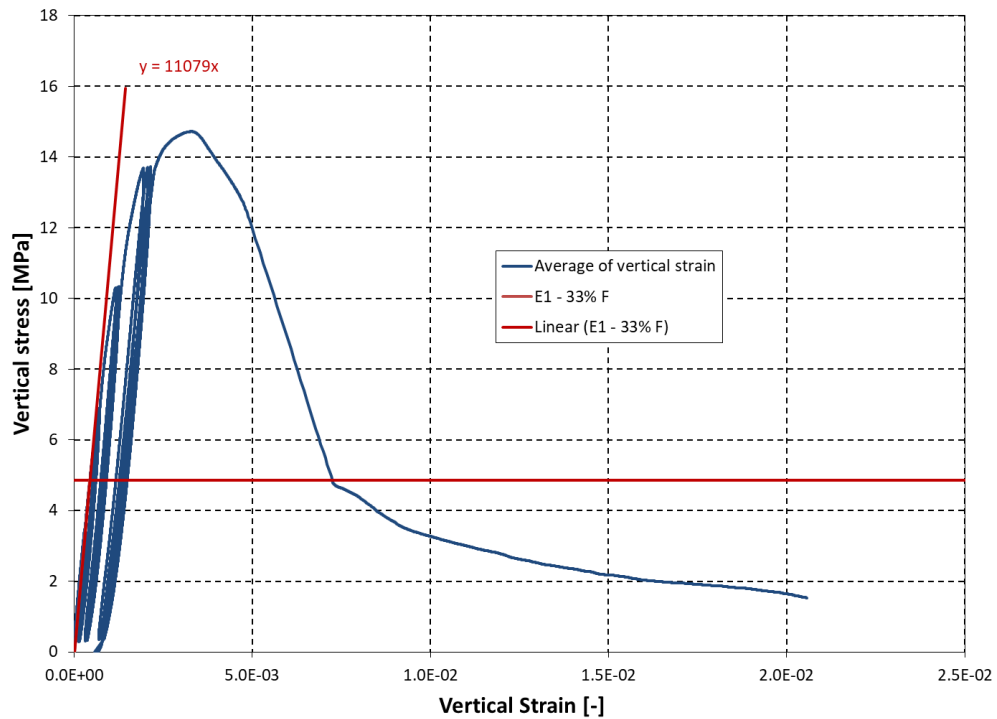


Figure 2.85 Vertical stress vs. vertical strain and determination of the modulus of elasticity for wallette WCL_0.

Figure 2.86 Vertical stress vs. vertical strain and determination of the modulus of elasticity for wallette WCL_1.

Figure 2.87 Vertical stress vs. vertical strain and determination of the modulus of elasticity for wallette WCL_2.

Figure 2.88 Vertical stress vs. vertical strain and determination of the modulus of elasticity for wallette WCL_3.

Figure 2.89 Vertical stress vs. vertical strain and determination of the modulus of elasticity for wallette WCL_4.

Figure 2.90 Vertical stress vs. vertical strain and determination of the modulus of elasticity for wallette WCL_5.

Figure 2.91 Vertical stress vs. vertical strain and determination of the modulus of elasticity for wallette WCL_6.

The results obtained for the modulus of elasticity E_1 for each clay *wallette* are summarised in Table 2.24, while Figure 2.92 shows their distribution.

Table 2.24 Summary of the modulus of elasticity for clay wallettes.

Specimen	Compression strength [MPa]	E_1 (33% F_{max}) [MPa]
WCL_00	15.95	14243
WCL_0	14.72	11079
WCL_1	15.81	
WCL_2	16.72	
WCL_3	17.56	
WCL_4	18.07	
WCL_5	15.32	
WCL_6	15.21	
Average [MPa]	16.17	
Standard deviation [MPa]	1.18	
Coefficient of variation [-]	0.073	

Figure 2.92 Distribution of moduli of elasticity obtained for clay wallettes.

2.3.3 Tests for the determination of bond strength

The purpose of this section is to describe the complementary destructive tests that were carried out on several samples for each type of masonry to determinate the bond strength of their horizontal bed-joints using the bond wrench method described in the standard EN 1052-5:2005 "Methods of test for masonry – Part 5: Determination of bond strength by the bond wrench

method" (CEN, 2005). The tests were carried out on CS *triplets* and clay *triplets*, as shown in Figure 2.93.

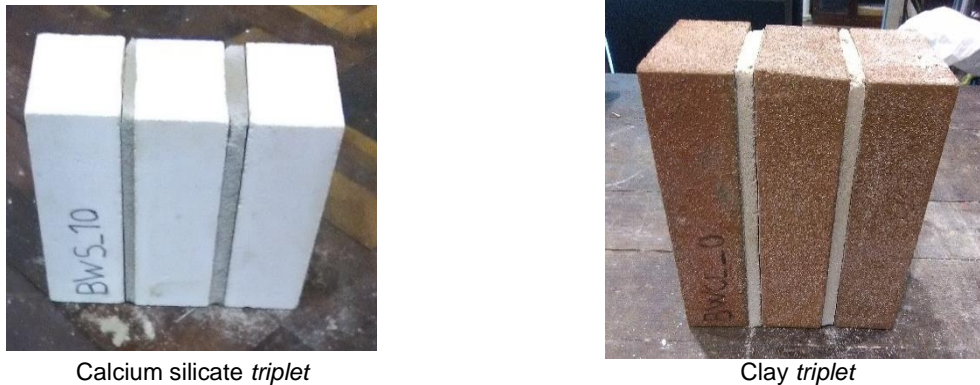


Figure 2.93 Type of specimens subjected to bond strength test.

The main idea of the test is to keep the specimen rigidly held while a clamp is applied to its top unit, see Figure 2.94. A bending moment is applied to the clamp by a lever until the top unit is torn from the remaining part of the specimen. From the stresses achieved by the specimen, the bond strength of the masonry can be evaluated.

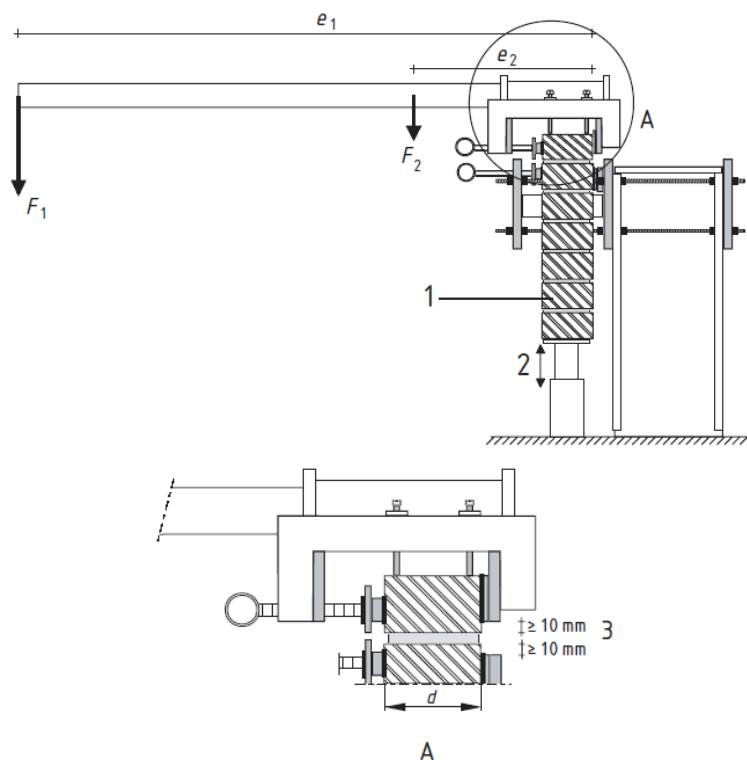
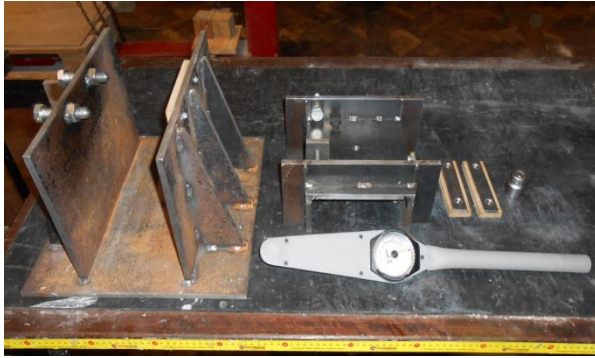


Figure 2.94 Example of a possible device for the test in accordance with EN 1052-5 (CEN, 2005).

A new device was created to carry out this test, which allows the use of a torque wrench with a memory needle for moment recording, instead of the test device used in the previous campaign (Tomassetti et al. 2017). All tests performed in calcium silicate *triplets* were performed using this new device. However, to ensure the validity of the results, the tests on clay triplets were performed with both devices: part of the specimens were tested using the new device and the other part using the device from the previous test campaign, which has an horizontal lever arm with a weight (sand) applied at its end.



Device used with a torque wrench



Device used in the previous test campaign

Figure 2.95 Test setups for bond-wrench test.

The new equipment has two independent steel structures: a lower support frame with two side plates, reinforced with gussets, and welded to a base plate, which holds in place the unit beneath the top bed-joint of the specimen without applying any significant bending moment to any lower units; the upper structure is a lever with a clamp at one end, made up of three welded plates and a horizontal level steel rebar, which can be applied to the top unit of the *triplet*.

The test procedure was as follows:

1. The lower frame was attached to a rigid plate and a position for the *triplet* was defined, according with the standard. The screws were clamping approximately with equal torque (a ratchet torque wrench was used). Bricks and small pieces of timber were used with the thickness of the joints to ensure the same fixing height as defined in the standard. This was envisaged for two reasons: i) since the lower structure is common to the two types of *triplets* which have different heights; and ii) so that after the first failure of the connection the specimen could be raised to the required height, allowing the second connection to be tested, as shown in Figure 2.96 and Figure 2.97;



Figure 2.96 Test of the two connections in CS blocks using the same test device.



Figure 2.97 Test of the two connections in clay bricks using the same test device.

2. The *triplet* was securely clamped in the retaining frame such that the second from top unit had a reasonable degree of restraint against rotation but the joint to be tested remained between 10 and 15 mm clear of the lower clamp. The clamp was intertwined with thin layers of a material such as plywood to ensure an even grip;
3. Fix the upper clamp with lever arm on the upper block to be tested, respecting the tightening location indicated by the standard (a distance equal to or greater than 10 mm from the test joint) and ensuring that the lever is horizontal;
4. Apply the vertical force on the torque wrench and read the value of the moment that leads to a bond failure, as shown in Figure 2.98;
5. Weighing of the top unit and the adherent mortar leading to a bond failure, as shown in Figure 2.99.

The main difference between the two devices consists mainly in the way in which the load is applied and in the reading of the applied moment that leads to the rupture of the sample. The tests performed with the torque wrench were shown to have led to greater efficiency and speed of execution.



Figure 2.98 Application of vertical force until bond failure.



Figure 2.99 Measure of the weight of the top unit and adherent mortar.

For each valid failure the bond strength was calculated using the following expression, which includes the effects of both applied bending moment and compression:

$$f_{wi} = \frac{F_1 e_1 + F_2 e_2 - \frac{2}{3} d (F_1 + F_2 + W/4)}{\frac{bd^2}{6}} \quad (7)$$

where:

f_{wi} bond strength in masonry [MPa];

b width of the bed-joint tested [mm];

d depth of the specimen [mm];

e_1 distance from the applied load (F_1) to the tension face of the specimen [mm];

e_2 distance from the centre of gravity of the lower and upper clamp (F_2) from the tension face of the specimen [mm];

F_1 applied load [N];

F_2 weight of the bond wrench [N];

W weight of the masonry unit pulled off the specimen and any adherent mortar [N].

The modes of failure represented in Figure 2.100 were considered valid to calculate the bond strength, according to EN 1052-5 (2005). The type of bond failure mechanisms obtained in the tests exemplified in Figure 2.101. In Annex VIII, the pictures for all tested specimens are presented.

The bond strength values obtained from the tests for the two types of specimens are presented in Table 2.25, Table 2.26 and Table 2.27, while their average values are shown in Table 2.28.

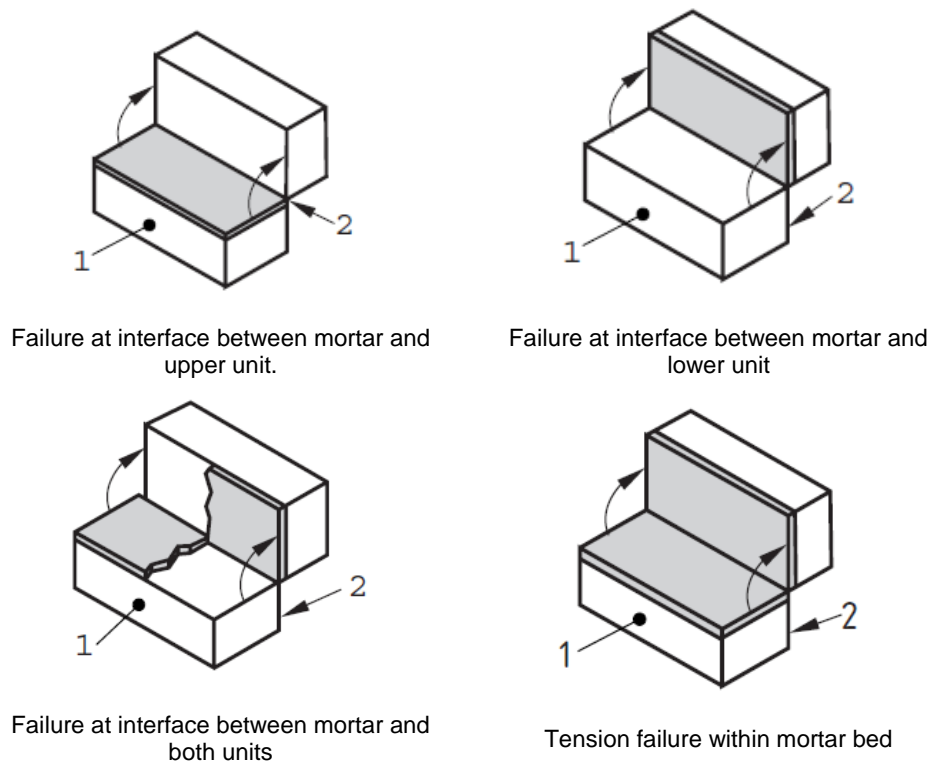


Figure 2.100 Admissible failure mechanisms for the bond wrench test.



Calcium silicate triplets



Clay triplets

Figure 2.101 Example of failure mechanisms obtained for each triplet type in the bond wrench test.

Table 2.25 Bond strength for the CS triplets.

Specimen	<i>b</i>	<i>d</i>	<i>Z</i>	<i>e</i> ₁	<i>e</i> ₂	<i>F</i> ₁	<i>F</i> ₂	<i>W</i>	<i>M</i> ₁	<i>M</i> ₂	<i>f</i> _{wi}
	[mm]	[mm]	[mm ³]	[mm]	[mm]	[N]	[N]	[N]	[N.mm]	[N.mm]	[MPa]
BWS_0	235.00	102.45	411093.43	450	90	346.91	98.79	2.75	165	8891	0.33
BWS_0	235.00	102.45	411093.43	450	90	409.13	98.79	3.73	193	8891	0.38
BWS_1	236.00	102.18	410669.59	450	90	386.91	98.79	2.85	183	8891	0.36
BWS_1	236.00	102.18	410669.59	450	90	353.58	98.79	2.73	168	8891	0.33
BWS_2	237.00	102.50	414996.88	450	90	280.24	98.79	2.79	135	8891	0.26
BWS_2	237.00	102.50	414996.88	450	90	313.58	98.79	2.95	150	8891	0.29
BWS_3	237.00	103.28	421336.96	450	90	98.02	98.79	2.84	53	8891	0.09
BWS_3	237.00	103.28	421336.96	450	90	402.46	98.79	3.32	190	8891	0.37
BWS_4	236.00	102.65	414456.22	450	90	475.80	98.79	2.84	223	8891	0.44
BWS_4	236.00	102.65	414456.22	450	90	242.46	98.79	3.71	118	8891	0.23
BWS_5	233.00	102.21	405687.33	450	90	402.46	98.79	2.88	190	8891	0.38
BWS_5	233.00	102.21	405687.33	450	90	424.69	98.79	3.24	200	8891	0.40
BWS_6	237.00	102.97	418811.43	450	90	353.58	98.79	2.89	168	8891	0.33
BWS_6	237.00	102.97	418811.43	450	90	349.13	98.79	2.79	166	8891	0.32
BWS_7	238.00	102.42	416097.64	450	90	380.24	98.79	2.88	180	8891	0.35
BWS_7	238.00	102.42	416097.64	450	90	309.13	98.79	2.78	148	8891	0.29
BWS_8	236.00	103.27	419477.92	450	90	469.13	98.79	2.84	220	8891	0.43
BWS_8	236.00	103.27	419477.92	450	90	424.69	98.79	2.90	200	8891	0.39
BWS_9	236.00	102.35	412037.22	450	90	424.69	98.79	2.89	200	8891	0.40
BWS_9	236.00	102.35	412037.22	450	90	335.80	98.79	3.23	160	8891	0.32
BWS_10	235.00	101.86	406372.17	450	90	362.46	98.79	2.80	172	8891	0.35
BWS_10	235.00	101.86	406372.17	450	90	215.80	98.79	2.79	106	8891	0.21
BWS_11	235.00	101.15	400726.8	450	90	269.13	98.79	2.78	130	8891	0.26
BWS_11	235.00	101.15	400726.8	450	90	309.13	98.79	3.31	148	8891	0.30

Table 2.26 Bond strength for the clay triplets performed with the device with a torque wrench.

Specimen	<i>b</i>	<i>d</i>	<i>Z</i>	<i>e</i> ₁	<i>e</i> ₂	<i>F</i> ₁	<i>F</i> ₂	<i>W</i>	<i>M</i> ₁	<i>M</i> ₂	<i>f</i> _{wi}
	[mm]	[mm]	[mm ³]	[mm]	[mm]	[N]	[N]	[N]	[N.mm]	[N.mm]	[MPa]
BWCL_0	167.44	100.97	284506.8	450	90	206.91	98.79	21.77	102	8891	0.28
BWCL_0	167.44	100.97	284506.8	450	90	204.69	98.79	22.60	101	8891	0.28
BWCL_1	165.99	100.48	279312.2	450	90	184.69	98.79	21.72	92	8891	0.26
BWCL_1	165.99	100.48	279312.2	450	90	102.46	98.79	22.75	55	8891	0.15
BWCL_2	170.76	100.51	287510.3	450	90	224.69	98.79	21.96	110	8891	0.31
BWCL_2	170.76	100.51	287510.3	450	90	95.80	98.79	23.61	52	8891	0.13
BWCL_3	172.29	100.60	290606.1	450	90	226.91	98.79	21.80	111	8891	0.31
BWCL_3	172.29	100.60	290606.1	450	90	124.69	98.79	18.65	65	8891	0.17
BWCL_4	172.77	100.44	290489.5	450	90	224.69	98.79	17.36	110	8891	0.30
BWCL_4	172.77	100.44	290489.5	450	90	46.91	98.79	23.28	30	8891	0.07
BWCL_5	174.13	100.11	290855.5	450	90	113.58	98.79	22.56	60	8891	0.16
BWCL_5	174.13	100.11	290855.5	450	90	69.13	98.79	23.50	40	8891	0.10
BWCL_6	176.14	101.20	300654.5	450	90	162.46	98.79	17.93	82	8891	0.21
BWCL_6	176.14	101.20	300654.5	450	90	193.58	98.79	24.25	96	8891	0.25

Specimen	<i>b</i>	<i>d</i>	<i>Z</i>	<i>e</i> ₁	<i>e</i> ₂	<i>F</i> ₁	<i>F</i> ₂	<i>W</i>	<i>M</i> ₁	<i>M</i> ₂	<i>f</i> _{wi}
	[mm]	[mm]	[mm ³]	[mm]	[mm]	[N]	[N]	[N]	[N.mm]	[N.mm]	[MPa]
BWCL_7	175.60	101.43	301096.8	450	90	0.21	98.79	18.34	95	8891	0.01
BWCL_7	175.60	101.43	301096.8	450	90	0.13	98.79	23.02	60	8891	0.01

Table 2.27 Bond strength for the clay triplets performed with the device used in the previous campaign.

Specimen	<i>b</i>	<i>d</i>	<i>Z</i>	<i>e</i> ₁	<i>e</i> ₂	<i>F</i> ₁	<i>F</i> ₂	<i>W</i>	<i>M</i> ₁	<i>M</i> ₂	<i>f</i> _{wi}
	[mm]	[mm]	[mm ³]	[mm]	[mm]	[N]	[N]	[N]	[N.mm]	[N.mm]	[MPa]
BWCL_8	176.06	100.38	295667.7	945	205	92.68	100.68	22.61	87.58721	20639	0.32
BWCL_8	176.06	100.38	295667.7	945	205	39.77	100.68	18.56	37.5824	20639	0.16
BWCL_9	175.51	101.43	300942.5	945	205	-	100.68	-	-	20639	(*)
BWCL_9	175.51	101.43	300942.5	945	205	20.72	100.68	24.50	19.57919	20639	0.10
BWCL_10	173.16	99.93	288196.1	945	205	100.79	100.68	22.14	95.2446	20639	0.35
BWCL_10	173.16	99.93	288196.1	945	205	52.15	100.68	18.74	49.28171	20639	0.21
BWCL_11	173.31	100.78	293373.6	945	205	12.47	100.68	22.93	11.78274	20639	0.08
BWCL_11	173.31	100.78	293373.6	945	205	56.17	100.68	18.67	53.0826	20639	0.21

(*) The specimen was damaged before the start of the test.

Table 2.28 Summary of bond strength in the two types of tested specimens.

Type of specimen	Bond strength		
	Average [MPa]	Standard deviation [MPa]	Coefficient of variation [-]
Calcium silicate triplets	0.33	0.08	0.240
Clay triplets	0.19	0.10	0.527

2.4 Analysis of the materials characterisation results

The main objective of this section of the work consisted on an in-depth characterisation of the various constituent materials of masonry cavity walls that were used in a real-scale model subjected to seismic tests until its collapse. These tests enabled to obtain relevant data for the interpretation of the tests carried out on the full-scale model, as well as to the validation of the representativeness of the experimental results, using numerical models, regarding the properties of masonry in real buildings in the Groningen region.

Concerning the bedding mortars that were analysed, in addition to the values obtained being consistent with the reference bibliography, a good ratio between the modulus of elasticity and the compressive strength obtained experimentally for the different ages was verified. On the other hand, in comparison to the previous campaign, the mortar for the CS masonry had lower strength properties. The mortar for the characterisation test specimens gave results similar the ones of the mortar for the real-scale model.

With respect to the masonry *wallettes* and *triplets*, it was found that, in terms of strength, the load-bearing masonry composed of CS blocks has a compressive strength substantially lower than the masonry composed of clay bricks. However, the bond strength obtained was significantly larger for the CS *triplets*.

3 INSTRUMENTATION OF THE SPECIMEN

In order to detect and monitor the structural response under different levels of input motion, several kinematic measuring instruments were installed on the building. The location and typology of the instruments was determined based on the identification of the critical zones and on the physical quantity to be recorded. The instrumentation consisted of 28 accelerometers and 21 displacement transducers.

Figure 3.1 (a) shows the ID number and the locations of the accelerometers installed on both inner and outer leaves, the timber roof beams, the RC slab, and the auxiliary steel structures. Figure 3.1 (b) shows, instead, the displacement transducers installed on the specimen: 9 wire potentiometers and 12 linear variable displacement transducers (LVDTs). The displacements measured between the specimen and the rigid reference frame were considered equivalent to the relative displacements with respect to the shake table surface. The wire potentiometers were installed in order to record the out-of-plane response of the East and West façades, at a height of about 0.65 m and 1.30 m from the top of slab, as well as the displacement of the roof ridge beam. The LVDTs were installed to monitor the possible slippage between the roof ridge beam and the top of the gable walls, as well as the uplift at the base of the gable walls. They were also used to measure any undesired slippage between the steel foundation and the shake table, between the slab and the timber plates, and between the RC slab and the reference steel frame.

Table 3.1 and Table 3.2 list the accelerometers and the displacement transducers, respectively, describing their location in the specimen and the column (Col. #) identifying the recorded histories in the .txt files containing the test experimental data. The data is organised in matrix form and named in accordance to Table 4.1. The data acquisition time step is 0.005 s and columns 31 to 58 contain the acceleration histories recorded by the accelerometers mounted on the structure. The displacement histories recorded by wire potentiometers are listed in columns 10 to 18, while those recorded by LVDTs are found in columns 19 to 30. Columns 2 to 9 contain the shake table control data, in terms of longitudinal (x direction), transverse (y direction) and vertical (z direction) displacements and accelerations. Column 1 contains the time values, corresponding to a sampling frequency of 200 Hz. Column 59 lists the force in one of the two longitudinal actuators, while the last columns (60 to 67) contain quantities that were not directly measured, such as average accelerations, ridge beam relative displacements, total base-shear force, etc. In general, the authors suggest using these last sets of data. Table 3.1 specifies also the lumped masses associated to each instrument for computing the inertial forces.

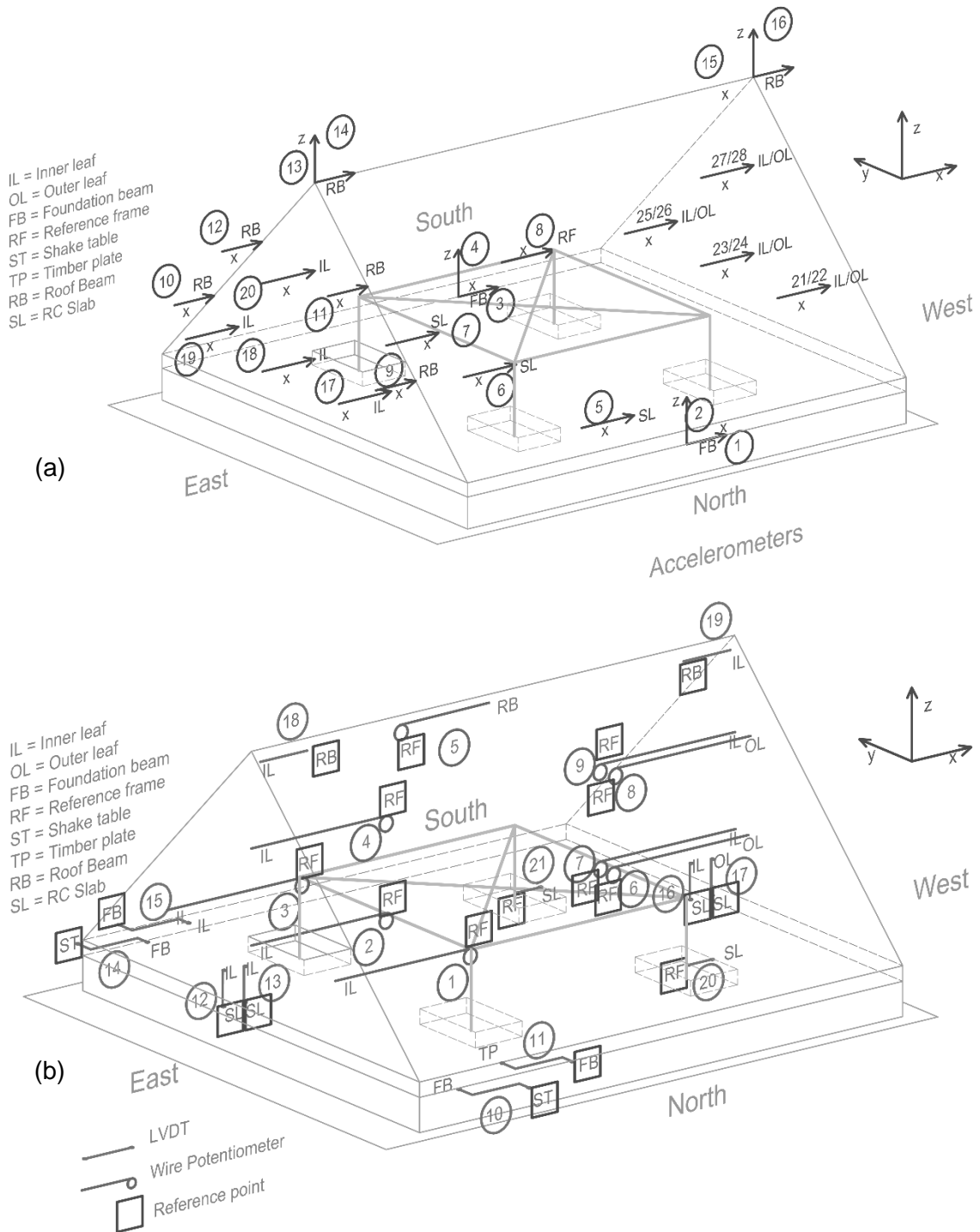


Figure 3.1 Locations of the instrumentation: (a) accelerometers and (b) displacement transducers (letters indicate the component at which the transducers is attached to: SL = slab, RF = reference frame, IL = inner leaf, OL = outer leaf, FB = foundation beam, ST = shaking table, TP = timber plate and RB = roof beam).

Table 3.1 Summary of the accelerometers and their location.

Instr. #	Col. #	UM	Mass [kg]	Location of the instrument
1	31	[g]	0	installed on the foundation beam on the South side and used to record the accelerations in the x direction at the foundation level
2	32	[g]	0	installed on the foundation beam on the South side and used to record the accelerations in the z direction at the foundation level
3	33	[g]	0	installed on the foundation beam on the North side and used to record the accelerations in the x direction at the foundation level
4	34	[g]	0	installed on the foundation beam on the North side and used to record the accelerations in the z direction at the foundation level
5	35	[g]	236.24	installed on the slab on the North side and used to record the accelerations in the x direction at slab level
6	36	[g]	0	installed on the slab on the centre and used to record the accelerations in the x direction at slab level
7	37	[g]	236.24	installed on the slab on the South side and used to record the accelerations in the x direction at slab level
8	38	[g]	0	installed on the steel frame and recording the accel. in the x direction
9	39	[g]	472.49	installed on the 1/3 height roof beam on North-East side and used to record the accelerations in the x direction
10	40	[g]	472.49	installed on the 1/3 height roof beam on South-East side and used to record the accelerations in the x direction
11	41	[g]	0	installed on the 2/3 height roof beam on North-East side and used to record the accelerations in the x direction
12	42	[g]	944.97	installed on the 2/3 height roof beam on South-East side and used to record the accelerations in the x direction
13	43	[g]	236.24	installed on the ridge beam on East side and used to record the accelerations in the x direction at slab level
14	44	[g]	0	installed on the ridge beam on East side and used to record the accelerations in the z direction at slab level
15	45	[g]	236.24	installed on the ridge beam on West side and used to record the accelerations in the x direction at slab level
16	46	[g]	0	installed on the ridge beam on West side and used to record the accelerations in the z direction at slab level
17	47	[g]	563.64	installed at 8 th brick layer of the East OOP CS veneer on the North side recording the accelerations in the x direction
18	48	[g]	242.76	installed at 8 th brick layer of the East OOP CS veneer on the centre recording the accelerations in the x direction
19	49	[g]	0	installed at 8 th brick layer of the East OOP CS veneer on the South side recording the accelerations in the x direction
20	50	[g]	355.96	installed at 20 th brick layer of the East OOP CS veneer on the centre recording the accelerations in the x direction
21	51	[g]	276.30	installed at 8 th brick layer of the West OOP CS veneer on the North side recording the accelerations in the x direction
22	52	[g]	339.52	installed at 11 th brick layer of the West OOP clay veneer on the North side recording the accelerations in the x direction
23	53	[g]	242.76	installed at 8 th brick layer of the West OOP CS veneer on the centre recording the accelerations in the x direction
24	54	[g]	280.15	installed at 11 th brick layer of the West OOP clay veneer on the centre recording the accelerations in the x direction
25	55	[g]	281.82	installed at 8 th brick layer of the West OOP CS veneer on the South side recording the accelerations in the x direction
26	56	[g]	332.86	installed at 11 th brick layer of the West OOP clay veneer on the South side recording the accelerations in the x direction
27	57	[g]	348.98	installed at 20 th brick layer of the West OOP CS veneer on the centre recording the accelerations in the x direction
28	58	[g]	406.20	installed at 27 th brick layer of the West OOP CS veneer on the centre recording the accelerations in the x direction

Shaded lines: instruments removed after test FEQ2-400%;

The readings from accelerometer 11 are not reliable from FEQ2-150% until the end of the test, while accelerometers 19 and 20 are not reliable during FEQ2-100% and FEQ2-400%, respectively.

Table 3.2 Summary of the displacement transducers and their location.

Instr. #	Col. #	UM	Location of the instrument
1	10	[mm]	installed at 9 th brick layer CS OOP East wall on North side recording its horizontal displacement
2	11	[mm]	installed at 9 th brick layer CS OOP East wall on centre recording its horizontal displacement
3	12	[mm]	installed at 9 th brick layer CS OOP East wall on South recording its horizontal displacement
4	13	[mm]	installed at 17 th brick layer CS OOP East wall on centre recording its horizontal displacement
5	14	[mm]	installed on the roof beam recording its horizontal displacement with respect to the steel frame
6	15	[mm]	installed at 14 th brick layer clay OOP West wall on centre recording its horizontal displacement
7	16	[mm]	installed at 9 th brick layer CS OOP West wall on centre recording its horizontal displacement
8	17	[mm]	installed at 25 th brick layer clay OOP West wall on centre recording its horizontal displacement
9	18	[mm]	installed at 17 th brick layer CS OOP West wall on centre recording its horizontal displacement
10	19	[mm]	installed to record the displacement of the foundation beam (North side) with respect to the shake table
11	20	[mm]	installed to record the displacement of the timber plate (North side) with respect to foundation beam
12	21	[mm]	installed to record the uplift of the East OOP CS veneer (Outer side) with respect to the slab
13	22	[mm]	installed to record the uplift of the East OOP CS veneer (Inner side) with respect to the slab
14	23	[mm]	installed to record the displacement of the foundation beam (South side) with respect to the shake table
15	24	[mm]	installed to record the displacement of the timber plate (South side) with respect to the foundation beam
16	25	[mm]	installed to record the uplift of the West OOP CS veneer with respect to the slab
17	26	[mm]	installed to record the uplift of the West OOP clay veneer with respect to the slab
18	27	[mm]	installed to record the detachment of the ridge beam with respect to the East OOP CS veneer
19	28	[mm]	installed to record the detachment of the ridge beam with respect to the West OOP CS veneer
20	29	[mm]	installed to record the displacement of the slab in the North-East side with respect to the steel frame
21	30	[mm]	installed to record the displacement of the slab in the South-West side with respect to the steel frame

Figure 3.2 presents some pictures of the instrumentation installed on the specimen, with the ID numbers shown therein referring to the instrument numbers listed in Table 3.1 and Table 3.2.



Figure 3.2 Pictures of the instrumentation.



Figure 3.2 (continued) Pictures of the instrumentation.

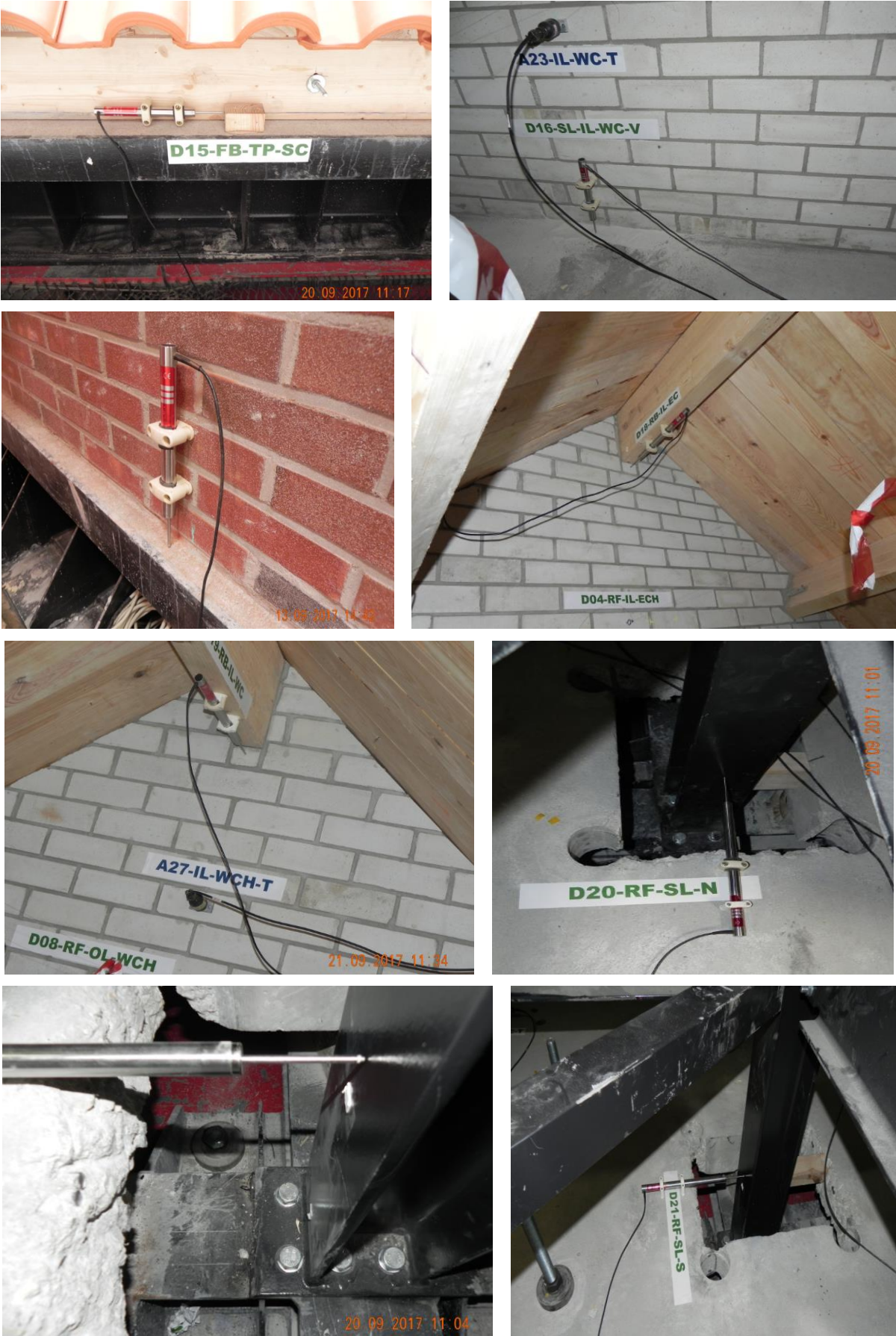


Figure 3.2 (continued) Pictures of the instrumentation.

4 SHAKE TABLE TEST PROCEDURE

The roof specimen was subjected to a sequence of incremental dynamic tests. A series of shake table motions of increasing intensity were applied with the aim of assessing the ultimate capacity and the failure mechanism leading to the specimen collapse. Since the specimen constitutes a reduced version of LNECBUILD-1 and of EUCBUILD-1 (i.e. only the roof was built), the second-floor accelerations recorded in the test carried out by Graziotti et al. (2015) have been adopted as input at the base of the specimen. Therefore, the actual horizontal longitudinal inputs were floor accelerograms of the EUCBUILD-1 specimen subjected to incremental dynamic tests with two records: EQ1 and EQ2, representative of the dynamic characteristics of induced seismicity ground motions. The two original inputs correspond to two main scenarios with different return periods (scenario 1 and scenario 2), identified after a detailed study on the seismic hazard characteristics of the region (see Appendix B2 of Technical Report EUC318/2015U).

4.1 Shake Table Input Sequence

The specimen was subjected to two different types of base motion: i) dynamic identification tests using the response of the specimen to a random white noise shake table input, with frequencies up to 40 Hz and nominal peak-to-peak amplitude of 4 mm; and ii) two-component earthquake records.

As mentioned above, the horizontal components of the records were floor accelerograms recorded on the second floor of the specimen EUCBUILD-1; for practicality and to allow a better control of the shake table performance, only the floor accelerograms produced by EQ1-100%, EQ1-150%, EQ2-100%, EQ2-150% and EQ2-200% were adopted as horizontal input components. These five floor accelerograms have been considered well representative of the progressive damage evolution occurring in the EUCBUILD-1 specimen, thus allowing for a realistic comparison between the two tests; Figure 4.1 presents the horizontal component acceleration histories of the adopted accelerograms. Figure 4.2 shows the 5% damped acceleration response spectrum of the selected experimental inputs, which reflect the induced seismicity input already filtered by the dynamics of the EUCBUILD-1 specimen and of the shake table system of EUCENTRE.

The sequence of incremental tests followed strictly the one performed for EUCBUILD-1, increasing gradually the intensity of the ground motions and applying first FEQ1, followed by FEQ2. Table 4.1 presents the applied testing sequence specifying the input typology and the corresponding scaling factor. Each test with increasing intensity was alternated by the white noise excitation which, by means of a dynamic identification procedure, allowed the changes in the dynamic properties of the structure to be detected as the damage level increased. The incremental testing sequence stopped at test FEQ2-600% with the collapse of the East CS gable wall, which failed out-of-plane.

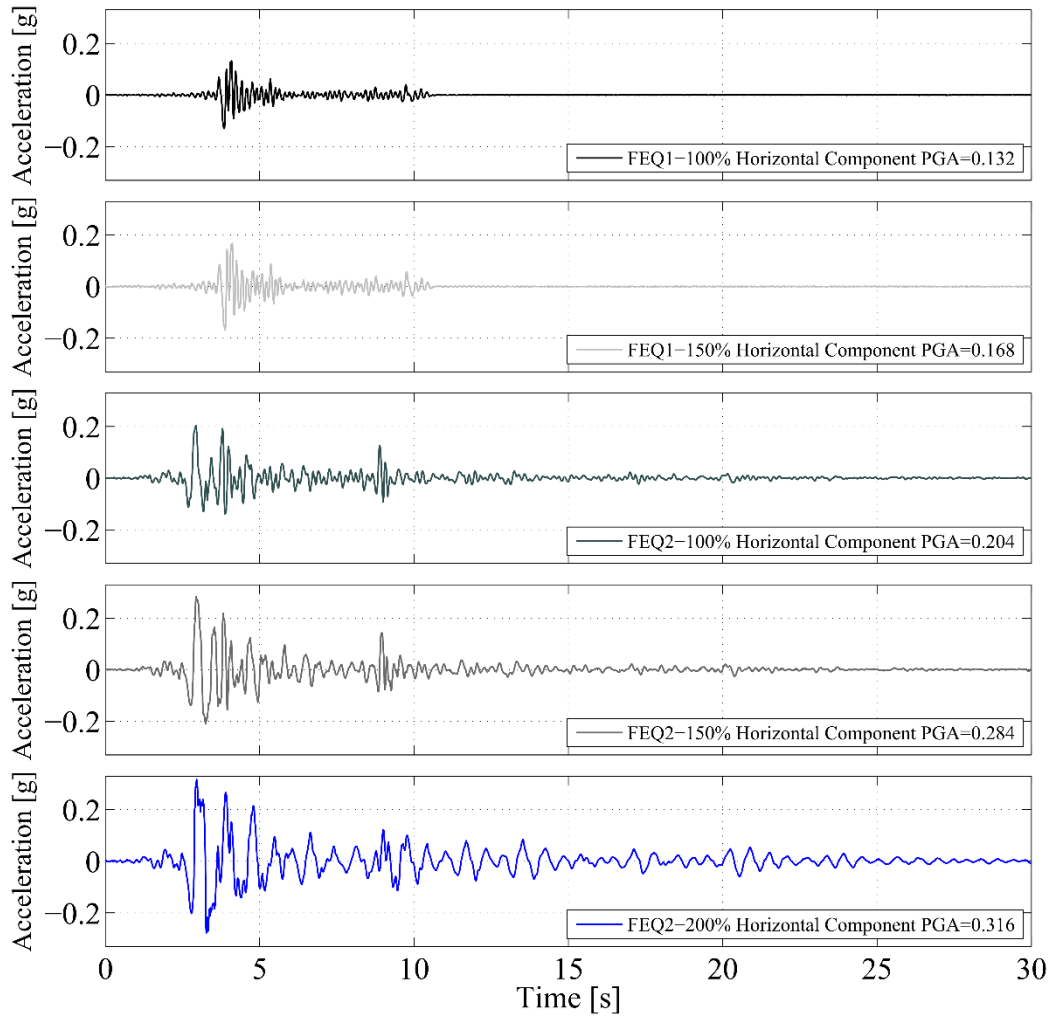


Figure 4.1 Theoretical horizontal components of the adopted floor accelerograms.

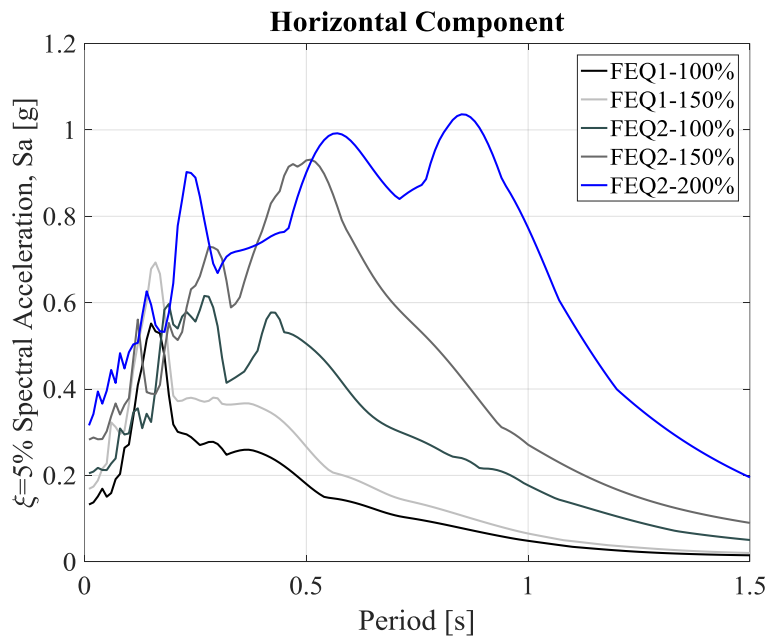


Figure 4.2 Theoretical horizontal 5% damped acc. response spectra of the experimental inputs.

Table 4.1 Applied testing sequence.

Test #	Test Name	Horizontal Input Component	Scaling Factor
1	FEQ1-50%	2 nd Floor Acc. of EUCBUILD-1 subjected to EQ1-100%	50%
2	FEQ1-100%	2 nd Floor Acc. of EUCBUILD-1 subjected to EQ1-100%	100%
3	FEQ1-150%	2 nd Floor Acc. of EUCBUILD-1 subjected to EQ1-150%	100%
4	FEQ2-50%	2 nd Floor Acc. of EUCBUILD-1 subjected to EQ2-100%	50%
5	FEQ2-100%	2 nd Floor Acc. of EUCBUILD-1 subjected to EQ2-100%	100%
6	FEQ2-150%	2 nd Floor Acc. of EUCBUILD-1 subjected to EQ2-150%	100%
7	FEQ2-200%	2 nd Floor Acc. of EUCBUILD-1 subjected to EQ2-200%	100%
8	FEQ2-300%	2 nd Floor Acc. of EUCBUILD-1 subjected to EQ2-200%	150%
9	FEQ2-400%	2 nd Floor Acc. of EUCBUILD-1 subjected to EQ2-200%	200%
10	FEQ2-500%	2 nd Floor Acc. of EUCBUILD-1 subjected to EQ2-200%	250%
11	FEQ2-100%-C	2 nd Floor Acc. of EUCBUILD-1 subjected to EQ2-100%	100%
12	FEQ2-600%	2 nd Floor Acc. of EUCBUILD-1 subjected to EQ2-200%	300%

4.2 Characterisation of the induced ground motion tests

Table 4.2 presents the applied testing sequence specifying the floor motions and the following quantities:

- Nominal horizontal PGA;
- Nominal horiz. spectral acceleration (5% damping) at the fundamental period, $S_a(T_1)$;
- Recorded horizontal PGA;
- Calculated spectral acceleration (5% damping) at the fundamental period, $S_a(T_1)$;
- Recorded horizontal PGD;
- Calculated horizontal PGV.

Further intensity measures characterising the input sequence are listed in Table 4.3:

- Calculated average spectral acceleration (5% damping) between the fundamental period one ($S_a(T_1)$, $T_1=0.08$ s) and the damaged period ($S_a(T_1)$, $T_1=0.10$ s), $S_{a_{av}}$;
- Housner Intensity: defined as the integral of the pseudo-velocity elastic response spectrum between a structural period of 0.1 and 2.5 s:

$$HI(5\%) = \int_{0.1}^{2.5} PSV(5\%, T) dT \quad (13)$$

- Modified Housner Intensity: defined as the integral of the pseudo-velocity elastic response spectrum between a structural period of 0.1 and 0.5 s (which corresponds to the range of periods of interest for the tested specimen):

$$mHI(5\%) = \int_{0.1}^{0.5} PSV(5\%, T) dT \quad (14)$$

- Arias Intensity;
- Cumulative absolute velocity;
- Significant duration (5-75%);
- Significant duration (5-95%).

Table 4.2 Summary of the floor motion testing sequence dynamic characteristics.

Test #-Test Name	Nom. H-PGA [g]	Nom. Sa(T ₁) [g]	H-PGA [g]	Sa(T ₁) [g]	H-PGD [mm]	H-PGV [mm/s]
1-FEQ1-50%	0.066	0.102	0.074	0.105	3.2	34.9
2-FEQ1-100%	0.132	0.203	0.143	0.205	6.4	64.5
3-FEQ1-150%	0.168	0.296	0.170	0.286	8.6	95.0
4-FEQ2-50%	0.102	0.154	0.106	0.182	10.6	61.9
5-FEQ2-100%	0.204	0.309	0.207	0.312	21.7	136.0
6-FEQ2-150%	0.284	0.341	0.245	0.380	23.9	160.2
7-FEQ2-200%	0.316	0.483	0.487	0.640	53.0	274.1
8-FEQ2-300%	0.475	0.725	0.668	0.774	82.5	415.3
9-FEQ2-400%	0.633	0.966	0.935	1.138	102.5	538.3
10-FEQ2-500%	0.791	1.208	0.955	1.091	124.2	614.8
11-FEQ2-100%-C	0.204	0.309	0.201	0.339	21.5	128.3
12-FEQ2-600%	0.949	1.449	1.138	1.410	137.4	677.9

Table 4.3 Summary of the floor motion dynamic characteristics.

Test #-Test Name	Sa _{av} [g]	HI [mm]	mHI [mm]	IA [mm/s]	CAV [mm/s]	SD _{5-75%} [s]	SD _{5-95%} [s]
1-FEQ1-50%	0.11	80.3	27.4	23.2	667.0	0.74	5.08
2-FEQ1-100%	0.21	164.9	56.5	99.8	1409.1	0.76	5.08
3-FEQ1-150%	0.29	227.0	76.1	173.4	1932.0	1.04	5.84
4-FEQ2-50%	0.19	224.6	51.8	91.8	1975.2	2.00	6.96
5-FEQ2-100%	0.32	451.6	106.3	383.0	4008.2	2.00	6.82
6-FEQ2-150%	0.38	516.1	122.8	466.8	4068.2	1.74	6.46
7-FEQ2-200%	0.64	1305.2	143.6	1351.0	8673.1	2.79	11.36
8-FEQ2-300%	0.78	2005.6	215.0	3166.0	13361.0	2.92	11.59
9-FEQ2-400%	1.14	2603.8	278.6	5432.9	17612.5	3.39	11.66
10-FEQ2-500%	1.10	3134.8	301.3	8067.9	21831.6	3.70	12.91
11-FEQ2-100%-C	0.35	444.4	103.0	368.1	3946.2	2.01	7.14
12-FEQ2-600%	1.42	3530.1	345.1	10752.2	25567.5	4.465	14.13

5 SHAKE TABLE TEST RESULTS

5.1 Damage evolution

The roof prototype suffered almost no damage during the transportation phase to the shake table, with only a very thin crack appearing at the central part of the base of the West wall outer leaf. Given that this clay wall was not load-bearing, it was assumed that such initial damage did not affect the response of the specimen. Figure 5.1 shows a view of the specimen transportation to the shaking table.

Figure 5.2 shows the evolution of the damage surveyed on both gable walls, the single leaf CS wall on the East side and the double leaf cavity wall on the West side, with inner leaf CS wall and outer leaf clay wall, throughout the entire testing sequence. At the end of each stage of the shake table testing sequence, detailed surveys were carried out for reporting any possible evidence of damage having affected the structure. The outside of the East CS wall was covered with a white plaster layer, making the detection of new cracks easier.

The first visible damage associated to a shake table motion was detected during test FEQ1-100% ($S_a(T_1) = 0.205\text{ g}$). Minor cracking was observed on the East gable wall, around the L-shaped steel anchors connecting the CS wall to the timber roof beams. This was a very minor damage, only visible on the plastered wall and not represented in Figure 5.2. No particular additional damage was visible during tests FEQ1-150% and FEQ2-50%, although a slight reduction of the specimen's fundamental frequency of vibration was detected.

There was a crack opening at the base the CS East gable wall during test FEQ2-100% ($S_a(T_1) = 0.312\text{ g}$), with a permanent crack width of around 0.1 mm, as shown later in Figure 5.34 where a clear rocking response in that wall is well documented. Despite no crack being visible on the inner CS West wall, a coupled rocking response was measured between the two leafs and a crack was observed at the outer clay wall.

Test FEQ2-150% caused no new damage on the structure, while FEQ2-200% ($S_a(T_1) = 0.640\text{ g}$) has only extended already existing cracks. Nevertheless, a new significant reduction of the fundamental frequency of the roof specimen was observed after FEQ2-200%, similar to the reduction observed after FEQ2-100%.



Figure 5.1 Specimen transportation to the shake table.

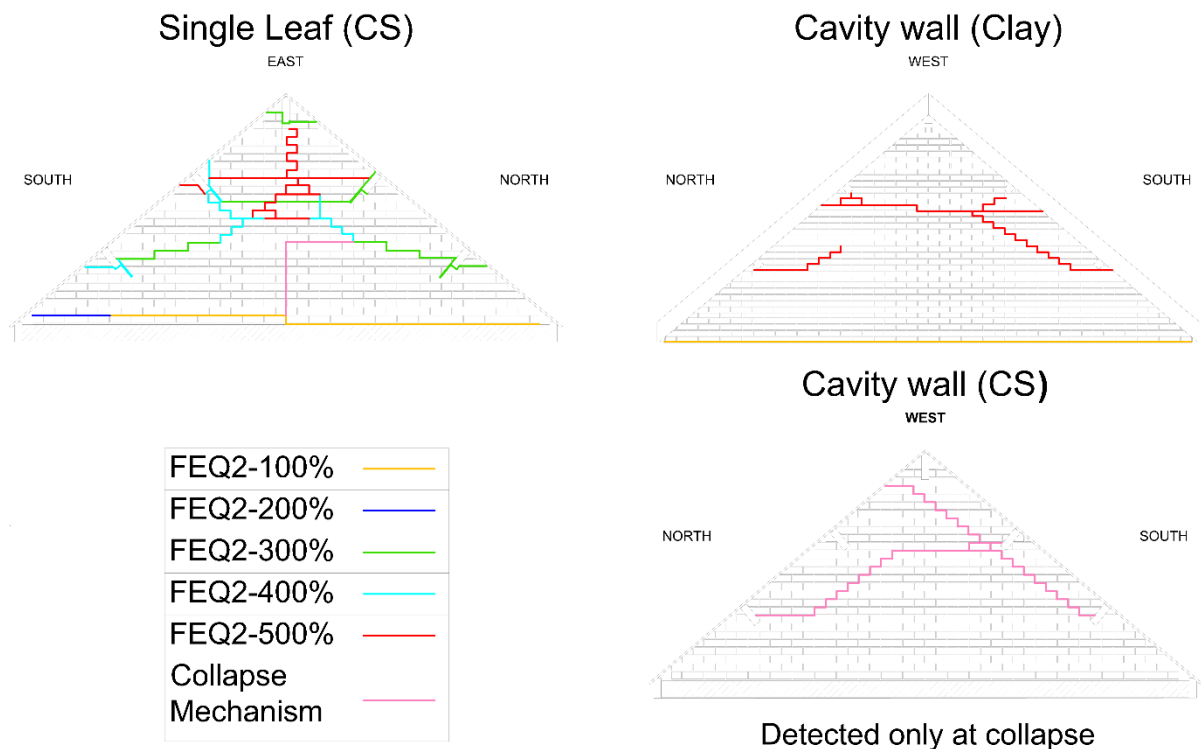


Figure 5.2 Evolution of the crack pattern in the gable walls along the test stages.

During test FEQ2-300% ($Sa(T_1) = 0.774$ g), several new sub-horizontal cracks formed on the East gable wall with their origin at the connection between the CS wall and the roof beams. No new cracks were identified on the West wall for this test, nor for the following one: FEQ2-400% ($Sa(T_1) = 1.138$ g). On the other hand, the latter test induced an enlargement of the cracks on the East wall, interconnecting several of the pre-existing ones. At this point, several instruments were removed for safety reasons.

Afterwards, test stage FEQ2-500% ($Sa(T_1) = 1.091$ g) generated a set of cracks on the outer clay leaf of the West wall very similar to the one produced on the East wall during FEQ2-300%. On the East wall, the main crack opening was a vertical one from the ridge beam downwards, largely contributing to the formation of the collapse mechanism mobilised on the subsequent test, FEQ2-600% ($Sa(T_1) = 1.410$ g). During this last test, another vertical crack formed on the East gable wall, now originating from the bottom of the wall and completing its collapse mechanism. Only then important cracks on the inner leaf CS West wall were detected. The (partial) collapse of the specimen prototype was thus attained during test FEQ2-600%, as described in the following section, exhibiting a rather fragile behaviour.

5.2 Description of the collapse mechanism

Figure 5.3 illustrates a sequence of frames of the video when the building prototype exhibited a local collapse of the East wall. Figure 5.3 (a) to (d) represent a first impulse, with the gable wall bending to the interior of the model. The crack at the base of the wall opened significantly due to flexure/rocking, followed by the opening of the horizontal crack between the 2/3 height roof beams. In Figure 5.3 (d) the motion was opposite, with the closure of those cracks and the opening of the vertical crack at the upper third of the gable which moved outward of the model.

Figure 5.3 (e) to (g) represent a second impulse of the gable towards the interior of the model, with the two horizontal cracks opening very significantly and leading to the formation of the vertical crack at half span and in the lower 2/3 of the wall, visible in Figure 5.3 (f). The collapse

mechanism was then completely formed and that portion of the East gable wall had a full collapse towards the interior of the model, illustrated in Figure 5.3 (g).



Figure 5.3 Snapshots of the FEQ2-600% test.

Afterwards, the upper third of the gable wall, which was fully cracked and with complete loss of connection to the roof beams, also collapsed. The timber roof had a flexural response with a deflection towards the interior of the model, since it had no longer any support on the East side of the model, as represented in Figure 5.3 (h) to (j).

Figure 5.4 illustrates the final damaged state of the model and the permanent deformations that were not recovered. It is especially interesting to note that, even at this post-collapse state, the West wall and the timber roof system still retained a full load-carrying capacity for gravity loads.

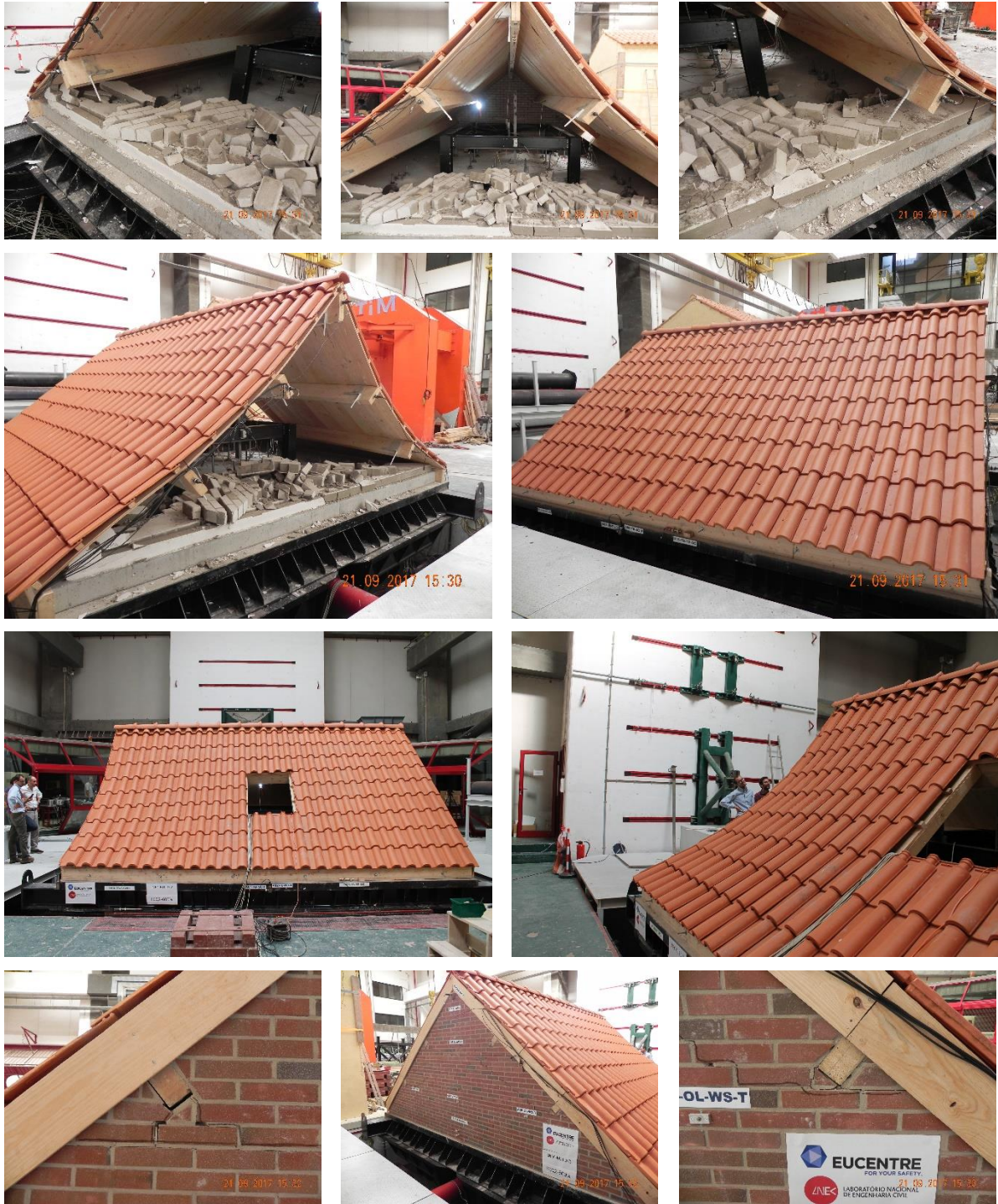


Figure 5.4 Pictures of the specimen at the end of the test FEQ2-600%.

5.3 Shake Table Performance

Similarly to the previous test performed at LNEC, the target shake table motions for this specimen were very demanding. In fact, LNEC's shake table should reproduce a floor motion observed on the building prototype tested in EUCENTRE, in a different shake table system (with LNEC's shake table having more degrees of freedom), and with a specimen with different dynamic properties than the one tested in EUCENTRE.

However, the roof specimen proved to be a stiff structure, with a stable dynamic response, and with several components retaining most of their initial capacity even at the post-collapse state. On the other hand, the control system of LNEC's shake table was improved after the test of LNEC-BUILD-1, allowing for a better adjustment of the shake table response to the target spectra. Therefore, the comparison between the theoretical response spectra (shown in Figure 4.2) and those obtained from the accelerations recorded on the specimen's foundation results in a very good match, as depicted in Figure 5.5.

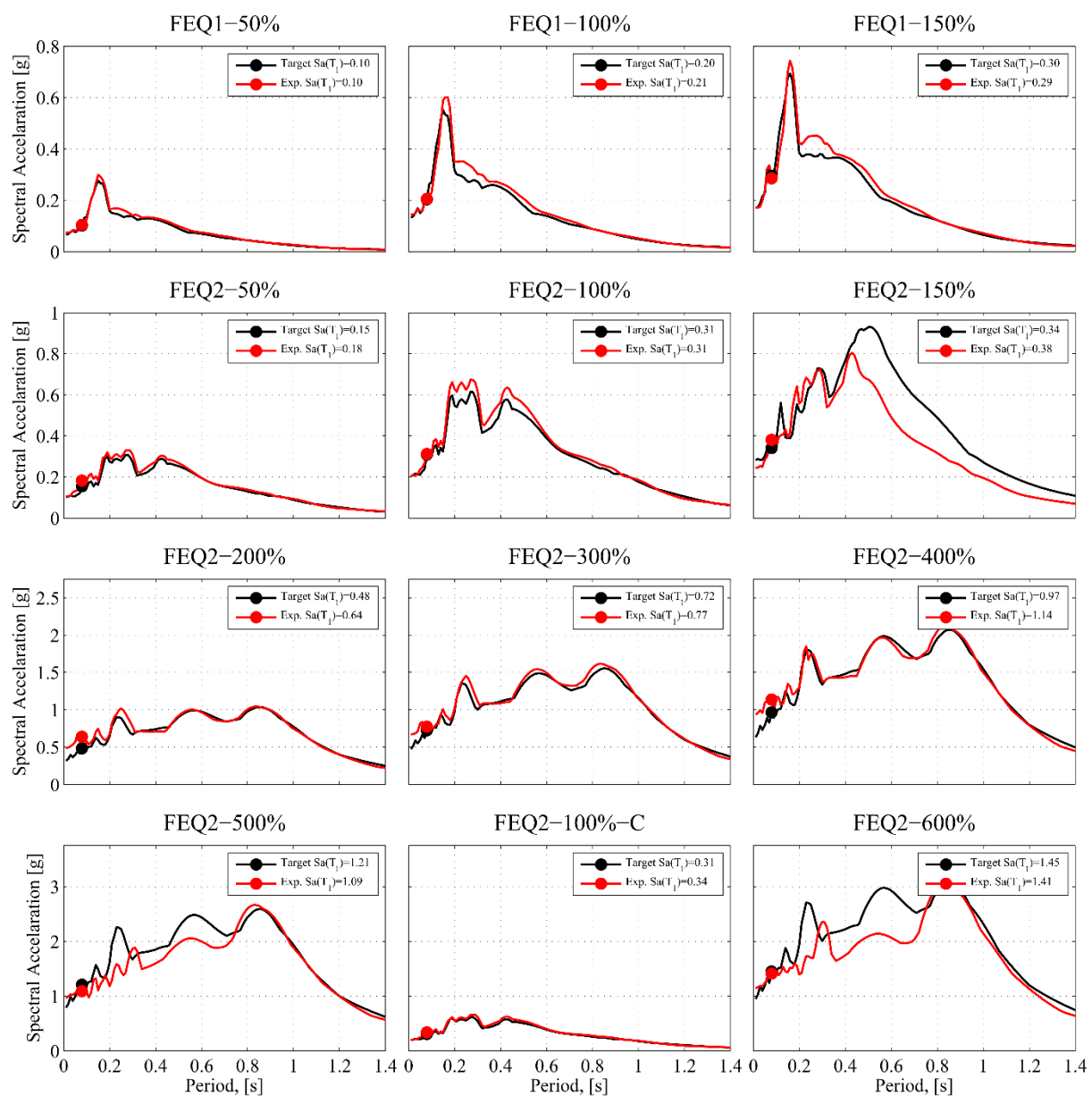


Figure 5.5 Theoretical-experimental 5% damped response spectra for all test stages.

It should be noted, nevertheless, that the shake table velocity limits prevent it from fulfilling completely the spectra for intensities larger than FEQ2-400%, reason why the target spectra for FEQ2-500% and FEQ2-600% are underachieved. Additionally, the experimental spectrum for FEQ2-150% was apparently not followed with enough precision. The reason for this is because the actual target spectra used, by mistake, was the one recorded in EUC-BUILD1 for stage FEQ2-125%. Still, the two acceleration time-histories are very close and the target spectral acceleration at the period of the roof specimen was relatively well achieved. For the above reasons, the test stage results will be compared to FEQ2-150% test results in the previous specimens.

5.4 Specimen dynamic identification

5.4.1 Introduction and methodology

Many signals are appropriate for use in experimental modal analysis, such as random white noise vibration or impulsive signals. In the estimation of frequency response functions, the choice depends upon the characteristics of the system, the theory underlying the parameter estimation and the expected utilization of the data. Different types of excitation signals have their own characteristics and some are more suited for some goals than others.

In this test, a random white noise vibration was adopted, with frequency content between 0.1 Hz and 40 Hz, nominal peak-to-peak amplitude of 4 mm, and 160 s of duration, for estimating the frequency response functions (FRFs) based on input-output relationships. This signal was used either for characterisation of the entire test system (shake table + specimen) in the adaptive tuning process of the desired target signals to be imposed in the shake table, or for a dynamic identification of the specimen (on the shake table). In this last case, the FRFs were used to quantify the specimen dynamic characteristics along the testing stages as a means to assess its damage evolution (decrease of natural frequencies and increase of modal damping). From the point of view of damage assessment, measured through the changes in the FRFs along the entire test protocol, it is important to use always the same type and amplitude of the input signals in order to be able to compare compatible results.

The dynamic identification through the specimen's responses is obtained from the acceleration histories shown in Figure 5.6. The FRFs are computed by LNEC-SPA (Mendes and Campos Costa 2007) taking into account the single-input / multi-output relations (SIMO) between the acquired signals. Figure 5.7 represents one of those functions obtained considering the slab acceleration as input and the ridge beam motion as response.

The estimation of the complex FRF $H_i(f)$ is done, according to the method described in Bendat et al. (2010), by the following formula:

$$H_i(f) = \frac{G_{xy_i}(f)}{G_{xx}(f)} \quad (15)$$

where x stands for shaking table input acceleration in each direction independently, y_i a given response acceleration at any location and direction on the structure, $G_{xy_i}(f)$ is the cross spectral density estimate between input and output signals and $G_{xx}(f)$ is the auto spectrum density estimate of the input signal.

The coherency function, which measures the quality of the transfer function, is computed as:

$$\gamma_{xy_i}^2(f) = \frac{|G_{xy_i}(f)|^2}{G_{xx}(f)G_{y_iy_i}(f)} \quad (16)$$

where $G_{y_iy_i}(f)$ is the auto spectrum density estimate of the output signal. For a given frequency f , the closest the coherency function is to one the more related is the input to the output signals.

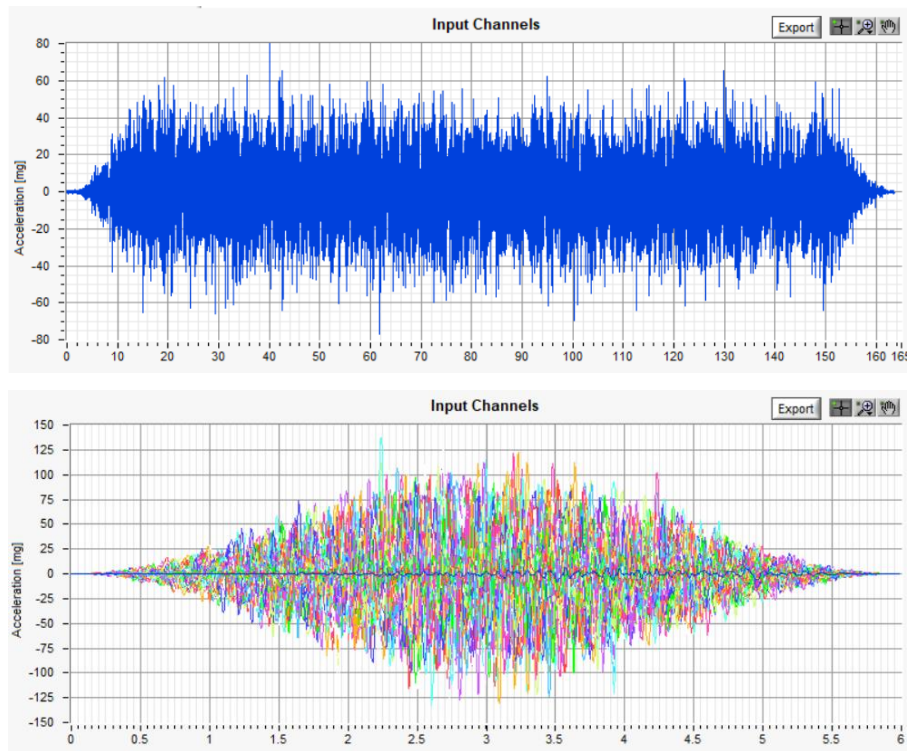


Figure 5.6 Input acceleration history (above) and windowed average input (below).

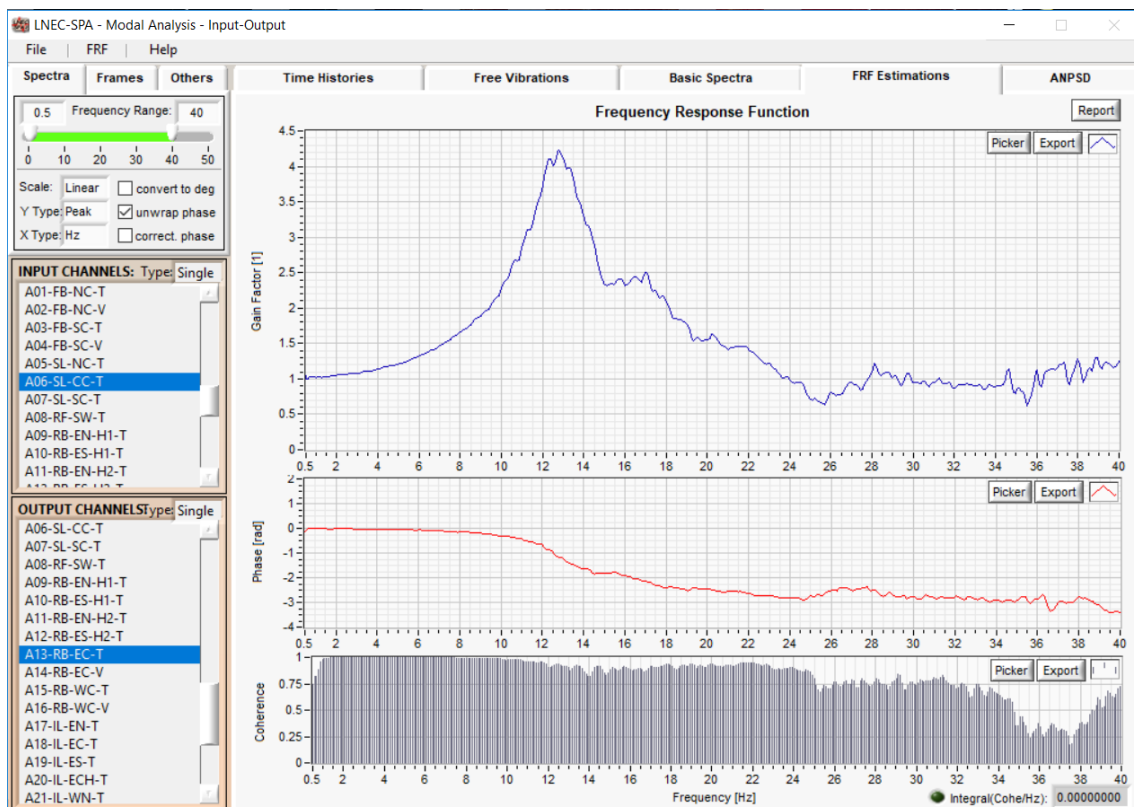


Figure 5.7 Frequency response function from rectangular impulses in the horizontal direction.

In the following sections, the methods used to estimate the natural frequencies, modal damping values and mode shapes are briefly introduced.

5.4.1.1 Frequency-Domain Decomposition method

The FDD method is based on the diagonalization of the spectral response density matrices, in order to decompose them into the modal contributions at each frequency. The diagonalization can be done through the Singular Value Decomposition (SVD) of each of the datasets. This decomposition corresponds to a single degree of freedom identification of the system for each singular value. This method can be described as:

- i. The structural response can be defined in modal coordinates and obtained from the sum of the contributions of the modes of vibration, through:

$$y(t) = \Phi q(t) \quad (17)$$

where Φ is the matrix containing the configuration of the vibration modes, ordered by columns, and q is the vector of modal coordinates;

- ii. The matrix of auto-correlation response functions can be calculated using:

$$C_{yy}(\tau) = E\{y(t + \tau)y(t)^T\} \quad (18)$$

- iii. Introducing (1) in the previous equation:

$$C_{yy}(\tau) = E\{\Phi q(t + \tau)q(t)^H \Phi^H\} = \Phi C_{qq}(\tau) \Phi^H \quad (19)$$

where $(.)^H$ represents the conjugate transposed operator for Hermitian matrices. The previous equation indicates that the matrix of the vibration modes' configurations allows to relate the matrices of the auto-correlation functions of the response and the auto-correlation functions, written in modal coordinates;

- iv. Applying the Fourier transform to the previous equation in the frequency domain yields:

$$G_{yy}(f) = \Phi G_{qq}(f) \Phi^H; \quad (20)$$

For uncorrelated modal coordinates, G_{qq} is a diagonal matrix and the modes of vibration present in the columns of Φ are orthogonal, concluding that the previous expression is similar to the one resulting from the decomposition into singular values:

$$SVD(A) = U(f) S U(f)^H = [\{u_i(f)\}, \dots] \begin{bmatrix} \ddots & & \\ & S_i & \\ & & \ddots \end{bmatrix} [\{u_i(f)\}, \dots]^H \quad (21)$$

where the matrix S is a diagonal real matrix with the singular values in descending order and has a representation along the various frequencies of the type indicated in Figure 5.8. It presents peaks coincident with the vibration modes and other dynamic phenomena that may introduce concentrated vibrations in a given frequency, for example rotary machines. The matrix U is of the complex type and contains in its columns the orthogonal vectors which are estimates of the modal configurations for each mode of vibration identified. It should be noted that when using the SVD algorithm, the matrix U depends on the frequency due to the rearrangement of the singular values involved in the algorithm.

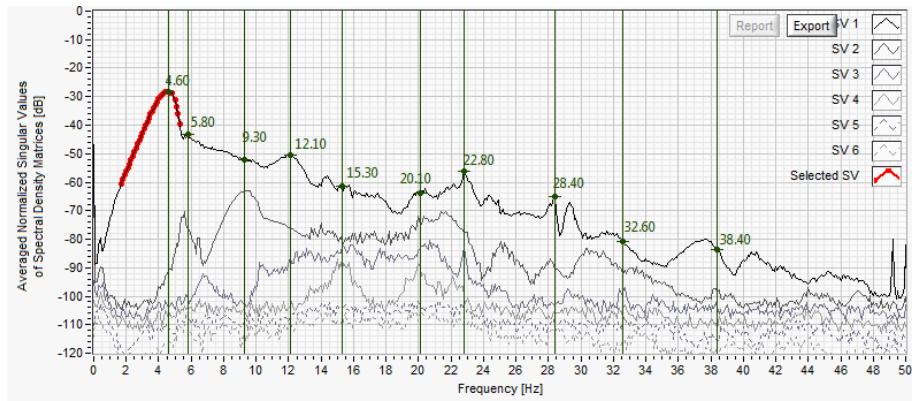


Figure 5.8 Representation of the Singular Values matrix.

5.4.1.2 Enhanced Frequency-Domain Decomposition method

The Enhanced Frequency-Domain Decomposition method (EFDD), proposed by Brincker et al. (2001), which provides estimates of modal damping and better estimates of vibration frequencies than the FDD method, was also used. This method consists of making an adjustment to the auto-correlation functions of a single degree of freedom, obtained from the functions of spectral density, selecting through a chosen criterion and weighing a set of points in the vicinity of each resonance, and finally applying the inverse of the Fourier transform. The criteria used in this method consists in defining a limit value of the MAC coefficient (Modal Assurance Criterion) which takes values between 0 and 1, obtaining the unit value when the vibration modes have the same configuration and null value when they are orthogonal.

This method allows more accurate estimates of the vibration frequencies, since it is based on the adjustment to the zero-crossings of the auto-correlation function and not only on a peak value, which can be influenced by several factors such as frequency resolution. The modal damping can be obtained from the logarithmic decrement of the impulse response function, as shown in Figure 5.9.

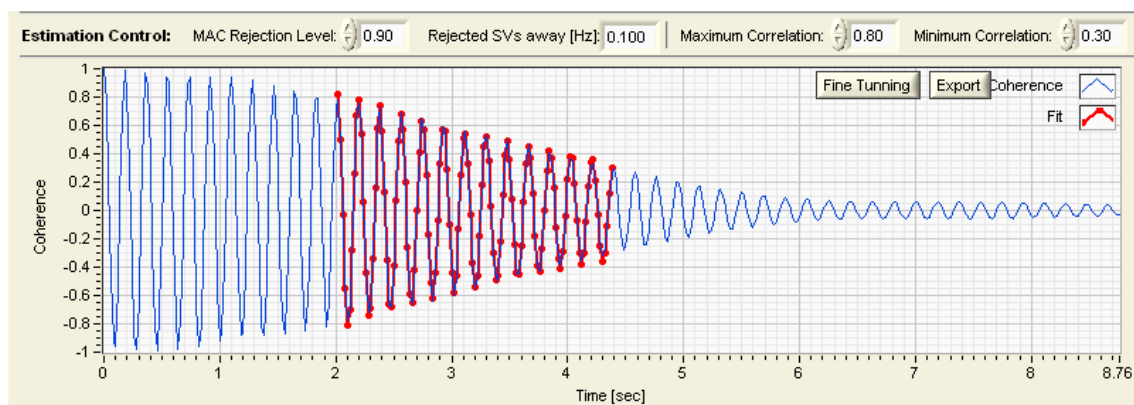


Figure 5.9 Frequency estimate (zero-crossings) and damping (logarithm decrement) of the impulse response estimate.

The numerical correlation of the mode shape vectors of the undamaged state of the model and the subsequent damaged states can also be obtained by computing the abovementioned MAC coefficient as shown in the equation below.

$$MAC_{u,d} = \frac{|\sum_{i=1}^n \varphi_i^u \varphi_i^d|^2}{\sum_{i=1}^n (\varphi_i^u)^2 \sum_{i=1}^n (\varphi_i^d)^2} \quad (22)$$

where φ^u is the mode shape vector corresponding to the undamaged condition of the model, φ^d is the mode shape vector corresponding to the damaged condition of the model and n is the number of estimated degrees of freedom (Allemang et al. 1982). The result of this expression is a scalar value in the range of 0 and 1 and indicates the extent of correlation between the two cases.

5.4.2 Dynamic identification results

5.4.2.1 Initial dynamic identification (CAT 00 – before any test)

After transportation and positioning of the model on the shake table, Figure 5.10, a dynamic identification test was performed. The accelerometer setup for modal animation of the vibration modes is depicted in Figure 5.11, while the FDD results are shown in Figure 5.12.



Figure 5.10 Test specimen fully instrumented on the shake table.

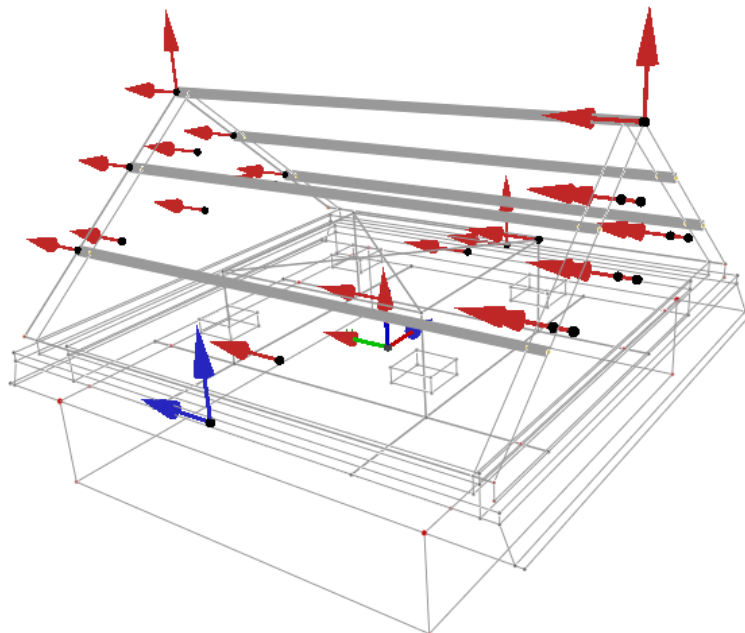


Figure 5.11 3D view of the accelerometers setup for dynamic identification.

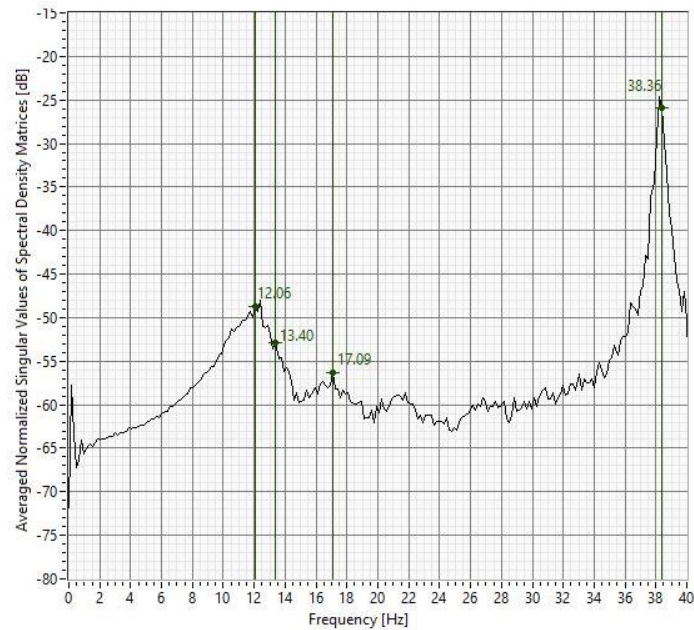


Figure 5.12 FDD results for 1st dynamic identification (CAT 00 – before any test).

It can be seen that there are two eigenfrequencies around 12-13 Hz, corresponding to two different modes of vibration. They are difficult to distinguish in most of the stages but are clearly separated in later stages of the test. The third natural frequency occurs around 17 Hz, while a fourth one clearly appears around 38 Hz.

The modal frequencies and damping values estimated through FDD and EFDD methods are summarised in Table 5.1, while the mode shapes are presented in Figure 5.13 and their MAC coefficients in Table 5.2. The latter show that the first three modes of vibration have similar shapes, which is natural because, for such a rigid structure, they all involve a significant motion of the shake table and not so much structural deformation.

Table 5.1 Summary of vibration modes' characteristics for 1st dynamic identification (CAT 00 – before any test).

Mode	FDD Frequency [Hz]	EFDD Frequency [Hz]	Damping [%]
1	12.06	12.08	2.07
2	13.40	13.34	1.84
3	17.09	17.07	1.42
4	38.36	38.41	0.29

Table 5.2 MAC coefficients for 1st dynamic identification (CAT 00 – before any test).

MODE_i_j		MODE_01_00	MODE_02_00	MODE_03_00	MODE_04_00
	Frequency [Hz]	12.08	13.34	17.07	38.41
MODE_01_00	12.08	1.00	0.99	0.95	0.08
MODE_02_00	13.34	0.99	1.00	0.97	0.07
MODE_03_00	17.07	0.95	0.97	1.00	0.12
MODE_04_00	38.41	0.08	0.07	0.12	1.00

i Mode

j dynamic identification

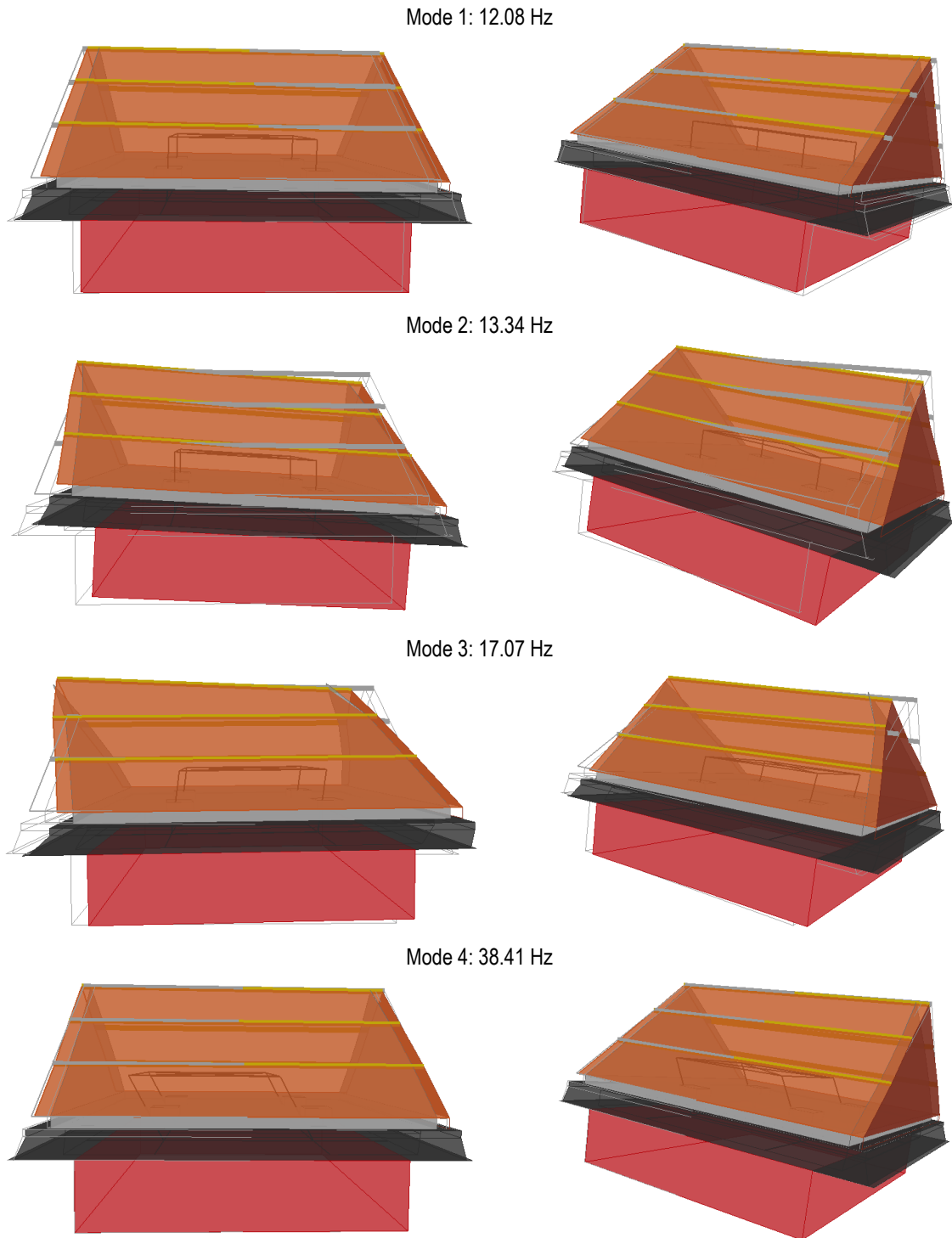


Figure 5.13 Mode shapes for 1st dynamic identification (CAT 00 – before any test).

These mode shapes will be used from now on as the reference mode shapes for computing the evolution of the MAC coefficients in subsequent dynamic identification tests.

The first vibration mode presents a configuration where the model and the shake table move in phase in the longitudinal direction, while the second mode shows an opposite phase motion between the top of the building specimen, going to one side, and the shake table and base of the model, moving to the opposite side. The shake table on the second mode has a rocking motion.

The third mode is similar to the second one, except that the shake table has a translational motion instead of rotational. There also seems to be a more significant motion of the gable walls with respect to the motion of the roof beams. The fourth mode of vibration is a localised one, consisting mainly on the vibration of the steel reference structure inside the model. This mode is obviously not degrading during the increasingly intense test stages.

5.4.2.2 4th dynamic identification (CAT 03 – after test FEQ2-100%)

There was no significant change in the modal properties of the roof specimen until test FEQ2-100%. After this test, on which the base of the gable walls cracked, the fundamental vibration frequency decreased, as represented in Figure 5.14 and Table 5.3. The MAC coefficients relating the current mode shapes to the initial ones are presented in Table 5.4, while the mode shapes are shown in Figure 5.15.

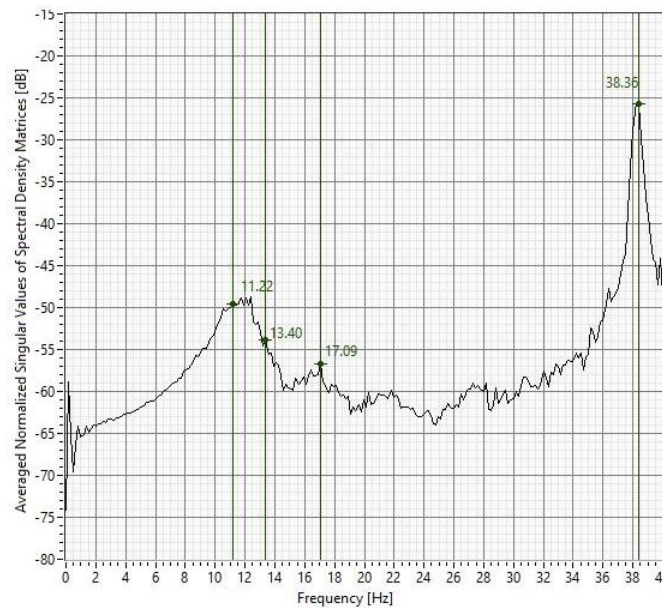


Figure 5.14 FDD results for 4th dynamic identification (CAT 03 – after test FEQ2-100%).

Table 5.3 Summary of vibration modes' characteristics for 4th dynamic identification (CAT 03 – after test FEQ2-100%).

Mode	FDD Frequency [Hz]	EFDD Frequency [Hz]	Damping [%]
1	11.22	11.22	2.17
2	13.40	13.35	1.85
3	17.09	17.05	1.40
4	38.36	38.41	0.29

Table 5.4 MAC coefficients for 4th dynamic identification (CAT 03 – after test FEQ2-100%).

MODE _i _j		MODE_01_03	MODE_02_03	MODE_03_03	MODE_04_03
	Frequency [Hz]	11.22	13.35	17.05	38.41
MODE_01_00	12.08	0.99	1.00	0.94	0.09
MODE_02_00	13.34	0.98	0.99	0.96	0.08
MODE_03_00	17.07	0.94	0.95	1.00	0.12
MODE_04_00	38.41	0.09	0.08	0.13	1.00

i Mode

j dynamic identification

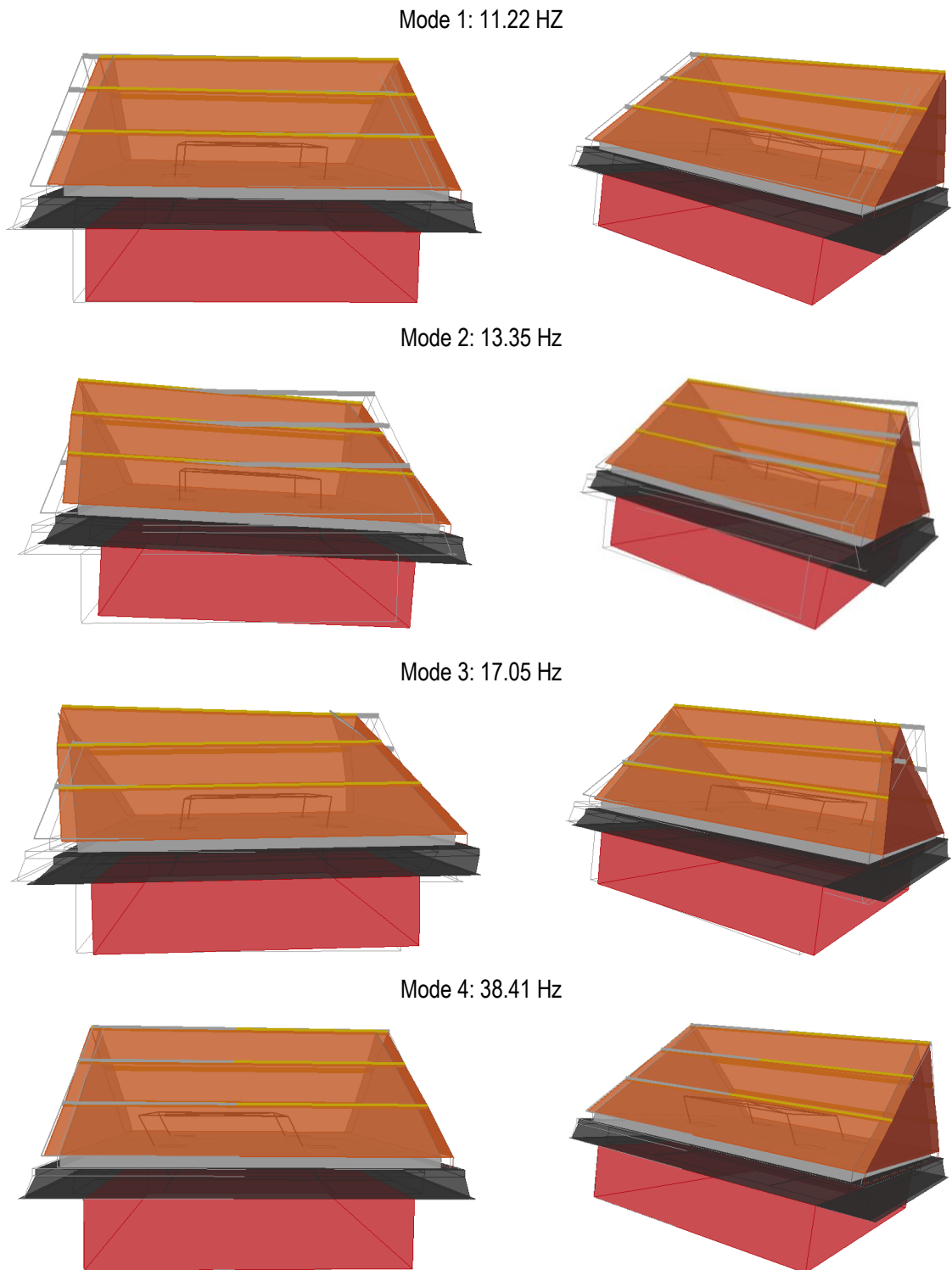


Figure 5.15 Mode shapes for 4th dynamic identification (CAT 03 – after test FEQ2-100%).

Between the 4th dynamic identification and the 7th dynamic identification (after test FEQ2-300%) there was no major evolution in the specimen's dynamic properties. All results are presented in Annex I, following the same organisation of the ones presented above.

5.4.2.3 7th dynamic identification (CAT 06 – after test FEQ2-300%)

A new significant decrease in the fundamental frequency of vibration occurred during test FEQ2-300%, on which several new cracks formed. The second modal frequency also decreased significantly, as shown in the following figures and tables. It is also apparent from the mode shapes that the gable walls are moving more independently of the roof beams. Finally, the MAC coefficients indicate a reduced correspondence between the current mode shapes and the initial ones.

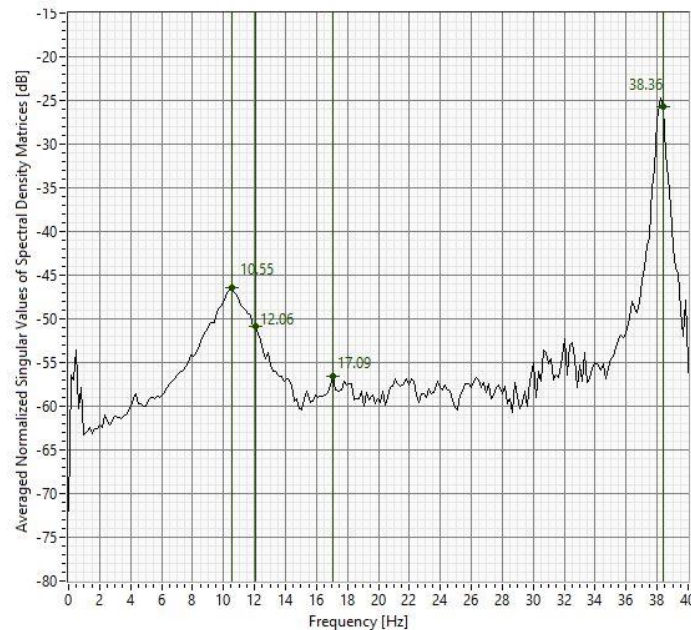


Figure 5.16 FDD results for 7th dynamic identification (CAT 06 – after test FEQ2-300%).

Table 5.5 Summary of vibration modes' characteristics for 7th dynamic identification (CAT 06 – after test FEQ2-300%).

Mode	FDD Frequency [Hz]	EFDD Frequency [Hz]	Damping [%]
1	10.55	10.46	1.83
2	12.06	12.01	2.03
3	17.09	17.07	1.40
4	38.36	38.40	0.30

Table 5.6 MAC coefficients for 7th dynamic identification (CAT 06 – after test FEQ2-300%).

MODE_i_j		MODE_01_06	MODE_02_06	MODE_03_06	MODE_04_06
	Frequency [Hz]	10.46	12.01	17.07	38.4
MODE_01_00	12.08	0.94	0.87	0.95	0.05
MODE_02_00	13.34	0.92	0.87	0.95	0.05
MODE_03_00	17.07	0.90	0.88	0.96	0.09
MODE_04_00	38.41	0.09	0.08	0.13	0.99

i Mode

j dynamic identification

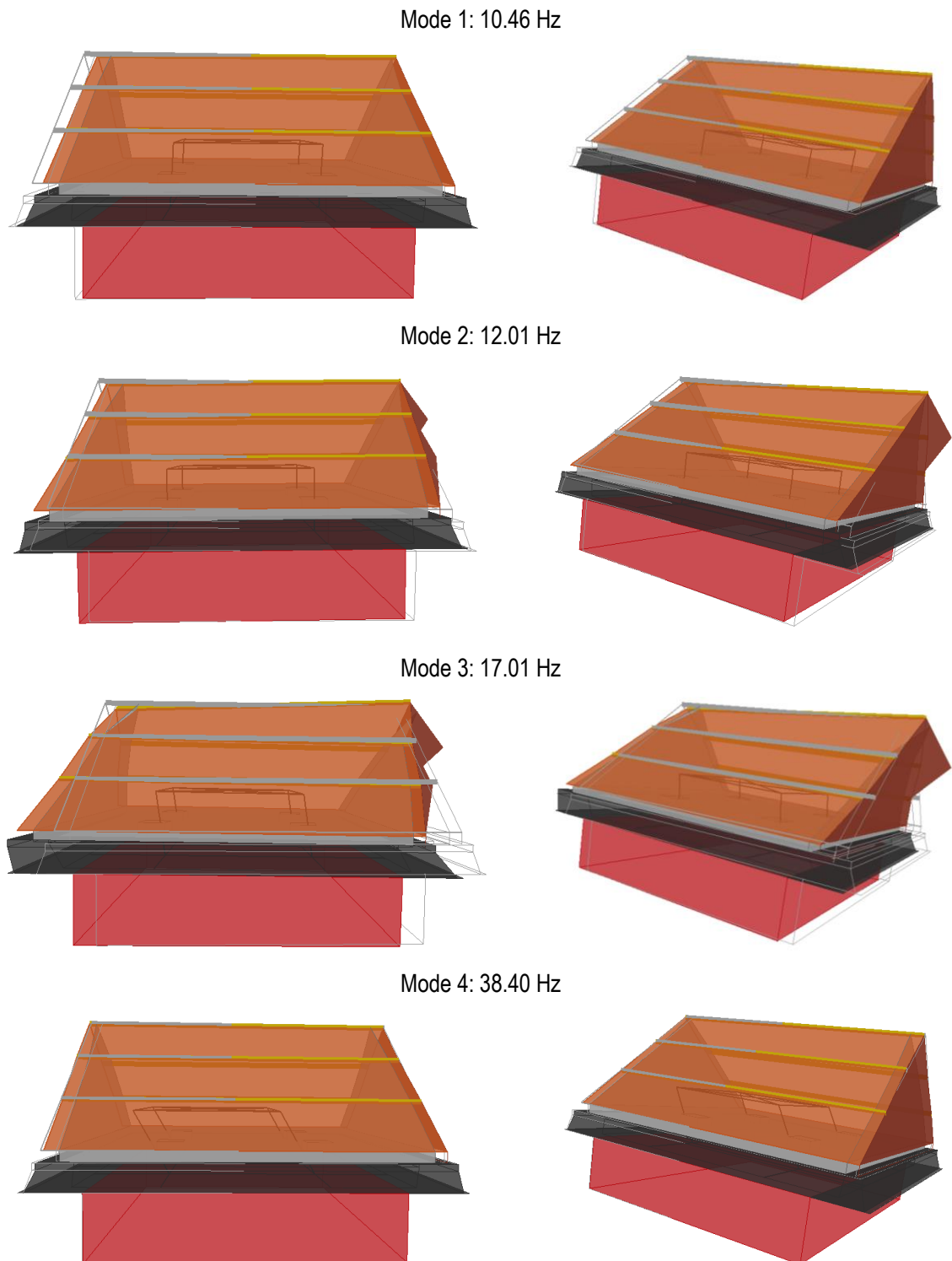


Figure 5.17 Mode shapes for 7th dynamic identification (CAT 06 – after test FEQ2-300%).

5.4.2.4 8th dynamic identification (CAT 07 – after test FEQ2-400%)

After test FEQ2-400%, there is a slight reduction in the fundamental frequency of vibration, but there is an evident change in the singular values decomposition plot, with a smoothing of the peak in the region of that mode of vibration (see Figure 5.18). The fundamental frequency of vibration is now reduced to around 10.2 Hz, as shown in the following figures and tables,

corresponding to a stiffness reduction of about 25-30% with respect to the initial stiffness. Consistently, the modal damping of the first two modes increased with respect to the initial state, implying larger energy dissipation in the existing cracks even for very small deformations.

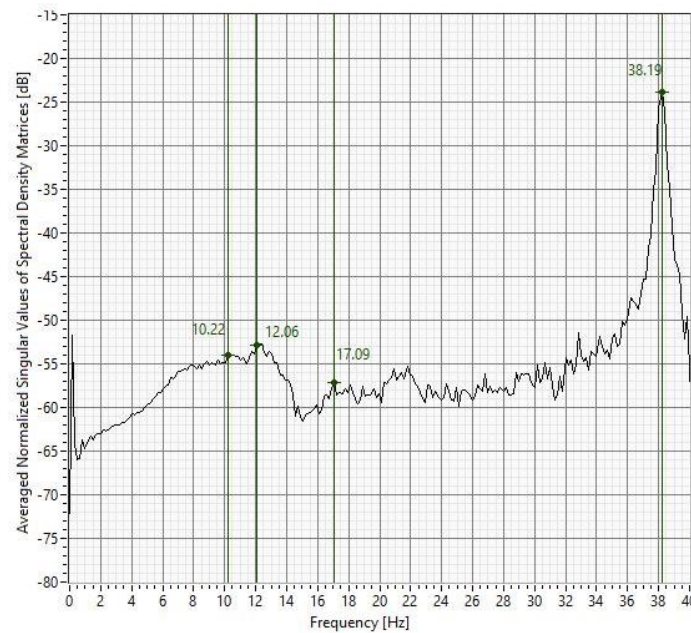


Figure 5.18 FDD results for 8th dynamic identification (CAT 07 – after test FEQ2-400%).

Table 5.7 Summary of vibration modes' characteristics for 8th dynamic identification (CAT 07 – after test FEQ2-400%).

Mode	FDD Frequency [Hz]	EFDD Frequency [Hz]	Damping [%]
1	10.22	10.23	2.41
2	12.06	12.07	2.00
3	17.09	17.07	1.42
4	38.19	38.25	0.25

Table 5.8 MAC coefficients for 8th dynamic identification (CAT 07 – after test FEQ2-400%).

MODE_i_j		MODE_01_07	MODE_02_07	MODE_03_07	MODE_04_07
	Frequency [Hz]	10.22	12.07	17.07	38.25
MODE_01_00	12.08	0.97	0.97	0.93	0.06
MODE_02_00	13.34	0.94	0.96	0.94	0.05
MODE_03_00	17.07	0.93	0.93	0.95	0.09
MODE_04_00	38.41	0.12	0.09	0.12	0.98

i Mode

j dynamic identification

Mode 1: 10.23 Hz

102 *Shake Table Test up to Collapse on a Roof Substructure of a Dutch Terraced House*

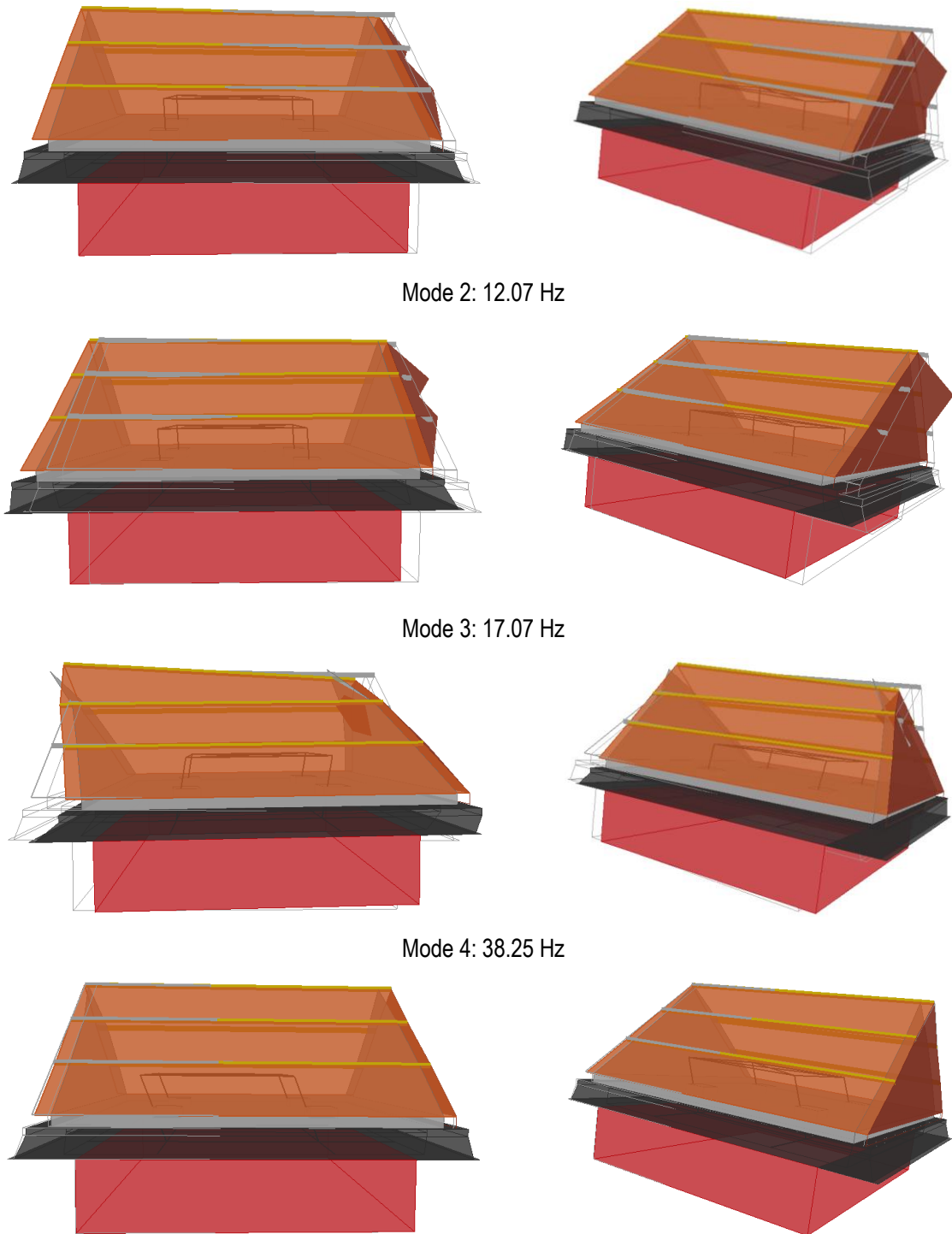


Figure 5.19 Mode shapes for 8th dynamic identification (CAT 07 – after test FEQ2-400%).

5.4.2.5 *9th dynamic identification (CAT 08 – after test FEQ2-500%)*

A further reduction on the second frequency of vibration was observed after test FEQ2-500%, with the other modal frequencies maintaining the values of the previous test stage, as shown in the following figures and tables. It is also more and more clear from the mode shapes in Figure 5.21 that the gable walls are moving independently of the roof beams.

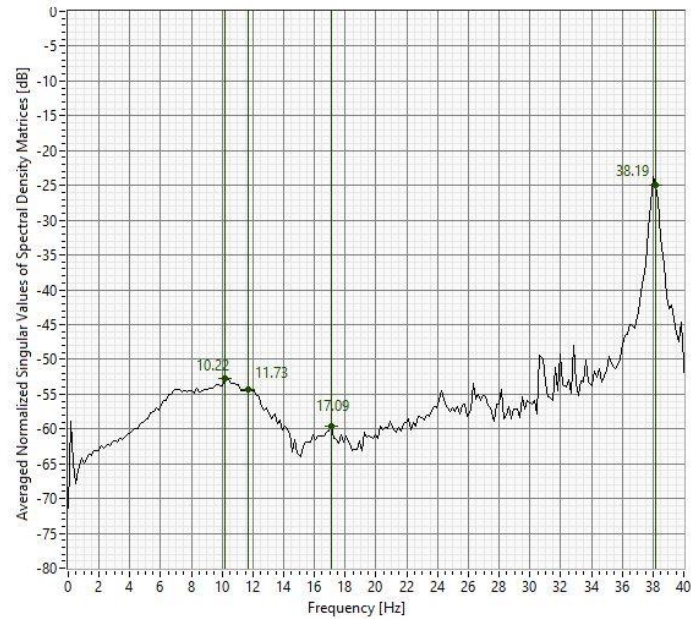


Figure 5.20 FDD results for 9th dynamic identification (CAT 08 – after test FEQ2-500%).

Table 5.9 Summary of vibration modes' characteristics for 9th dynamic identification (CAT 08 – after test FEQ2-500%).

Mode	FDD Frequency [Hz]	EFDD Frequency [Hz]	Damping [%]
1	10.22	10.23	2.35
2	11.73	11.71	2.06
3	17.09	17.05	1.44
4	38.26	38.26	0.25

Table 5.10 MAC coefficients for 9th dynamic identification (CAT 08 – after test FEQ2-500%).

MODE _i _j		MODE_01_08	MODE_02_08	MODE_03_08	MODE_04_08
	Frequency [Hz]	10.23	11.71	17.05	38.26
MODE_01_00	12.08	0.94	0.94	0.82	0.09
MODE_02_00	13.34	0.91	0.92	0.81	0.08
MODE_03_00	17.07	0.87	0.87	0.80	0.12
MODE_04_00	38.41	0.11	0.09	0.14	0.97

i Mode

j dynamic identification

Mode 1: 10.23 Hz

104 *Shake Table Test up to Collapse on a Roof Substructure of a Dutch Terraced House*

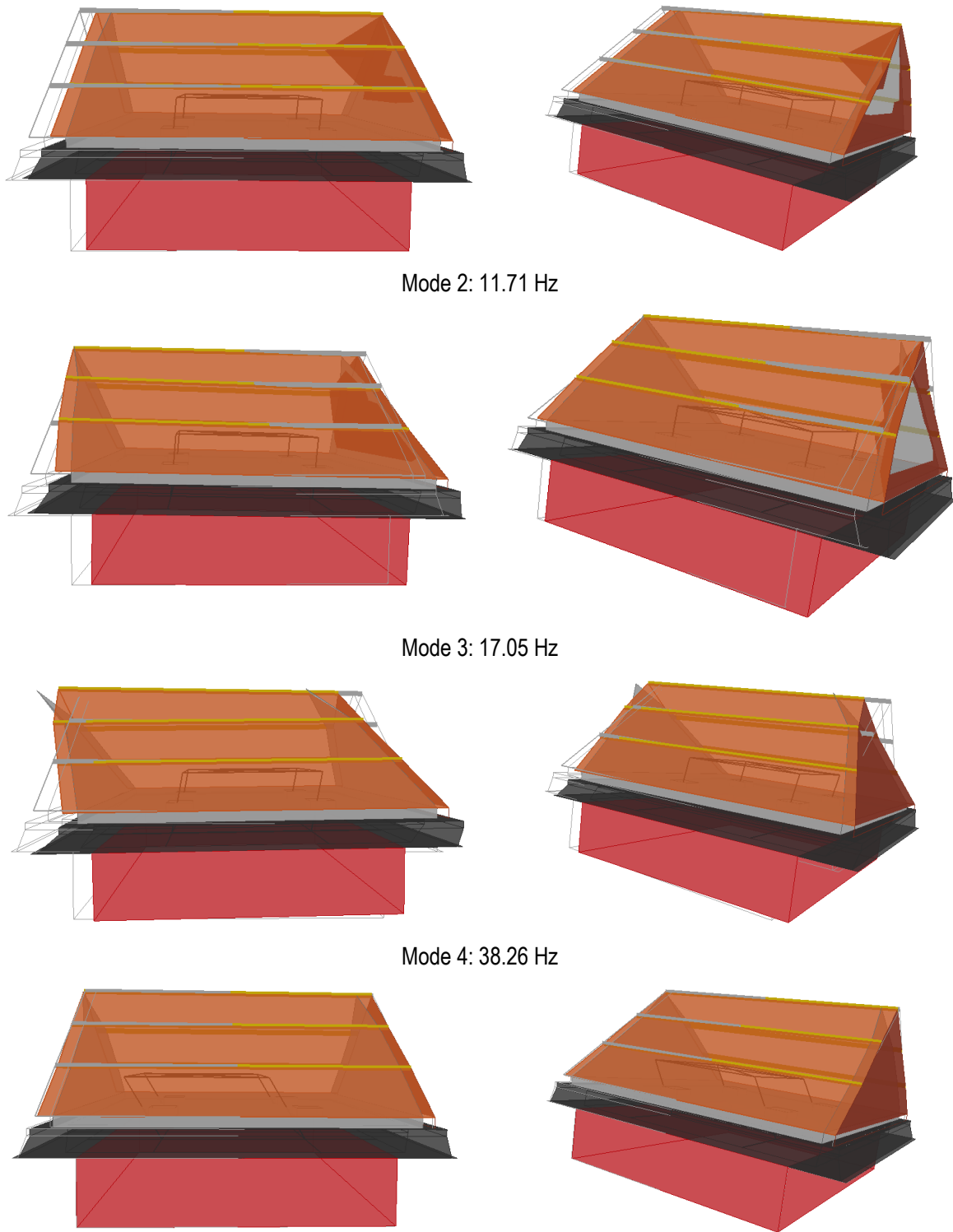


Figure 5.21 Mode shapes for 9th dynamic identification (CAT 08 – after test FEQ2-500%).

The evolution of the fundamental frequency of vibration of the specimen and of the corresponding modal damping is summarised in Table 5.11. These results show that the dynamic characteristics of the specimen, in terms of its first mode of vibration, had a consistent evolution with the increasing intensity of the test stages.

Table 5.11 Evolution of the fundamental mode of vibration of the model during the shaking table test.

Dynamic ident. test	Frequency [Hz]	Damping [%]
1 (initial state)	12.08	2.07
2 (after FEQ1-100%)	12.10	2.02
3 (after FEQ1-150%)	11.74	2.07
4 (after FEQ2-100%)	11.22	2.17
5 (after FEQ2-150%)	11.14	1.81
6 (after FEQ2-200%)	10.56	2.30
7 (after FEQ2-300%)	10.46	1.83
8 (after FEQ2-400%)	10.23	2.41
9 (after FEQ2-500%)	10.23	2.35

It should be noted that the estimation of modal damping values is significantly more uncertain than the one of modal frequencies, but there is a clear trend for an increase in the first mode damping values. Besides the degradation of the dynamic properties, the mode shapes also show some significant changes, namely related to the motion of the gable walls with respect to the timber roof beams.

5.5 Displacement and Acceleration Histories

The slab and ridge beam acceleration histories, as well as the horizontal displacement histories of both gable walls, at 1/3 and 2/3 of the roof height, and of the ridge beam, are shown in Figure 5.22 to Figure 5.33, for the successive test stages. The increase of displacement demand with height is approximately linear after test FEQ2-100%, corresponding to the rocking response of the gable walls after cracking at the base; conversely, the gable displacements at both heights is similar at earlier test stages, and significantly smaller than the corresponding ridge beam displacements.

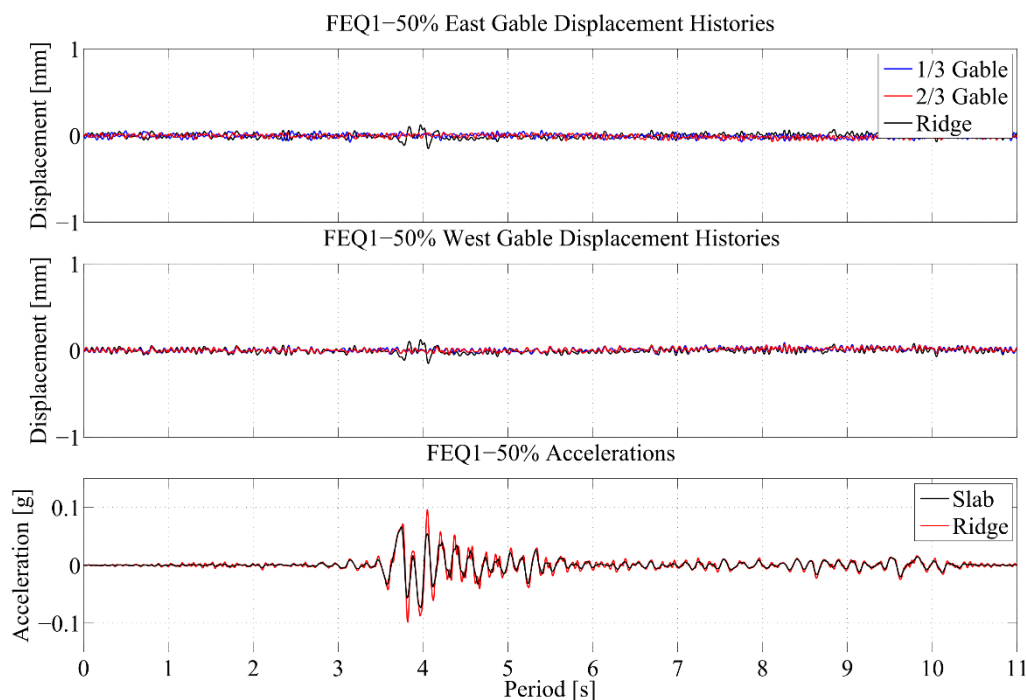


Figure 5.22 FEQ1-50%: Displacement and acceleration histories.

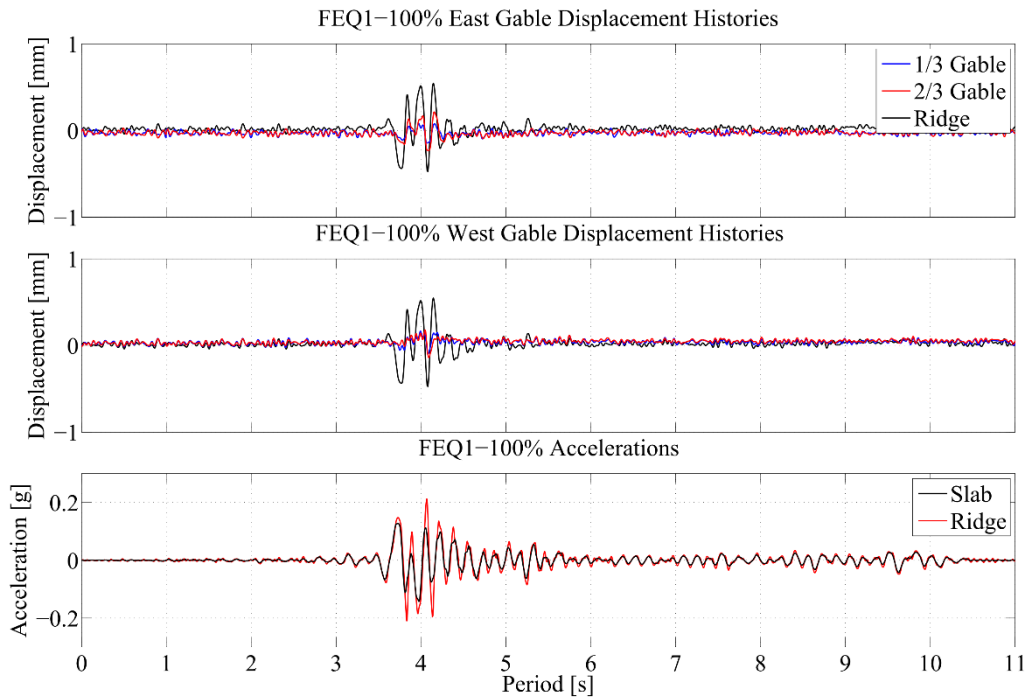


Figure 5.23 FEQ1-100%: Displacement and acceleration histories.

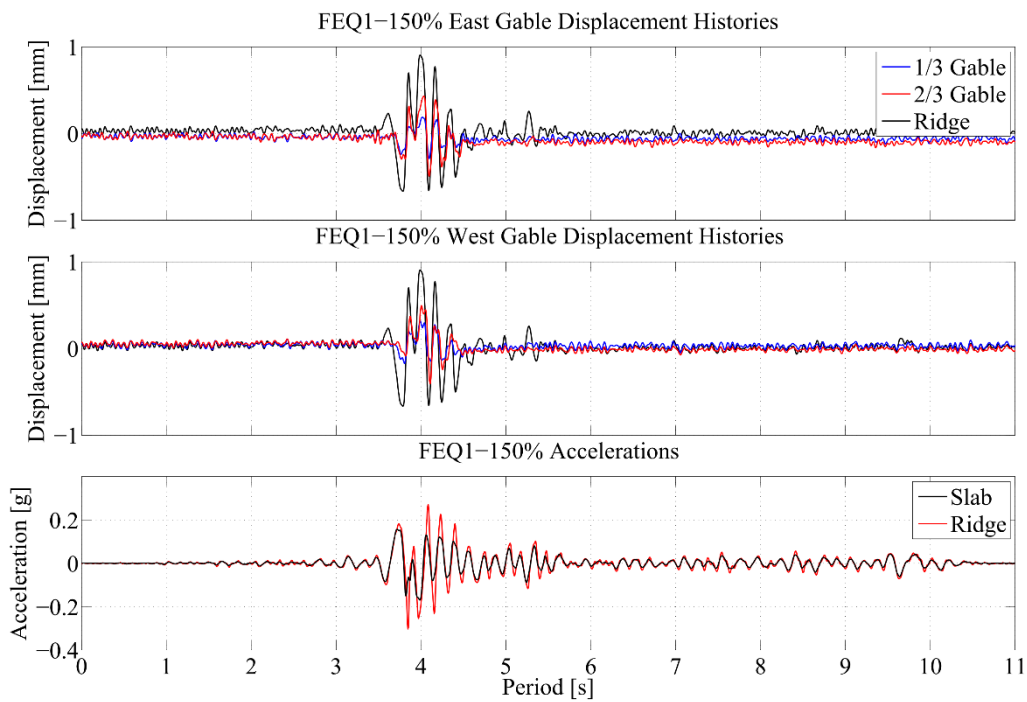


Figure 5.24 FEQ1-150%: Displacement and acceleration histories.

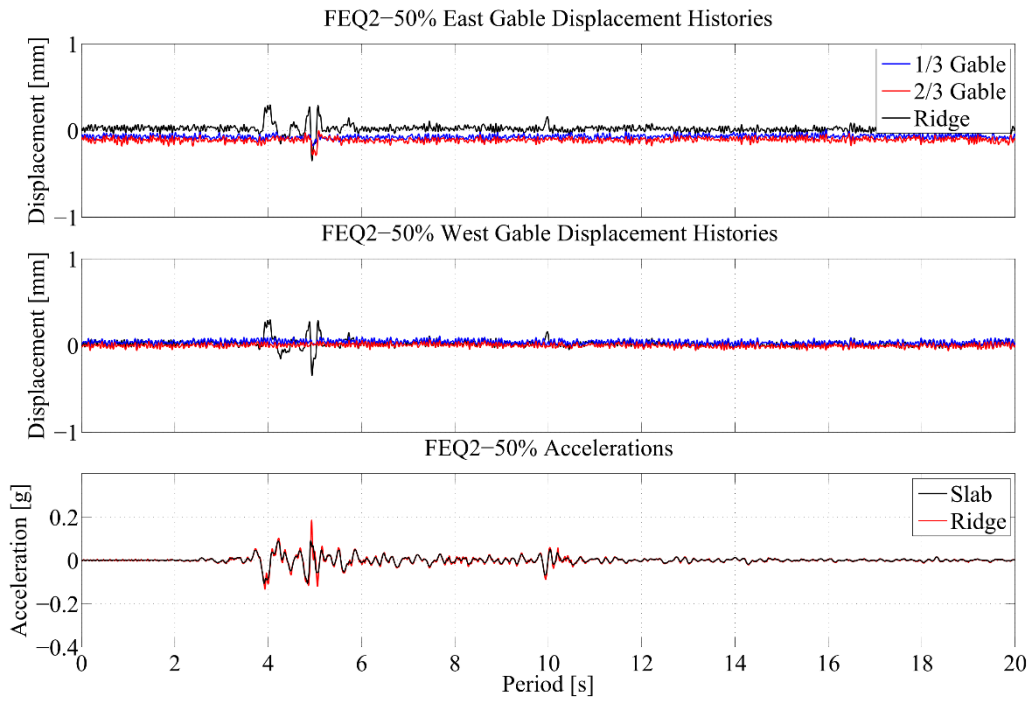


Figure 5.25 FEQ2-50%: Displacement and acceleration histories.

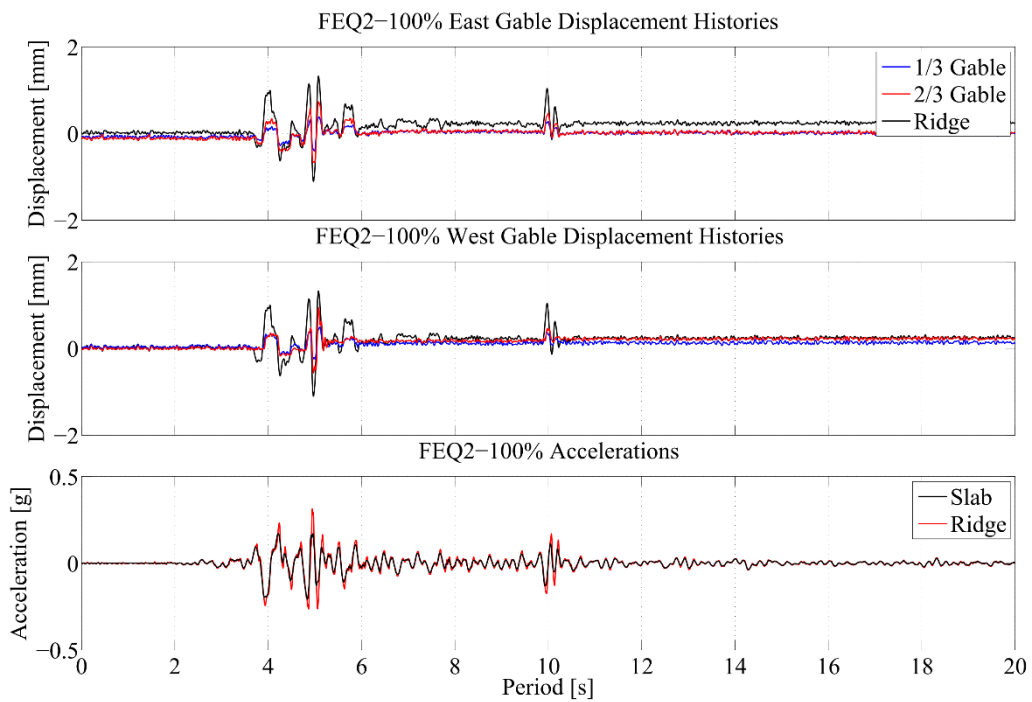


Figure 5.26 FEQ2-100%: Displacement and acceleration histories.

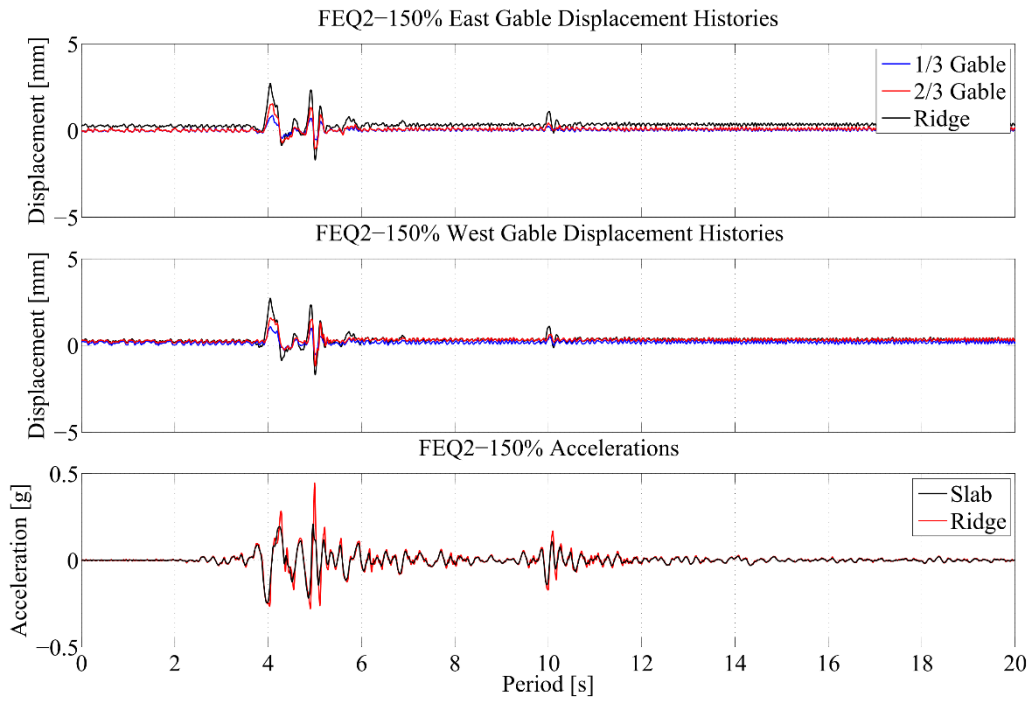


Figure 5.27 FEQ2-150%: Displacement and acceleration histories.

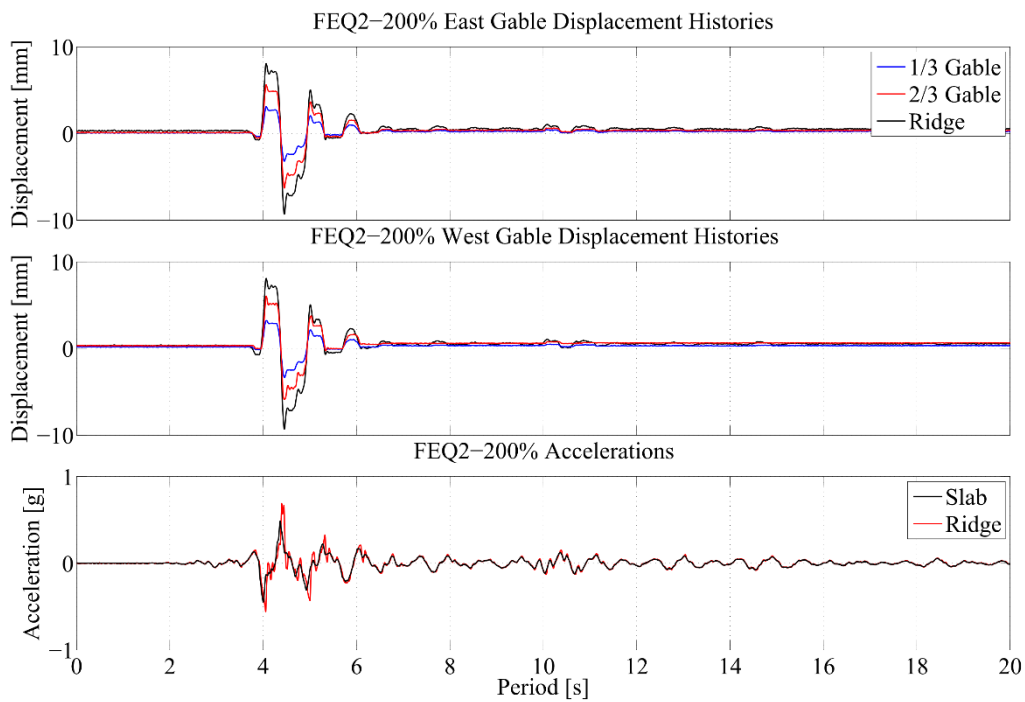


Figure 5.28 FEQ2-200%: Displacement and acceleration histories.

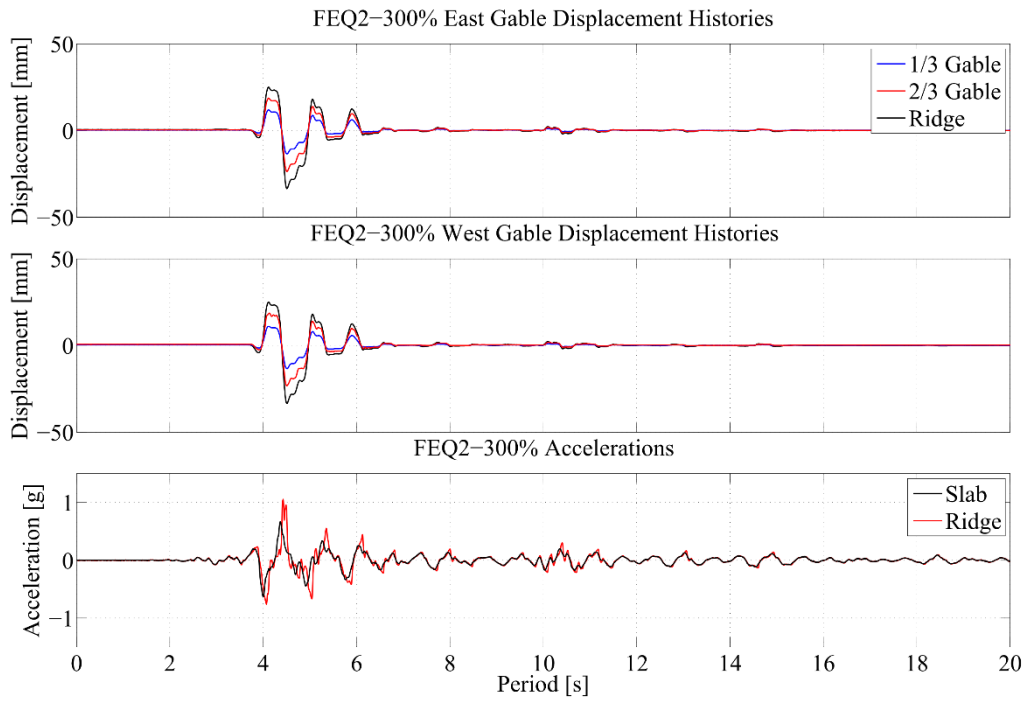


Figure 5.29 FEQ2-300%: Displacement and acceleration histories.

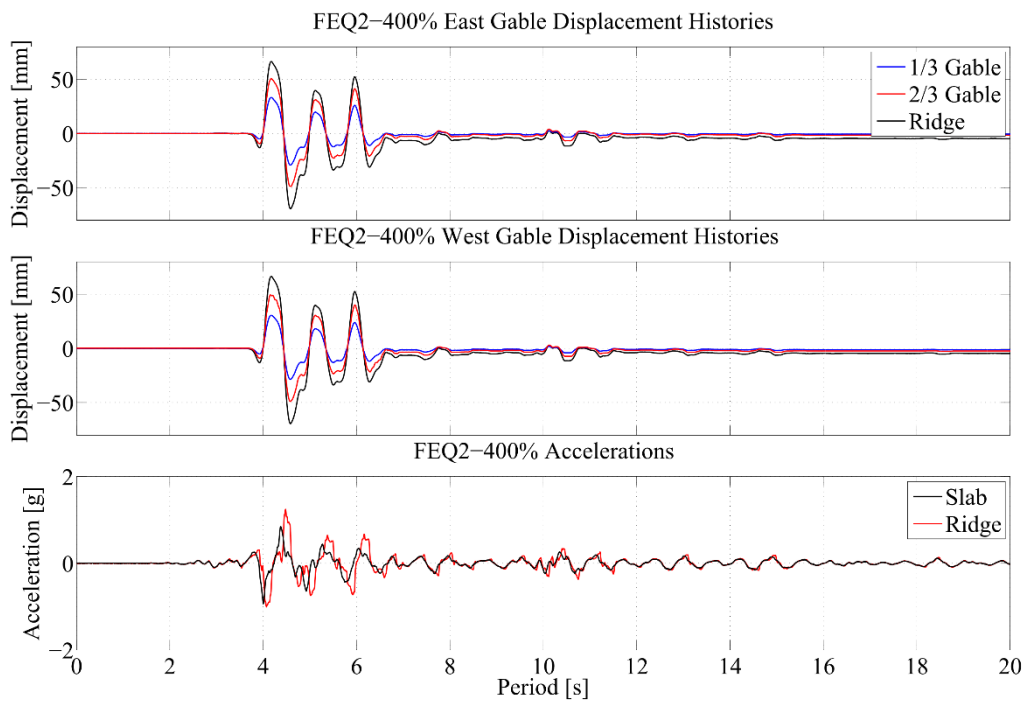


Figure 5.30 FEQ2-400%: Displacement and acceleration histories.

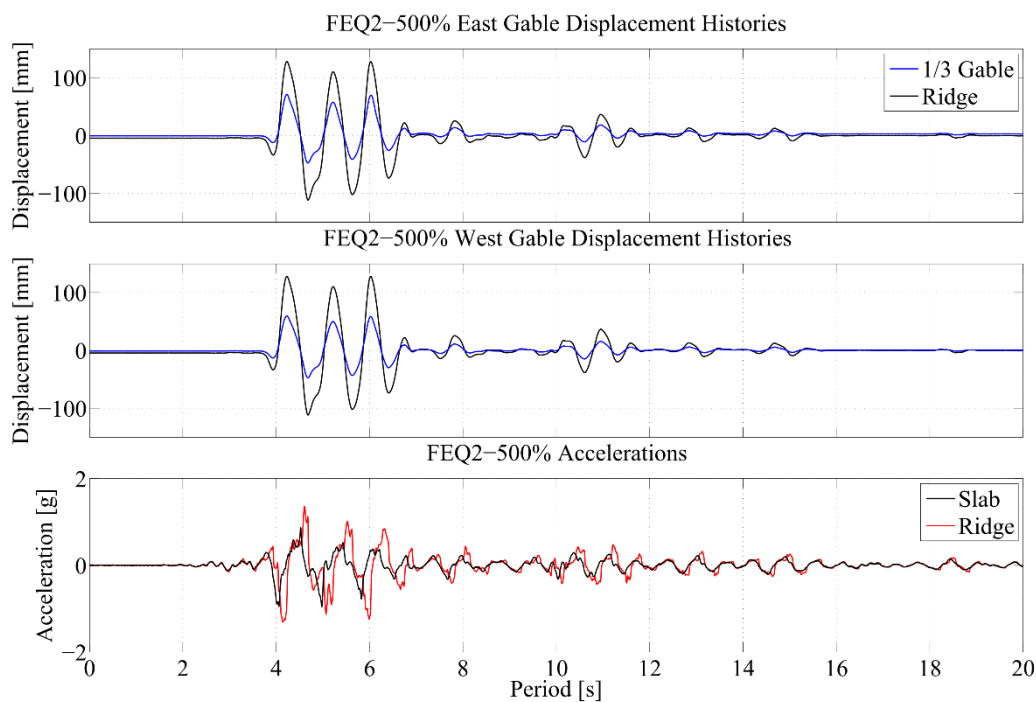


Figure 5.31 FEQ2-500%: Displacement and acceleration histories.

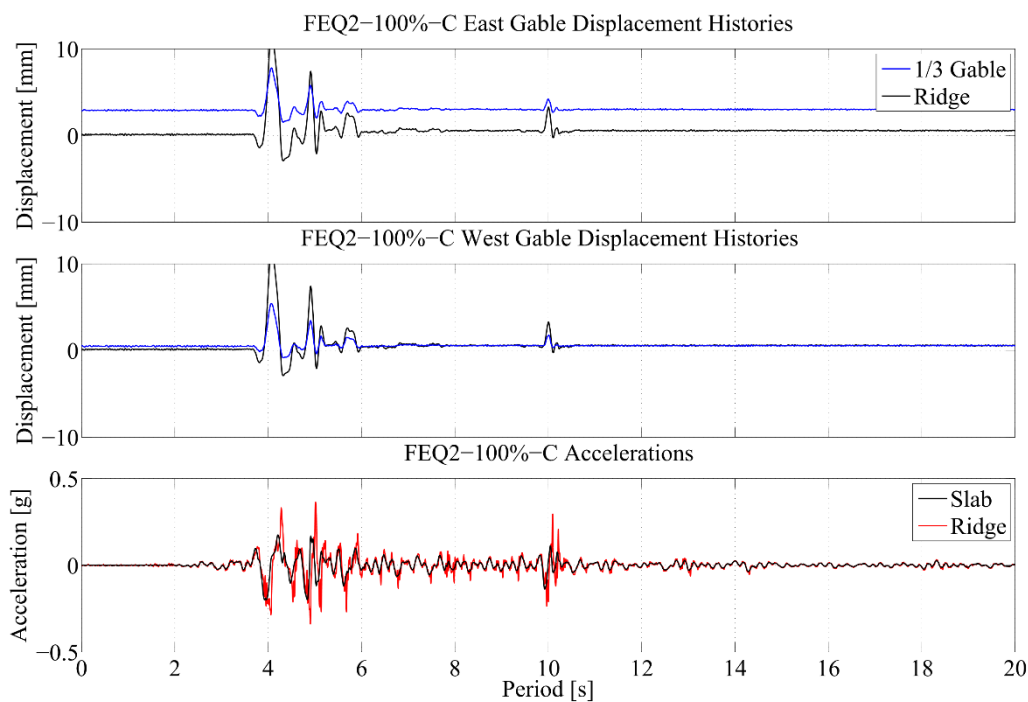


Figure 5.32 FEQ2-100%-C: Displacement and acceleration histories.

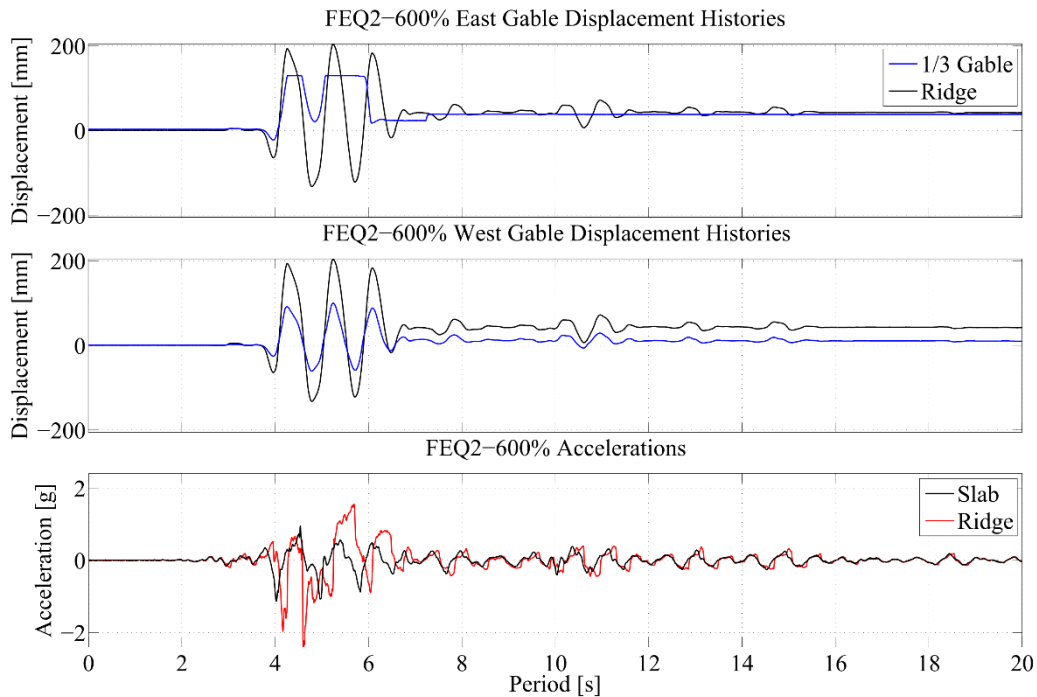


Figure 5.33 FEQ2-600%: Displacement and acceleration histories.

During FEQ2-600%, the wire potentiometer measuring the out-of-plane displacement of the collapsed East gable wall saturated and a full account of its displacement could not be retrieved. On the other hand, the ridge displacement was computed by the combination of two transducers, one measuring the positive displacement and the other measuring the negative displacement, in order to increase their range of measurement.

It is interesting to note the initial rocking behaviour observed in the gable walls at crack initiation during FEQ2-100% (PGA = 0.207 g), Figure 5.34, and at a later stage, during FEQ2-400% (PGA = 0.935 g), Figure 5.35.

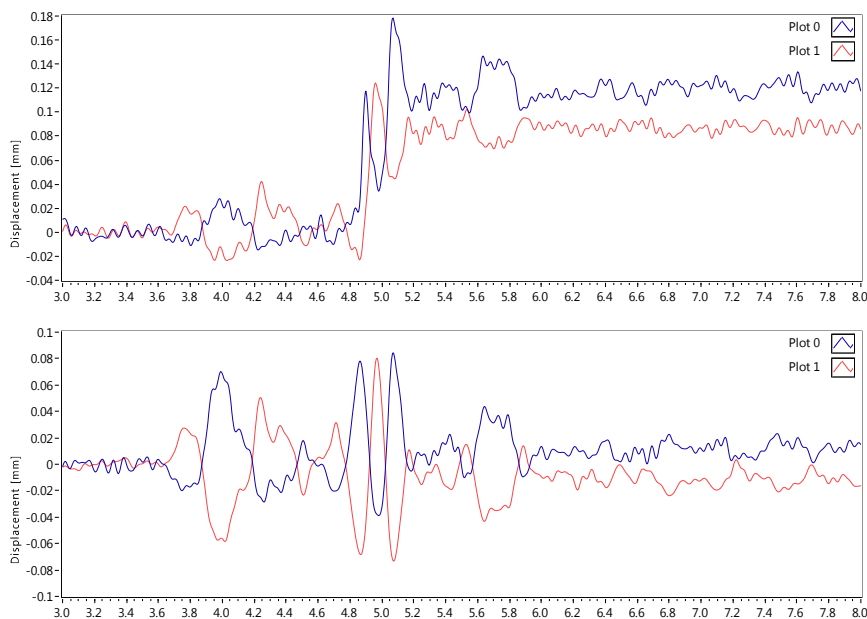


Figure 5.34 FEQ2-100%: Rocking response at crack formation in East gable (above) and West gable (below).

112 *Shake Table Test up to Collapse on a Roof Substructure of a Dutch Terraced House*

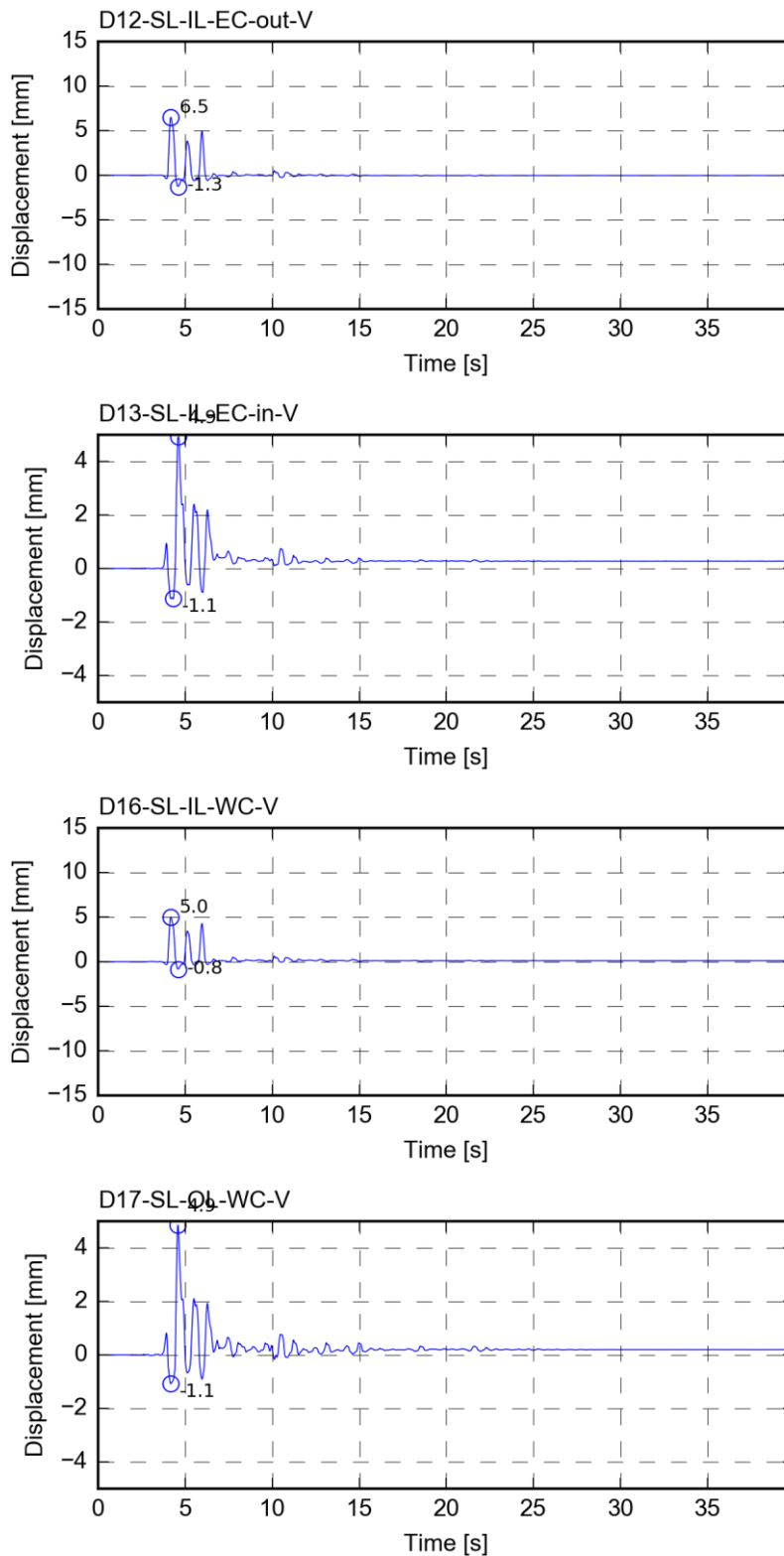


Figure 5.35 FEQ2-400%: Rocking response in East wall and West wall.

During FEQ2-400%, some motion of the timber plates of the roof, at the slab level, with respect to the foundation beam could be observed, as depicted in Figure 5.36. This was probably due to some enlargement of the holes of the threaded bars. No relative motion of the slab with respect to the foundation beam was observed.

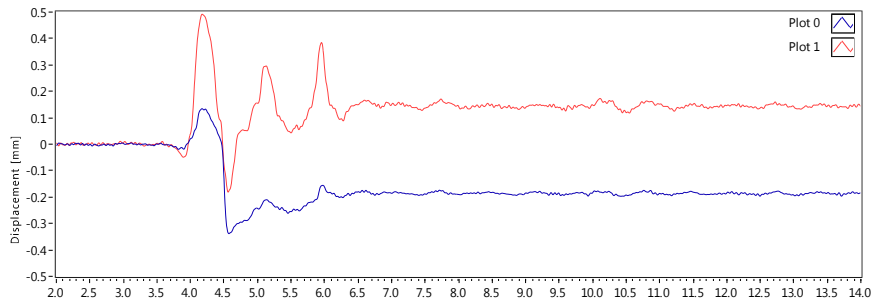


Figure 5.36 FEQ2-400%: Sliding of roof timber plates with respect to the foundation beam.

5.6 Deformed shape

Deformed shapes in elevation have been generated by plotting the average horizontal displacements recorded by the wire potentiometers located at 1/3 and 2/3 heights of the gable walls, as well as at the ridge of the roof. Figure 5.37 to Figure 5.45 schematically represent the out-of-plane deflected shape of a longitudinal cross section of the specimen at the instants of peak roof displacement. The deflected shapes have been amplified by a scaling factor indicated in the figures, which represent the slab at the base, the ridge beam at the top, and the measured points in between. The red line represents the West outer leaf clay wall, while the CS gables are represented by the vertical black lines.

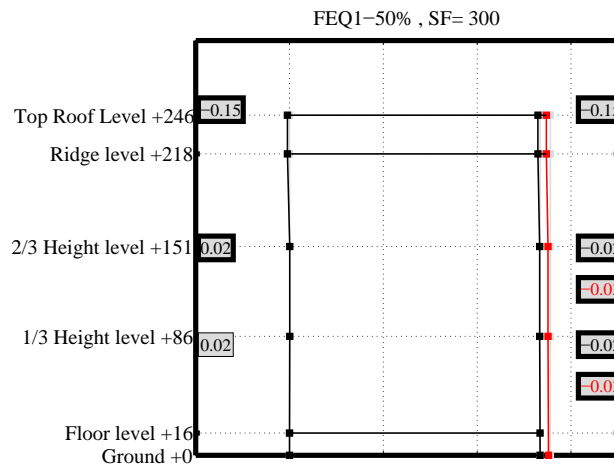


Figure 5.37 FEQ1-50%: Longitudinal cross section deflected shape.

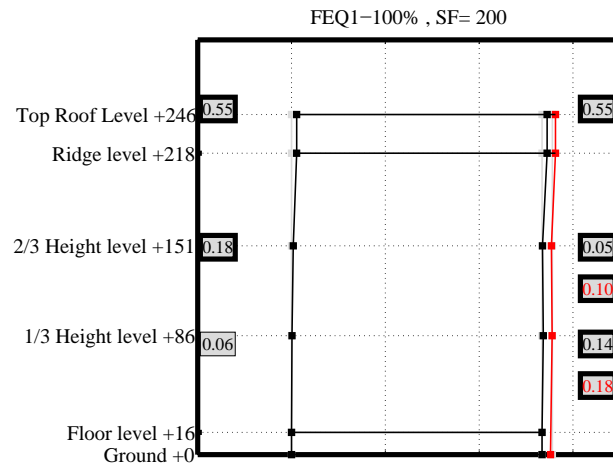


Figure 5.38 FEQ1-100%: Longitudinal cross section deflected shape.

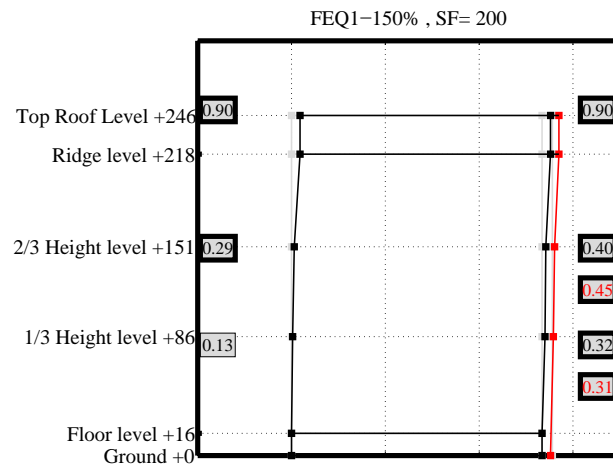


Figure 5.39 FEQ1-150%: Longitudinal cross section deflected shape.

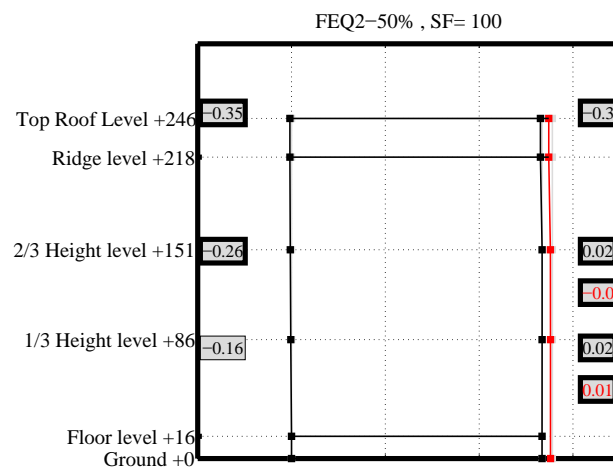


Figure 5.40 FEQ2-50%: Longitudinal cross section deflected shape.

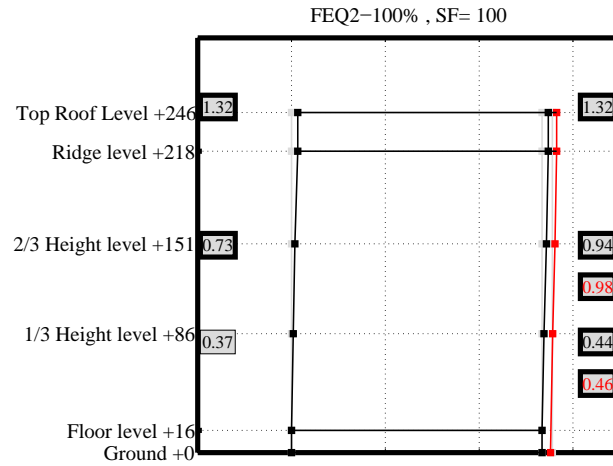


Figure 5.41 FEQ2-100%: Longitudinal cross section deflected shape.

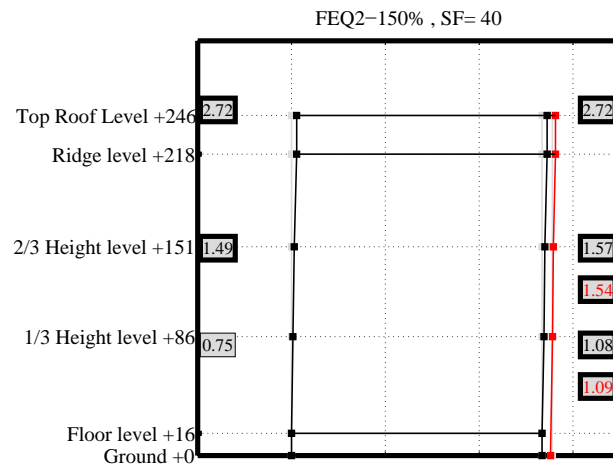


Figure 5.42 FEQ2-150%: Longitudinal cross section deflected shape.

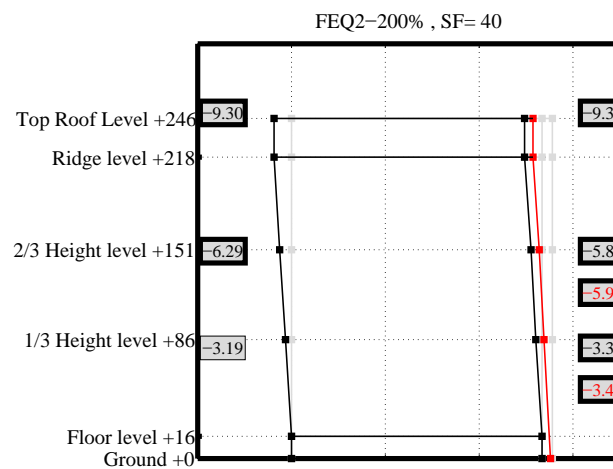


Figure 5.43 FEQ2-200%: Longitudinal cross section deflected shape.

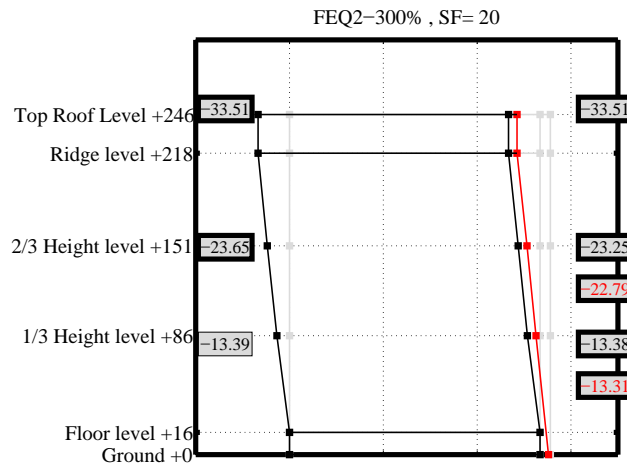


Figure 5.44 FEQ2-300%: Longitudinal cross section deflected shape.

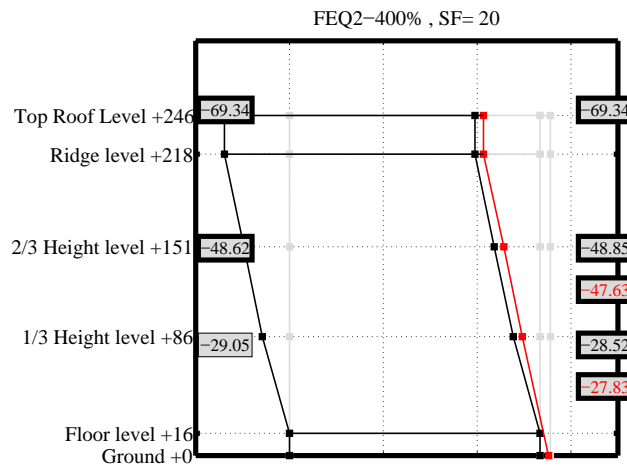


Figure 5.45 FEQ2-400%: Longitudinal cross section deflected shape.

5.7 Hysteretic Response

The evolution of the specimen's hysteretic response is shown in Figure 5.46, in terms of base shear, V , versus roof diaphragm drift, γ_R , for each test stage, which takes into account the residual displacements. The histories of the base shear have been computed as the sum of the products of each acceleration recording times the tributary mass of the corresponding accelerometer. Masses are assumed to be lumped at the accelerometer locations and listed in Table 3.1.

The black line in Figure 5.46, until test FEQ2-400%, represents the roof base shear computed based on those lumped masses; the grey line represents an approximate calculation of the roof base shear assigning one-half of the mass of the roof diaphragm and one-third of the mass of the gables to the average ridge beam acceleration and the remaining masses to the slab acceleration. As can be seen, the difference is rather small, which justifies the adoption of this second method to compute the inertial forces during the last three tests (FEQ2-500%, FEQ2-100%-C and FEQ2-600%), in which many instruments were removed. In each plot of Figure 5.46, the dots and squares represent the positive and negative peak force responses

with the corresponding displacements, respectively. The black dot in the plot for FEQ2-600% corresponds to the instant when the East gable wall collapsed.

Figure 5.47 compares the hysteretic response of the roof substructure to previous tests, showing that the boundary conditions of this specimen made it much stiffer and having a linear response up to later stages of the test. The roof base shear demand, nevertheless, was similar to the previous tests, although the later stages show that its base shear capacity was higher than the one of previous specimens (see Figure 5.50 below). Figure 5.48 shows, instead, the hysteretic response with the base shear computed assuming a mass of 2.6 t (half the mass of the roof diaphragm and one-third of the mass of the gables) as lumped at the ridge beam location, in order to perform a comparison between the different specimens and trying to remove the contribution of the different gables which presented different boundary conditions throughout the tests.

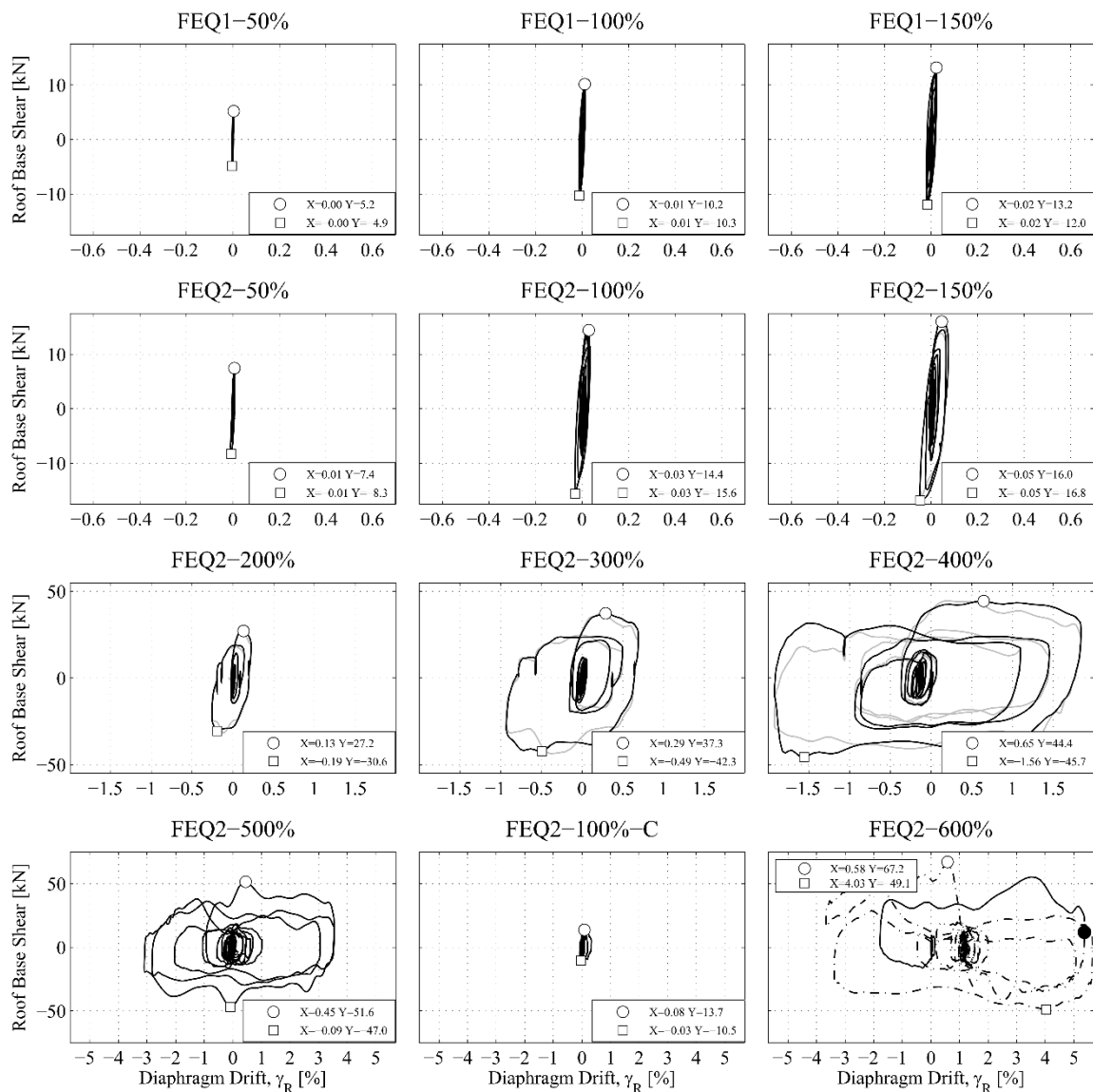


Figure 5.46 Evolution of specimen's hysteretic response.

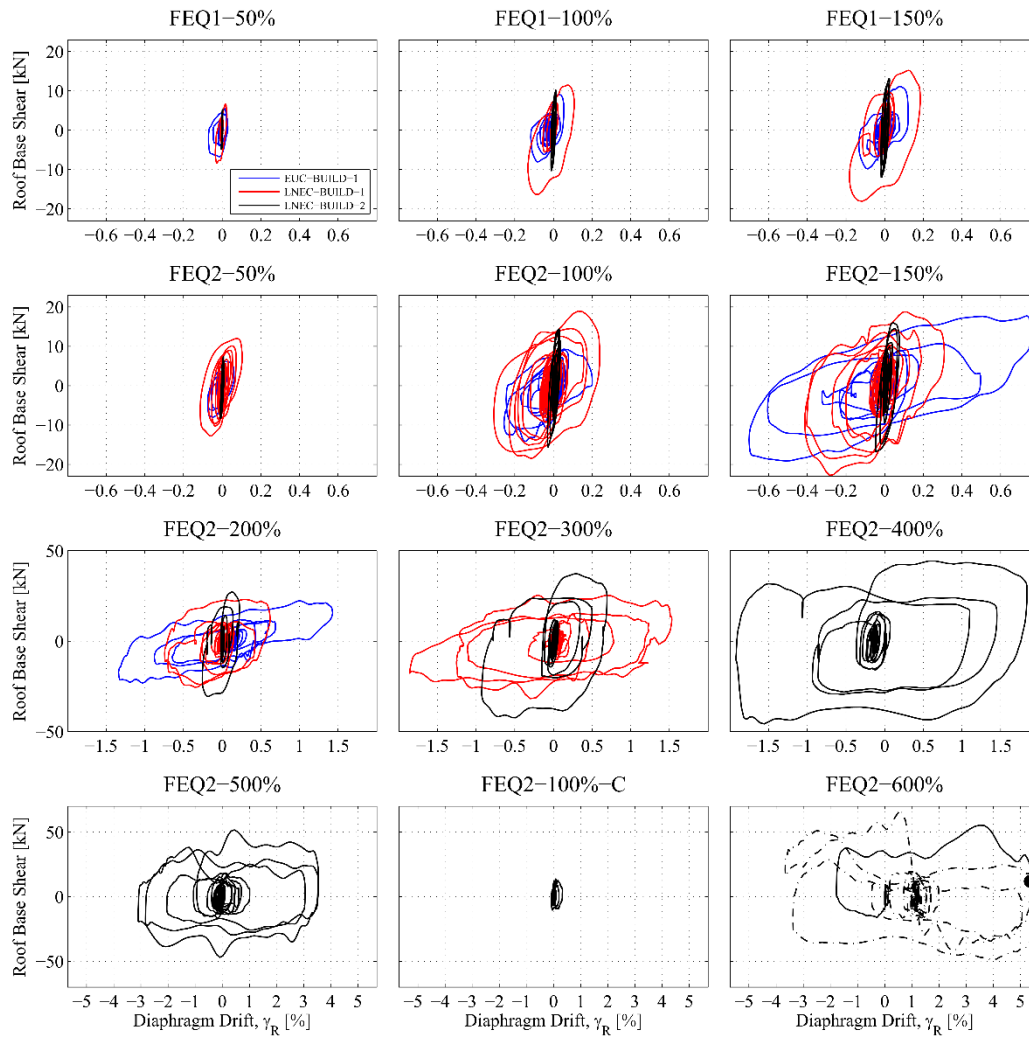


Figure 5.47 Comparison of specimen hysteretic response to previous tests.

The dynamic force-displacement backbone curve, represented in Figure 5.49, can be obtained by connecting the peak points of the experimental curves. In other words, it is defined as the plot of the maximum resisted base shear, V_{max} , and the corresponding drift depurated from residual displacements for each stage of testing (i.e. assuming that the displacement starts at zero on each test). The last point of both the positive and negative branch was obtained as the pair of the maximum drift attained and the corresponding base shear. The attainment of the higher base shear occurred for sway towards the negative direction (towards the single-leaf side, East), while the higher drift was in the opposite direction (towards the double-leaf side, West).

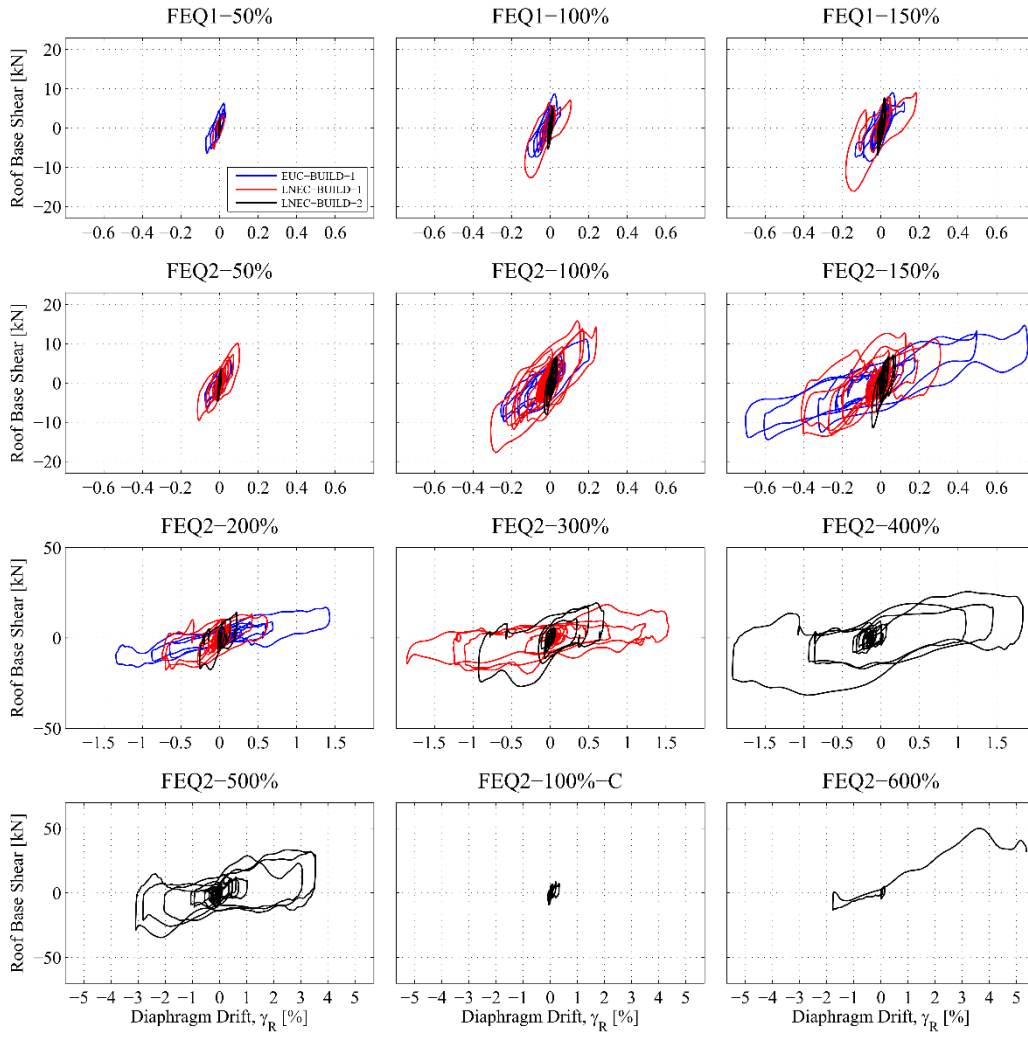
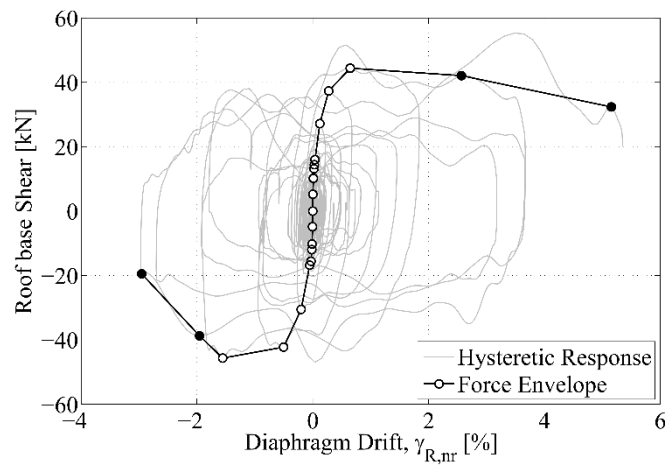


Figure 5.48 Comparison of specimen hysteretic response to previous tests – lumped case.



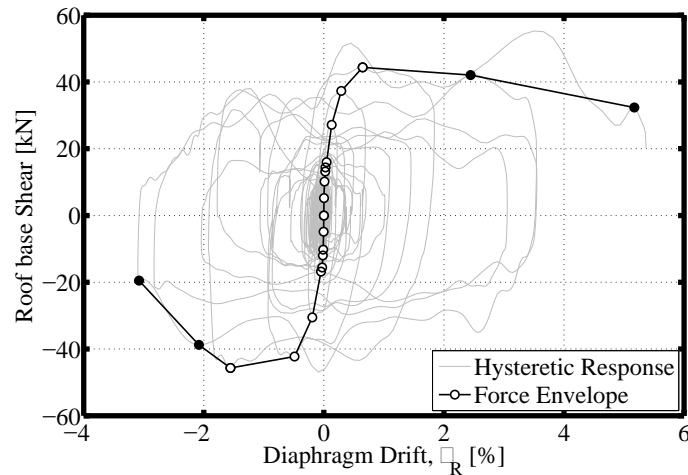


Figure 5.49 Backbone capacity curve.

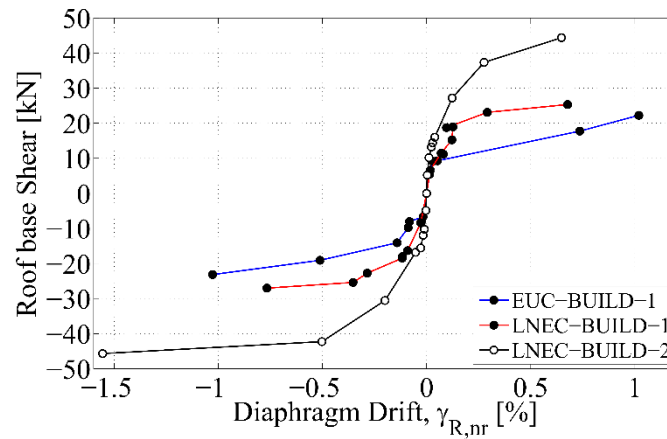


Figure 5.50 Comparison of backbone capacity curve with previous tests.

Table 5.12 lists the coordinates of the peak resisted base shear with the associated roof relative displacement (depurated from residuals) and the peak relative displacement with the associated base shear, in the negative and positive directions, for each stage of testing.

Table 5.12 List of peak force and displacement values.

Test Name	Max. Force, V [kN]	Ass. Disp. γ_R [mm]	Min. Force V [kN]	Ass. Disp. γ_R [mm]	Max. Disp. γ_R [mm]	Ass. Force V [kN]	Min. Disp. γ_R [mm]	Ass. Force V [kN]
FEQ1-50%	5.20	0.12	-4.87	-0.12	0.12	5.20	-0.15	-4.44
FEQ1-100%	10.16	0.44	-10.26	-0.38	0.55	7.20	-0.48	-7.17
FEQ1-150%	13.18	0.85	-11.96	-0.56	0.90	12.68	-0.67	-5.72
FEQ2-50%	7.44	0.25	-8.30	-0.31	0.29	1.45	-0.35	-6.91
FEQ2-100%	14.40	1.07	-15.59	-1.00	1.32	10.44	-1.10	-13.58
FEQ2-150%	15.99	1.68	-16.82	-1.65	2.72	10.79	-1.69	-16.12
FEQ2-200%	27.16	4.76	-30.55	-6.89	8.07	18.49	-9.30	-22.30
FEQ2-300%	37.31	10.51	-42.27	-17.60	25.01	22.20	-33.51	-27.95

FEQ2-400%	44.36	23.41	-45.67	-56.16	66.46	27.80	-69.34	-8.56
FEQ2-500%	51.61	16.15	-46.96	-3.20	128.08	9.71	-111.84	-16.05
FEQ2-100%-C	13.67	3.06	-10.50	-1.22	11.90	4.00	-2.91	-5.67
FEQ2-600%	55.26	125.6	-45.67	56.17	203.89	3.26	-132.31	20.85

5.8 Identification of specimen Damage Limit States

In this section, the identification of global quantitative thresholds that adequately describe the overall structural damage state of the building is attempted. Six damage states (DS) were considered: DS0, completely undamaged; DS1, no structural damage; DS2, minor structural damage; DS3, moderate structural damage; DS4, extensive structural damage; and DS5, very heavy structural damage, total or local collapse.

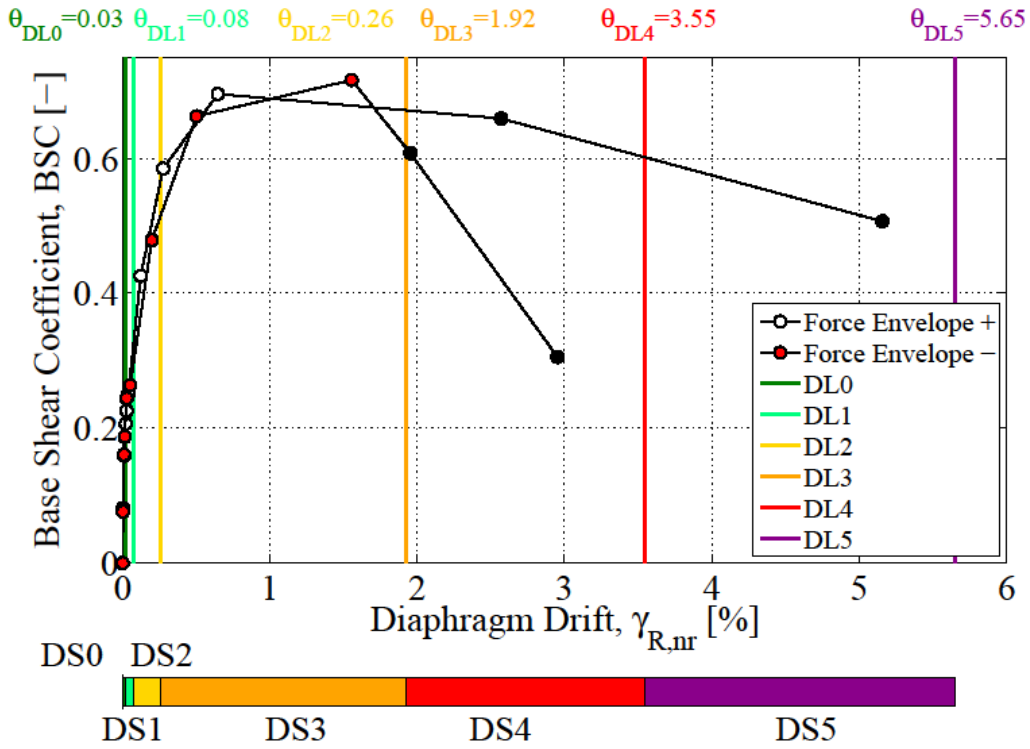
The damage limits (DL), defining quantitative boundaries in terms of inter-storey drift between the aforementioned damage states, have been defined as follow:

- DL0 is defined as the maximum achieved level of displacement with no visible seismic damage (structural or non-structural). It has been identified with a diaphragm drift equal to 0.03% achieved during FEQ1-150% ($S_a(T_1)=0.286$ g) which did not cause any further damage; (PGA=0.170 g; PGV=95.0 mm/s);
- DL1 is defined as the maximum achieved level of displacement with no visible structural damage. After tests FEQ2-100% ($S_a(T_1)=0.312$ g), a minor crack was detected on the plaster layer at the base of the East gable; (PGA=0.207 g; PGV=136.0 mm/s);
- DL2 is defined as the maximum achieved level of displacement with minor/slight structural damage. It has been identified at the end of the test FEQ2-200% ($S_a(T_1)=0.640$ g), when the complete cracking of the bottom layer of the East gable occurred. The recorded peak diaphragm drift was equal to 0.26%; (PGA=0.487 g; PGV=274.1 mm/s);
- DL3 is defined as the maximum achieved level of displacement with moderate structural damage (but still repairable). This state was associated with FEQ2-400% ($S_a(T_1)=1.138$ g) and the development of several cracks on the East gable due to a peak diaphragm drift equal to 1.92%; (PGA=0.935 g; PGV=538.3 mm/s);
- DL4 is defined as the maximum achieved level of displacement with extensive structural damage (e.g. not repairable). The limit could be considered as a collapse-prevention threshold. DL4 was addressed after a peak diaphragm drift of 3.55% recorded during test FEQ2-500% ($S_a(T_1)=1.091$ g) associated with heavy damage of the East gable and cracking of the West gable wall; (PGA=0.955 g; PGV=614.8 mm/s);
- DL5 is defined as the displacement associated with the failure of the East gable. It has been identified with the peak diaphragm drift of 5.65% during FEQ2-600% ($S_a(T_1)=1.410$ g; PGA=1.138 g; PGV=677.9 mm/s).

The base shear coefficient BSC is defined as:

$$BSC = \frac{V}{M \cdot g} \quad (23)$$

where Mg is the total weight of the specimen. Figure 5.51 identifies the DLs on the experimental backbone curve defined in terms of BSC and diaphragm drift (taking into account the residuals).



Figure

5.51 Identification of the DLs on the building backbone curve.

The evolution of damage along the consecutive damage states is shown in Figure 5.52 to Figure 5.55.

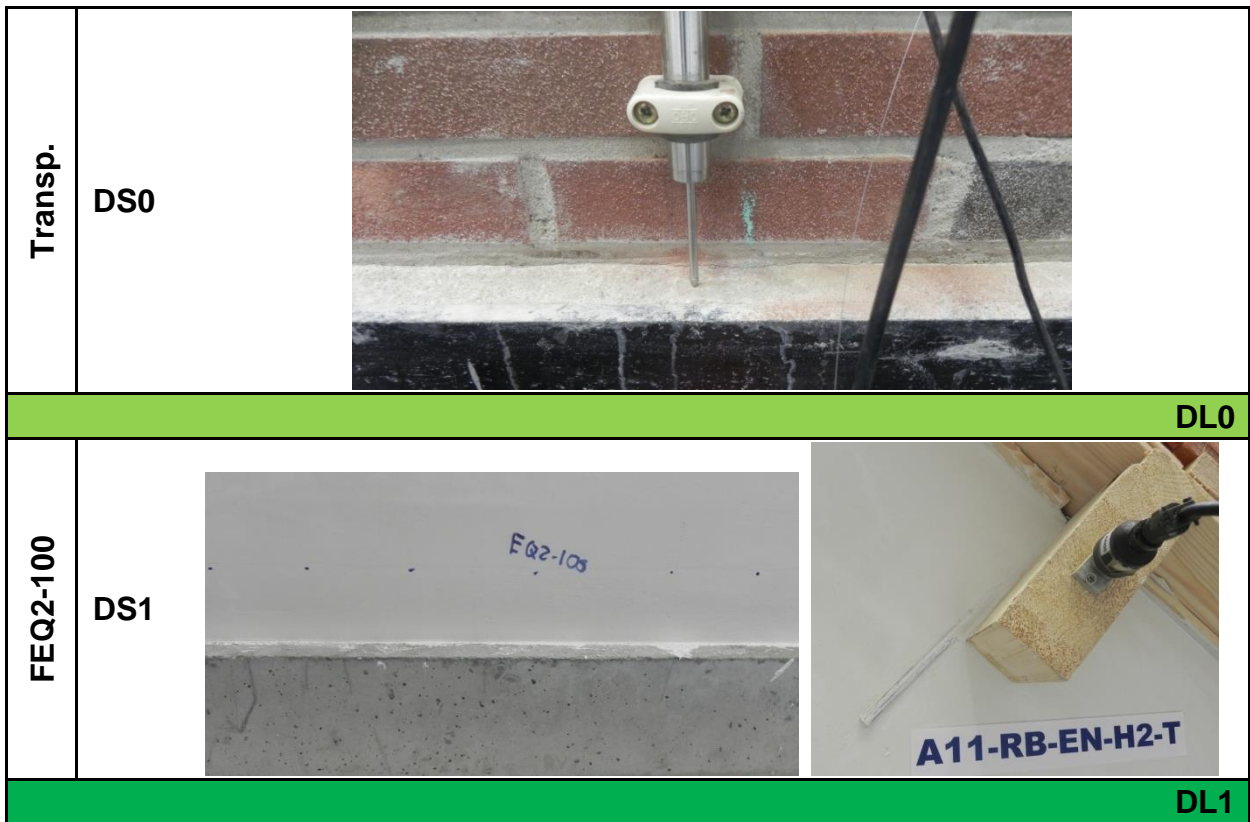




Figure 5.52 Evolution of damage in the gable walls along DL0 to DL2.

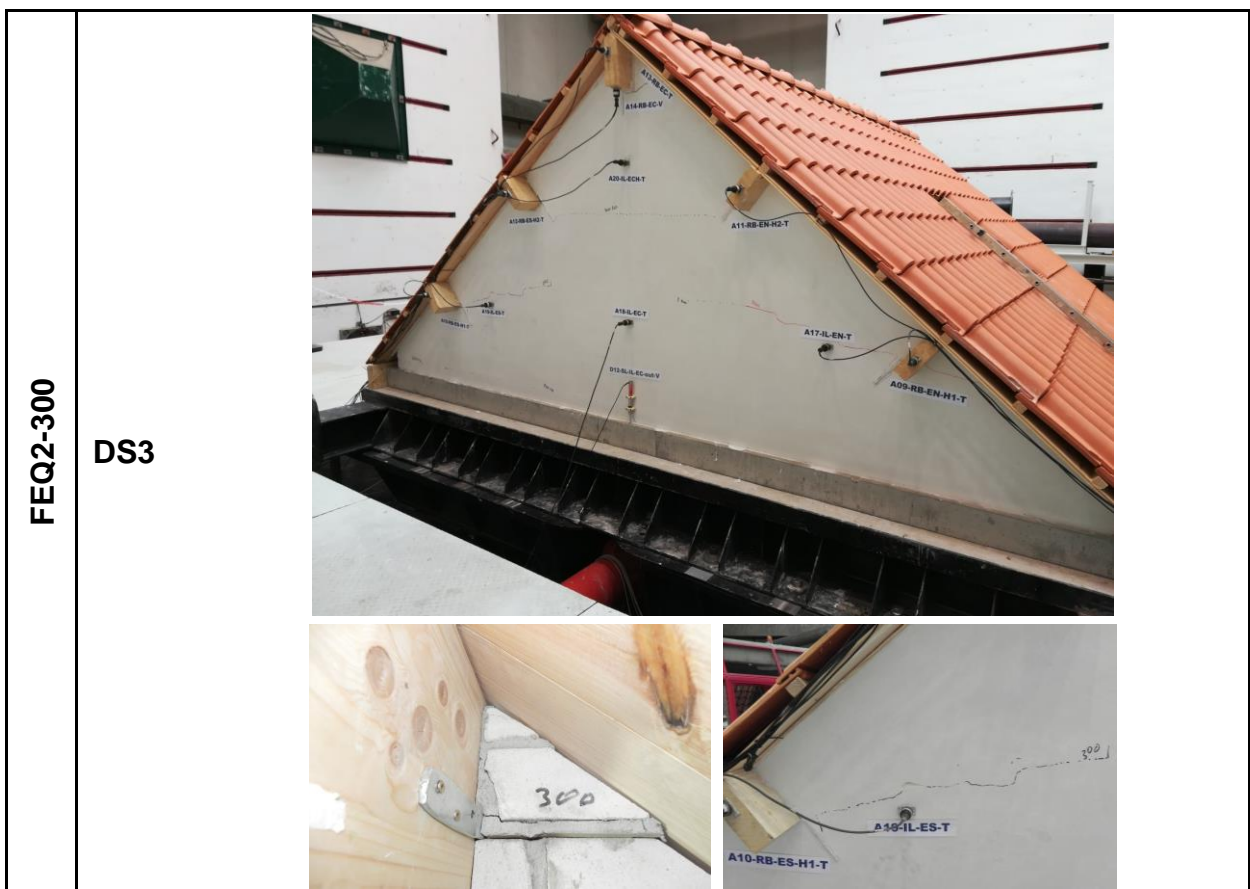




Figure 5.53 Evolution of damage in the gable walls up to DL3.



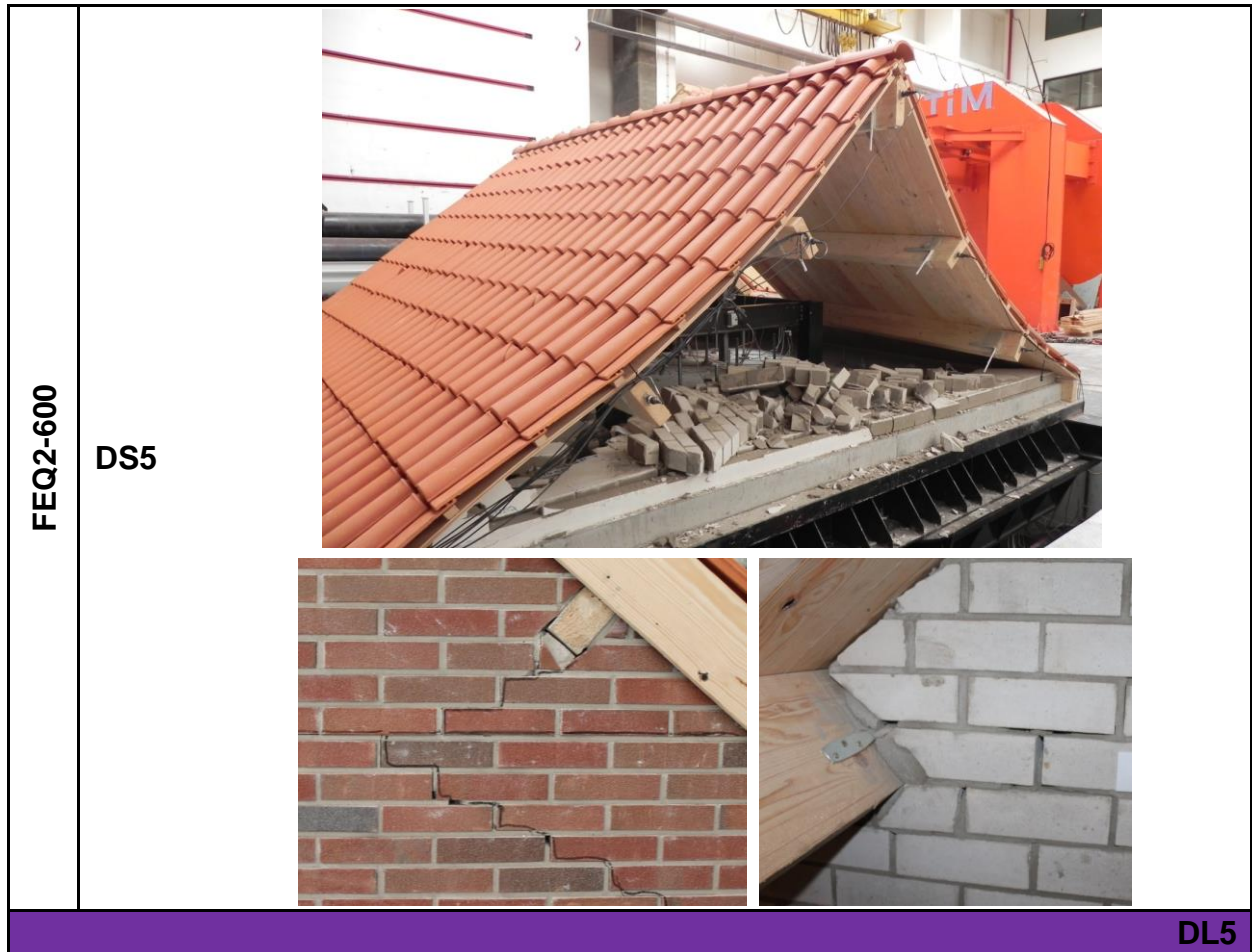


Figure 5.54 Evolution of damage in the gable walls along DL4 to DL5.

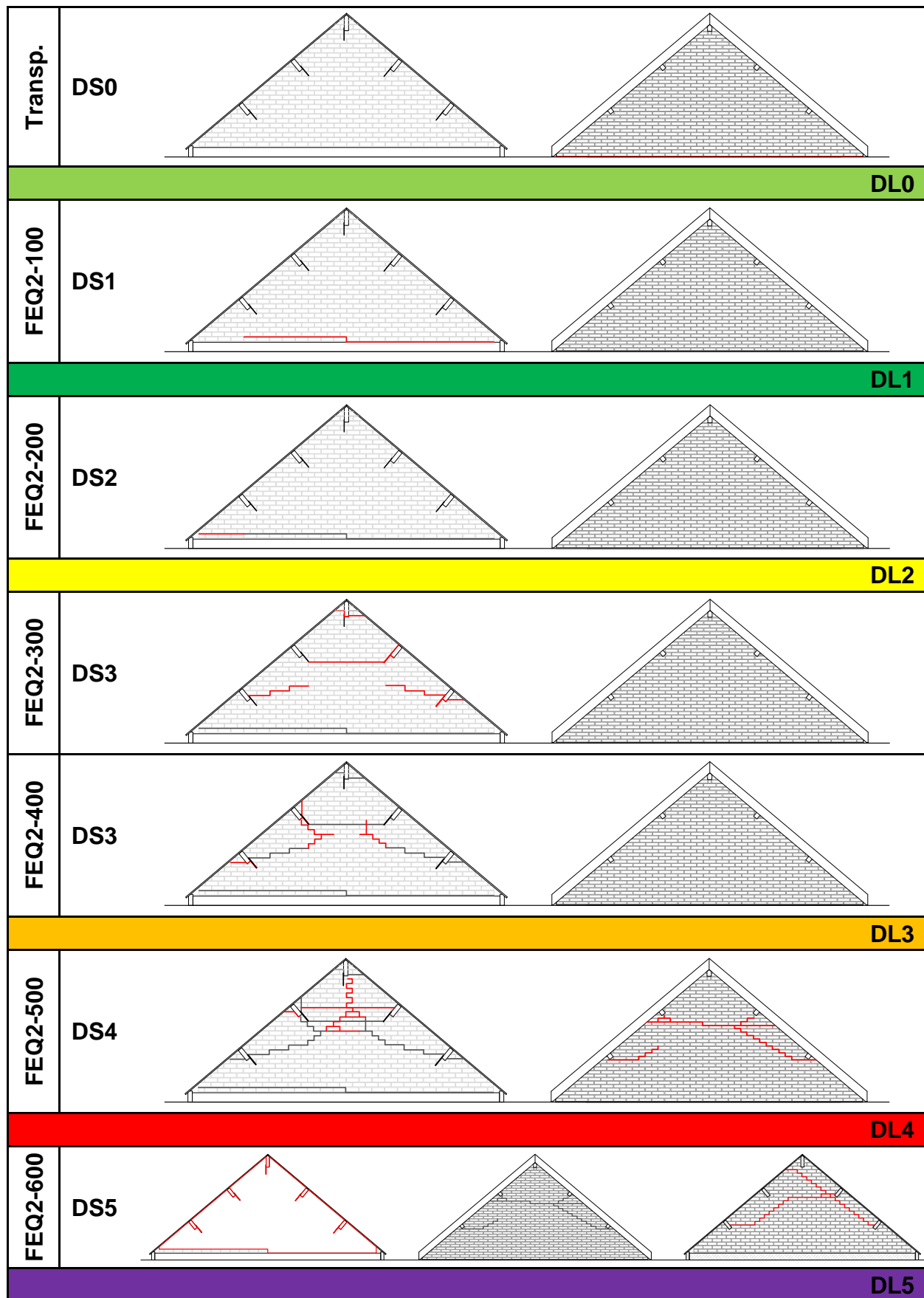


Figure 5.55 Evolution of the crack pattern in the gable walls along the DLs.

5.9 Derivation of EDP according to specimen performance

Figure 5.56 reports the building performance in terms of peak displacements and residual displacements, very often associated with a general damage and to damage accumulation. The response in terms of the Peak Ridge Acceleration divided by the Peak Roof Base Acceleration PFA/PRBA is also shown. This EDP could be correlated with the OOP performance of masonry (or more in general secondary) components or the damage occurring to acceleration sensitive non-structural components. The comparison of the performances exhibited by the two roof systems of EUC-BUILD-1 and LNEC-BUILD-1 is also shown.

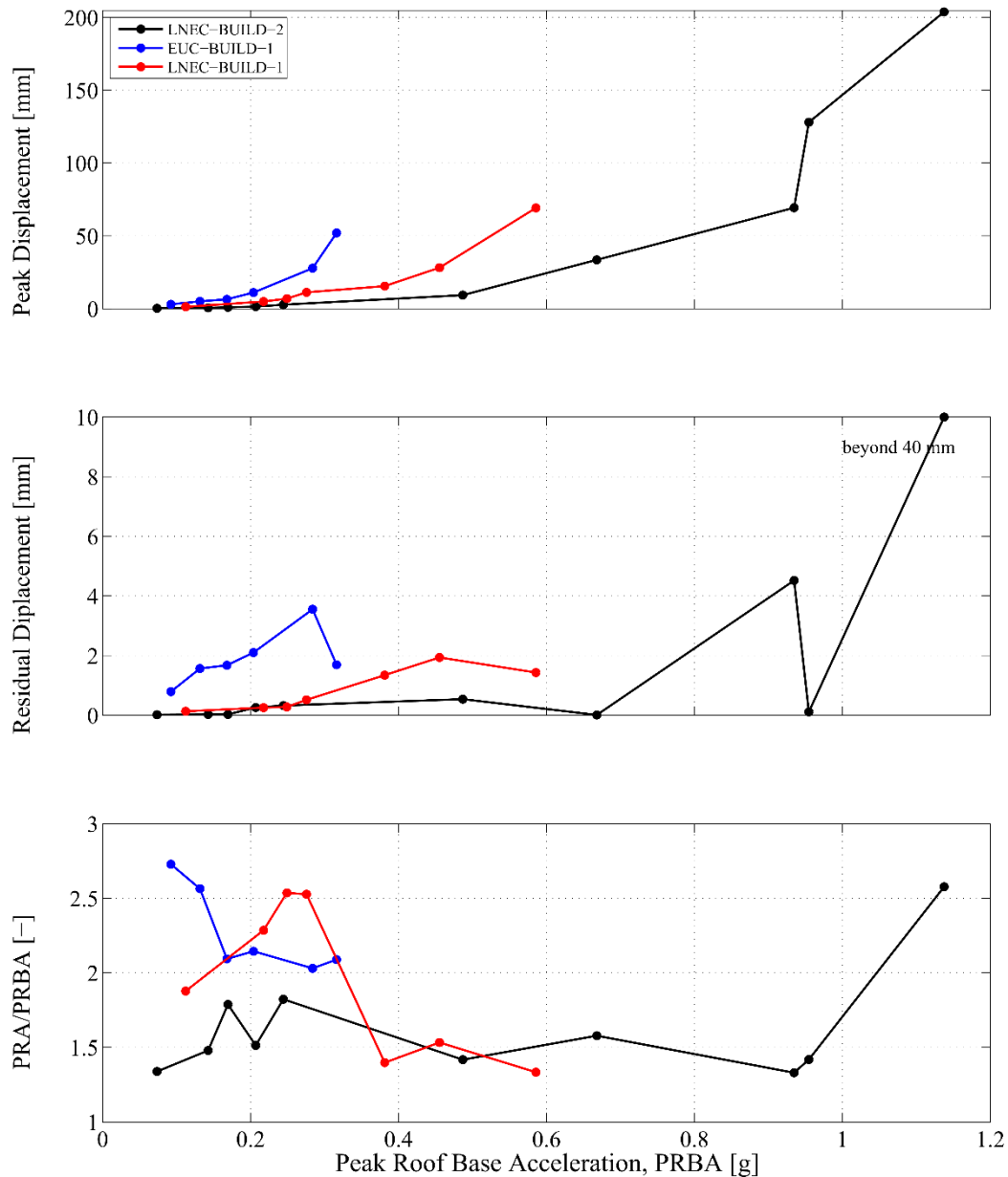


Figure 5.56 Summary of the performance of the building specimen.

6 QUASI-STATIC PUSHOVER TEST OF TIMBER ROOF SYSTEM

After the shake table test on the complete roof substructure, the remaining URM cavity walls were carefully removed and a support system was put in place to allow additional testing on the timber roof system. In fact, once the hysteretic response of the complete specimen is known, it is interesting to assess the load-displacement behaviour of the timber roof system alone, in order to better characterise the influence of the URM gable walls on the specimen's seismic response.

Therefore, given that the timber roof beams were directly supported on the gable walls, a support timber structure was assembled in order to restore the timber roof system's geometry and to carry its weight. Additionally, this support structure also served the purpose of guidance system for the timber roof, as depicted in Figure 6.1, with the use of Teflon plates between the timber surfaces. A cyclic pushover test could thus be performed using the shake table as actuator system and taking advantage of the particular characteristics of LNEC's shake table platform, which is surrounded by three reaction walls. The East and West extremities of the ridge beam were fixed to the reaction walls through steel ties, as shown in Figure 6.2.



Figure 6.1 Support and guidance system.

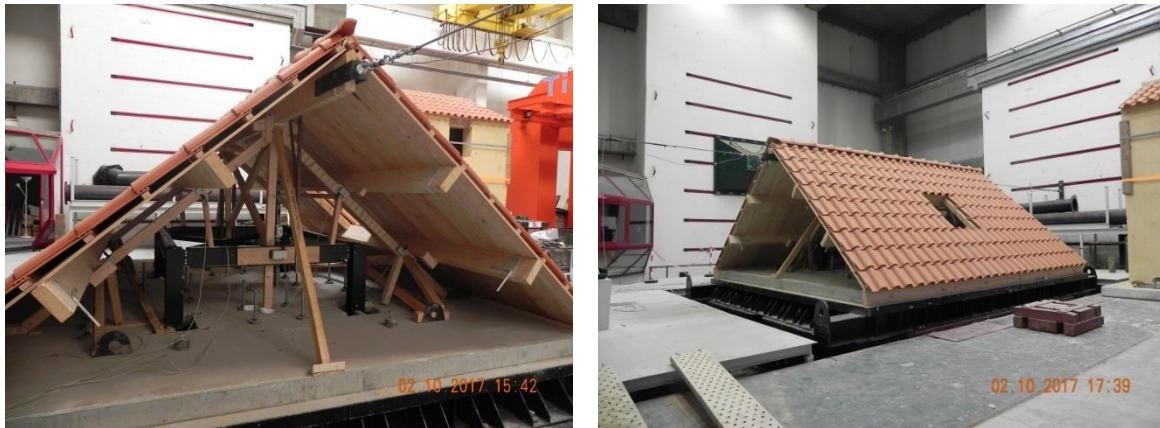


Figure 6.2 Steel ties connecting the ridge beam to the reaction walls.

Both steel ties were instrumented with load cells, allowing measuring the resulting force applied on the ridge beam. On the other hand, each of the five timber roof beams was instrumented with a wire potentiometer to measure its horizontal displacement with respect to the reference steel frame. The instrumentation adopted for this test is presented in Figure 6.3.

The control system of the shake table platform was prepared for using the relative displacement between the reference frame and the ridge beam as control variable, thus ensuring that the desired drift on the specimen was applied at each cycle. The roof structure was then subjected to two full cycles at ± 10 mm, ± 50 mm, ± 100 mm and ± 150 mm. The force-displacement curve obtained is represented in Figure 6.4.

It can be observed that the response is composed of three different stages: (i) an initial frictional response with a limit of about ± 3 kN; (ii) followed by a low-stiffness response corresponding to a sliding associated to the limits of the nails' free-deformation in their holes and to a relative distortion between the different timber planks; (iii) and a stiffening response associated to the dowel behaviour of the nails.

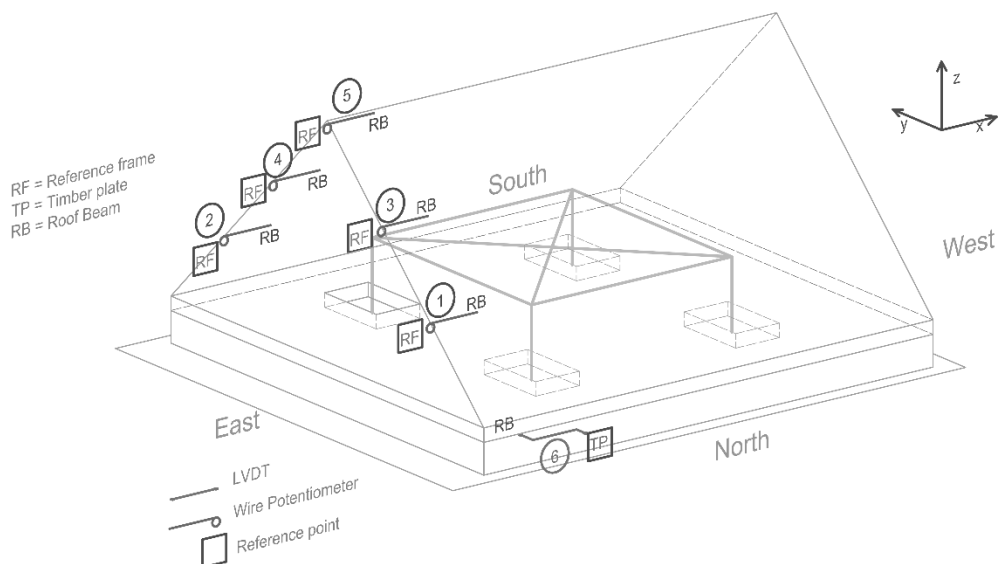


Figure 6.3 Instrumentation for pushover test of timber roof system.

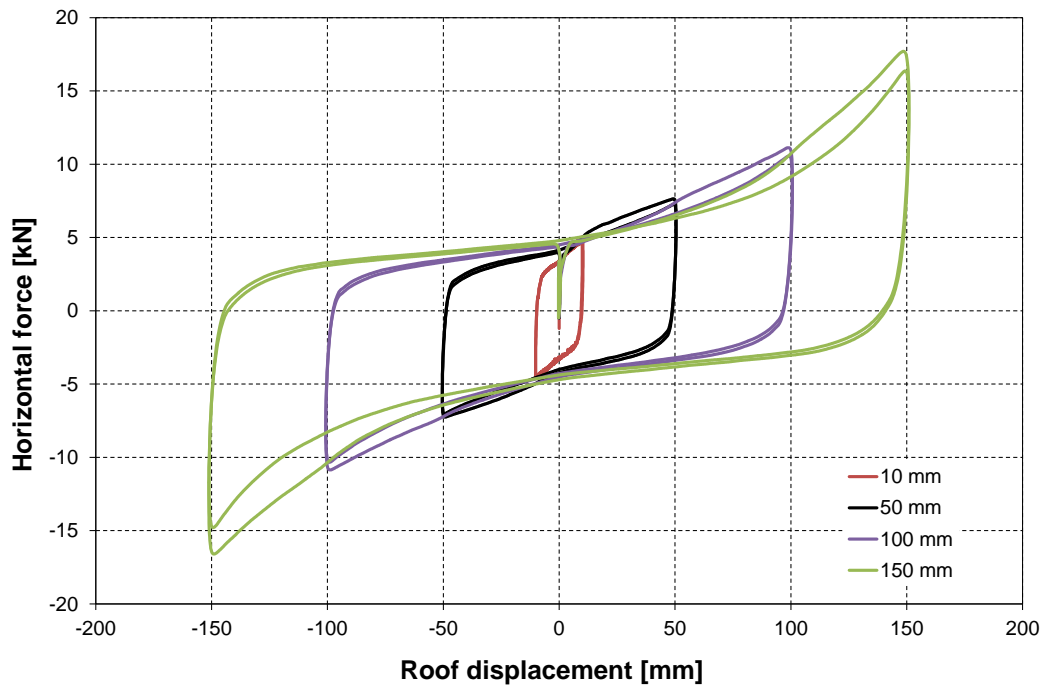


Figure 6.4 Cyclic response of the roof structure.

No particular damage was observed during the cyclic loading up to 150 mm, with the observed response being rather stable. Some cyclic strength degradation occurred in the second cycles, which may probably be attributed to the ovalisation of the nailed connections and to partial pull-out of the nails.

It is also interesting to observe that the evolution of displacements between the different roof beams remains linearly proportional to their elevation, as depicted in Figure 6.5, despite the load being applied at the ridge beam only. This indicates that each roof span is deforming in shear and not in flexure.

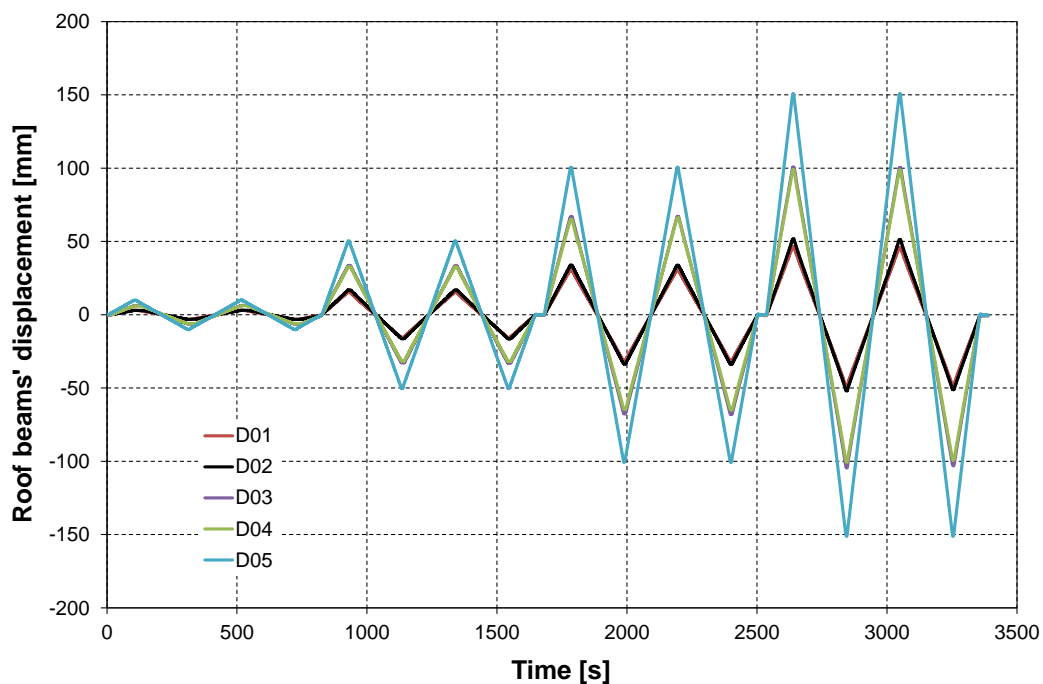


Figure 6.5 Evolution of displacements at the roof beams.

Due to the limits of the shake table motion, it was not possible to apply cyclic loading at larger amplitudes. Therefore, the roof was then pushed to 220 mm and unloaded. A permanent drift was visible, amounting to around 200 mm. The timber planks distorted, ones with respect to the others, and some nails at the base beams started to pull-out, opening gaps in their connections. The pictures in Figure 6.6 represent the observed damage.



Figure 6.6 Damage after the 220 mm pushover.

132 *Shake Table Test up to Collapse on a Roof Substructure of a Dutch Terraced House*

A significant increase of broken tiles occurred on the South side. No broken tiles appeared on the North side, since the mirrored configuration of the tiles was particularly fragile on the South side in the direction of pushing – the damage to the tiles seems to have no relation with the existence or not of a window opening.

Finally, the near collapse limit state was reached for a pushover of 350 mm. The nails connecting the timber planks and the base beams were completely pulled out, as depicted in the pictures of Figure 6.7 to Figure 6.9.



Figure 6.7 Video images of the damage during the 350 mm pushover.



Figure 6.8 Damage after the 350 mm pushover – West side.



Figure 6.9 Damage after the 350 mm pushover – East side.

The roof structure kept a significant permanent drift of over 400 mm, as represented in the load-displacement plot of Figure 6.10 and shown in Figure 6.11. The readings of the horizontal displacement above 370 mm were assumed to be non-realistic, since the wire of the potentiometer was inclined due to the uplift of the roof structure.

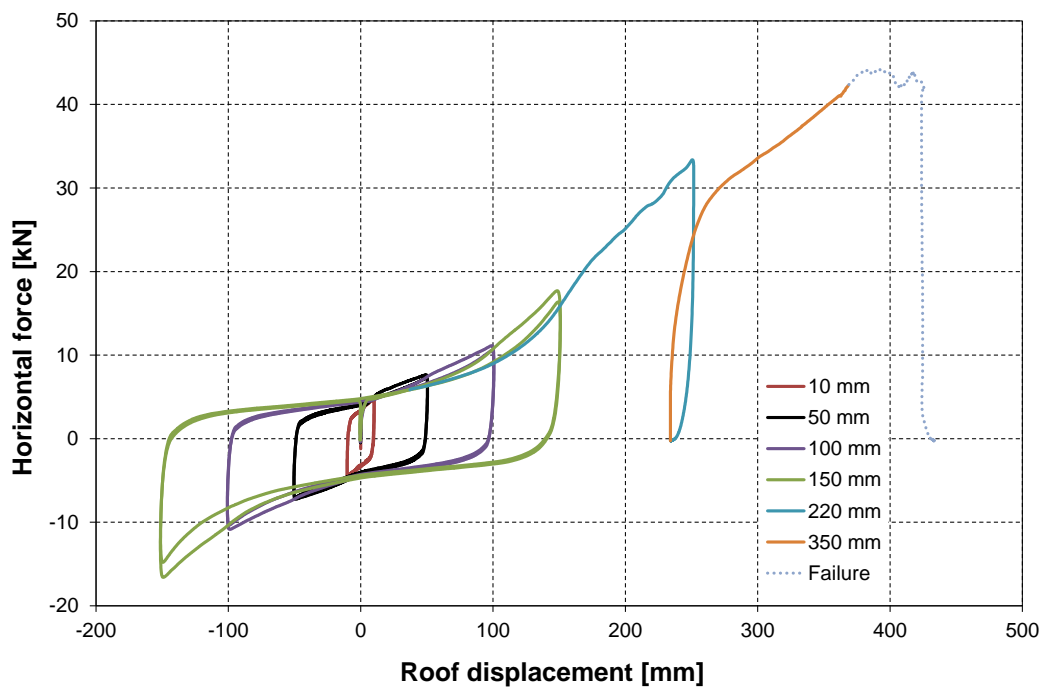


Figure 6.10 Full response of the roof structure.

134 Shake Table Test up to Collapse on a Roof Substructure of a Dutch Terraced House



Figure 6.11 Permanent drift after 350 mm pushover.

The damage to the ceramic tiles on the South side is documented in Figure 6.12, with broken and uplifted tiles visible throughout the roof plan but particularly at midspan.



Figure 6.12 Damage in roof tiles.

Figure 6.13 allows visualising the shear deformation of the roof plan due to distortion of the timber planks through sliding at their tongue and groove joints.

The maximum load attained reached about 45 kN, which corresponds to about 90% of the overall load-carrying capacity of the structure.



Figure 6.13 Distortion of timber planks.

REFERENCES

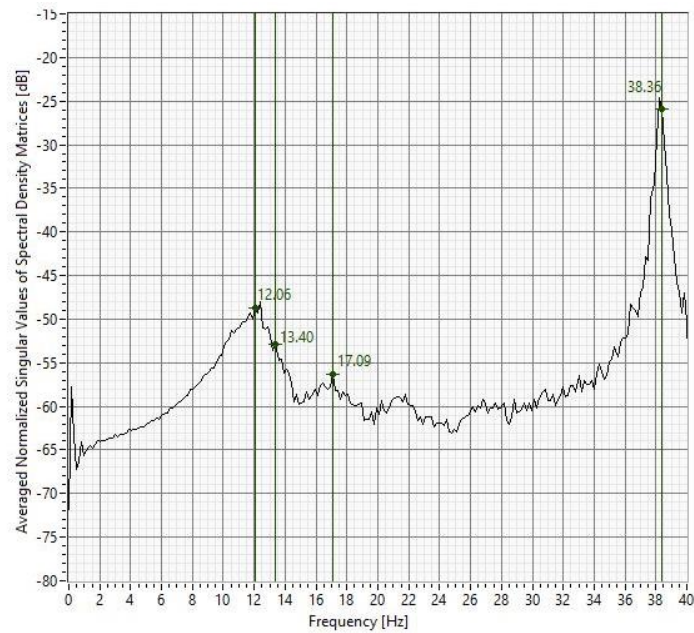
- Allemang, R.J., Brown, D.L. (1982) "A Correlation Coefficient for Modal Vector Analysis," Proceedings of the 1st International Modal Analysis Conference (IMAC I), Orlando, USA.
- Bendat, J.S., Piersol, A.G. (2010) "Random Data: Analysis and Measurement Procedures," 4th Edition, ISBN: 0470248777, Wiley Series in Probability and Statistics.
- Brincker, R., Ventura, C., et al. (2001) "Damping Estimation by Frequency Domain Decomposition," Proceedings of the 19th International Modal Analysis Conference (IMAC XIX), Kissimmee, USA.
- Graziotti, F., Tomassetti, U., Rossi, A., Kallioras, S., Mandirola, M., Cenja, E., Penna, A., Magenes, G. (2015) "Experimental campaign on cavity-wall systems representative of the Groningen building stock", Technical Report EUC318/2015U, Eucentre, Pavia, Italy. Available on URL: <http://www.eucentre.it/project-nam/>
- Graziotti, F., Tomassetti, U., Penna, A., Magenes, G. (2016b) "Out-of-plane shaking table tests on URM single leaf and cavity walls", Engineering Structures, 125, 455-470, doi:10.1016/j.engstruct.2016.07.011.
- CEN – European Committee for Standardization (1998a) "Methods of test for mortar for masonry - Part 6: Determination of bulk density of fresh mortar". EN 1015-6: 1998, Brussels.
- CEN – European Committee for Standardization (1998b) "Methods of test for masonry – Part 1: Determination of compressive strength" EN 1052-1:1998, Brussels.
- CEN – European Committee for Standardization (1999a) "Methods of test for mortar for masonry - Part 3: Determination of consistency of fresh mortar (by flow table)". EN 1015-3: 1999, Brussels.
- CEN – European Committee for Standardization (1999b) "Methods of test for mortar for masonry - Part 11: Determination of flexural and compressive strength of hardened mortar". EN 1015-11: 1999, Brussels.
- CEN – European Committee for Standardization (2005) "Methods of test for masonry - Part 5: Determination of bond strength by the bond wrench method". EN 1052-5: 2005, Brussels.
- CEN – European Committee for Standardization (2006) "Test methods for natural stone. Determination of dynamic modulus of elasticity (by measuring fundamental resonance frequency)". EN 14146: 2006, Brussels.
- CEN – European Committee for Standardization (2011) "Methods of test for masonry units - Part 1: Determination of compressive strength". EN 772-1: 2011, Brussels.
- Magenes, G., Penna, A., Senaldi, I.E., Rota, M., Galasco, A. (2014) "Shaking Table Test of a Strengthened Full-Scale Stone Masonry Building with Flexible Diaphragms", International Journal of Architectural Heritage: Conservation, Analysis, and Restoration, 8:3, 349-375.
- Mendes, L., Campos Costa, A., (2007) "LNEC-SPA – Signal Processing and Analysis Tool for Civil Engineers. Version 1.0 – Build 12," Report LNEC 29.
- Messali, F., Esposito, R., Maragna, M. (2016) "Pull-out strength of wall ties", Technical Report, TU Delft, NL.

- Tomassetti, U., Correia, A. A., Graziotti, F., Marques, A. I., Mandirola, M., Candeias, P. X. (2017) "Collapse shaking table test on a URM cavity wall structure representative of a Dutch terraced house", Technical Report EUC???/2017U, Eucentre, Pavia, Italy. Available on URL: <http://www.eucentre.it/project-nam/>
- Tomažević, M., Weiss, P. and Velechovsky, T. (1991) "The influence of rigidity of floors on the seismic behaviour of old stone-masonry buildings," European Earthquake Engineering, 3.
- Tondelli, M., Graziotti, F., Rossi, A., Magenes, G. (2015) "Characterisation of masonry materials in the Groningen area by means of in-situ and laboratory testing", Technical Report, Eucentre, Pavia, Italy. Available on URL: <http://www.eucentre.it/project-nam>

ANNEXES

ANNEX I
Modal identification analysis results

CAT 00 – Initial dynamic identification (before any test)



Frequency Domain Decomposition results for 1st dynamic identification (before any test)

Summary of vibration modes' characteristics for 1st dynamic identification (before any test):

Mode	FDD Frequency [Hz]	EFDD Frequency [Hz]	Damping [%]
1	12.06	12.08	2.07
2	13.40	13.34	1.84
3	17.09	17.07	1.42
4	38.36	38.41	0.29

MAC coefficients for 1st dynamic identification (before any test):

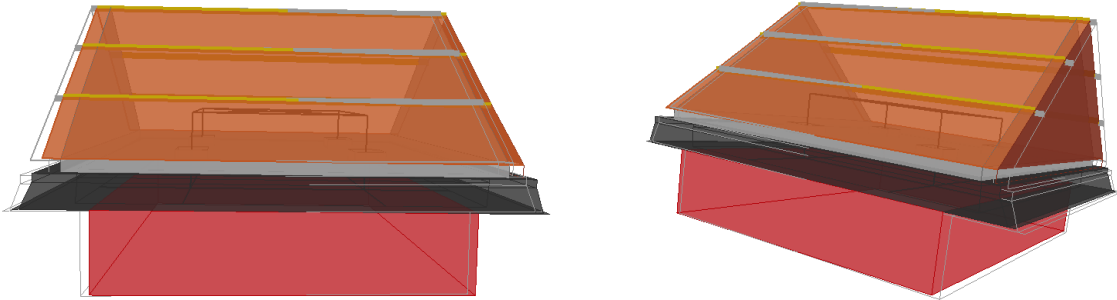
MODE_i_j		MODE_01_00	MODE_02_00	MODE_03_00	MODE_04_00
	Frequency [Hz]	12.08	13.34	17.07	38.41
MODE_01_00	12.08	1.00	0.99	0.95	0.08
MODE_02_00	13.34	0.99	1.00	0.97	0.07
MODE_03_00	17.07	0.95	0.97	1.00	0.12
MODE_04_00	38.41	0.08	0.07	0.12	1.00

i Mode

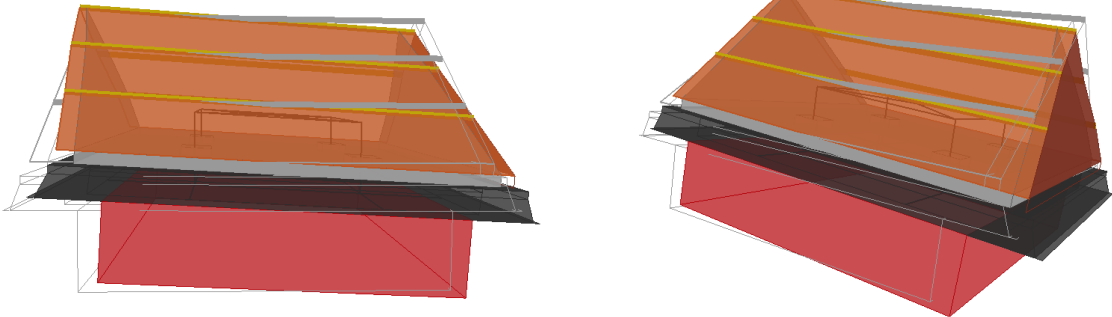
j dynamic identification

144 *Shake Table Test up to Collapse on a Roof Substructure of a Dutch Terraced House*

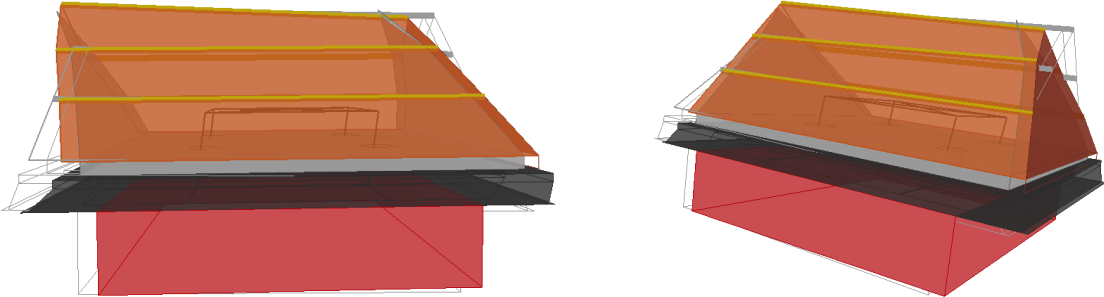
Mode 1: 12.08 Hz



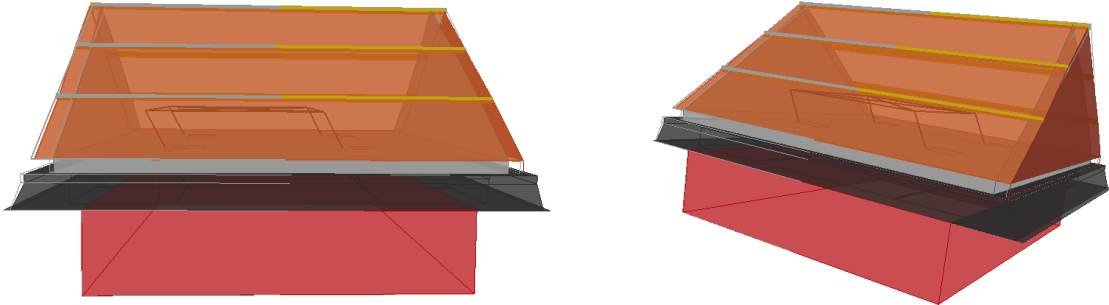
Mode 2: 13.34 Hz



Mode 3: 17.07 Hz

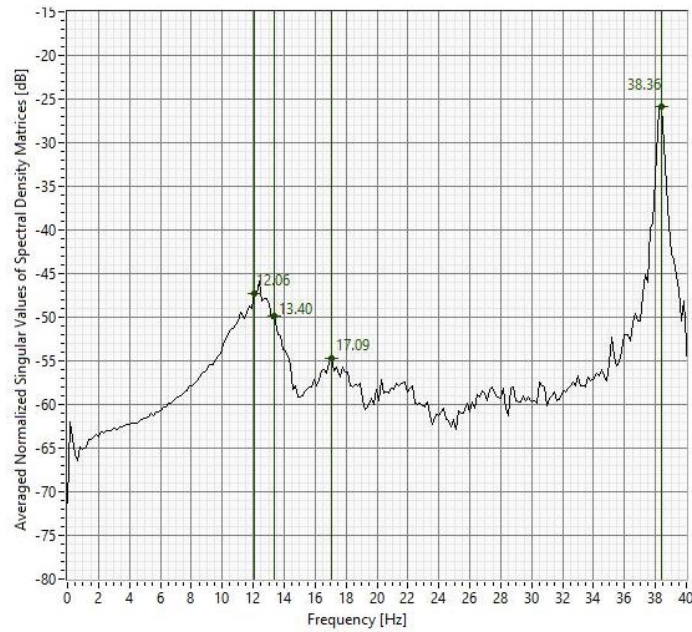


Mode 4: 38.41 Hz



Mode shapes for 1st dynamic identification (before any test)

CAT 01 – 2nd dynamic identification (after test FEQ1-100%)



Frequency Domain Decomposition results for 2nd dynamic identification (after test FEQ1-100%)

Summary of vibration modes' characteristics for 2nd dynamic identification (after test FEQ1-100%):

Mode	FDD Frequency [Hz]	EFDD Frequency [Hz]	Damping [%]
1	12.06	12.10	2.02
2	13.40	13.37	1.08
3	17.09	17.07	1.43
4	38.06	38.39	0.28

MAC coefficients for 2nd dynamic identification (after test FEQ1-100%):

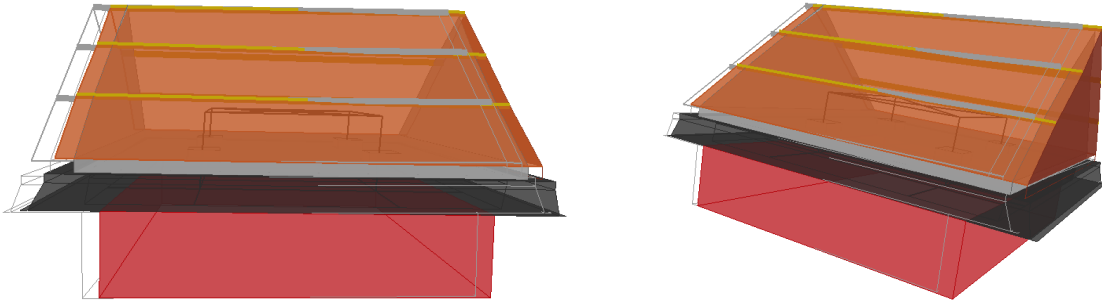
MODE_i_j		MODE_01_01	MODE_02_01	MODE_03_01	MODE_04_01
	Frequency [Hz]	12.1	13.37	17.07	38.39
MODE_01_00	12.08	1.00	0.99	0.96	0.07
MODE_02_00	13.34	0.99	1.00	0.98	0.07
MODE_03_00	17.07	0.95	0.96	1.00	0.11
MODE_04_00	38.41	0.08	0.07	0.11	1.00

i Mode

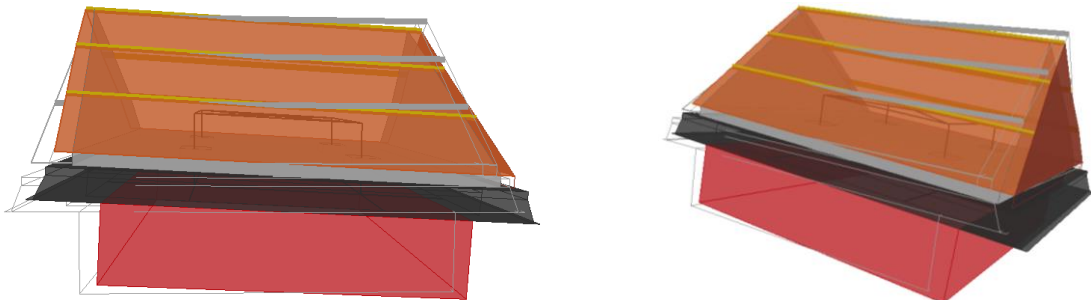
j dynamic identification

146 Shake Table Test up to Collapse on a Roof Substructure of a Dutch Terraced House

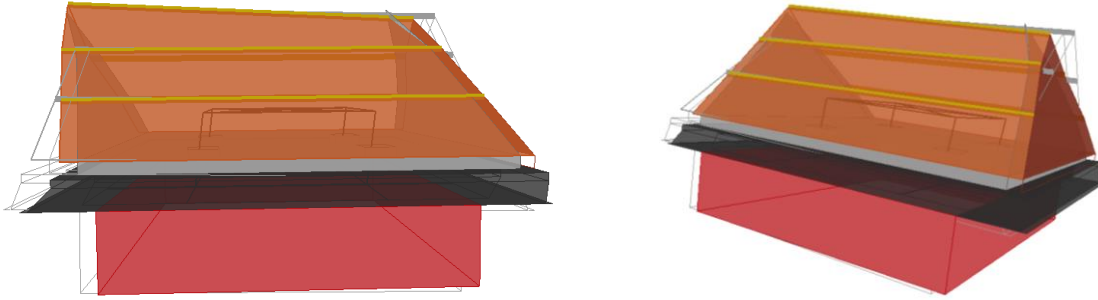
Mode 1: 12.10 Hz



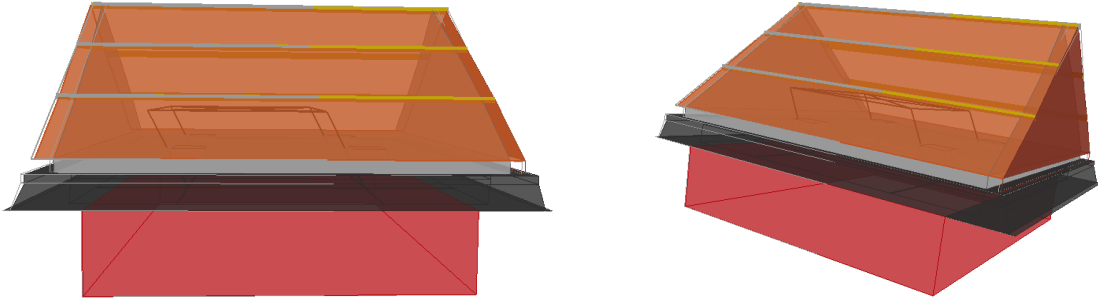
Mode 2: 13.37 Hz



Mode 3: 17.07 Hz

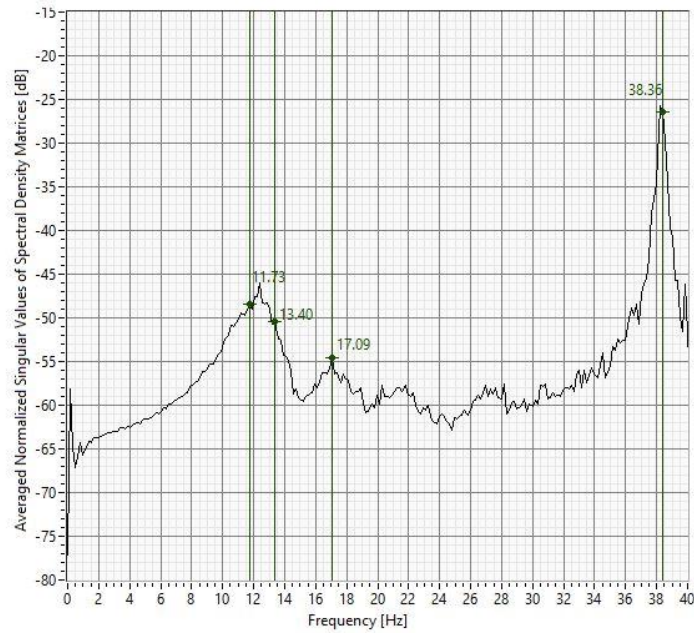


Mode 4: 38.39 Hz



Mode shapes for 2nd dynamic identification (after test FEQ1-100%)

CAT 02 – 3rd dynamic identification (after test FEQ1-150%)



Frequency Domain Decomposition results for 3rd dynamic identification (after test FEQ1-150%)

Summary of vibration modes' characteristics for 3rd dynamic identification (after test FEQ1-150%):

Mode	FDD Frequency [Hz]	EFDD Frequency [Hz]	Damping [%]
1	11.73	11.74	2.07
2	13.40	13.37	1.06
3	17.09	17.07	1.41
4	38.36	38.41	0.29

MAC coefficients for 3rd dynamic identification (after test FEQ1-150%):

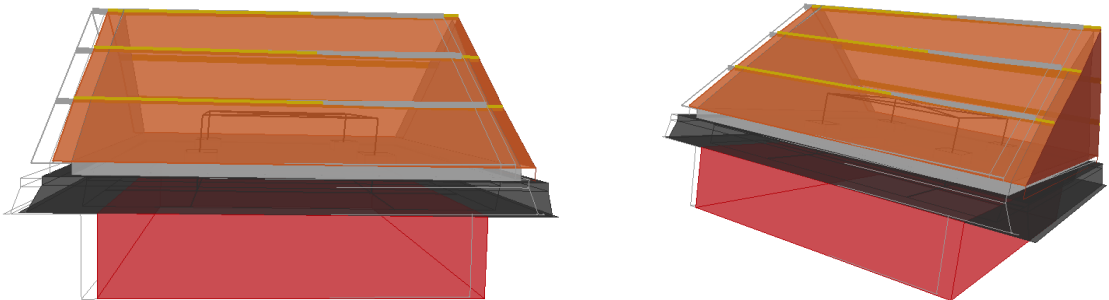
MODE_i_j		MODE_01_02	MODE_02_02	MODE_03_02	MODE_04_02
	Frequency [Hz]	11.74	13.37	17.07	38.41
MODE_01_00	12.08	1.00	0.99	0.96	0.08
MODE_02_00	13.34	0.98	1.00	0.97	0.08
MODE_03_00	17.07	0.95	0.96	1.00	0.12
MODE_04_00	38.41	0.09	0.07	0.11	1.00

i Mode

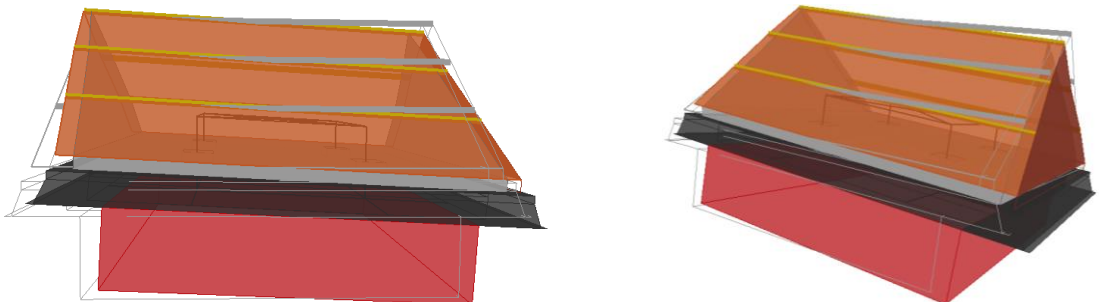
j dynamic identification

148 *Shake Table Test up to Collapse on a Roof Substructure of a Dutch Terraced House*

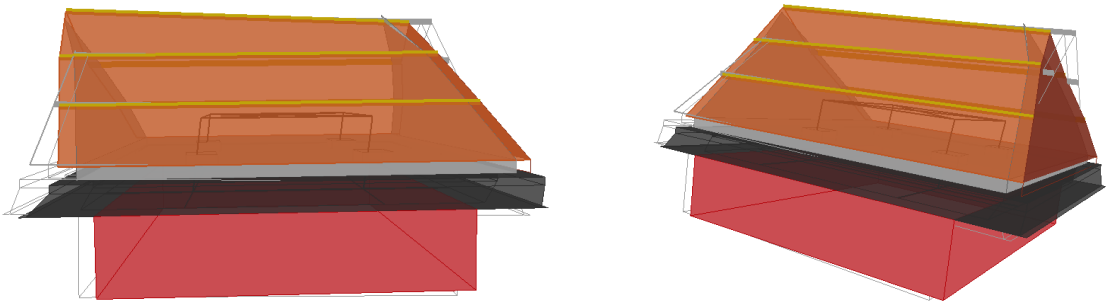
Mode 1: 11.74 Hz



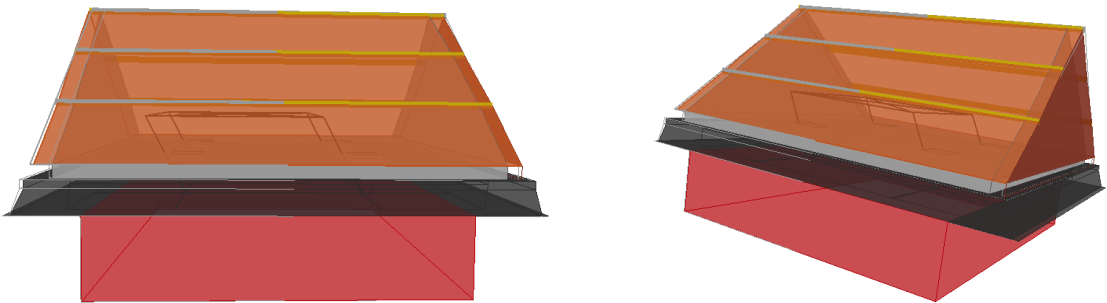
Mode 2: 13.37 Hz



Mode 3: 17.07Hz

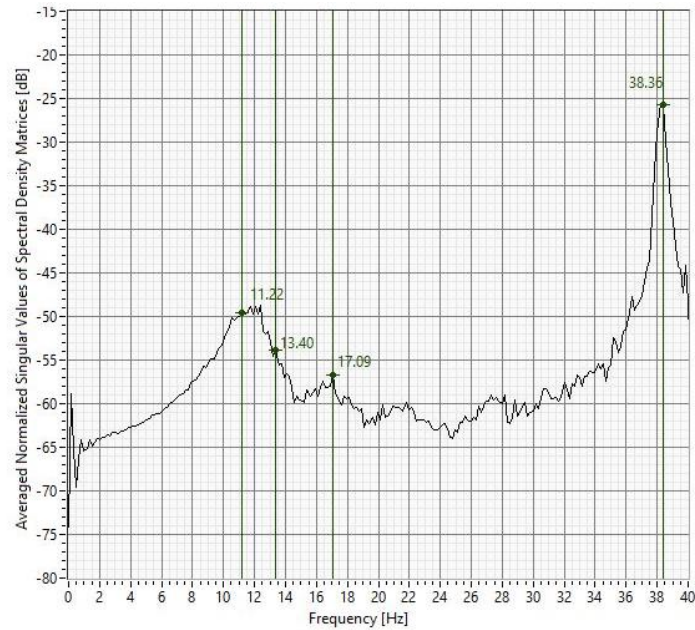


Mode 4: 38.41 Hz



Mode shapes for 3rd dynamic identification (after test FEQ1-150%)

CAT 03 – 4th dynamic identification (after test FEQ2-100%)



Frequency Domain Decomposition results for 4th dynamic identification (after test FEQ2-100%)

Summary of vibration modes' characteristics for 4th dynamic identification (after test FEQ2-100%):

Mode	FDD Frequency [Hz]	EFDD Frequency [Hz]	Damping [%]
1	11.22	11.22	2.17
2	13.40	13.35	1.85
3	17.09	17.05	1.40
4	38.36	38.41	0.29

MAC coefficients for 4th dynamic identification (after test FEQ2-100%):

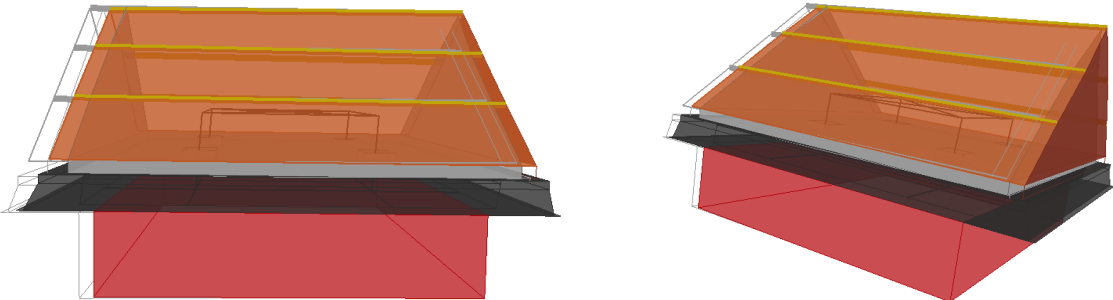
MODE _i _j		MODE_01_03	MODE_02_03	MODE_03_03	MODE_04_03
	Frequency [Hz]	11.22	13.35	17.05	38.41
MODE_01_00	12.08	0.99	1.00	0.94	0.09
MODE_02_00	13.34	0.98	0.99	0.96	0.08
MODE_03_00	17.07	0.94	0.95	1.00	0.12
MODE_04_00	38.41	0.09	0.08	0.13	1.00

i Mode

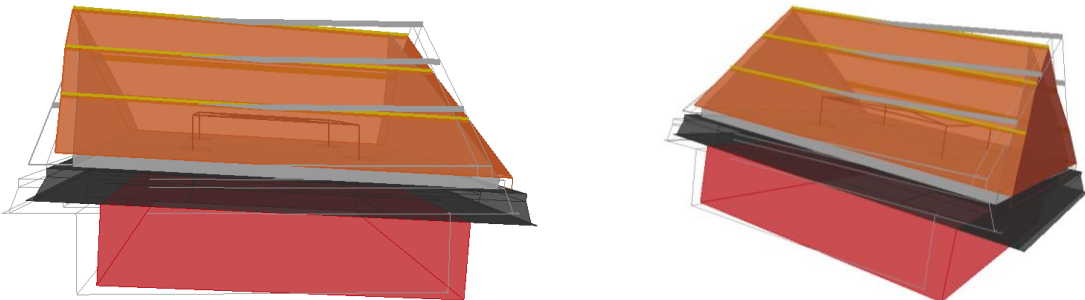
j dynamic identification

150 *Shake Table Test up to Collapse on a Roof Substructure of a Dutch Terraced House*

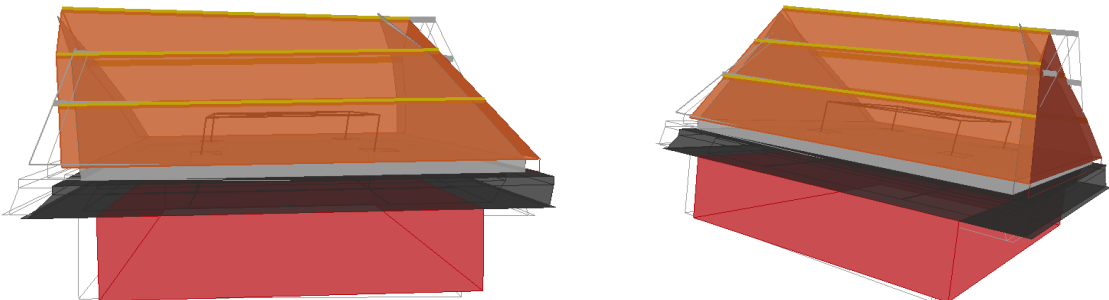
Mode 1: 11.22 HZ



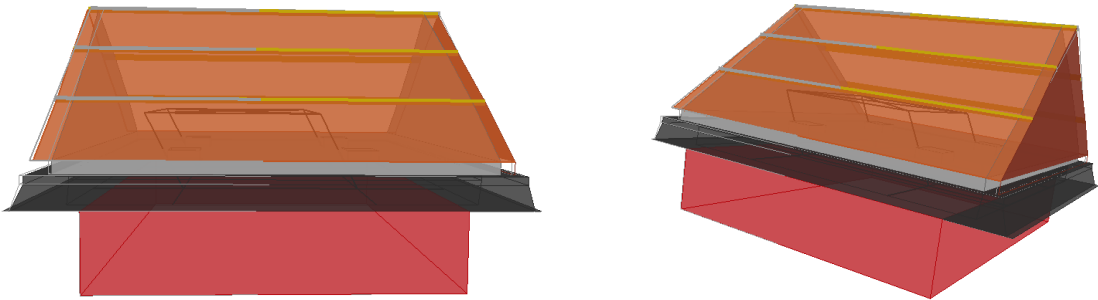
Mode 2: 13.35 Hz



Mode 3: 17.05 Hz

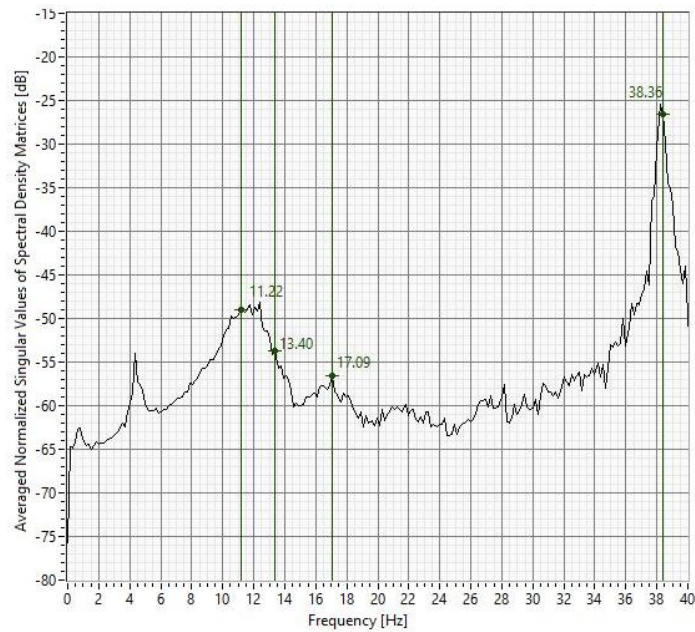


Mode 4: 38.41 Hz



Mode shapes for 4th dynamic identification (after test FEQ2-100%)

CAT 04 – 5th dynamic identification (after test FEQ2-150%)



Frequency Domain Decomposition results for 5th dynamic identification (after test FEQ2-150%)

Summary of vibration modes' characteristics for 5th dynamic identification (after test FEQ2-150%):

Mode	FDD Frequency [Hz]	EFDD Frequency [Hz]	Damping [%]
1	11.22	11.14	1.81
2	13.40	13.33	1.85
3	17.09	17.06	1.41
4	38.36	38.41	0.29

MAC coefficients for 5th dynamic identification (after test FEQ2-150%):

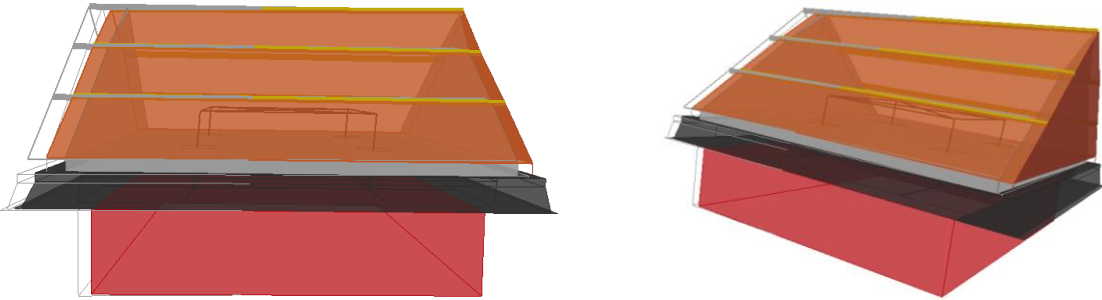
MODE _i _j		MODE_01_04	MODE_02_04	MODE_03_04	MODE_04_04
	Frequency [Hz]	11.14	13.33	17.06	38.41
MODE_01_00	12.08	0.99	0.99	0.93	0.10
MODE_02_00	13.34	0.97	1.00	0.95	0.10
MODE_03_00	17.07	0.94	0.97	0.99	0.14
MODE_04_00	38.41	0.09	0.07	0.13	0.99

i Mode

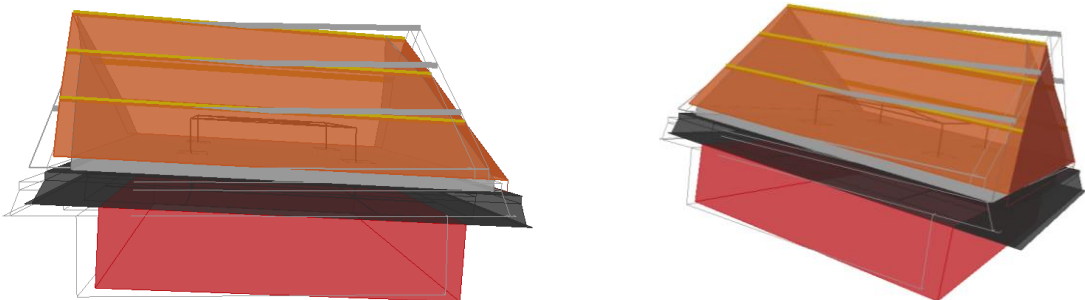
j dynamic identification

152 *Shake Table Test up to Collapse on a Roof Substructure of a Dutch Terraced House*

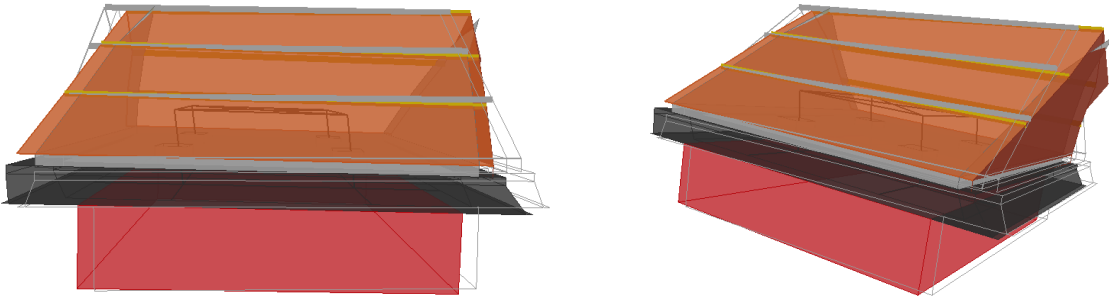
Mode 1: 11.14 HZ



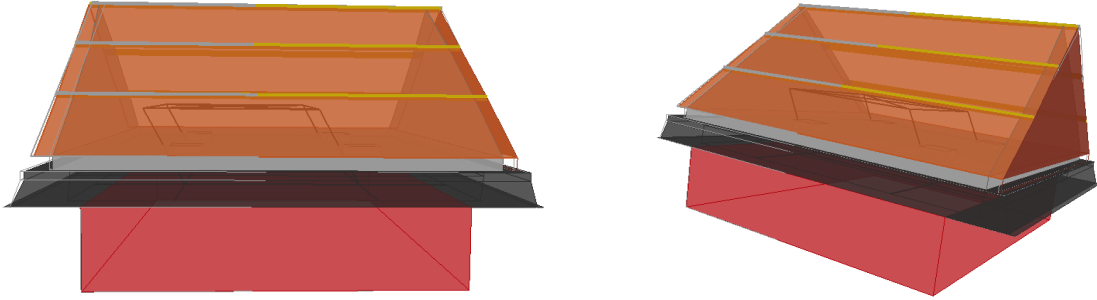
Mode 2: 13.33 Hz



Mode 3: 17.06 Hz

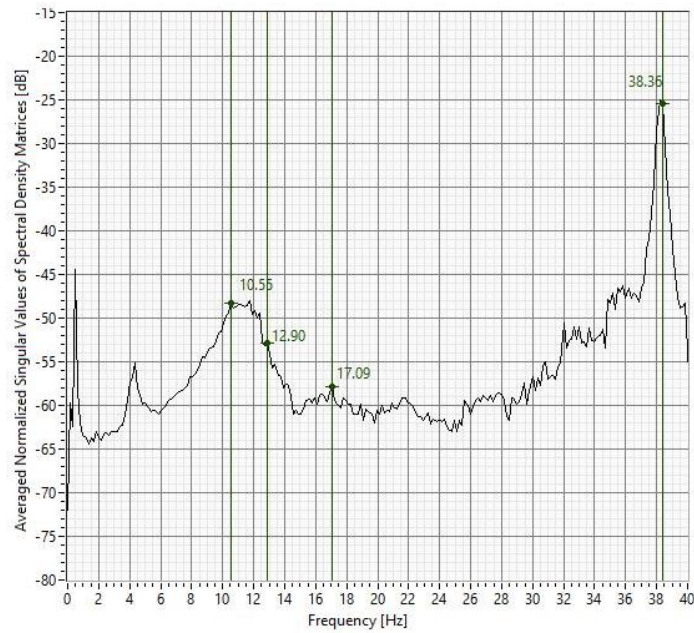


Mode 4: 38.41 Hz



Mode shapes for 5th dynamic identification (after test FEQ2-150%)

CAT 05 – 6th dynamic identification (after test FEQ2-200%)



Frequency Domain Decomposition results for 6th dynamic identification (after test FEQ2-200%)

Summary of vibration modes' characteristics for 6th dynamic identification (after test FEQ2-200%):

Mode	FDD Frequency [Hz]	EFDD Frequency [Hz]	Damping [%]
1	10.55	10.56	2.30
2	12.90	12.93	1.47
3	17.09	17.06	1.39
4	38.36	38.37	0.28

MAC coefficients for 6th dynamic identification (after test FEQ2-200%):

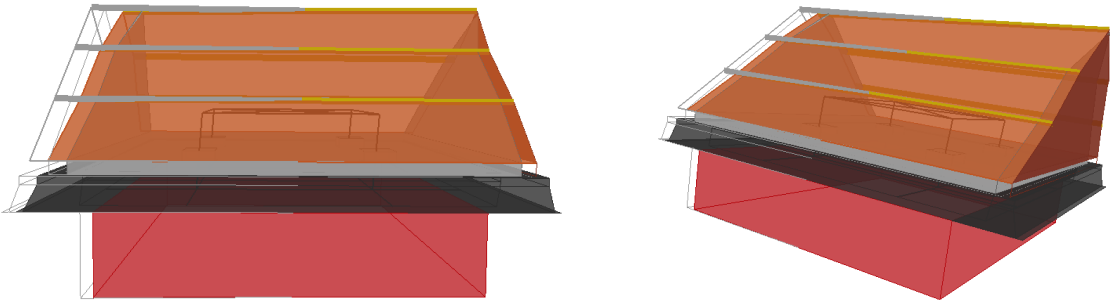
MODE_i_j	Frequency [Hz]	MODE_01_05	MODE_02_05	MODE_03_05	MODE_04_05
		10.56	12.93	17.06	38.37
MODE_01_00	12.08	0.98	0.95	0.84	0.07
MODE_02_00	13.34	0.96	0.95	0.85	0.07
MODE_03_00	17.07	0.93	0.95	0.92	0.11
MODE_04_00	38.41	0.09	0.08	0.14	1.00

i Mode

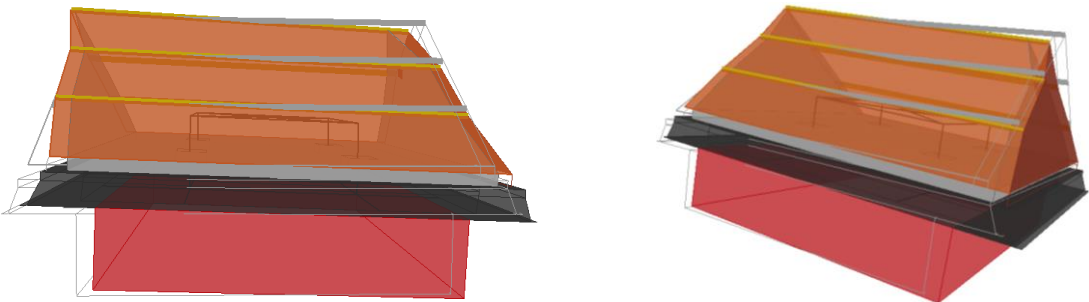
j dynamic identification

154 *Shake Table Test up to Collapse on a Roof Substructure of a Dutch Terraced House*

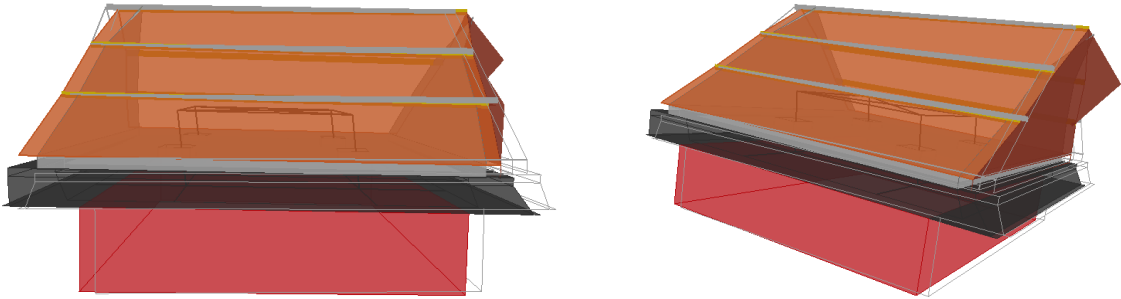
Mode 1: 10.56 Hz



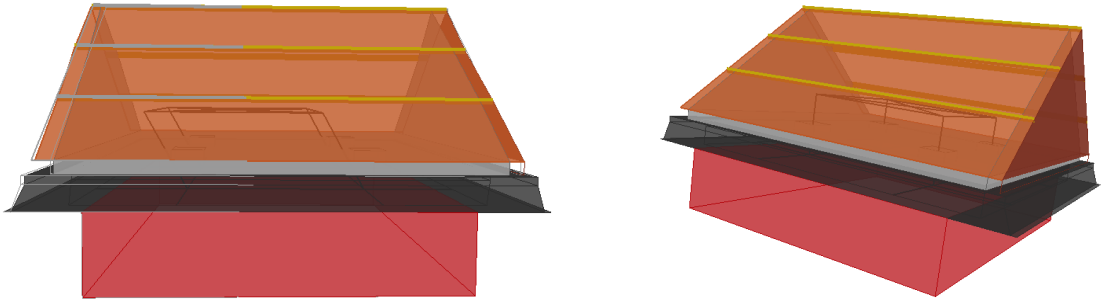
Mode 2: 12.93 Hz



Mode 3: 17.06 Hz

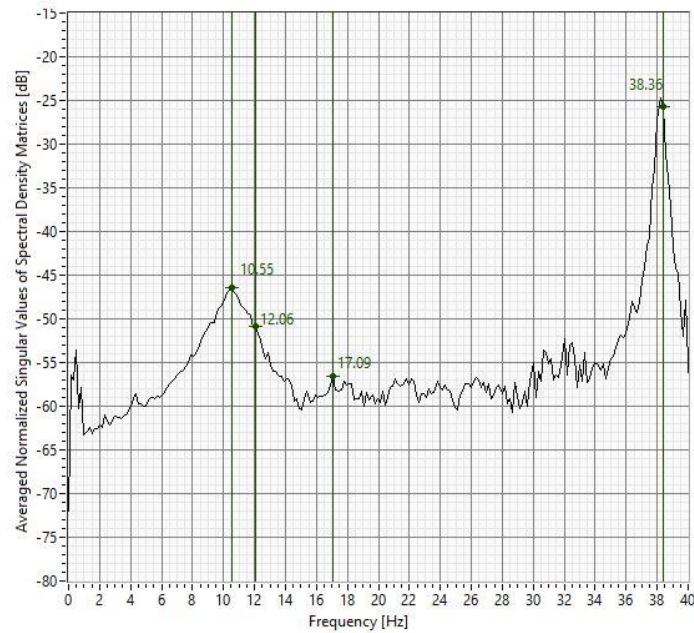


Mode 4: 38.37 Hz



Mode shapes for 6th dynamic identification (after test FEQ2-200%)

CAT 06 – 7th dynamic identification (after test FEQ2-300%)



Frequency Domain Decomposition results for 7th dynamic identification (after test FEQ2-300%)

Summary of vibration modes' characteristics for 7th dynamic identification (after test FEQ2-300%):

Mode	FDD Frequency [Hz]	EFDD Frequency [Hz]	Damping [%]
1	10.55	10.46	1.83
2	12.06	12.01	2.03
3	17.09	17.07	1.40
4	38.36	38.40	0.30

MAC coefficients for 7th dynamic identification (after test FEQ2-300%):

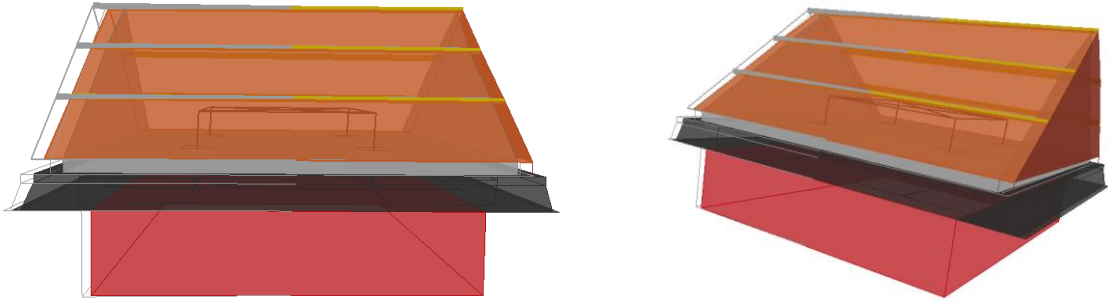
MODE_i_j		MODE_01_06	MODE_02_06	MODE_03_06	MODE_04_06
	Frequency [Hz]	10.46	12.01	17.07	38.4
MODE_01_00	12.08	0.94	0.87	0.95	0.05
MODE_02_00	13.34	0.92	0.87	0.95	0.05
MODE_03_00	17.07	0.90	0.88	0.96	0.09
MODE_04_00	38.41	0.09	0.08	0.13	0.99

i Mode

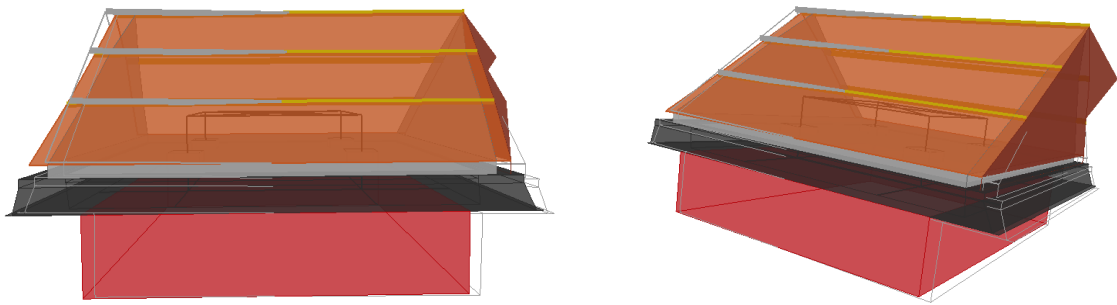
j dynamic identification

156 *Shake Table Test up to Collapse on a Roof Substructure of a Dutch Terraced House*

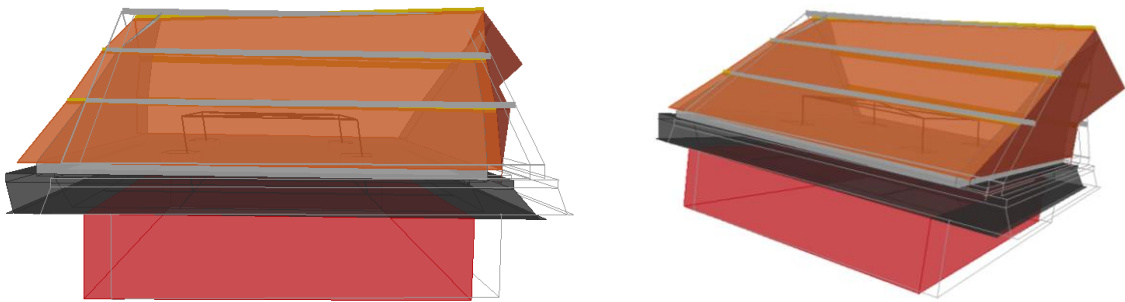
Mode 1: 10.46 Hz



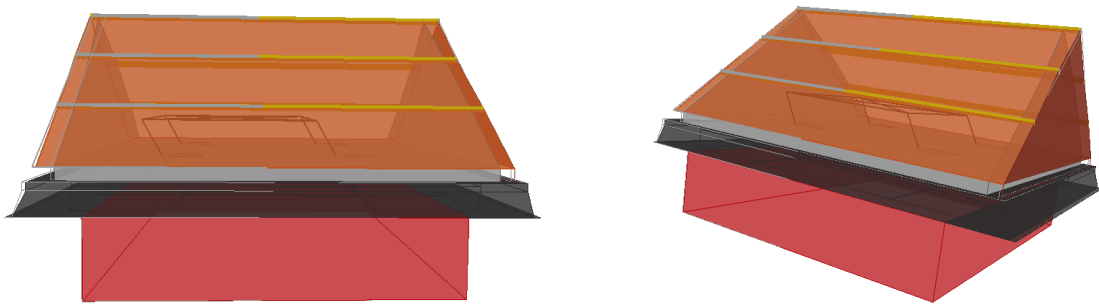
Mode 2: 12.01 Hz



Mode 3: 17.01 Hz

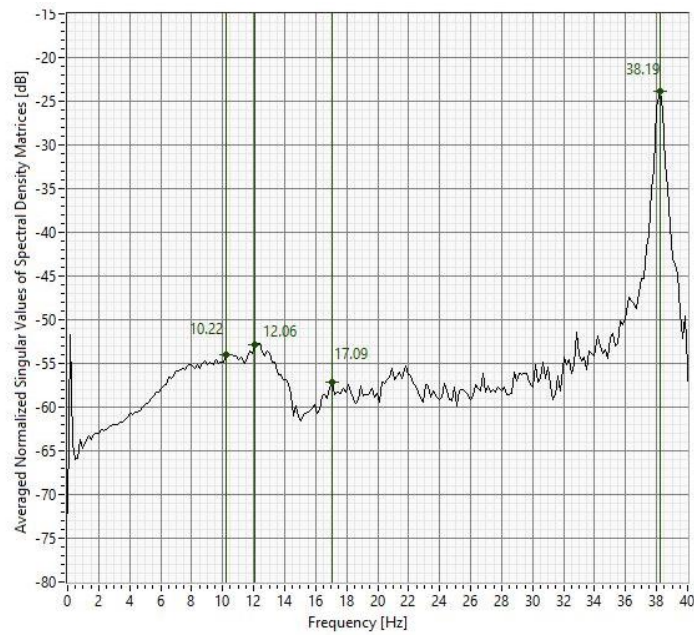


Mode 4: 38.40 Hz



Mode shapes for 7th dynamic identification (after test FEQ2-300%)

CAT 07 – 8th dynamic identification (after test FEQ2-400%)



Frequency Domain Decomposition results for 8th dynamic identification (after test FEQ2-400%)

Summary of vibration modes' characteristics for 8th dynamic identification (after test FEQ2-400%):

Mode	FDD Frequency [Hz]	EFDD Frequency [Hz]	Damping [%]
1	10.22	10.23	2.41
2	12.06	12.07	2.00
3	17.09	17.07	1.42
4	38.19	38.25	0.25

MAC coefficients for 8th dynamic identification (after test FEQ2-400%):

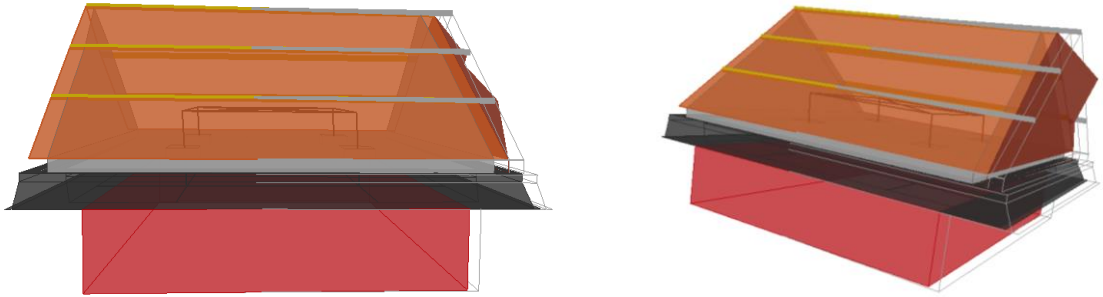
MODE_i_j	Frequency [Hz]	MODE_01_07	MODE_02_07	MODE_03_07	MODE_04_07
	12.08	0.97	0.97	0.93	0.06
MODE_01_00	13.34	0.94	0.96	0.94	0.05
MODE_02_00	17.07	0.93	0.93	0.95	0.09
MODE_03_00	38.41	0.12	0.09	0.12	0.98

i Mode

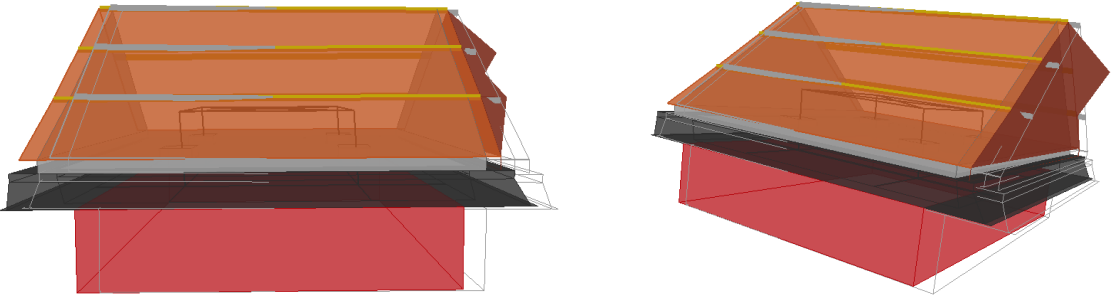
j dynamic identification

158 *Shake Table Test up to Collapse on a Roof Substructure of a Dutch Terraced House*

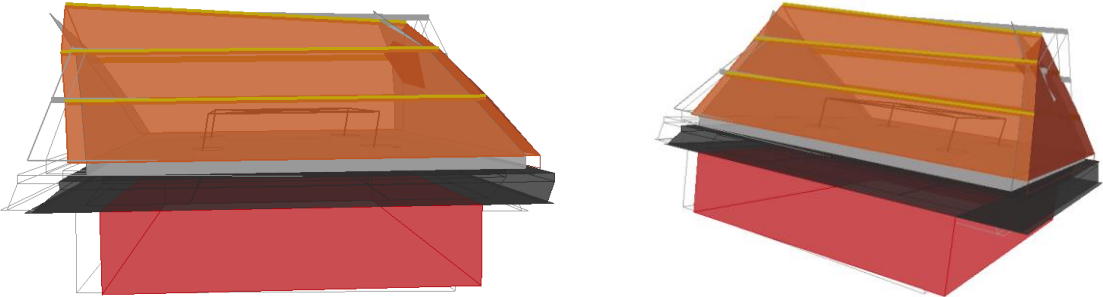
Mode 1: 10.22 Hz



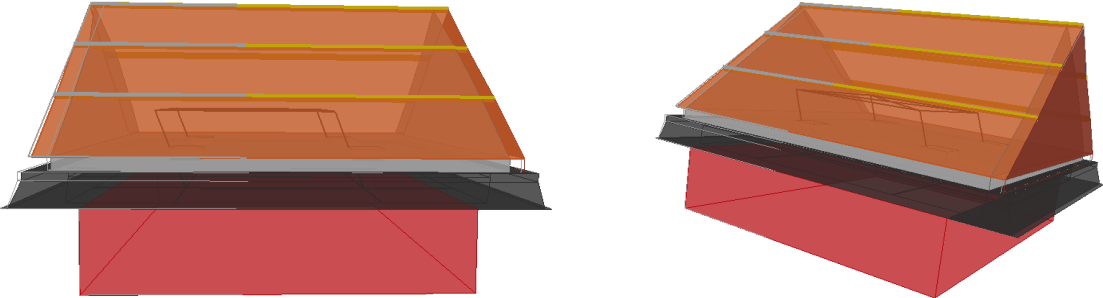
Mode 2: 12.07 Hz



Mode 3: 17.07 Hz

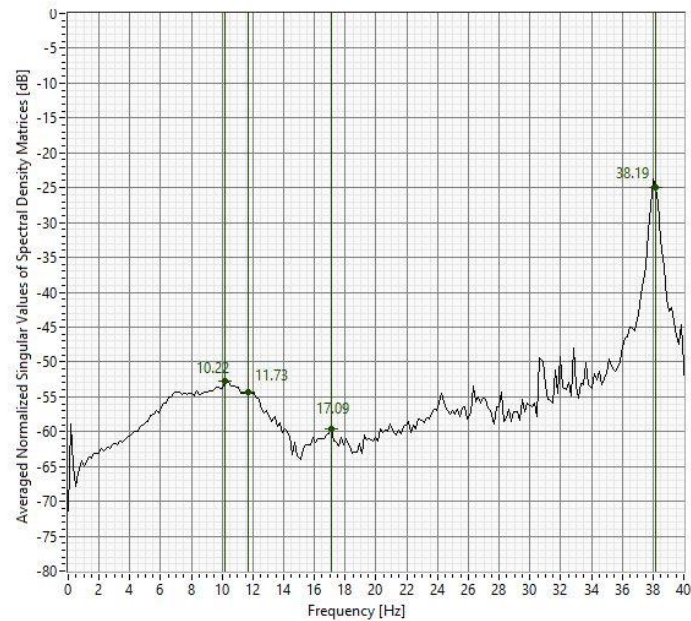


Mode 4: 38.25 Hz



Mode shapes for 8th dynamic identification (after test FEQ2-400%)

CAT 08 – 9th dynamic identification (after test FEQ2-500%)



Frequency Domain Decomposition results for 9th dynamic identification (after test FEQ2-500%)

Summary of vibration modes' characteristics for 9th dynamic identification (after test FEQ2-500%):

Mode	FDD Frequency [Hz]	EFDD Frequency [Hz]	Damping [%]
1	10.22	10.23	2.35
2	11.73	11.71	2.06
3	17.09	17.05	1.44
4	38.26	38.26	0.25

MAC coefficients for 9th dynamic identification (after test FEQ2-500%):

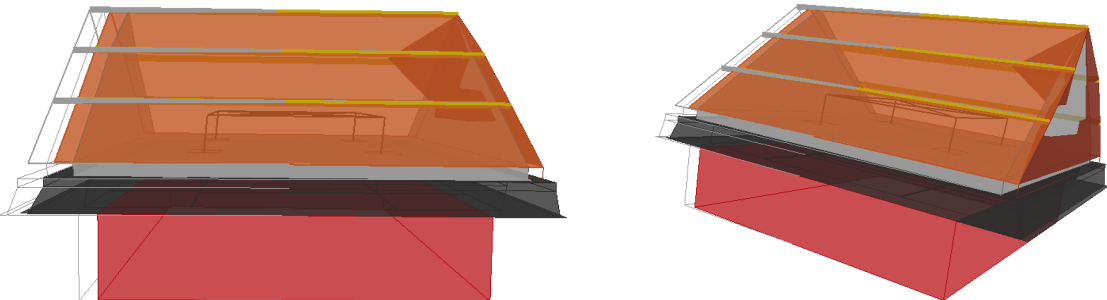
MODE _i _j		MODE_01_08	MODE_02_08	MODE_03_08	MODE_04_08
	Frequency [Hz]	10.23	11.71	17.05	38.26
MODE_01_00	12.08	0.94	0.94	0.82	0.09
MODE_02_00	13.34	0.91	0.92	0.81	0.08
MODE_03_00	17.07	0.87	0.87	0.80	0.12
MODE_04_00	38.41	0.11	0.09	0.14	0.97

i Mode

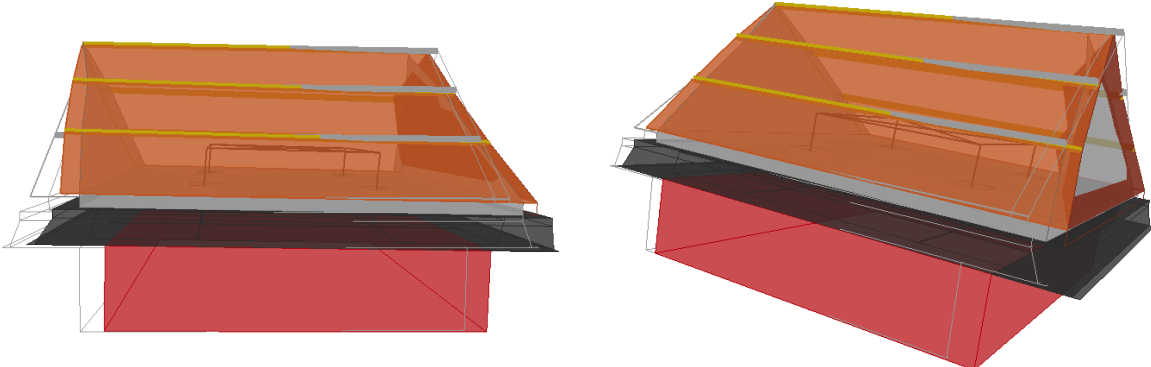
j dynamic identification

160 *Shake Table Test up to Collapse on a Roof Substructure of a Dutch Terraced House*

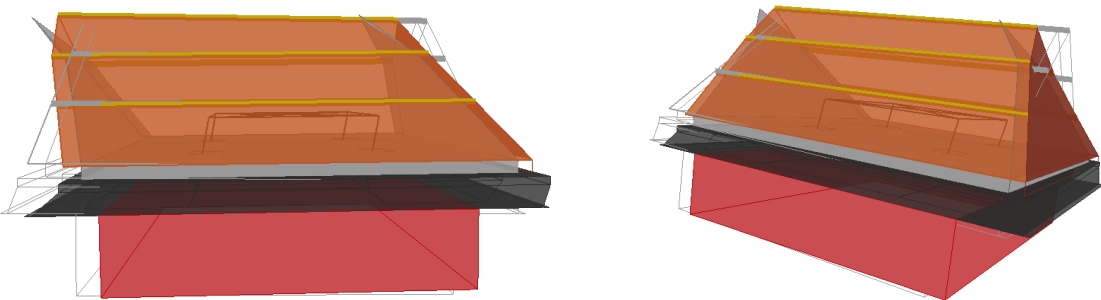
Mode 1: 10.23 Hz



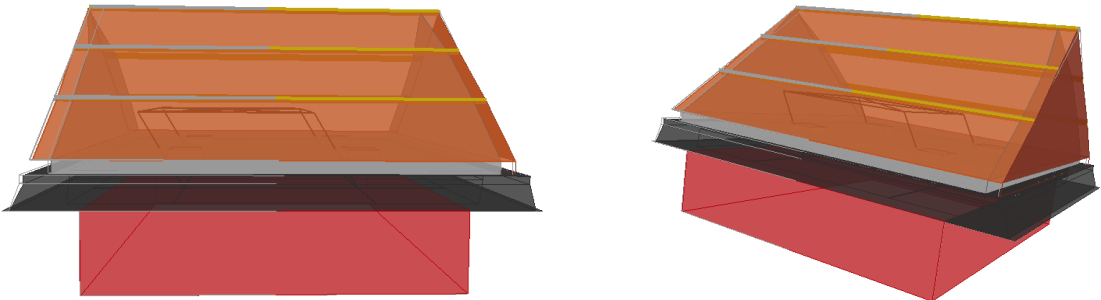
Mode 2: 11.71 Hz



Mode 3: 17.05 Hz

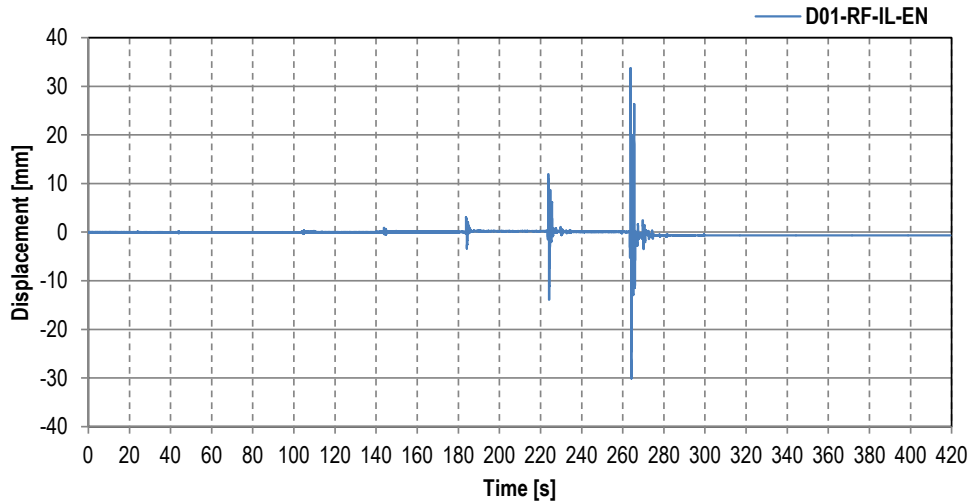


Mode 4: 38.26 Hz

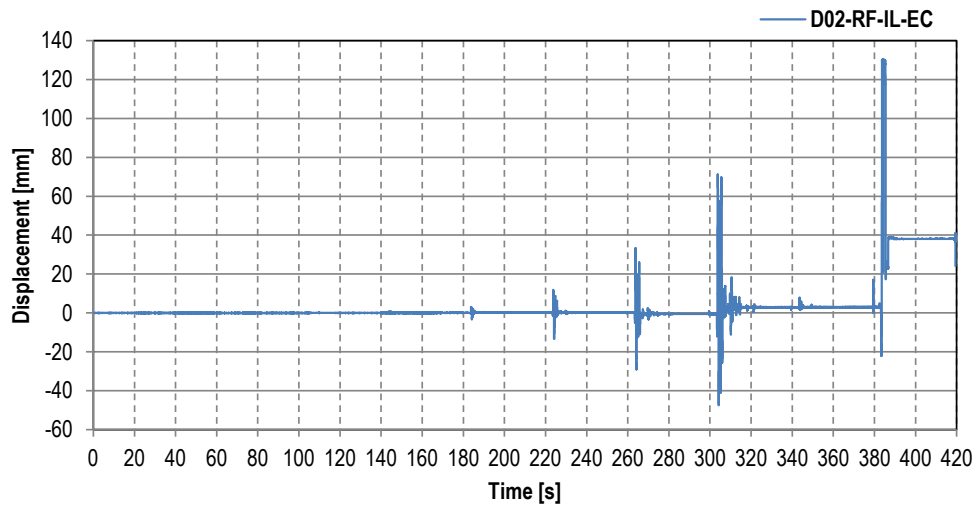


Mode shapes for 9th dynamic identification (after test FEQ2-500%)

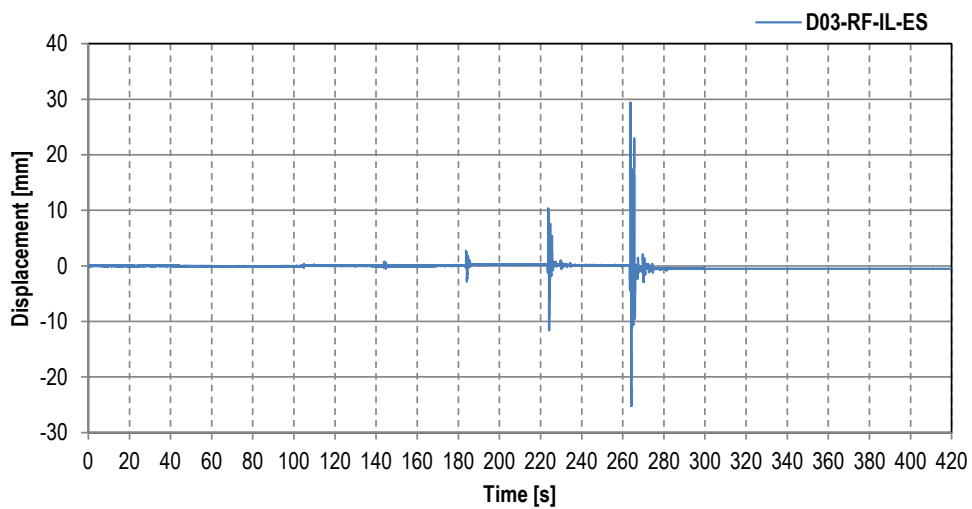
ANNEX II
Cumulative displacements from shake table tests



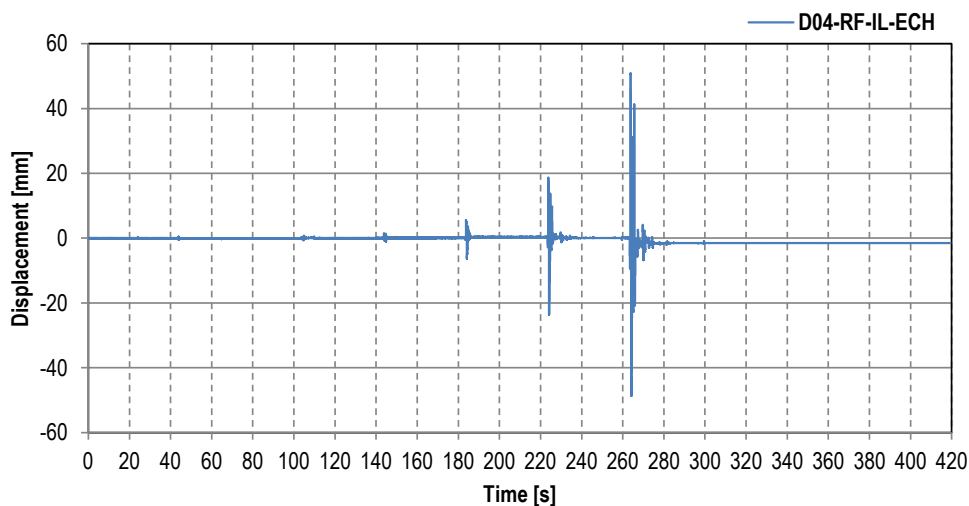
Channel D01-RF-IL-EN – Relative displacement



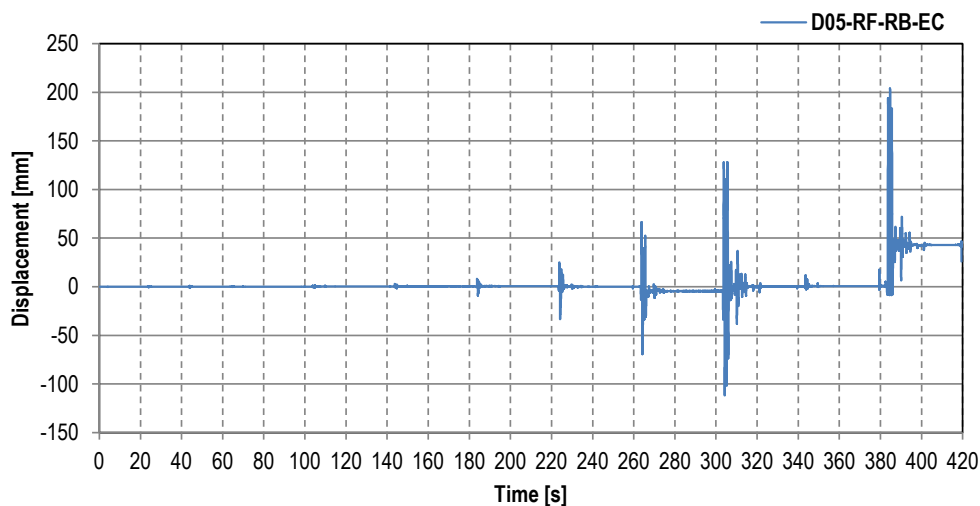
Channel D02-RF-IL-EC – Relative displacement



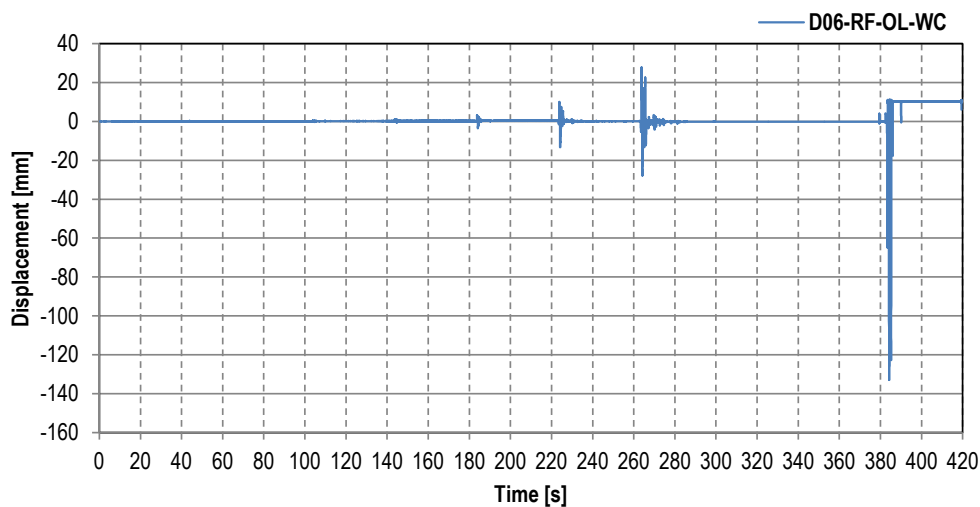
Channel D03-RF-IL-ES – Relative displacement



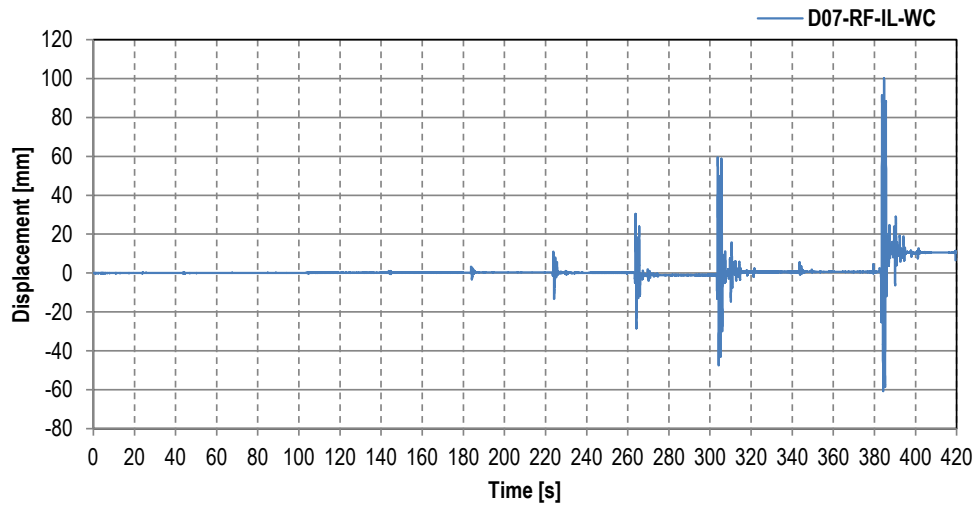
Channel D04-RF-IL-ECH – Relative displacement



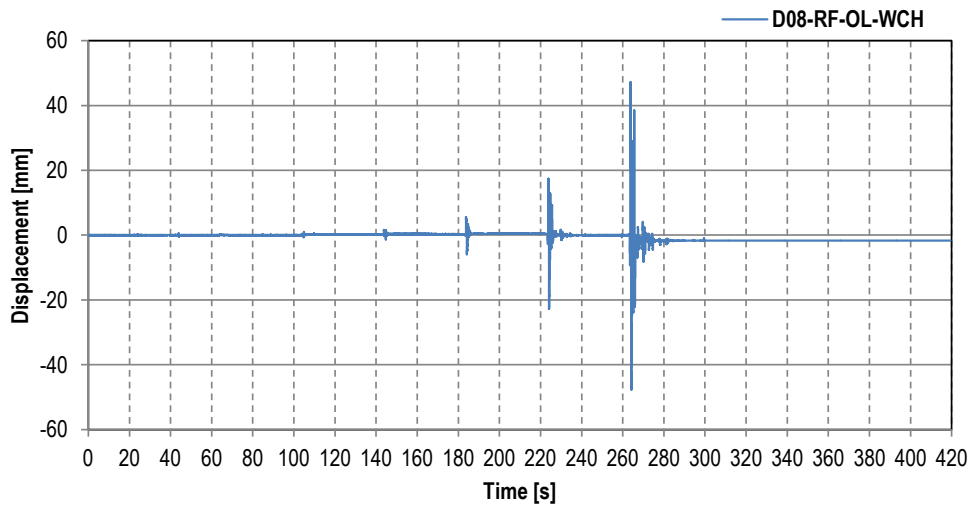
Channel D05-RF-RB-EC – Relative displacement



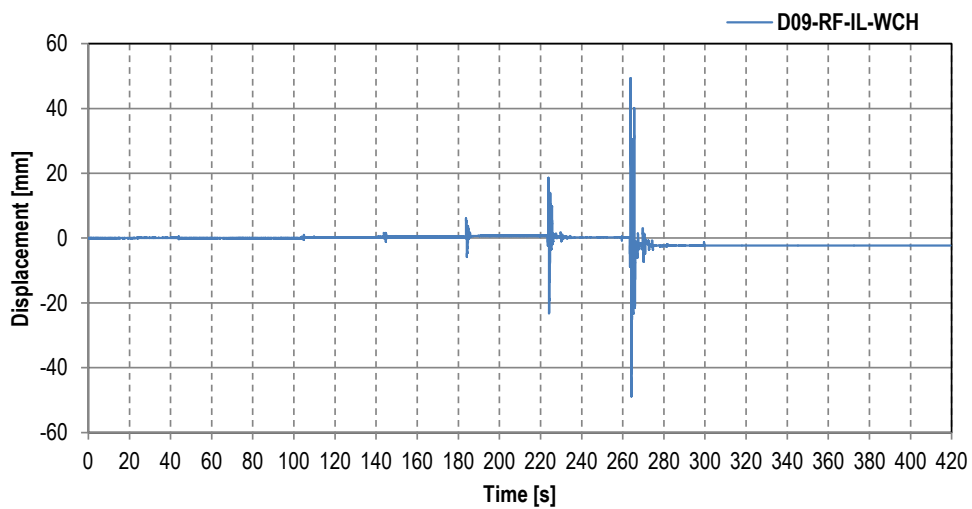
Channel D06-RF-OL-WC – Relative displacement



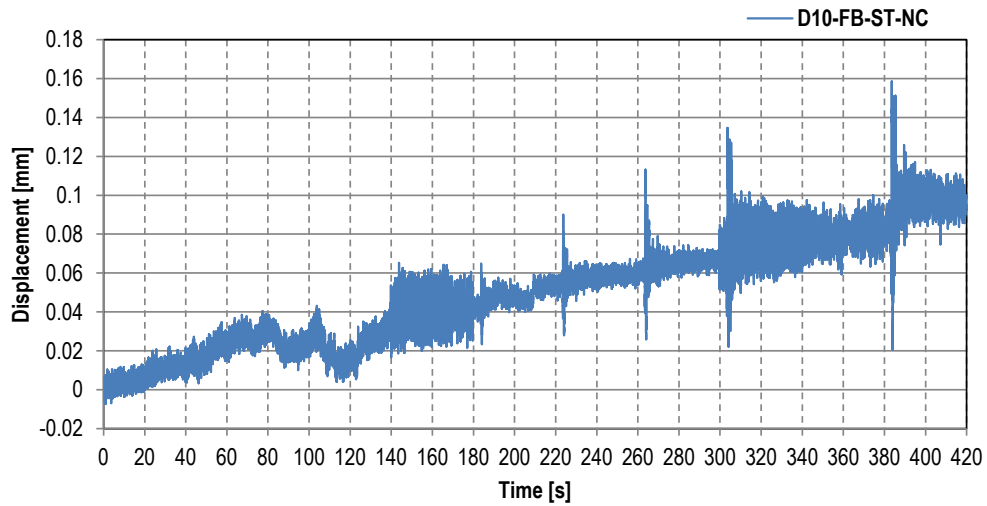
Channel D07-RF-IL-WC – Relative displacement



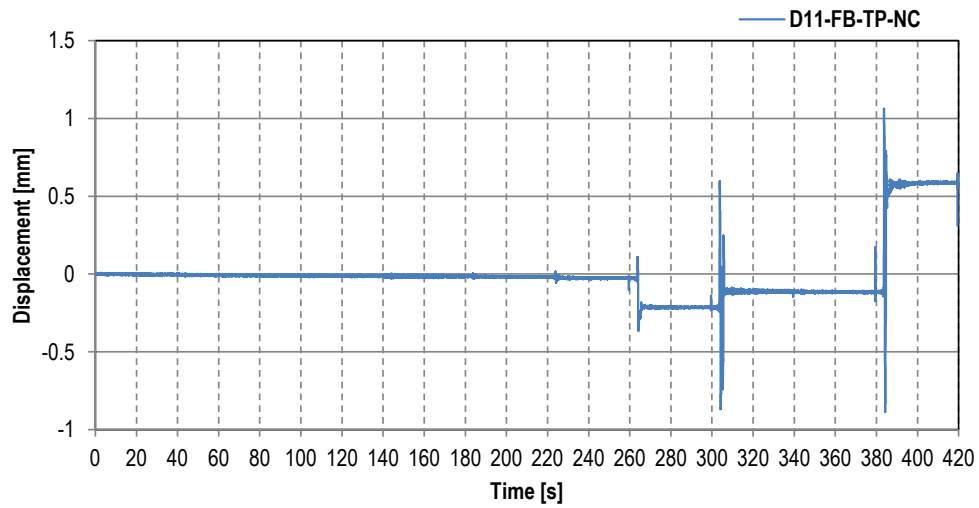
Channel D08-RF-OL-WCH – Relative displacement



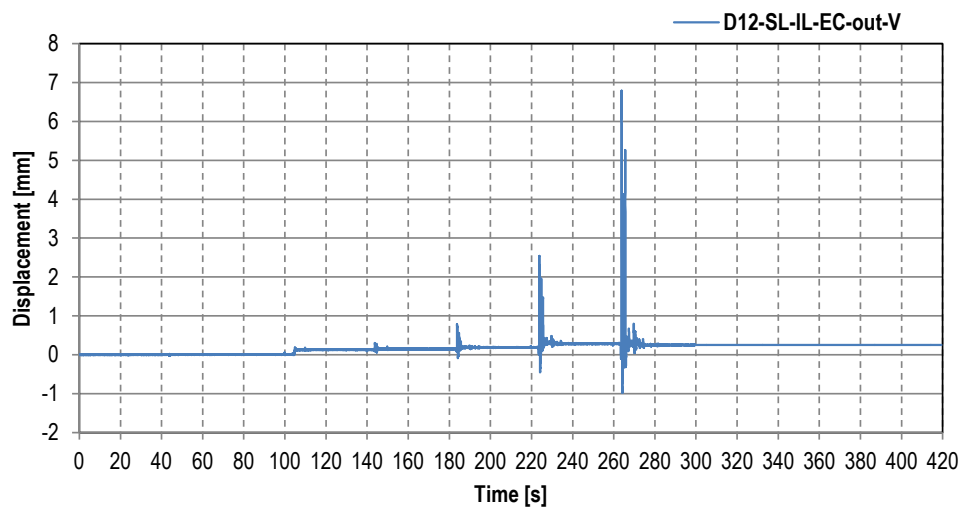
Channel D09- RF-IL-WCH – Relative displacement



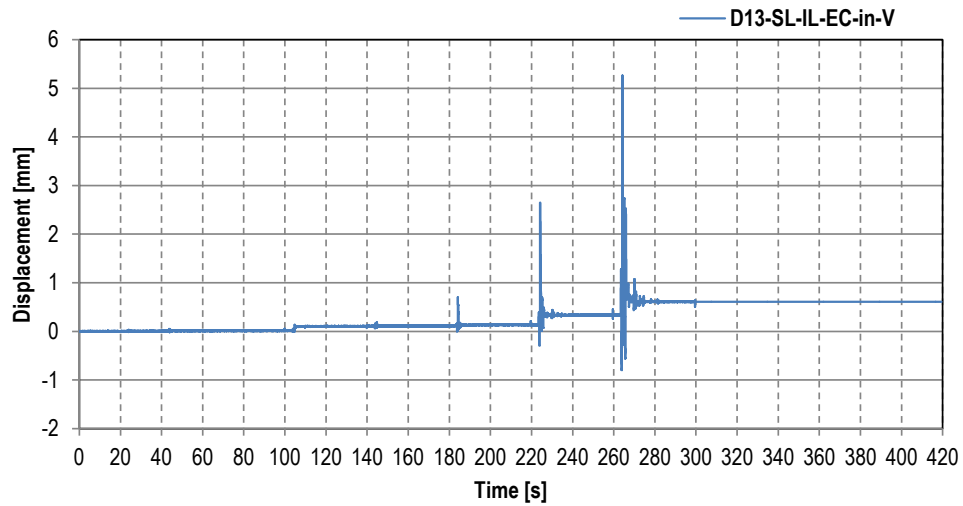
Channel D10-FB-ST-NC – Relative displacement



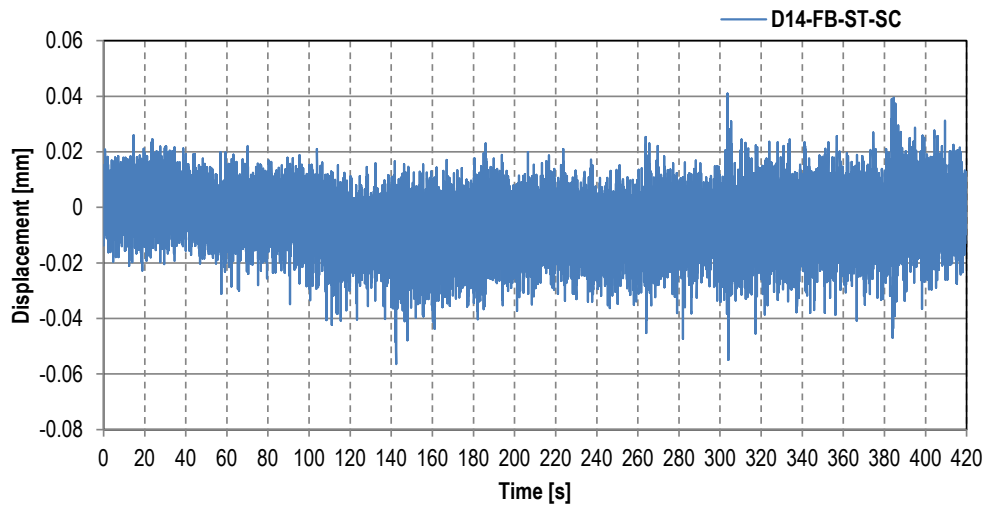
Channel D11-FB-TP-NC – Relative displacement



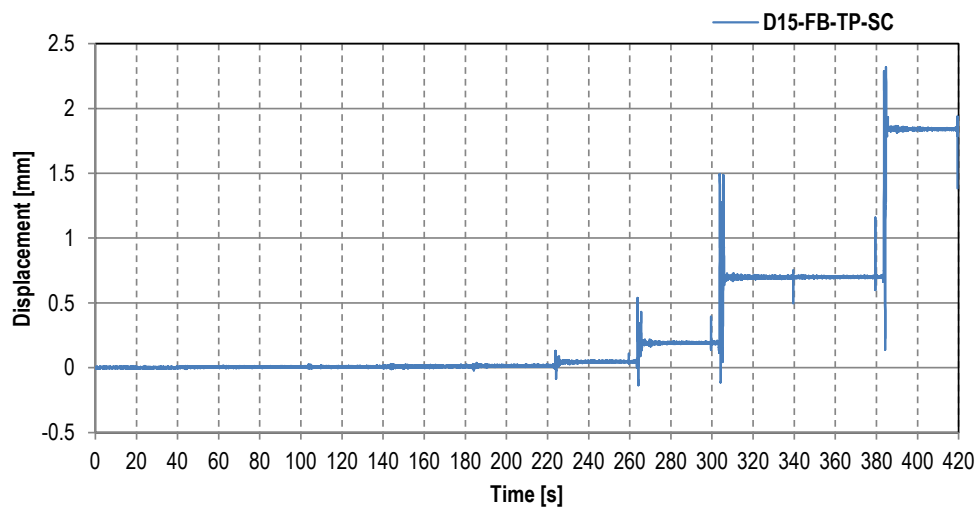
Channel D12-SL-IL-EC-out-V – Relative displacement



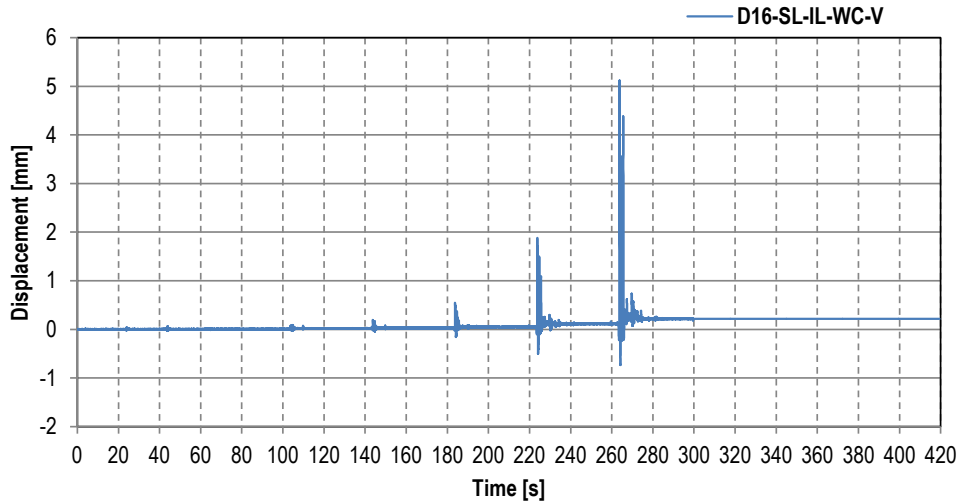
Channel D13-SL-IL-EC-in-V – Relative displacement



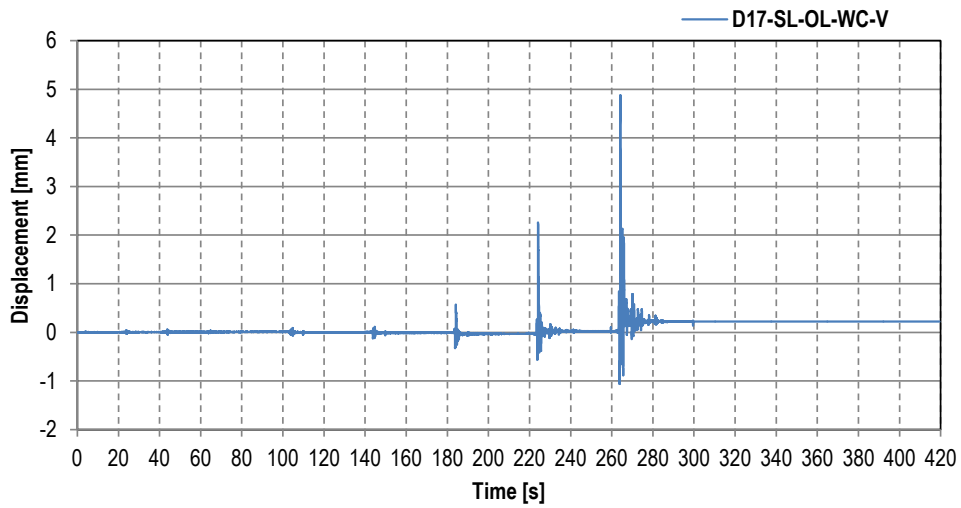
Channel D14-FB-ST-SC – Relative displacement



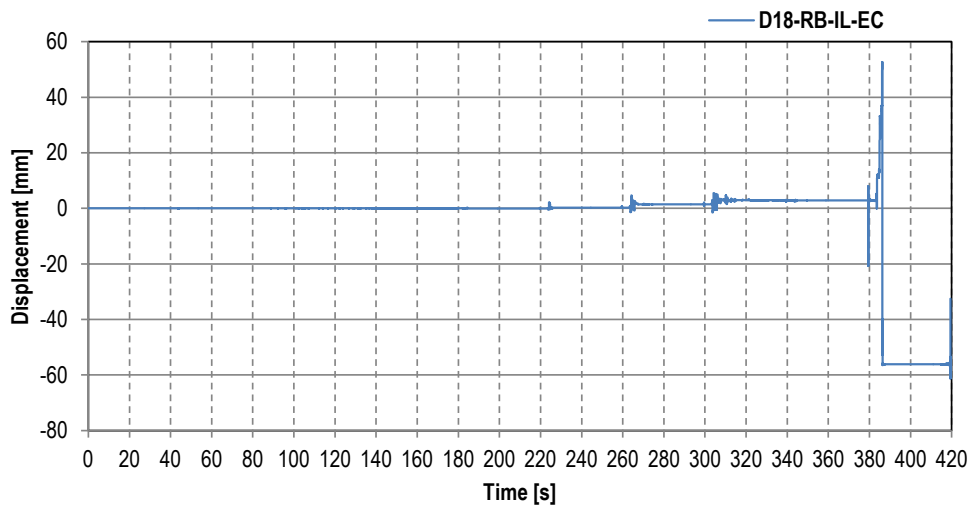
Channel D15-FB-TP-SC – Relative displacement



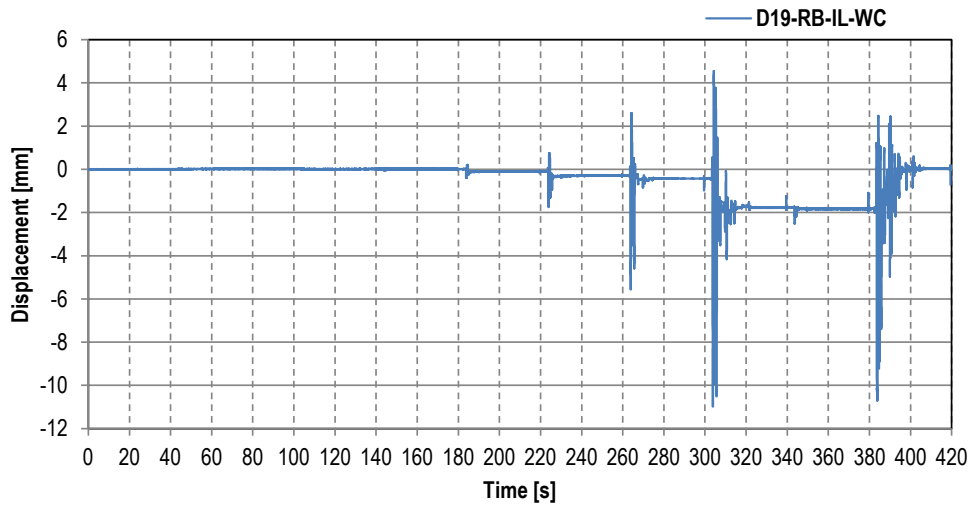
Channel D16-SL-IL-WC-V – Relative displacement



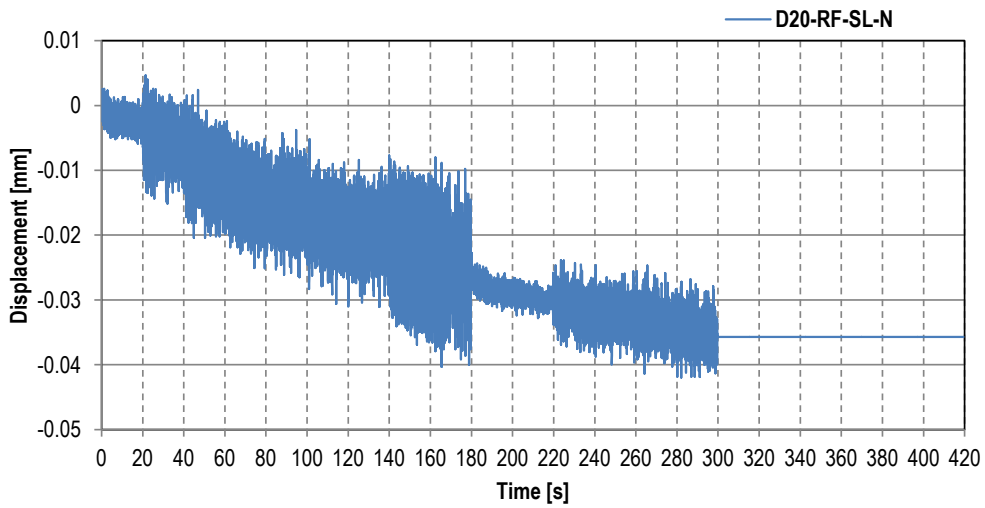
Channel D17-SL-OL-WC-V – Relative displacement



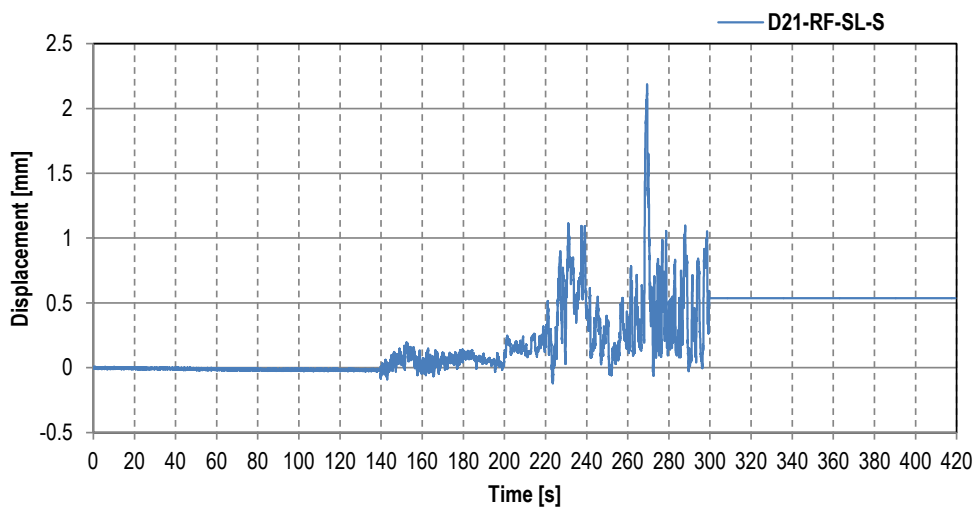
Channel D18-RB-IL-EC – Relative displacement



Channel D19-RB-IL-WC – Relative displacement

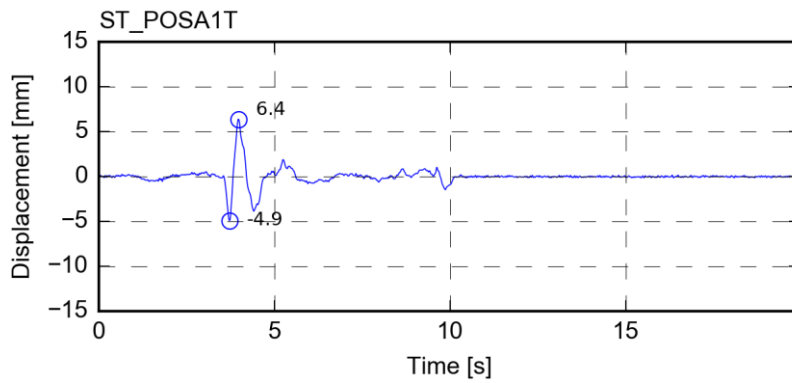


Channel D20-RF-SL-N – Relative displacement

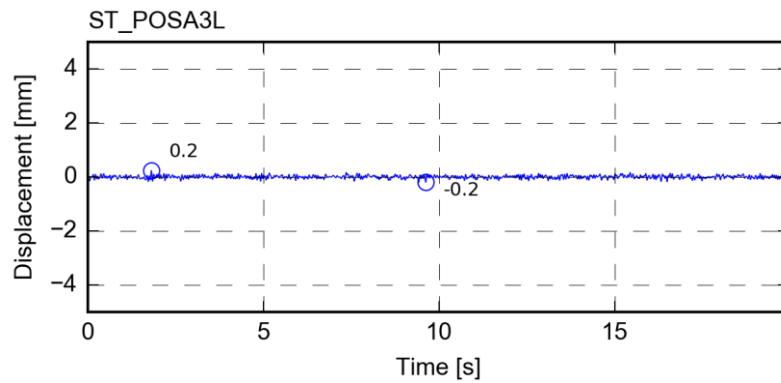


Channel D21-RF-SL-S – Relative displacement

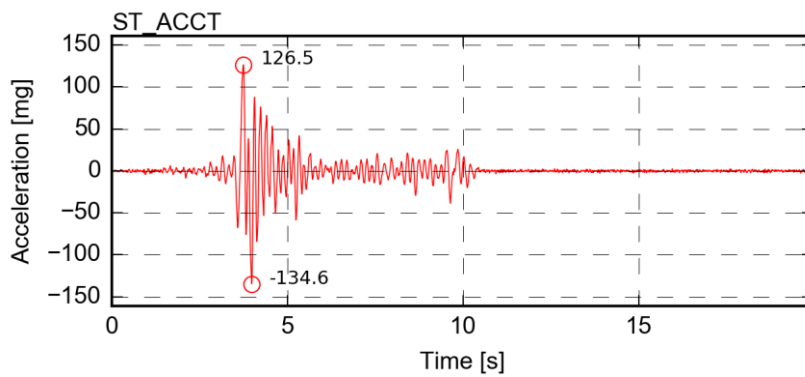
ANNEX III
Transducers' readings for FEQ1-100%



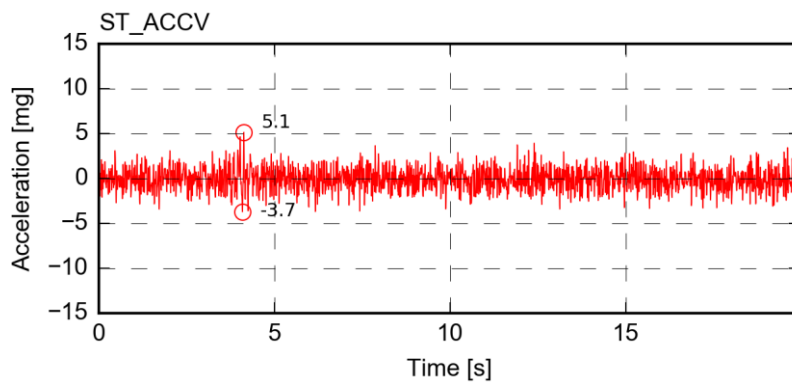
Channel *ST_POS_T* – Transverse displacement of the LNEC 3D shake table motion control



Channel *ST_POS_L* – Vertical displacement of the LNEC 3D shake table motion control

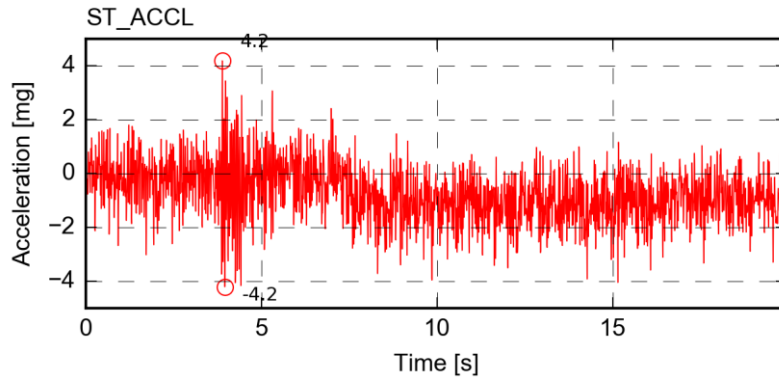


Channel *ST_ACC_T* – Transverse acceleration of the LNEC 3D shake table motion control

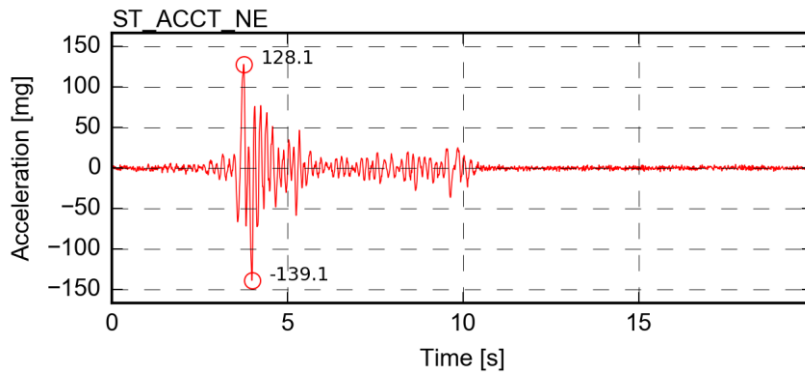


Channel *ST_ACC_L* – Vertical acceleration of the LNEC 3D shake table motion control

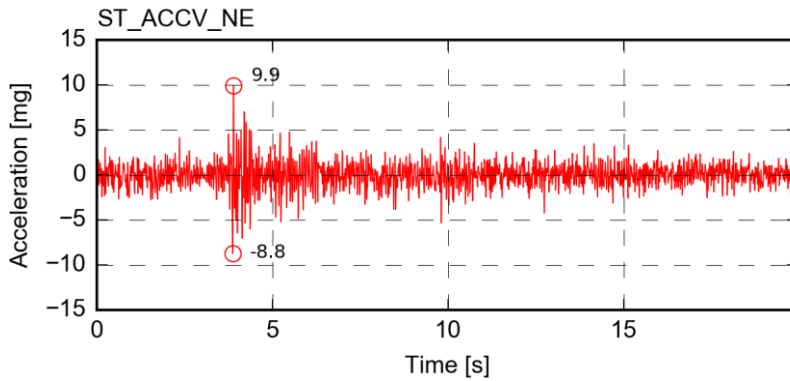
174 *Shake Table Test up to Collapse on a Roof Substructure of a Dutch Terraced House*



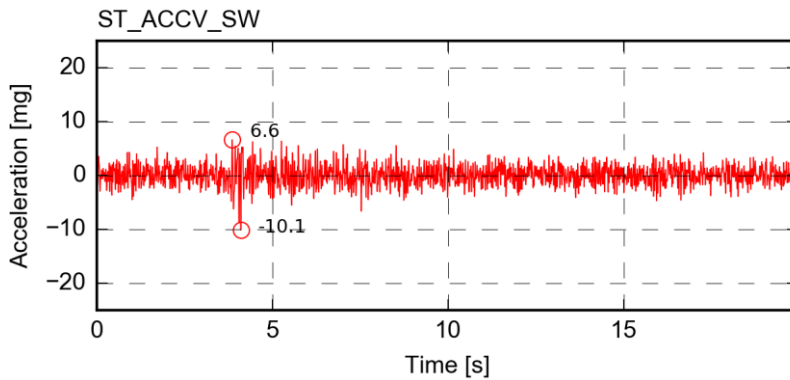
Channel *ST_ACC_V* – Longitudinal acceleration of the LNEC 3D shake table motion control



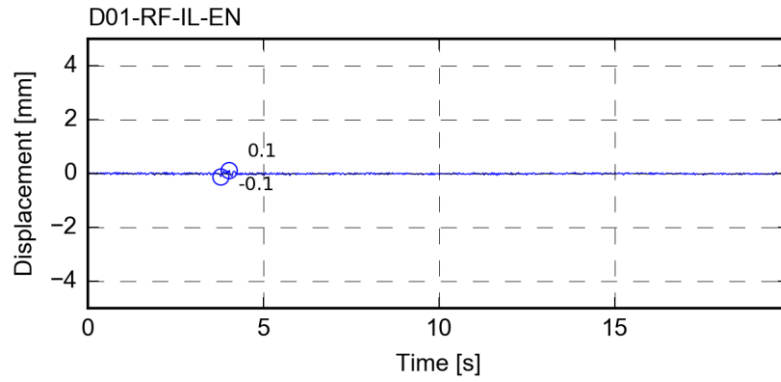
Channel *ST_ACCT_NE* – Transverse acceleration of the North-East LNEC 3D shake table platform



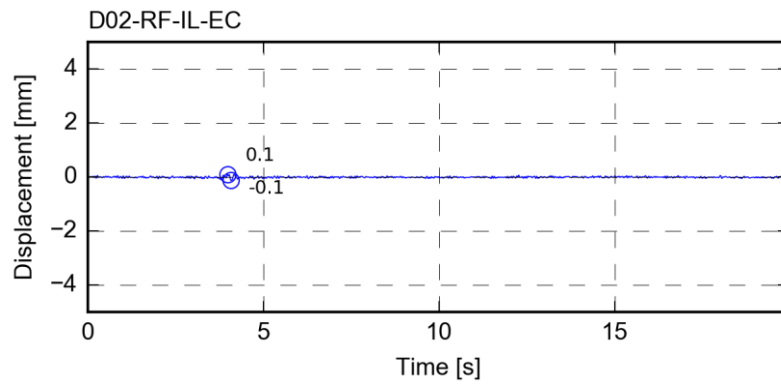
Channel *ST_ACCV_NE* – Vertical acceleration of the North-East LNEC 3D shake table platform



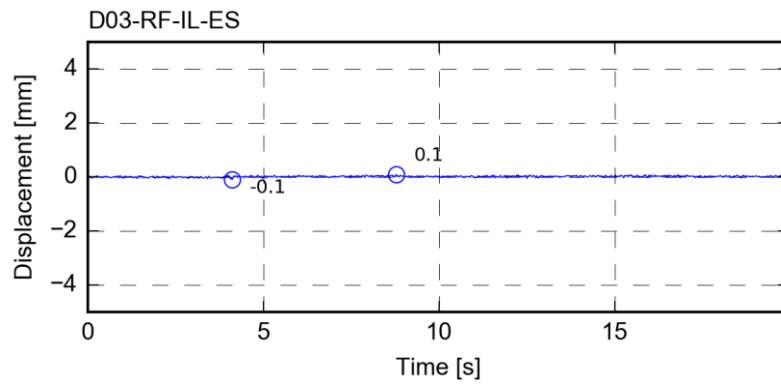
Channel *ST_ACCV_SW* – Vertical acceleration of the South-West LNEC 3D shake table platform



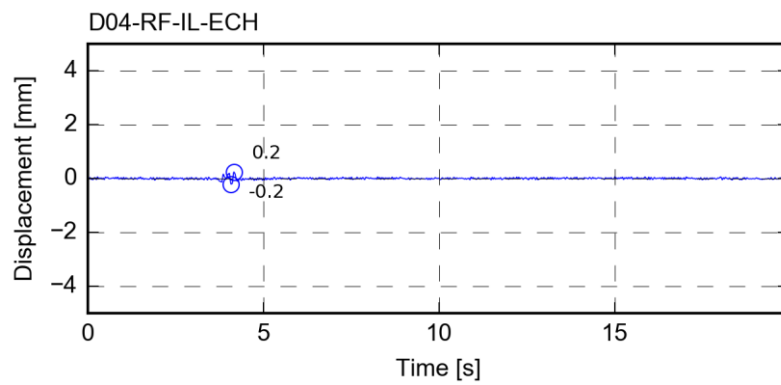
Channel D01-RF-IL-EN– displacement



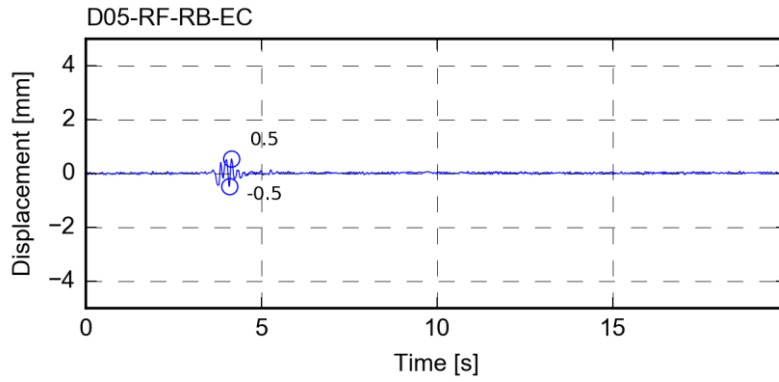
Channel D02-RF-IL-EC– displacement



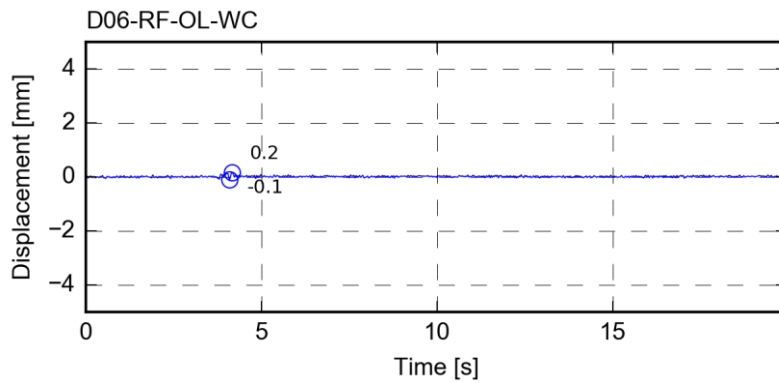
Channel D03-RF-IL-ES – displacement



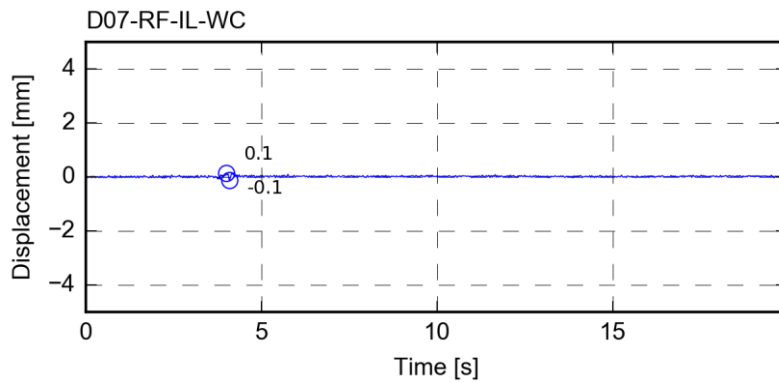
Channel D04-RF-IL-ECH – displacement



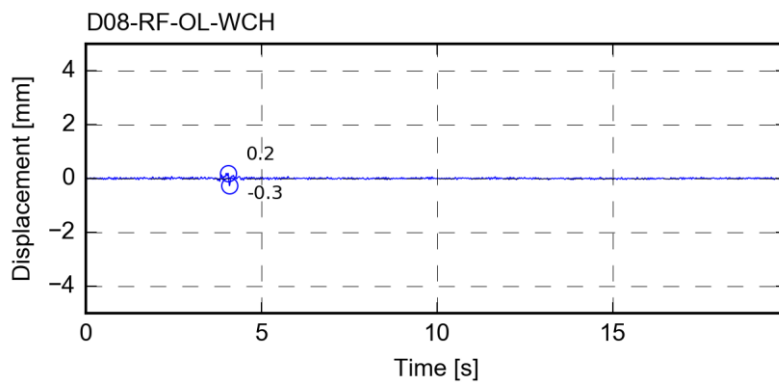
Channel D05-RF-RB-EC – displacement



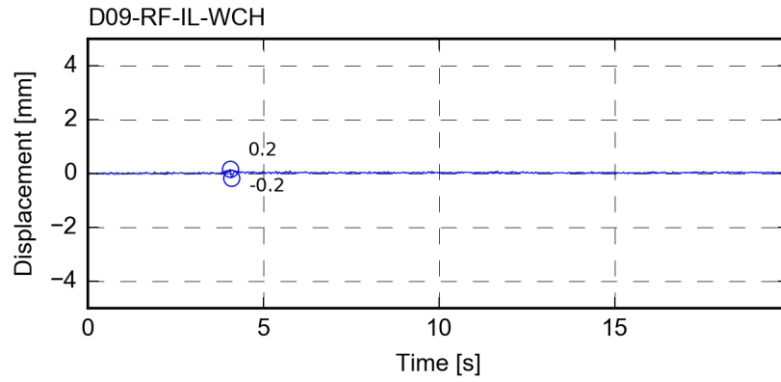
Channel D06-RF-OL-WC – displacement



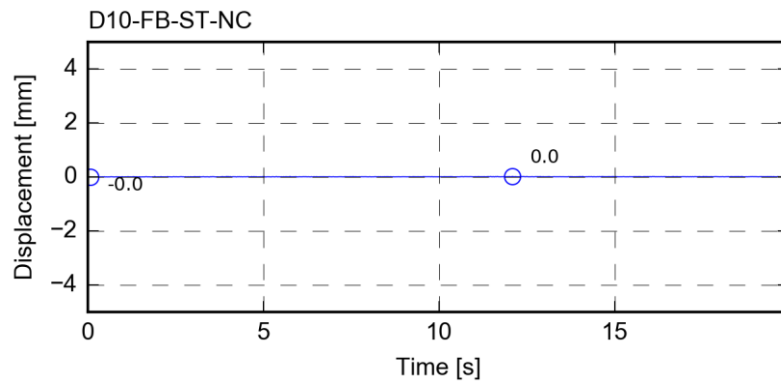
Channel D07-RF-IL-WC – displacement



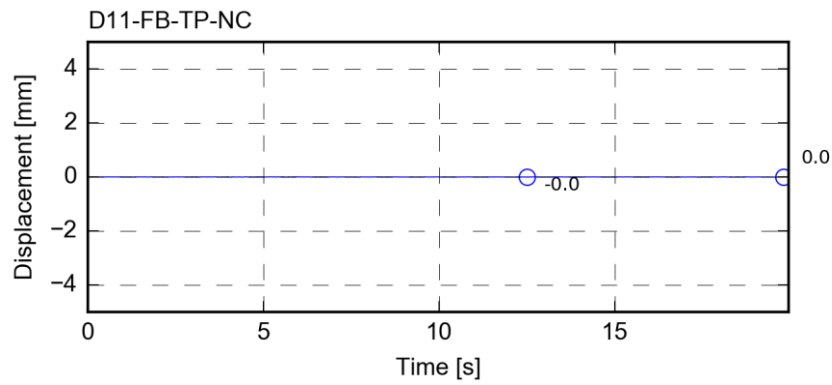
Channel D08-RF-OL-WCH – displacement



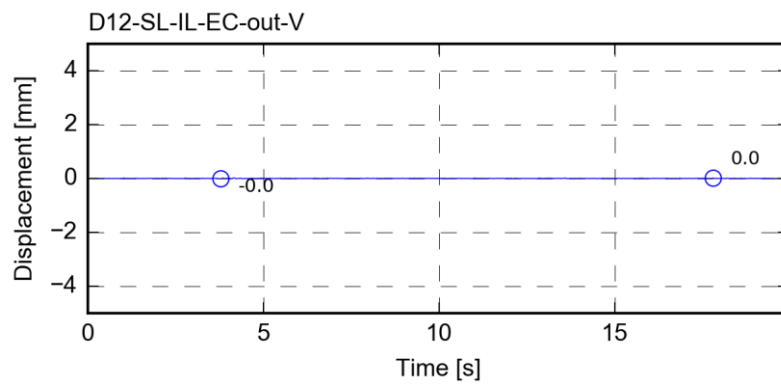
Channel D09-RF-IL-WCH – displacement



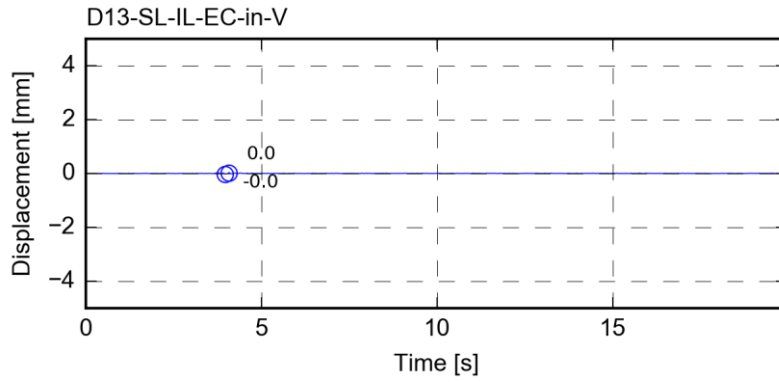
Channel D10-FB-ST-NC – displacement



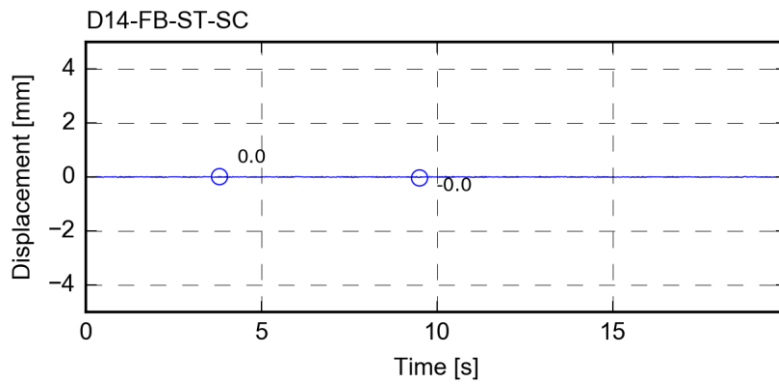
Channel D11-FB-TP-NC – displacement



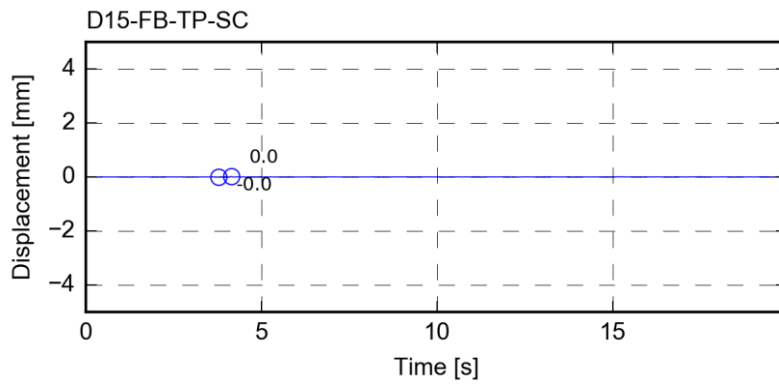
Channel D12-SL-IL-EC-out-V – displacement



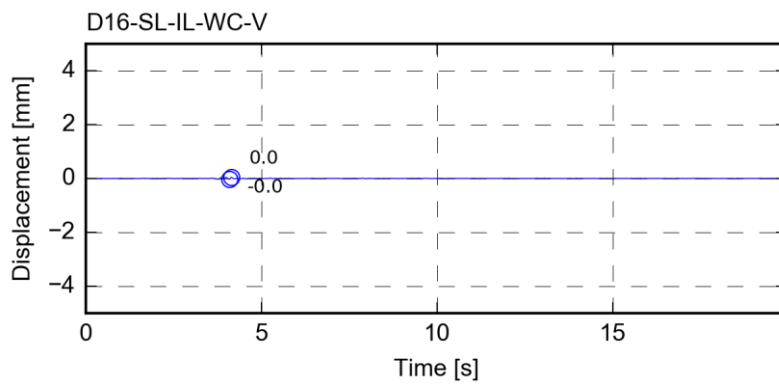
Channel D13-SL-IL-EC-in-V – displacement



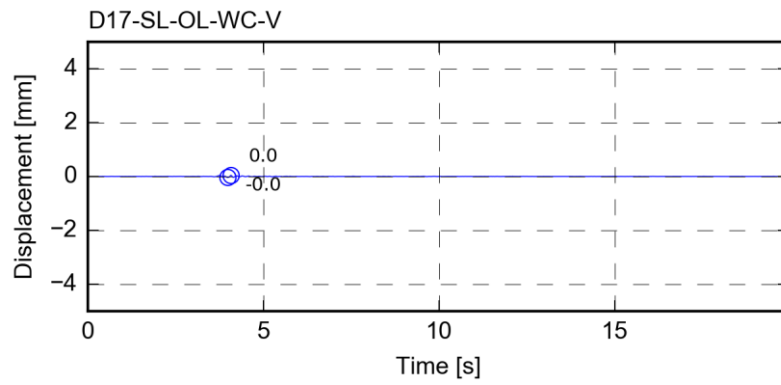
Channel D14-FB-ST-SC – displacement



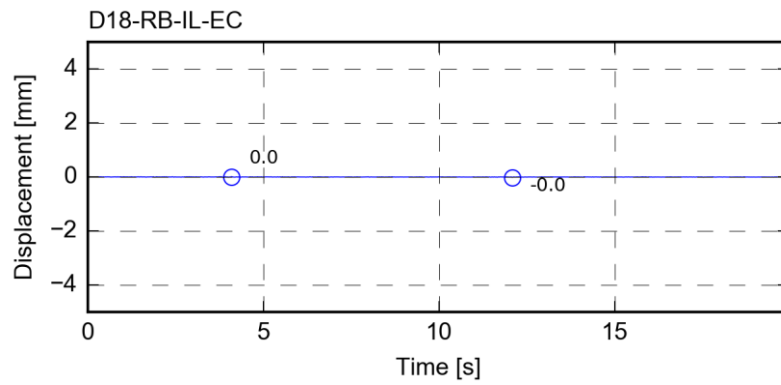
Channel D15-FB-TP-SC – displacement



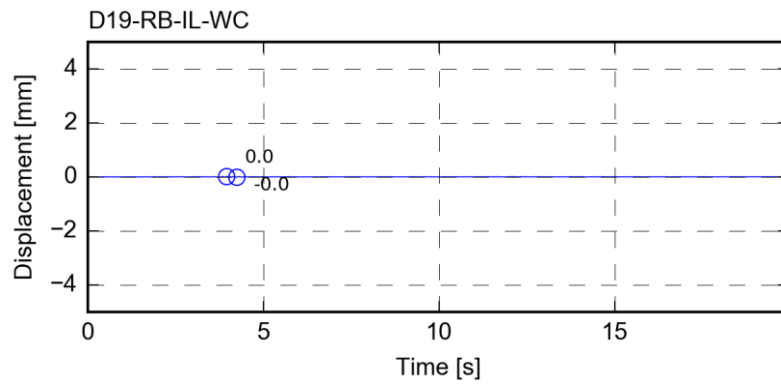
Channel D16-SL-IL-WC-V – displacement



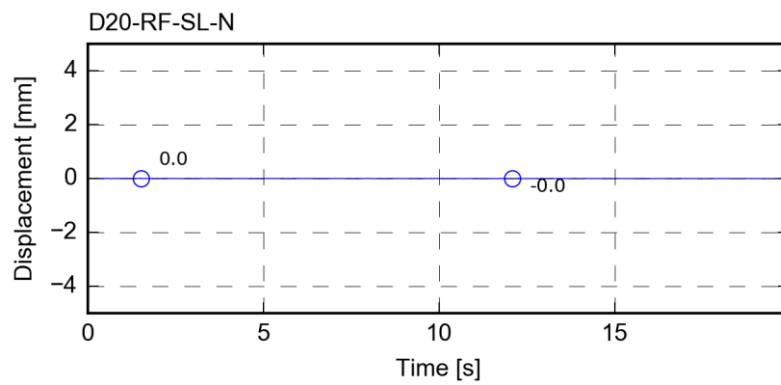
Channel D17-SL-OL-WC-V – displacement



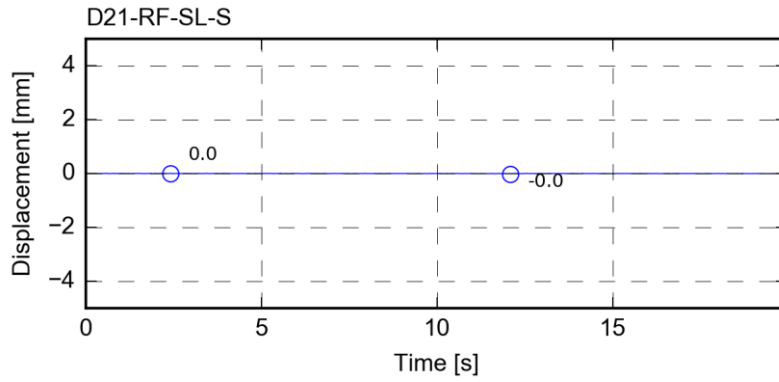
Channel D18-RB-IL-EC – displacement



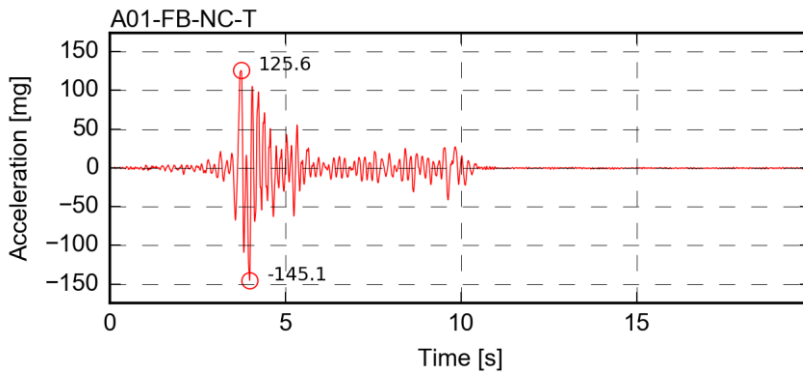
Channel D19-RB-IL-WC – displacement



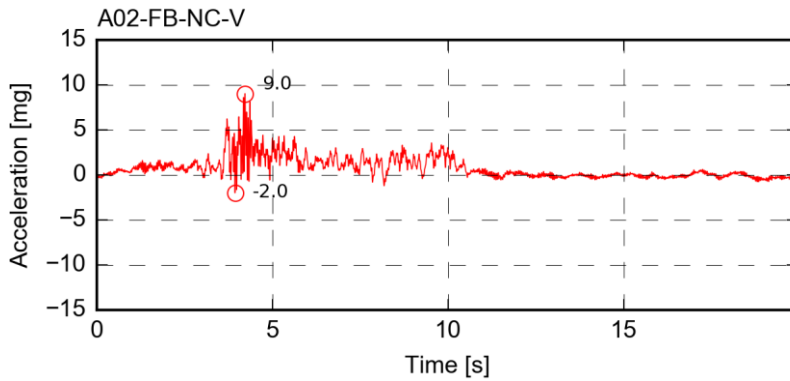
Channel D20-RF-SL-N – displacement



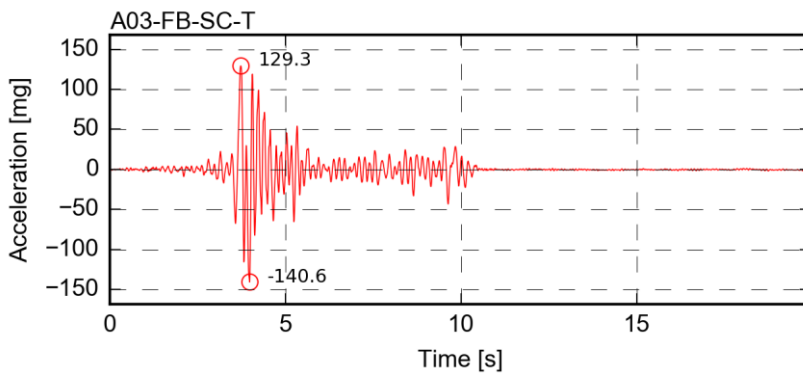
Channel D21-RF-SL-S – displacement



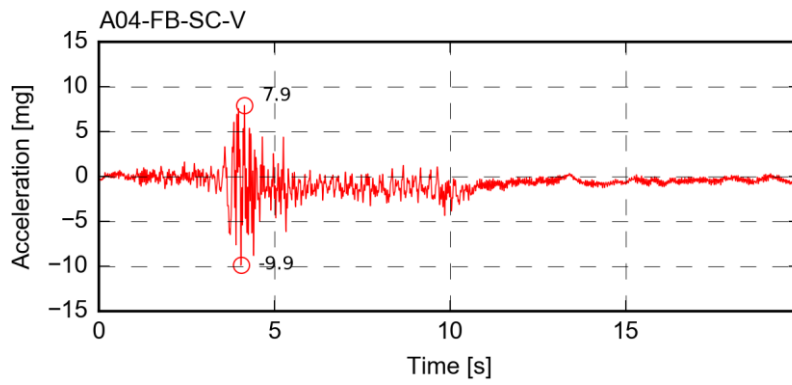
Channel A01-FB-NC-T – acceleration



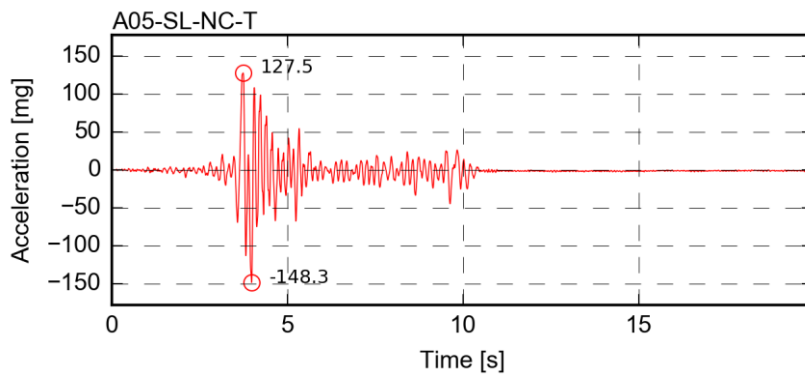
Channel A02-FB-NC-V – acceleration



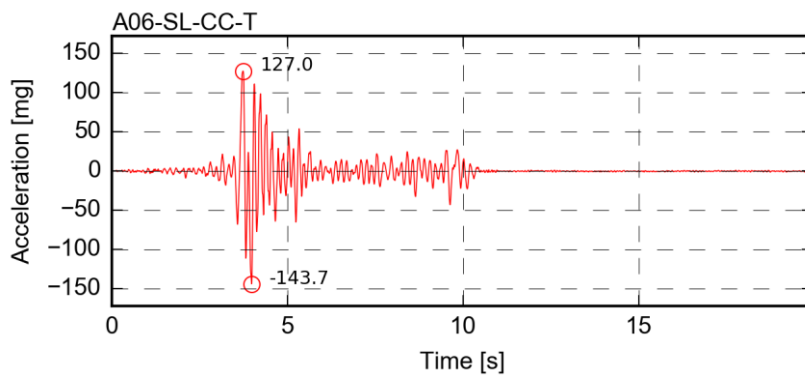
Channel A03-FB-SC-T – acceleration



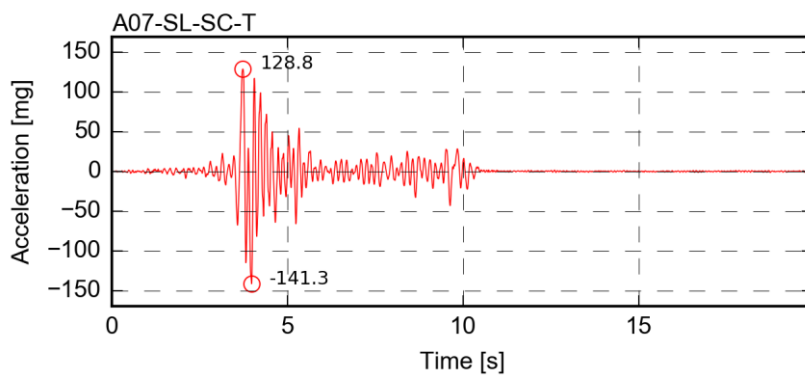
Channel A04-FB-SC-V – acceleration



Channel A05-SL-NC-T – acceleration

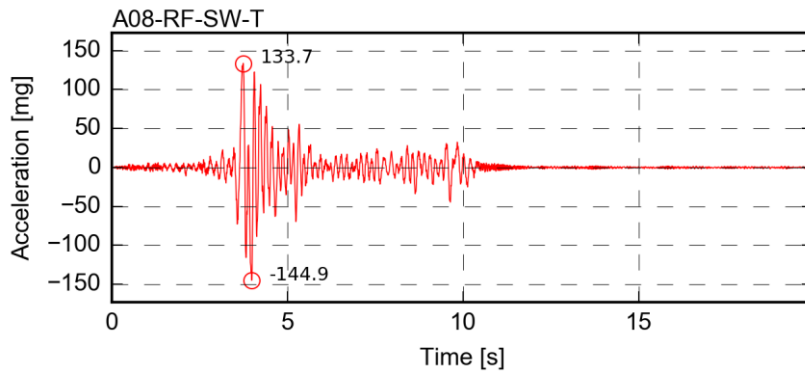


Channel A06-SL-CC-T – acceleration

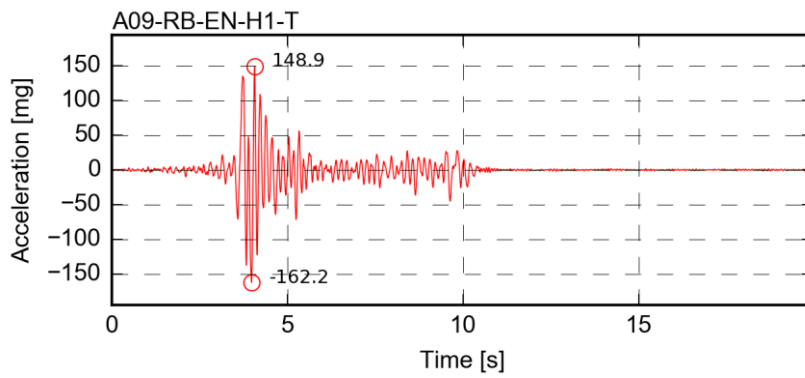


Channel A07-SL-SC-T – acceleration

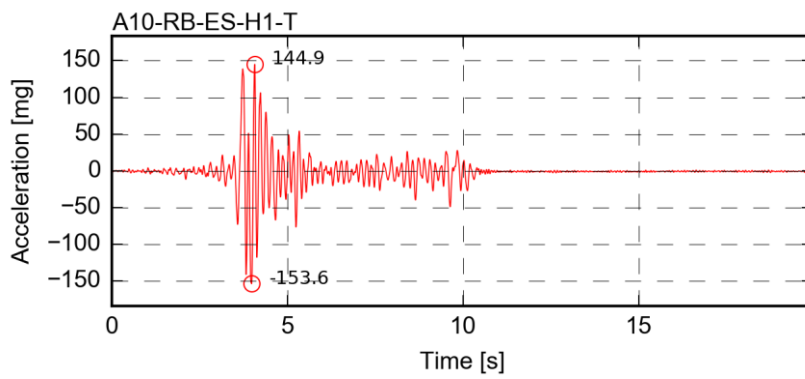
182 Shake Table Test up to Collapse on a Roof Substructure of a Dutch Terraced House



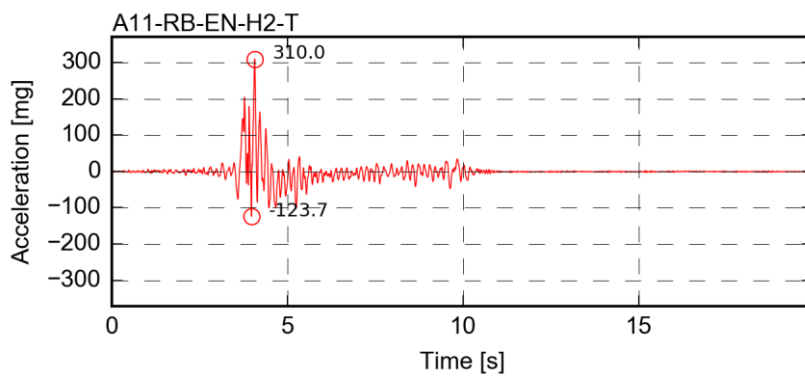
Channel A08-RF-SW-T – acceleration



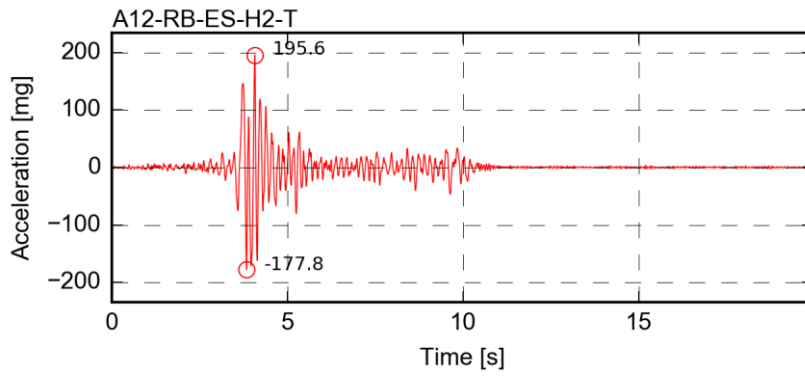
Channel A09-RB-EN-H1-T – acceleration



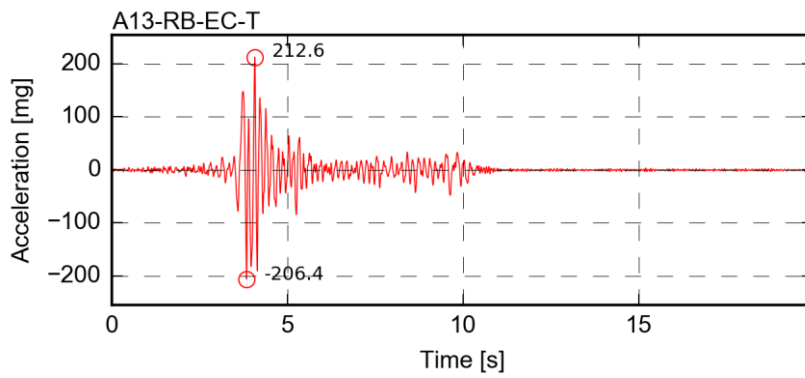
Channel A10-RB-ES-H1-T – acceleration



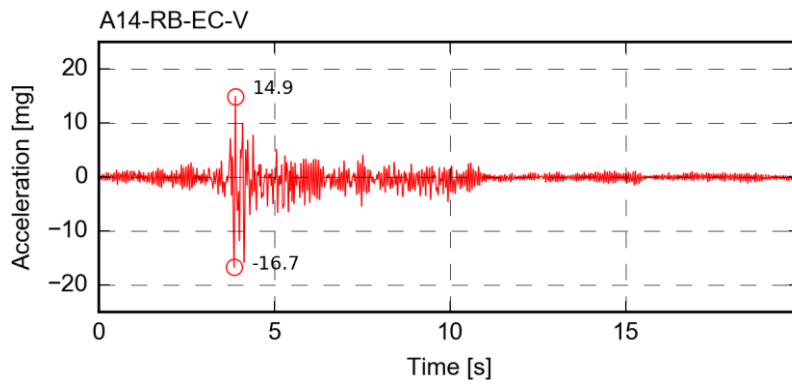
Channel A11-RB-EN-H2-T – acceleration



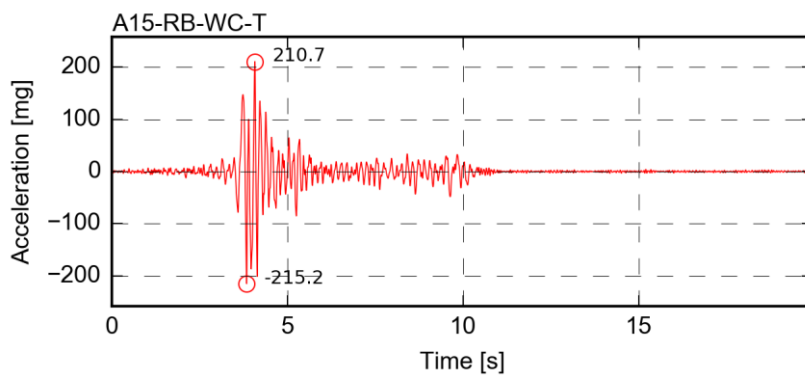
Channel A12-RB-ES-H2-T – acceleration



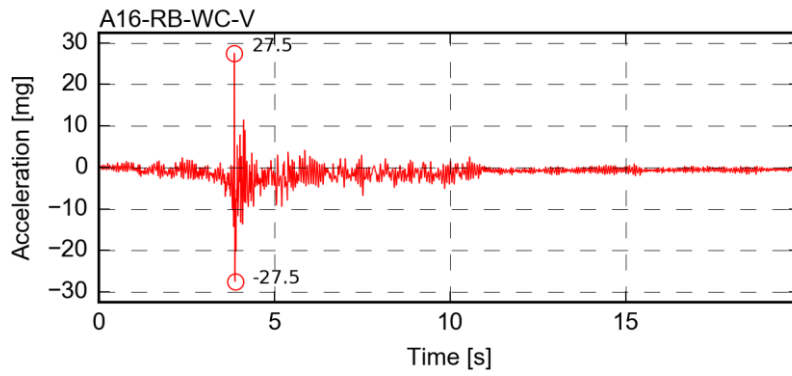
Channel A13-RB-EC-T – acceleration



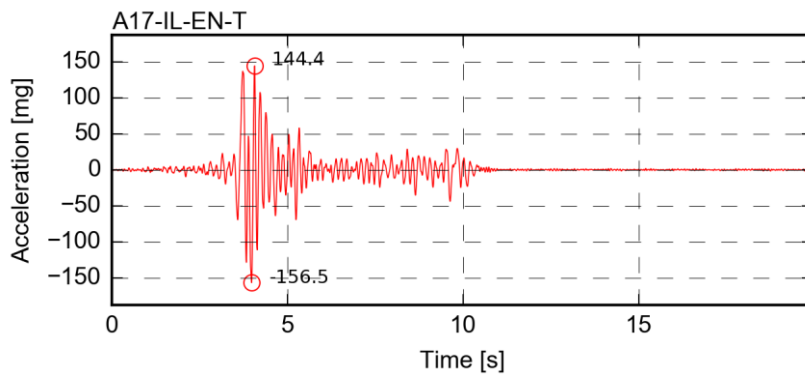
Channel A14-RB-EC-V – acceleration



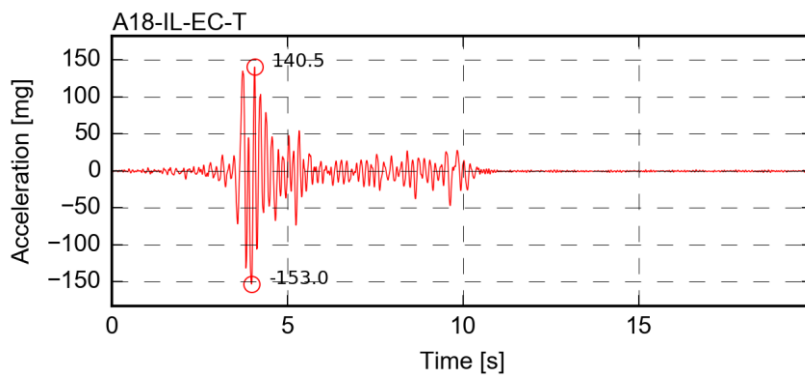
Channel A15-RB-WC-T – acceleration



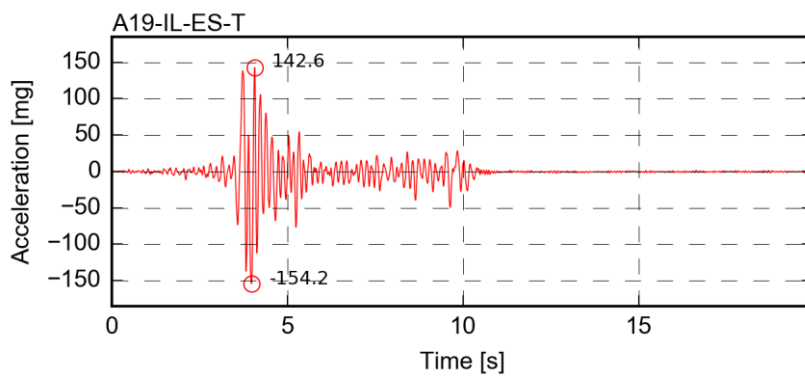
Channel A16-RB-WC-V – acceleration



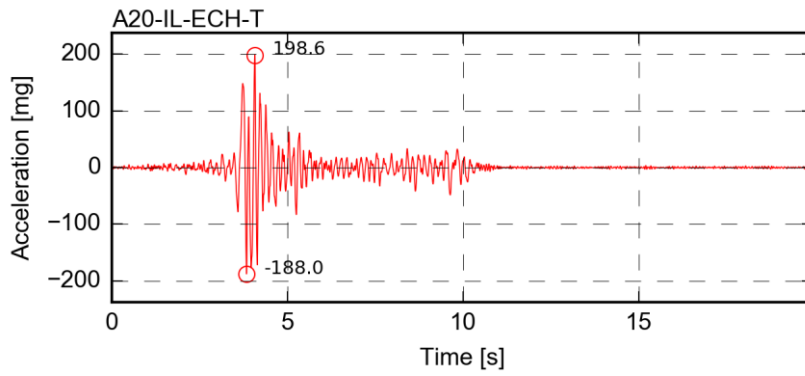
Channel A17-IL-EN-T – acceleration



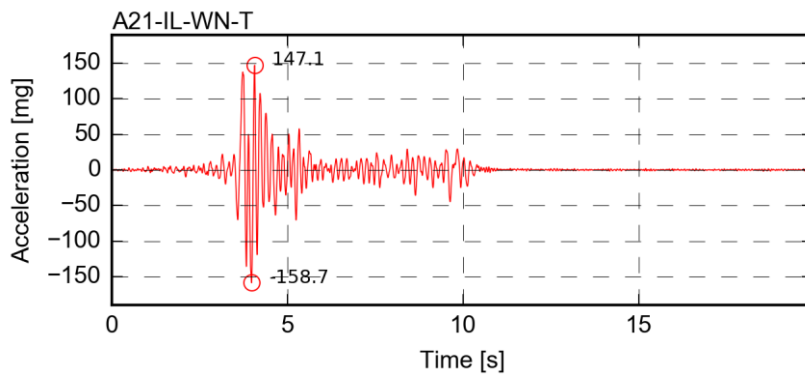
Channel A18-IL-EC-T – acceleration



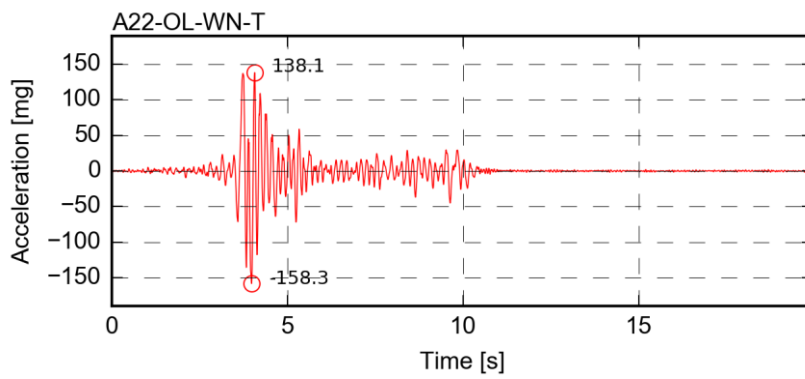
Channel A19-IL-ES-T – acceleration



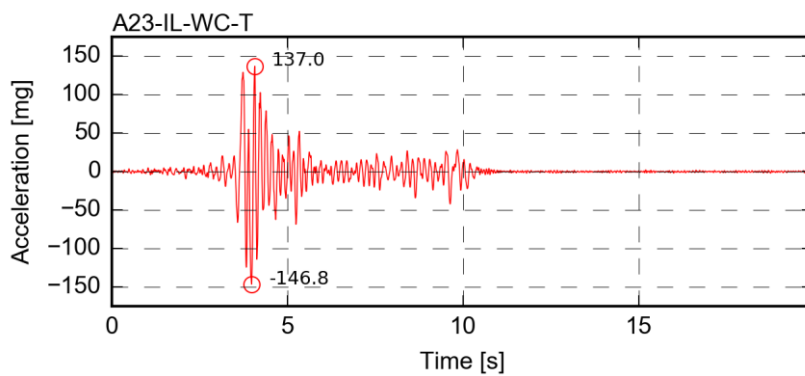
Channel A20-IL-ECH-T – acceleration



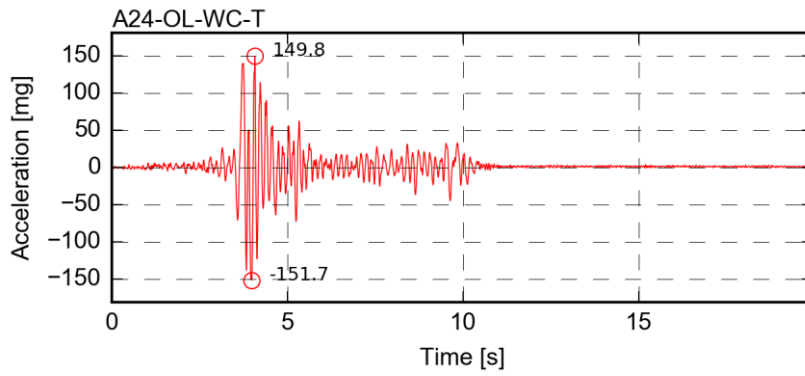
Channel A21-IL-WN-T – acceleration



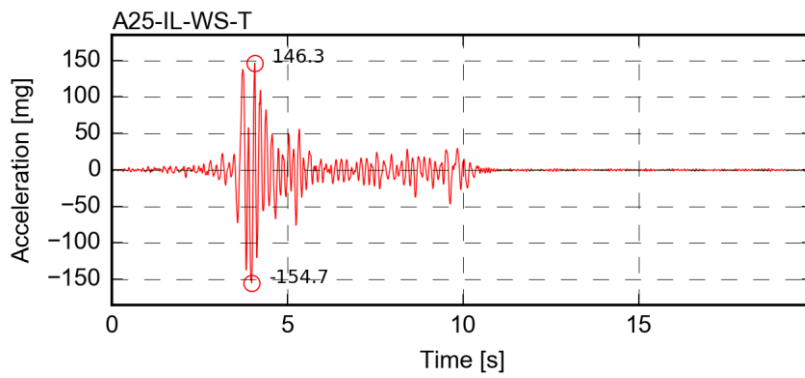
Channel A22-OL-WN-T – acceleration



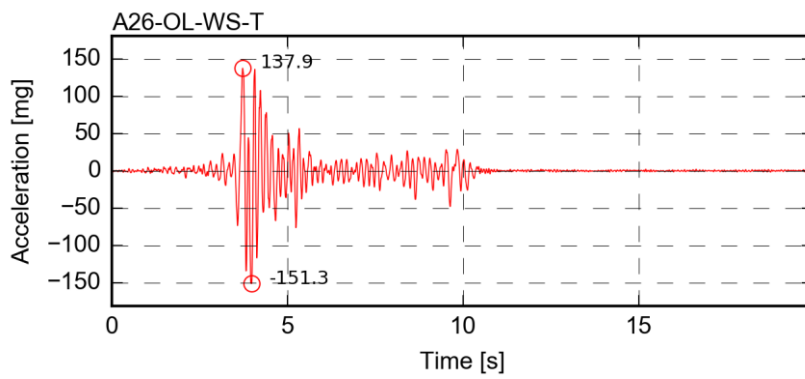
Channel A23-IL-WC-T – acceleration



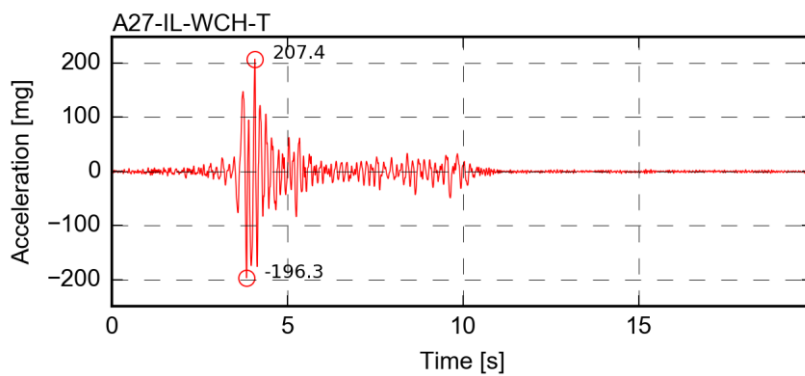
Channel A24-OL-WC-T – acceleration



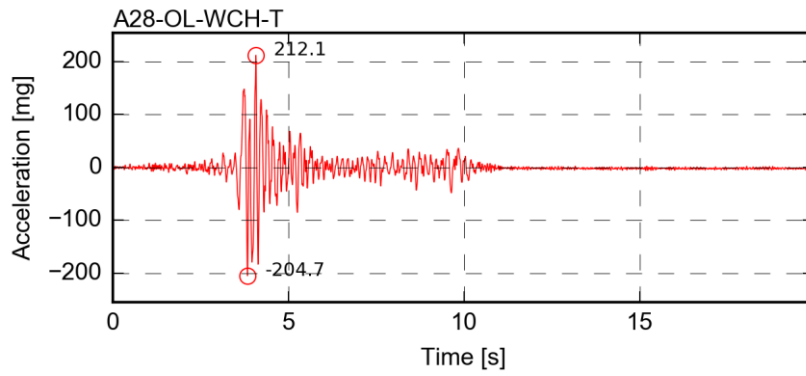
Channel A25-IL-WS-T – acceleration



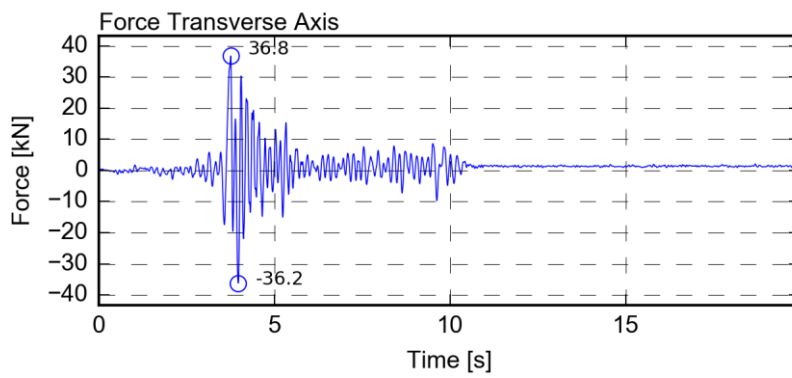
Channel A26-OL-WS-T – acceleration



Channel A27-IL-WCH-T – acceleration

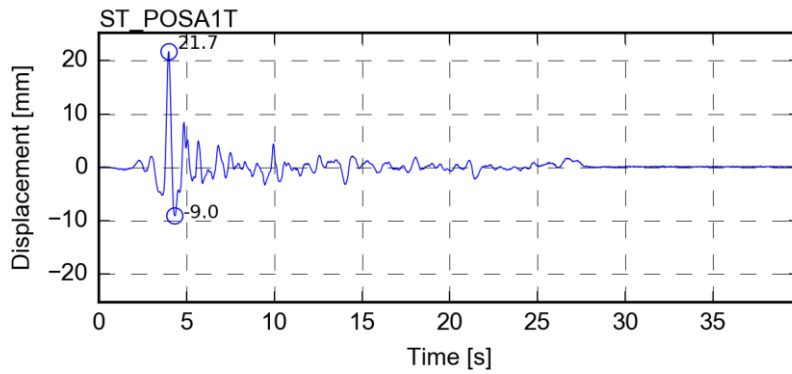


Channel A28-OL-WCH-T – acceleration

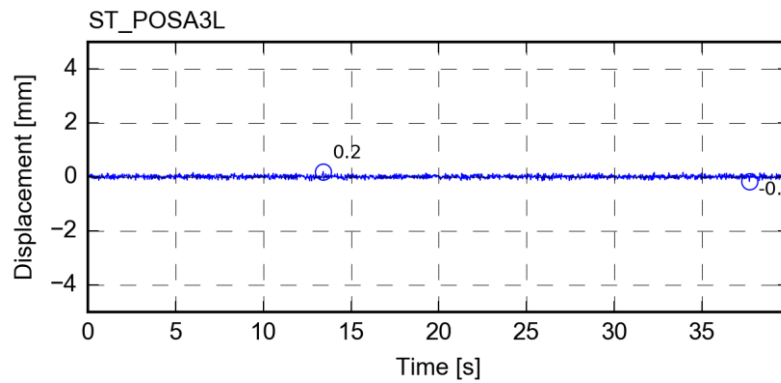


Channel Force Transverse Axis – Force

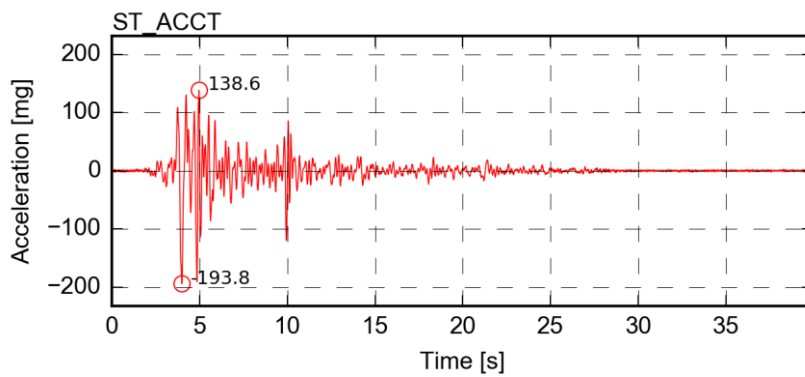
ANNEX IV
Transducers' readings for FEQ2-100%



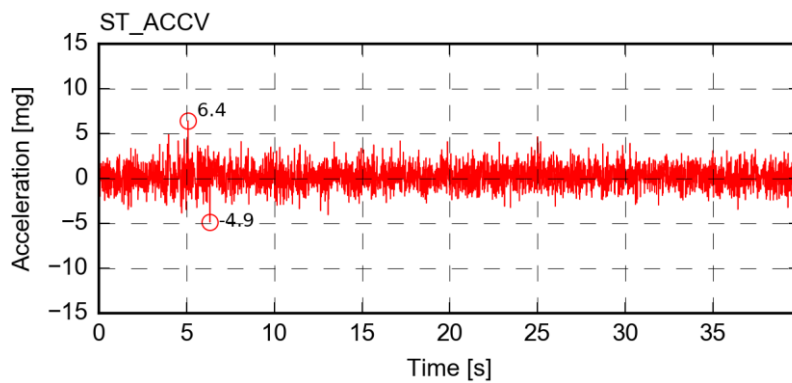
Channel ST_POS_T – Transverse displacement of the LNEC 3D shake table motion control



Channel ST_POS_L – Vertical displacement of the LNEC 3D shake table motion control

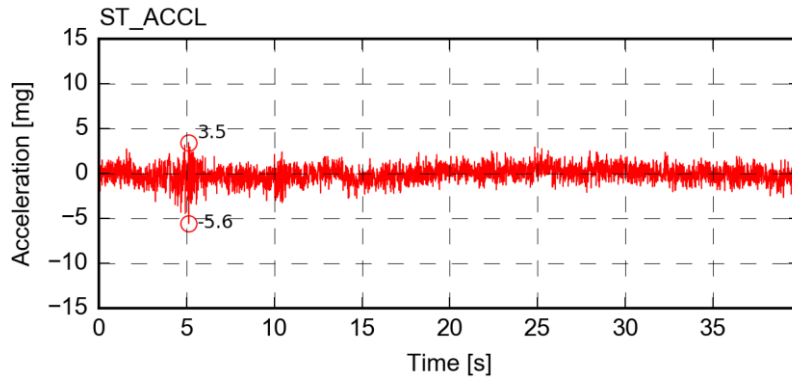


Channel ST_ACC_T – Transverse acceleration of the LNEC 3D shake table motion control

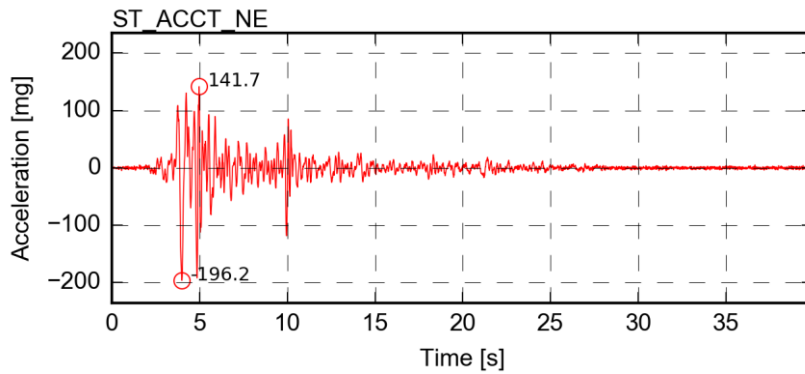


Channel ST_ACC_L – Vertical acceleration of the LNEC 3D shake table motion control

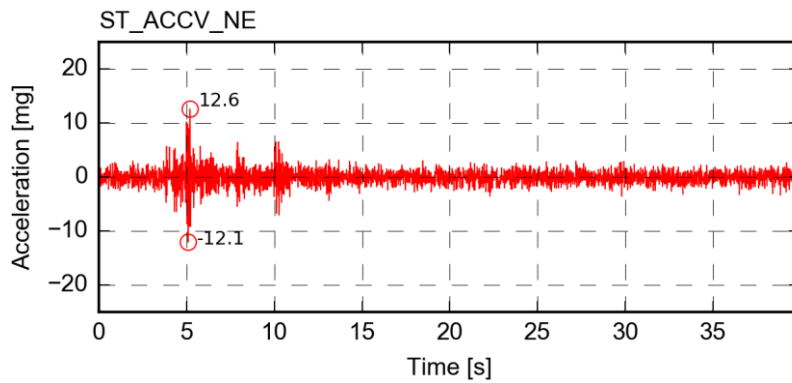
192 *Shake Table Test up to Collapse on a Roof Substructure of a Dutch Terraced House*



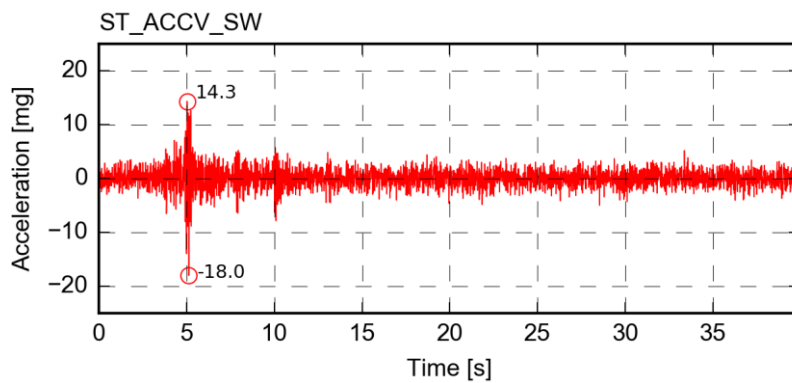
Channel ST_ACC_V – Longitudinal acceleration of the LNEC 3D shake table motion control



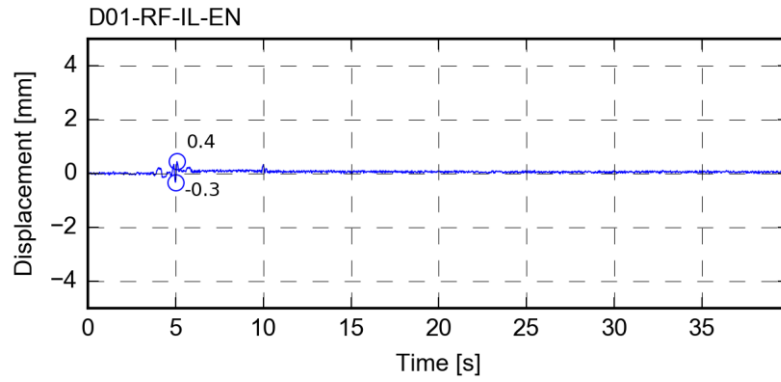
Channel ST_ACCT_NE – Transverse acceleration of the North-East LNEC 3D shake table platform



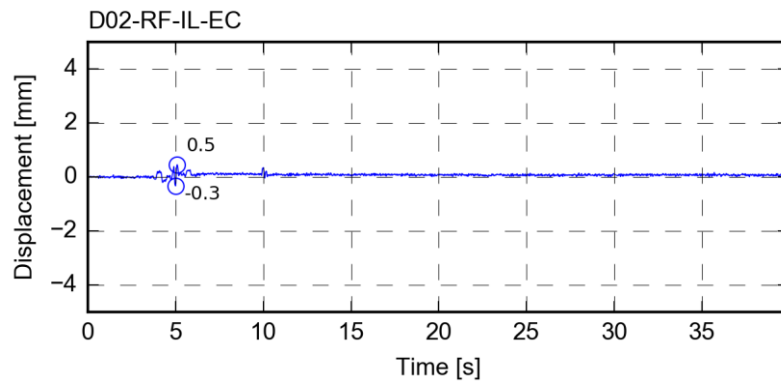
Channel ST_ACCV_NE – Vertical acceleration of the North-East LNEC 3D shake table platform



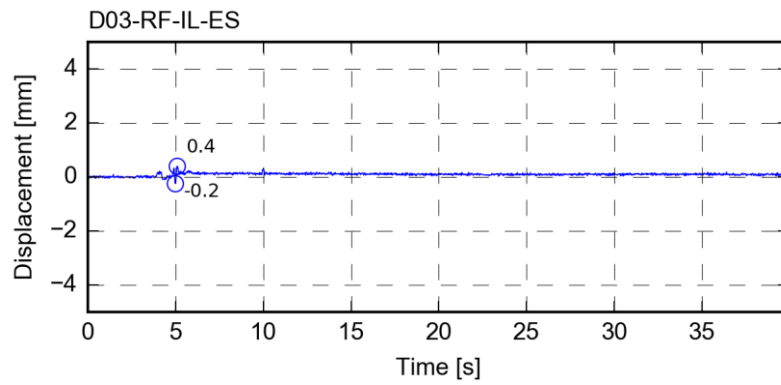
Channel ST_ACCV_SW – Vertical acceleration of the South-West LNEC 3D shake table platform



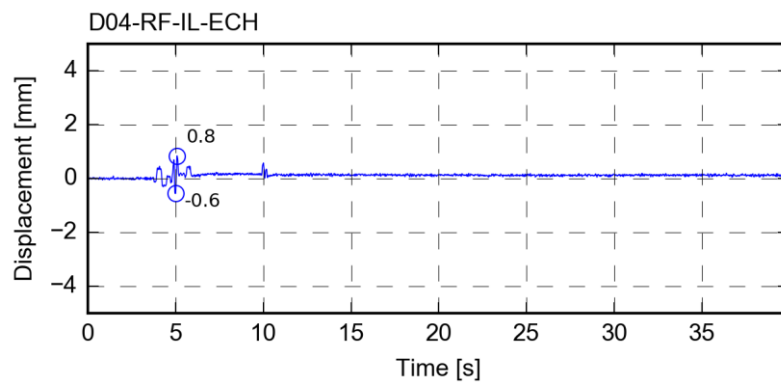
Channel D01-RF-IL-EN – displacement



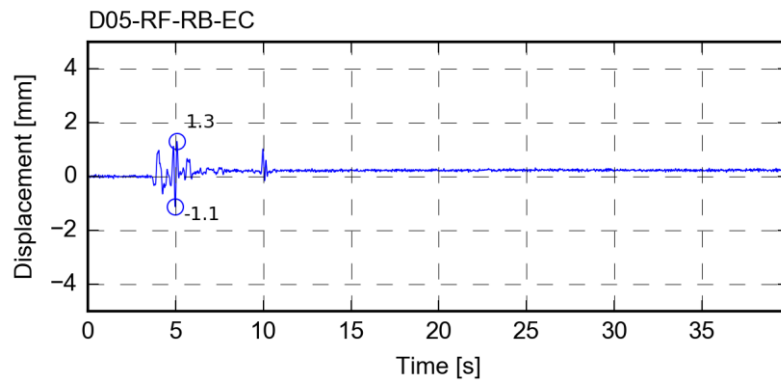
Channel D02-RF-IL-EC – displacement



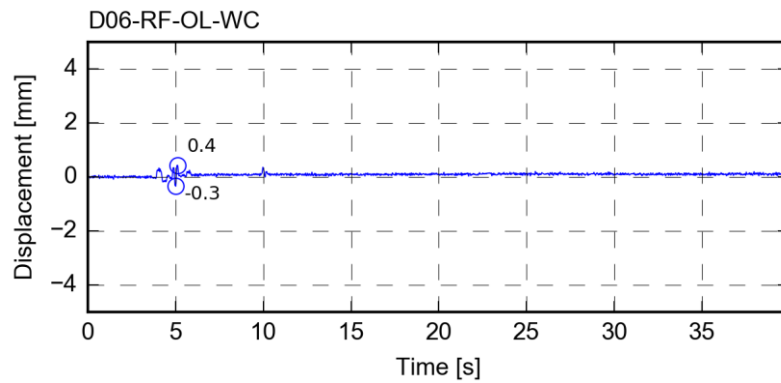
Channel D03-RF-IL-ES – displacement



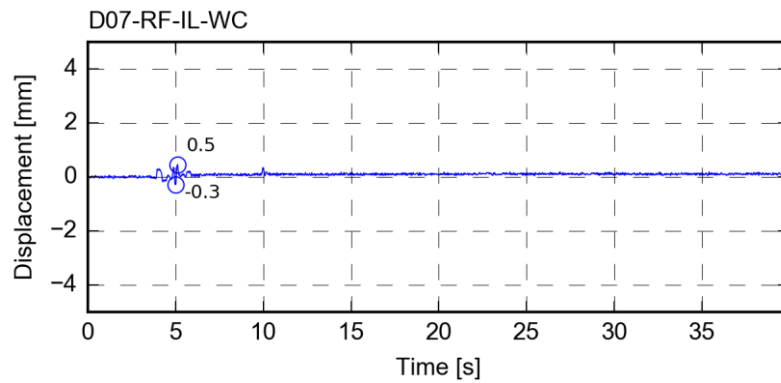
Channel D04-RF-IL-ECH – displacement



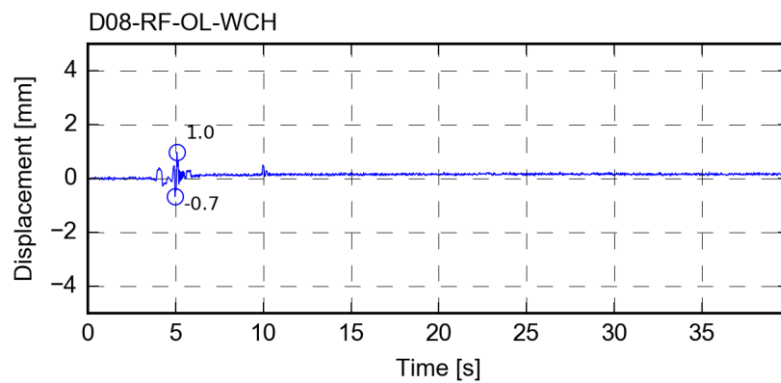
Channel D05-RF-RB-EC – displacement



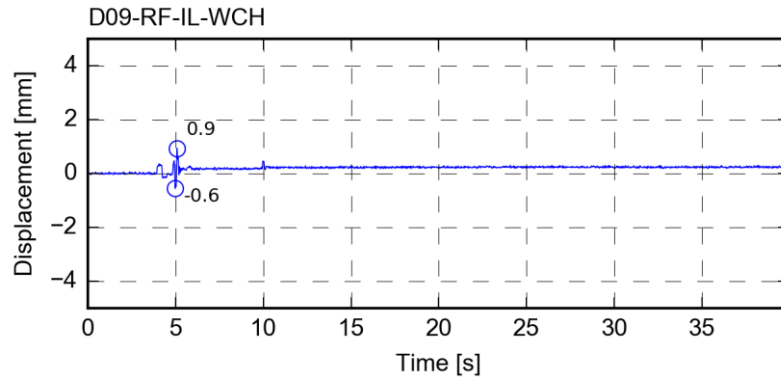
Channel D06-RF-OL-WC – displacement



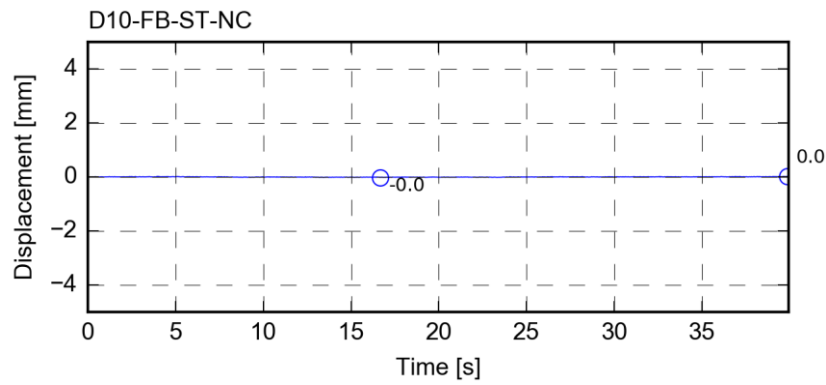
Channel D07-RF-IL-WC – displacement



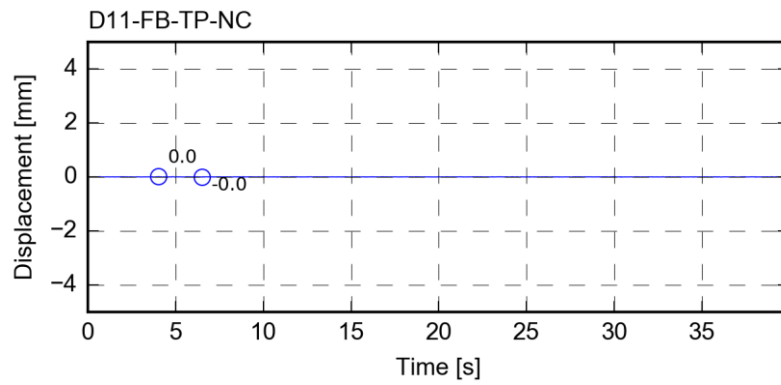
Channel D08-RF-OL-WCH – displacement



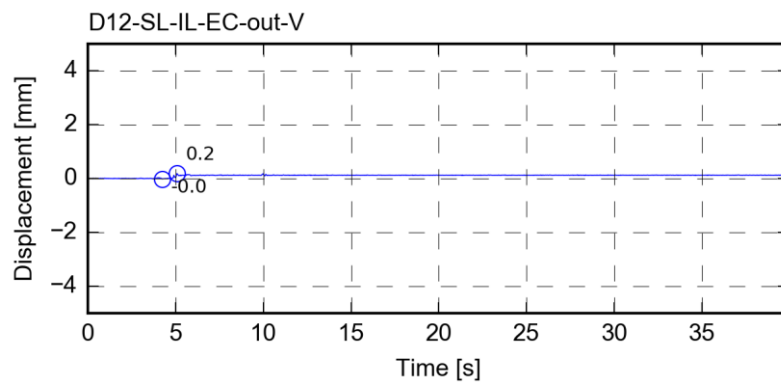
Channel D09-RF-IL-WCH – displacement



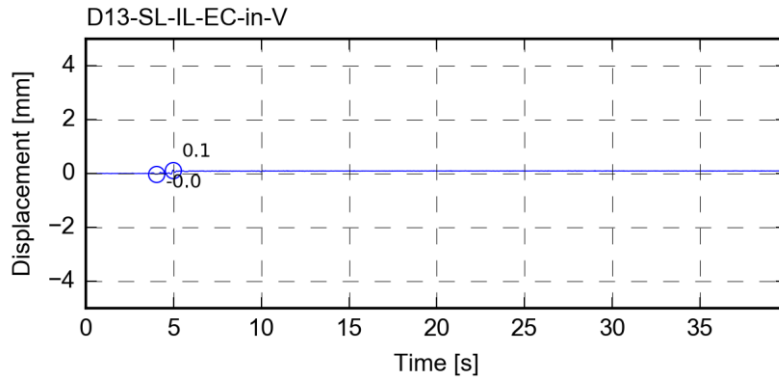
Channel D10-FB-ST-NC – displacement



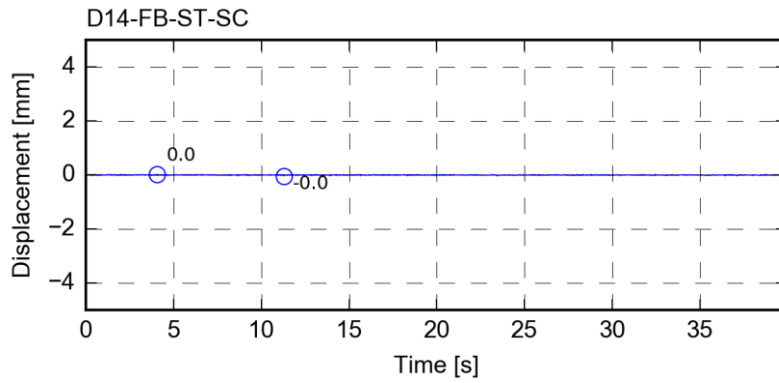
Channel D11-FB-TP-NC – displacement



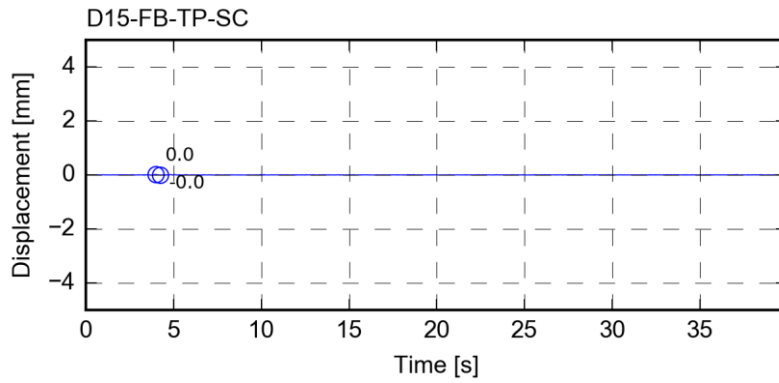
Channel D12-SL-IL-EC-out-V – displacement



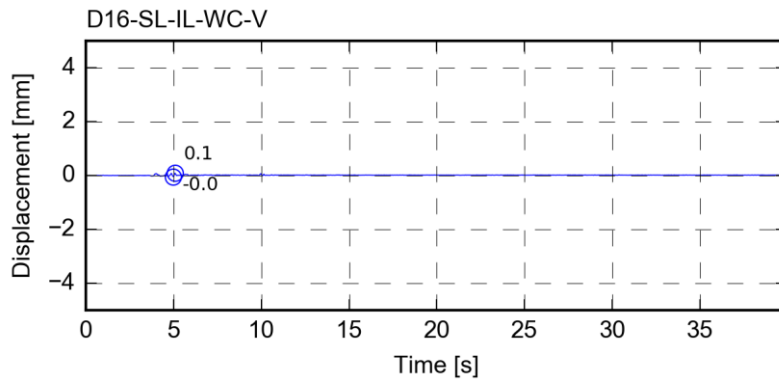
Channel D13-SL-IL-EC-in-V – displacement



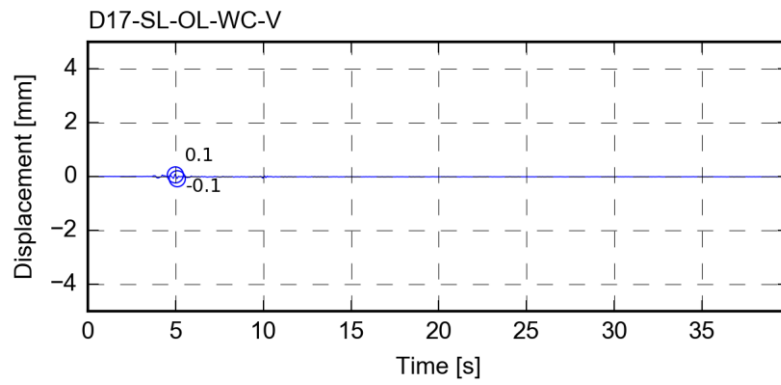
Channel D14-FB-ST-SC – displacement



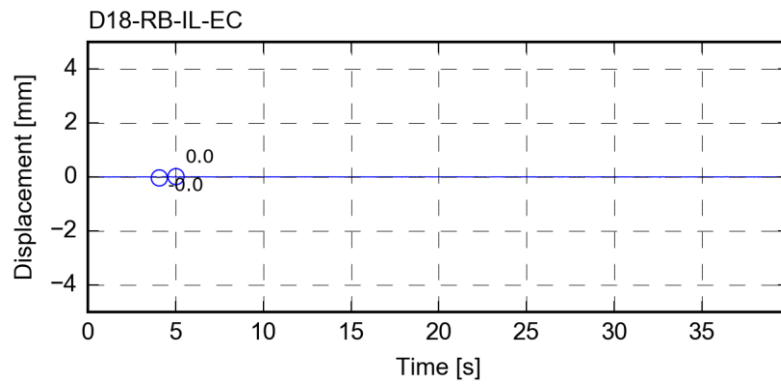
Channel D15-FB-TP-SC – displacement



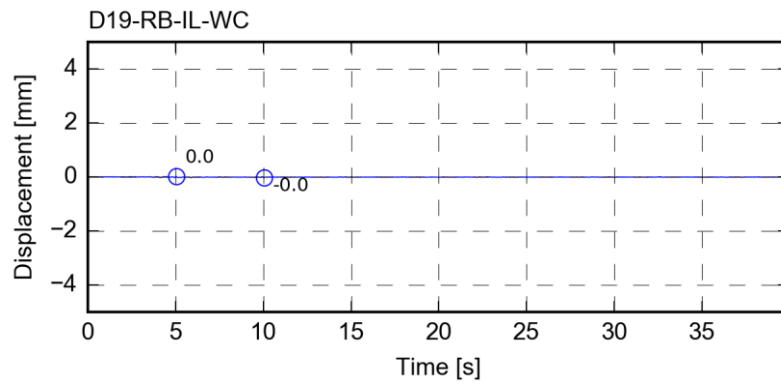
Channel D16-SL-IL-WC-V – displacement



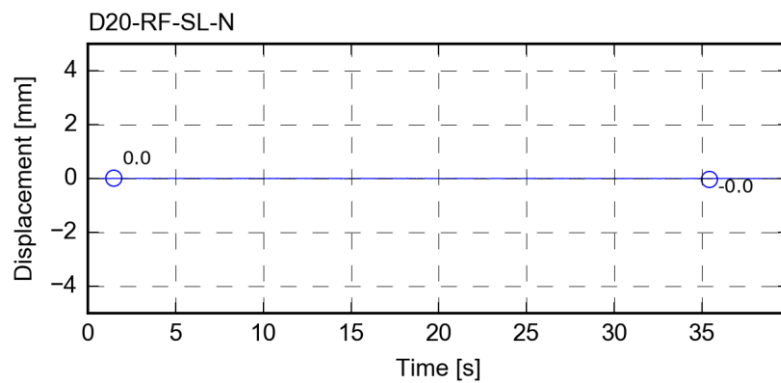
Channel D17-SL-OL-WC-V – displacement



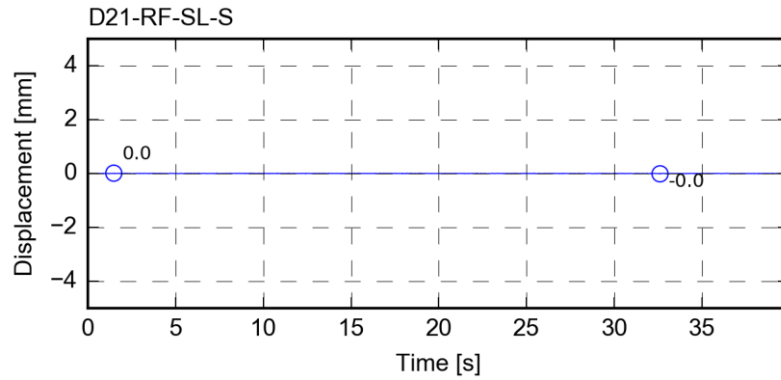
Channel D18-RB-IL-EC – displacement



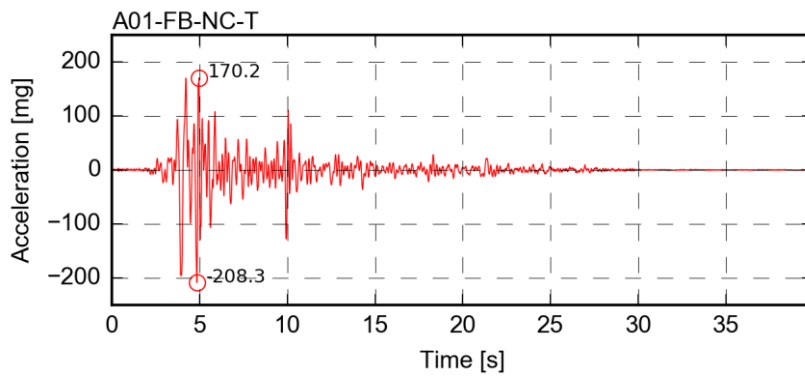
Channel D19-RB-IL-WC – displacement



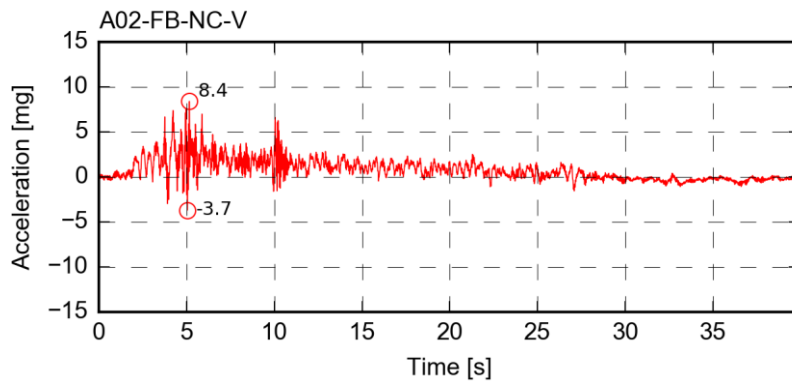
Channel D20-RF-SL-N – displacement



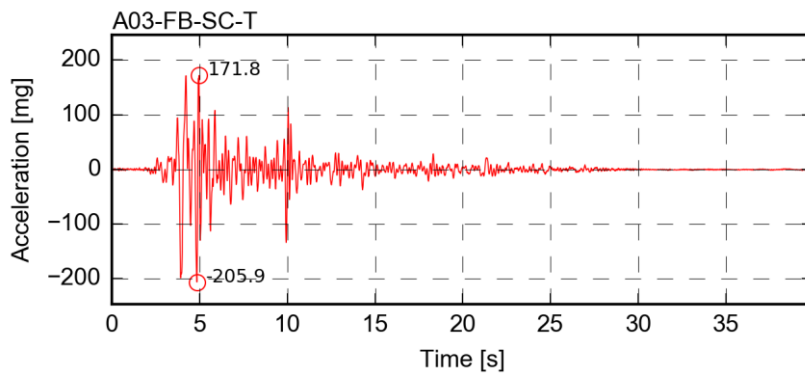
Channel D21-RF-SL-S – displacement



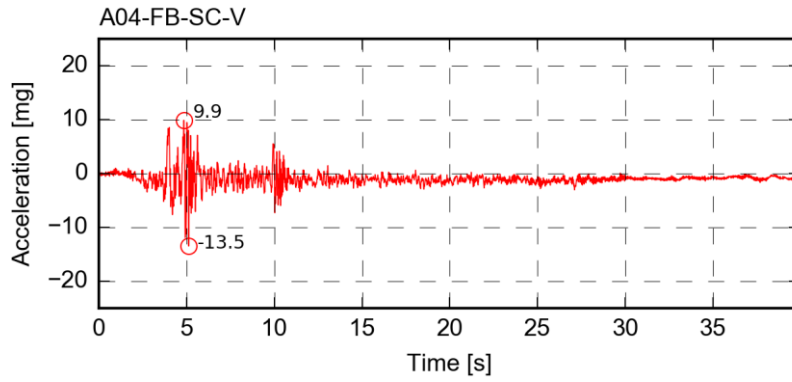
Channel A01-FB-NC-T – acceleration



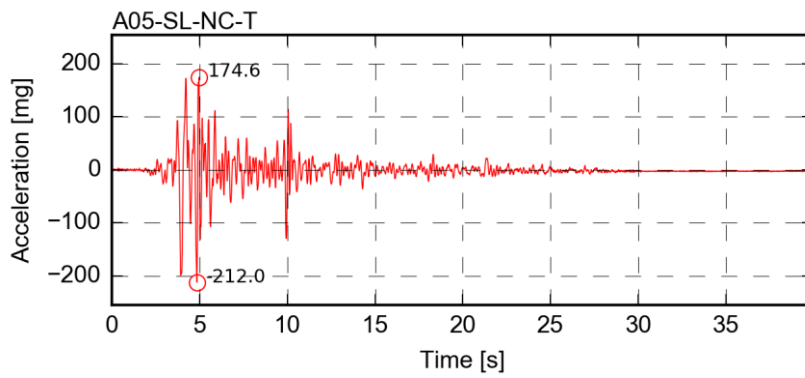
Channel A02-FB-NC-V – acceleration



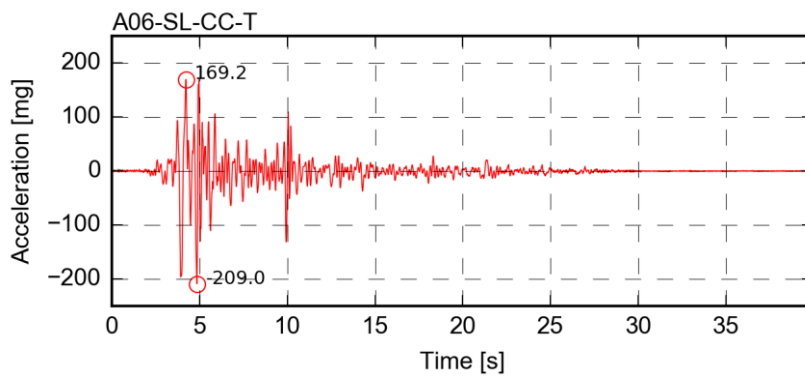
Channel A03-FB-SC-T – acceleration



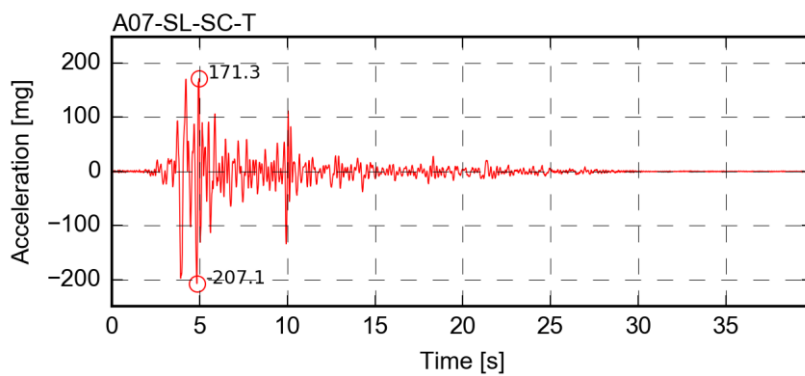
Channel A04-FB-SC-V – acceleration



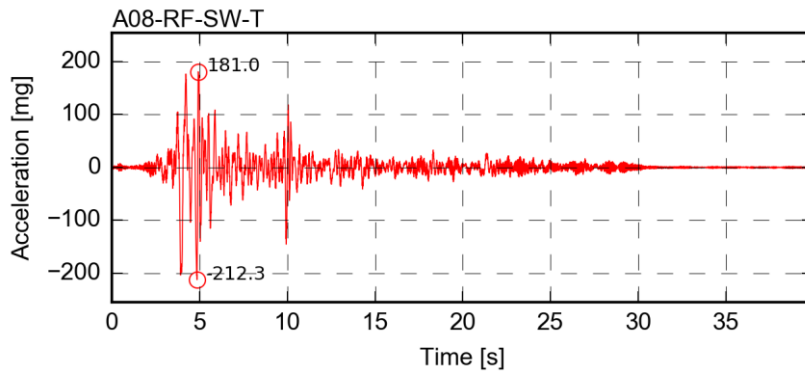
Channel A05-SL-NC-T – acceleration



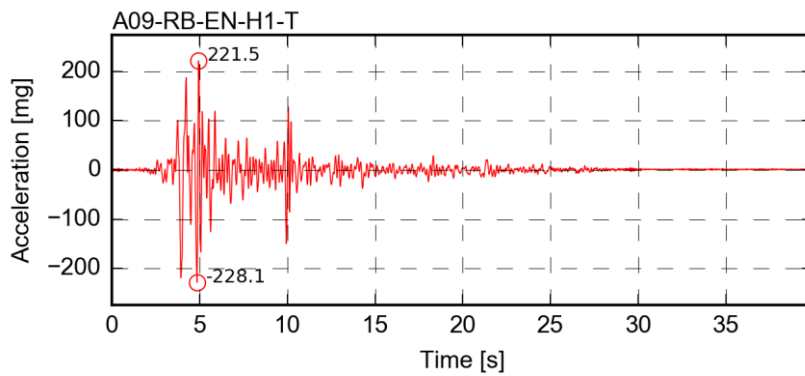
Channel A06-SL-CC-T – acceleration



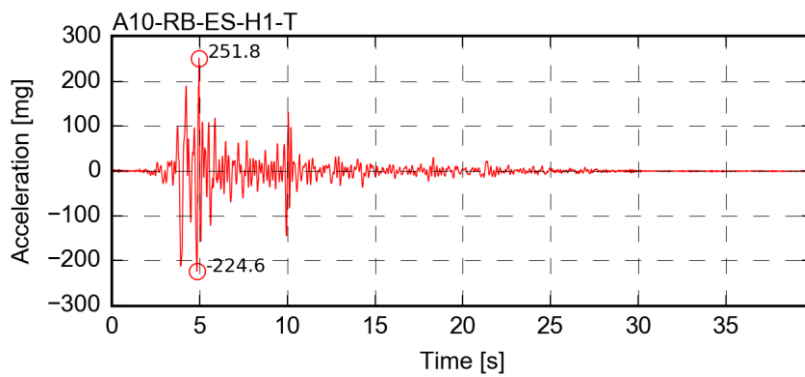
Channel A07-SL-SC-T – acceleration



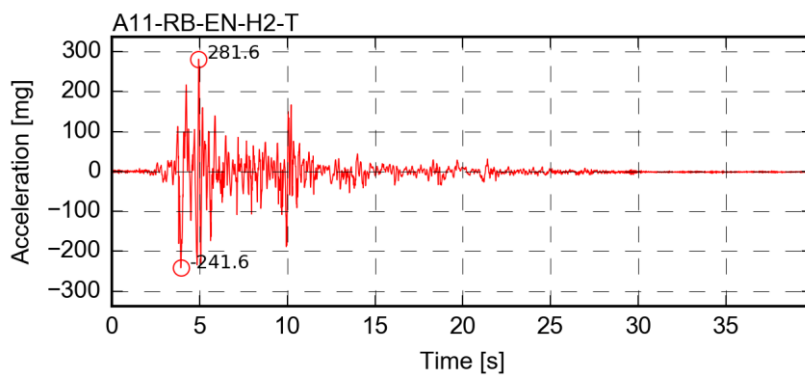
Channel A08-RF-SW-T – acceleration



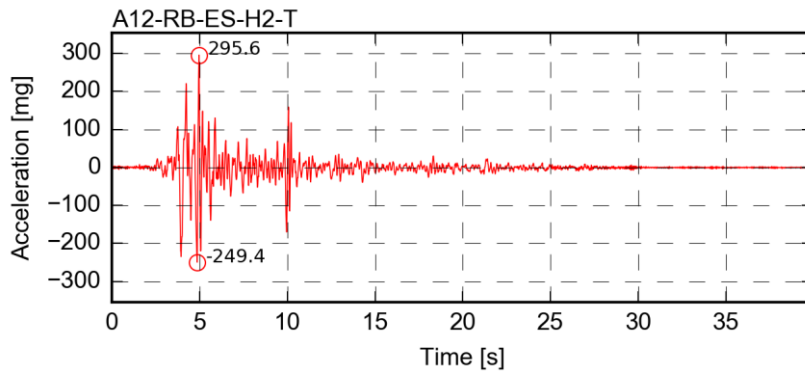
Channel A09-RB-EN-H1-T – acceleration



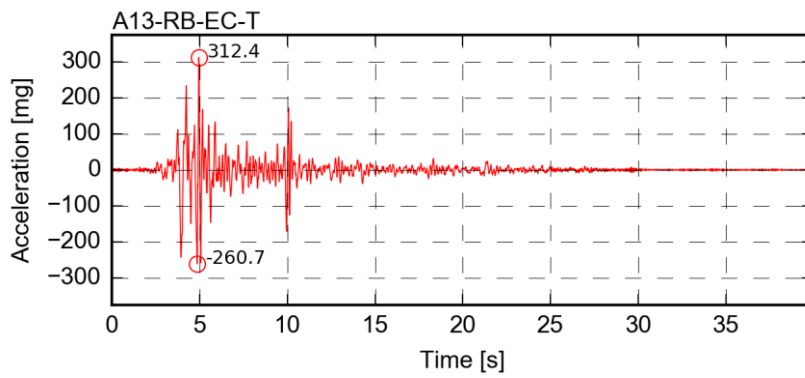
Channel A10-RB-ES-H1-T – acceleration



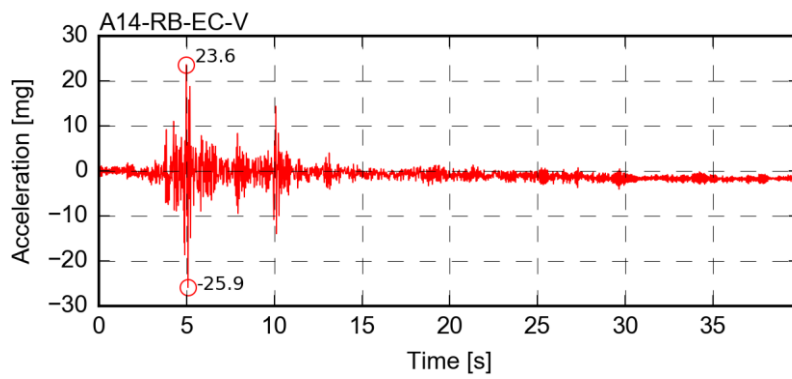
Channel A11-RB-EN-H2-T – acceleration



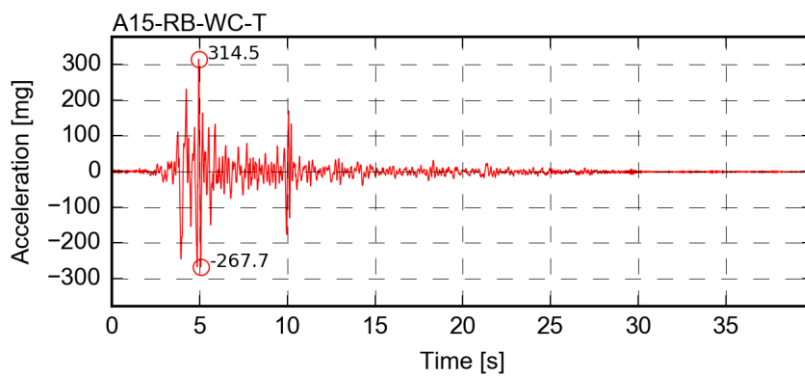
Channel A12-RB-ES-H2-T – acceleration



Channel A13-RB-EC-T – acceleration

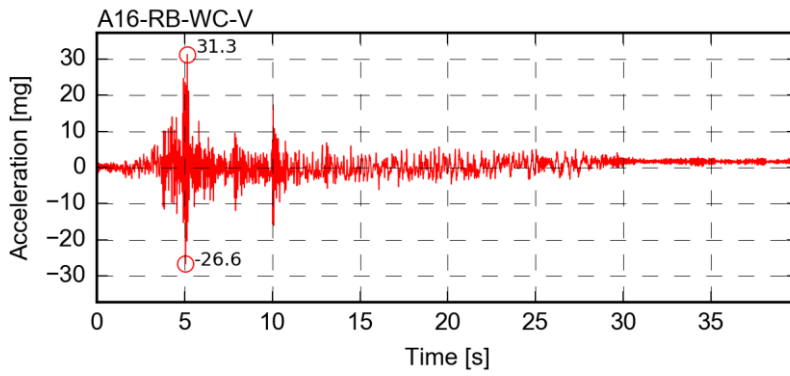


Channel A14-RB-EC-V – acceleration

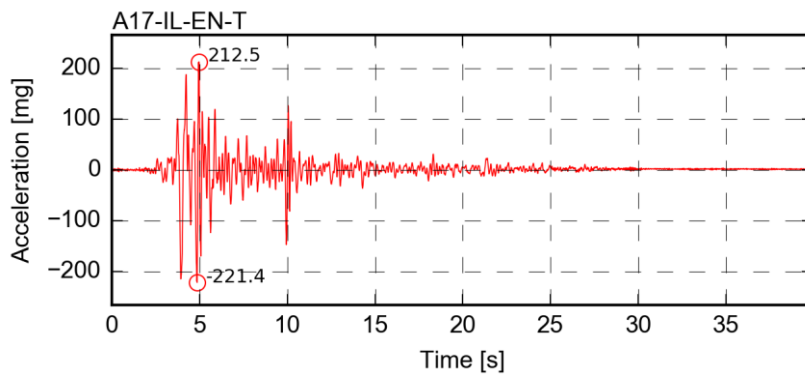


Channel A15-RB-WC-T – acceleration

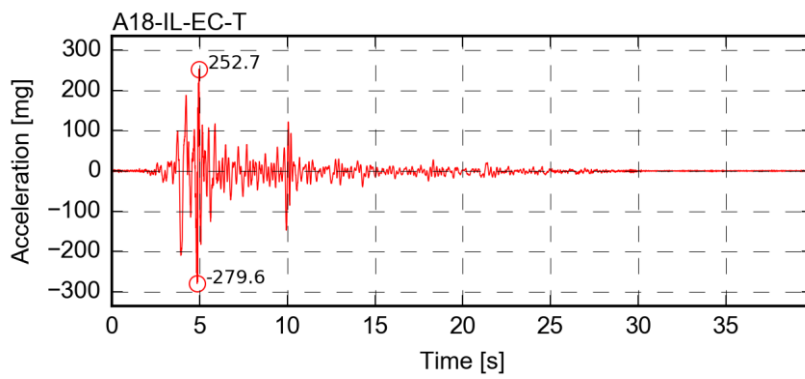
202 Shake Table Test up to Collapse on a Roof Substructure of a Dutch Terraced House



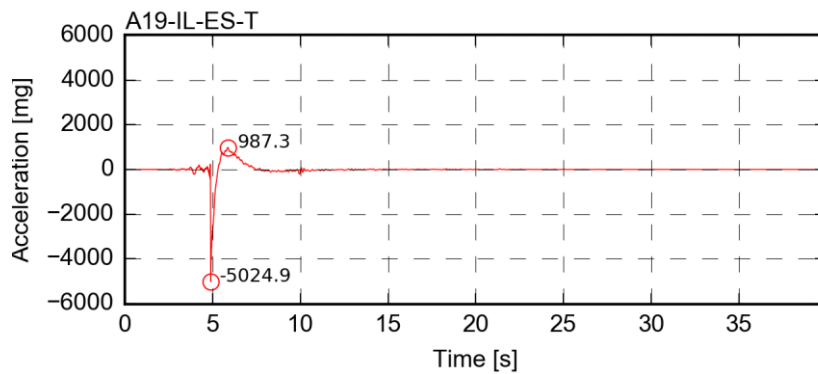
Channel A16-RB-WC-V – acceleration



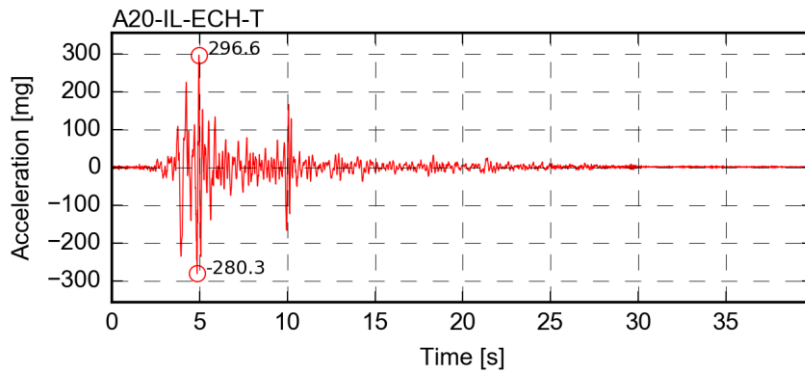
Channel A17-IL-EN-T – acceleration



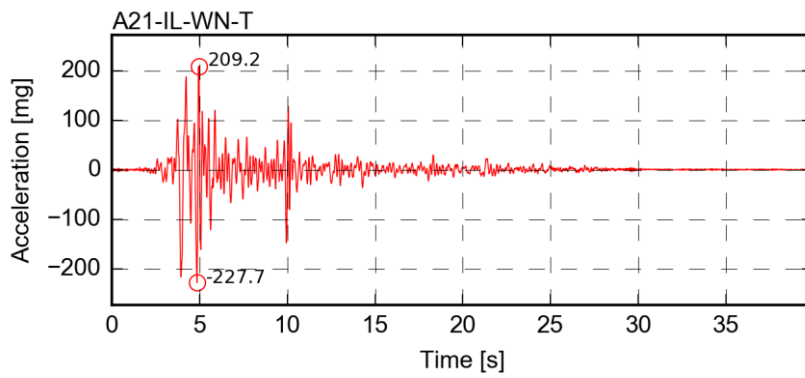
Channel A18-IL-EC-T – acceleration



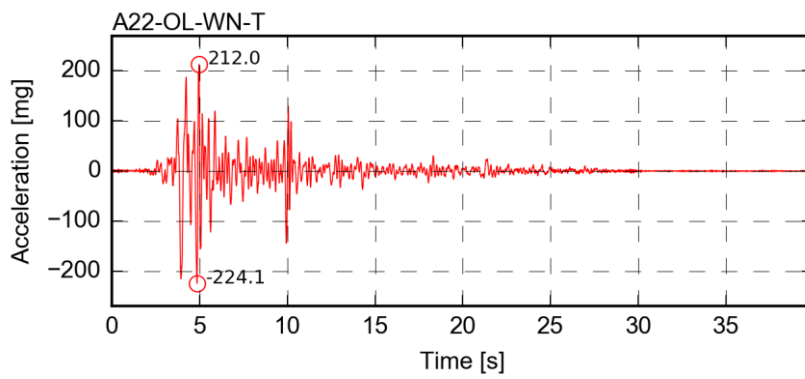
Channel A19-IL-ES-T – acceleration



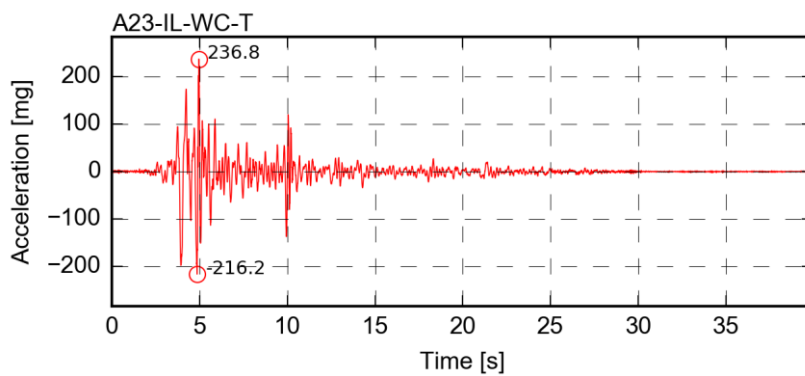
Channel A20-IL-ECH-T – acceleration



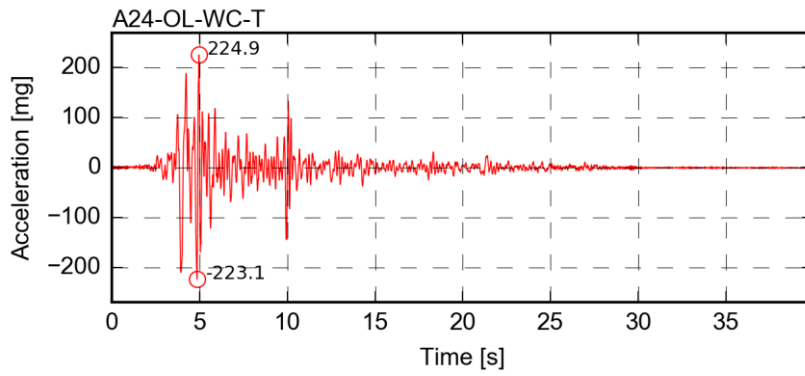
Channel A21-IL-WN-T – acceleration



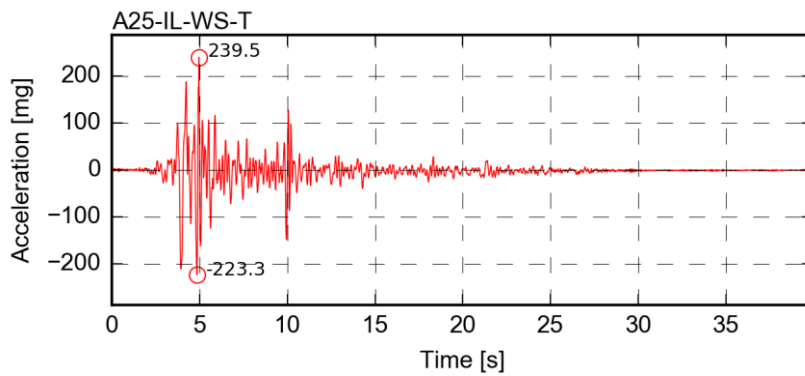
Channel A22-OL-WN-T – acceleration



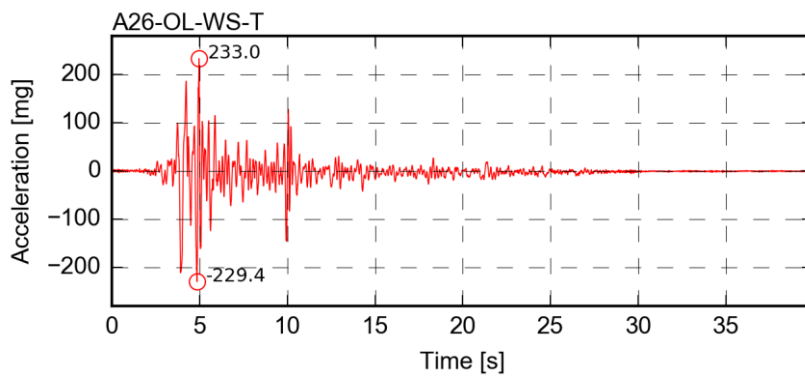
Channel A23-IL-WC-T – acceleration



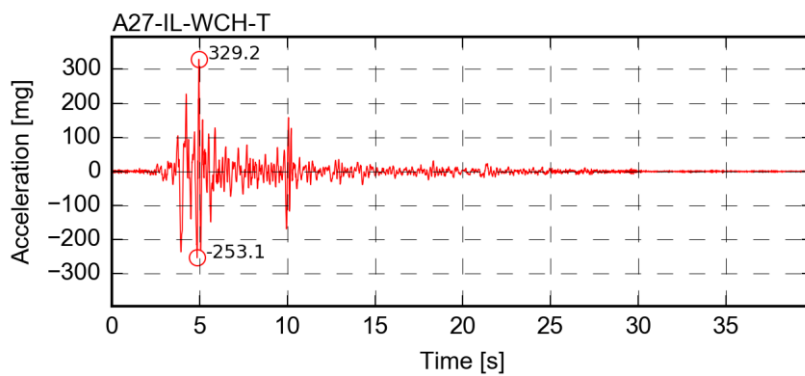
Channel A24-OL-WC-T- acceleration



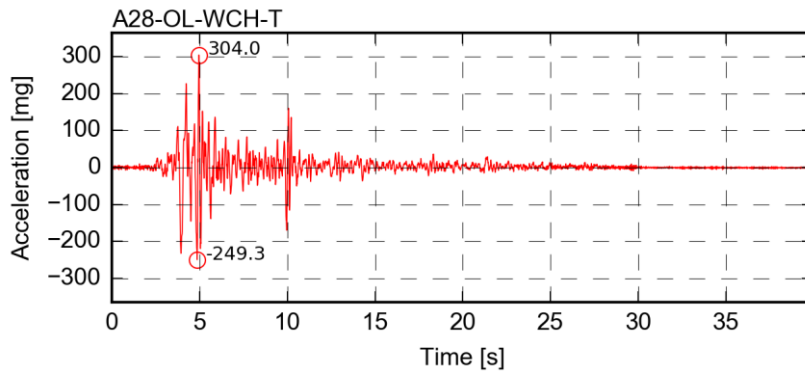
Channel A25-IL-WS-T- acceleration



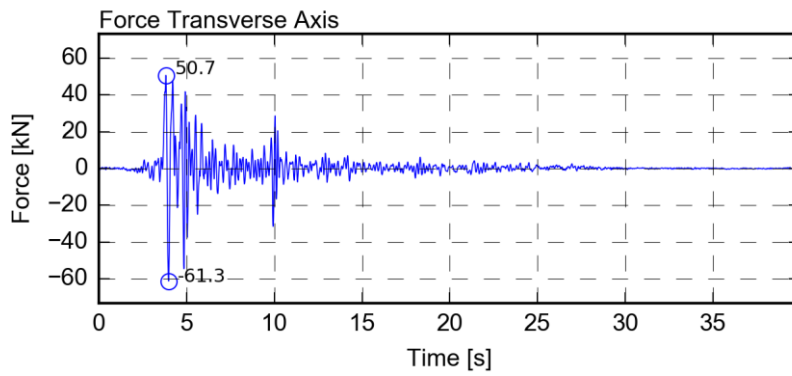
Channel A26-OL-WS-T- acceleration



Channel A27-IL-WCH-T- acceleration



Channel A28-OL-WCH-T- acceleration



Channel Force Transverse Axis- Force

ANNEX V
Additional information on mortar characterisation tests

Characteristics of mortar specimens for calcium silicate blocks (MS) selected for the tests:

Sample	Specimen	Age [days]	Length [mm]	Width [mm]	Height [mm]	Mass [g]
MS_1	MS_1_73	10	159.99	40.17	40.56	408.89
	MS_1_74		160.05	40.24	40.76	411.96
	MS_1_75		159.92	40.31	40.95	416.02
MS_2	MS_2_88		160.13	40.29	40.30	408.62
	MS_2_89		160.06	40.16	40.49	408.61
	MS_2_90		160.06	40.29	40.29	408.88
MS_C	MS_C_103		160.61	40.39	40.68	411.80
	MS_C_104		160.67	40.31	40.62	412.41
	MS_C_105		160.49	40.14	40.56	409.55
MS_1	MS_2_76		21	160.25	40.05	40.68
	MS_2_77	160.14		40.07	40.61	403.41
	MS_2_78	160.24		39.96	40.60	403.39
MS_2	MS_2_91	159.95		39.99	40.41	407.78
	MS_2_92	159.97		39.97	40.39	406.14
	MS_2_93	159.95		39.95	40.42	406.34
MS_C	MS_C_106	159.79		39.94	40.70	407.96
	MS_C_107	159.71		40.13	40.79	409.45
	MS_C_108	159.74		40.31	40.78	409.92
MS_1	MS_2_79	28		160.03	39.91	40.71
	MS_2_80		159.99	40.05	40.68	409.84
	MS_2_81		160.03	40.01	40.88	408.75
MS_2	MS_2_94		160.11	39.92	40.35	407.28
	MS_2_95		160.12	40.15	40.26	409.84
	MS_2_96		160.33	39.90	40.27	408.75
MS_C	MS_C_109		160.07	40.28	41.11	410.67
	MS_C_110		160.05	40.24	40.69	407.55
	MS_C_111		159.97	40.05	40.48	407.21

Characteristics of mortar specimens for clay bricks (MCL) selected for the tests:

Sample	Specimen	Age [days]	Length [mm]	Width [mm]	Height [mm]	Mass [g]
MCL_1	MCL_1_61	10	159.93	40.15	40.80	474.11
	MCL_1_62		159.19	40.10	40.63	477.20
	MCL_1_61		159.97	40.12	40.48	475.65
MCL_C	MCL_C_76		159.91	40.26	40.61	481.12
	MCL_C_77		159.89	40.15	40.63	481.87
	MCL_C_78		159.79	40.10	40.58	484.24
MCL_1	MCL_1_64	21	159.96	40.05	40.63	459.18
	MCL_1_65		159.98	40.06	40.40	458.69
	MCL_1_66		160.06	40.09	41.04	462.90
MCL_C	MCL_C_79		159.94	40.06	40.66	475.30
	MCL_C_80		159.86	40.05	40.60	475.90
	MCL_C_81		159.75	40.10	40.70	474.22
MCL_1	MCL_1_67	28	160.18	40.37	40.84	461.71
	MCL_1_68		160.32	39.93	41.16	460.66
	MCL_1_69		160.16	40.05	40.92	465.43
MCL_C	MCL_C_82		159.93	40.33	40.95	476.36
	MCL_C_83		160.09	40.17	41.18	476.09
	MCL_C_84		160.03	40.12	40.90	474.96

210 Shake Table Test up to Collapse on a Roof Substructure of a Dutch Terraced House

Test results for the determination of the dynamic modulus of elasticity after 10 days, 20 days and 28 days of the bedding mortar of calcium silicate blocks (MS):

Specimen	Date of test	Age of specimen [days]	Density [kg/m ³]		Frequency of resonance [Hz]		Dynamic modulus of elasticity [MPa]	
			Individual values	Average	Individual values	Average	Individual values	Average
MS_1_73	2017-08-10	10	1570	1570	7093.3	7086.2	8080	8080
MS_1_74			1570		7031.4		7949	
MS_1_75			1580		7134.0		8205	
MS_2_88	2017-08-10	10	1570	1570	6965.8	7041.7	7820	7990
MS_2_89			1570		7080.9		8066	
MS_2_90			1570		7078.3		8080	
MS_C_103	2017-08-11	10	1560	1570	6956.2	6955.2	7792	7810
MS_C_104			1570		6900.1		7707	
MS_C_105			1570		7009.3		7933	
MS_1_76	2017-08-21	21	1560	1550	7017.1	6924.7	7870	7640
MS_1_77			1550		6818.1		7282	
MS_1_78			1550		6939.0		7674	
MS_2_91	2017-08-21	21	1580	1570	7114.9	7091.2	8173	8100
MS_2_92			1570		6987.2		7859	
MS_2_93			1570		7171.6		8282	
MS_C_106	2017-08-22	21	1570	1570	7271.8	7242.2	8481	8380
MS_C_107			1570		7261.9		8428	
MS_C_108			1560		7193.0		8244	
MS_1_79	2017-08-28	28	1570	1570	6492.0	6504.3	6763	6790
MS_1_80			1570		6447.6		6692	
MS_1_81			1560		6573.3		6912	
MS_2_94	2017-08-28	28	1580	1580	7084.0	7111.7	8128	8220
MS_2_95			1580		7120.4		8233	
MS_2_96			1590		7130.8		8296	
MS_C_109	2017-08-29	28	1550	1560	7021.6	7077.8	7828	8000
MS_C_110			1560		7078.6		7984	
MS_C_111			1570		7133.2		8179	

Test results for the determination of the dynamic modulus of elasticity after 10 days, 20 days and 28 days of the bedding mortar of clay bricks (MCL):

Specimen	Date of test	Age of specimen [days]	Density [kg/m ³]		Frequency of resonance [Hz]		Dynamic modulus of elasticity [MPa]	
			Individual values	Average	Individual values	Average	Individual values	Average
MCL_1_61	2017-08-10	10	1810	1830	7654.5	7653.1	10850	10910
MCL_1_62			1840		7667.4		10964	
MCL_1_61			1830		7637.5		10931	
MCL_C_76	2017-08-11	10	1840	1850	7816.0	7879.9	11500	11750
MCL_C_77			1850		7840.2		11613	
MCL_C_78			1860		7983.5		12124	
MCL_1_64	2017-08-21	21	1760	1760	7816.0	7876.3	11031	11210
MCL_1_65			1770		7816.0		11079	
MCL_1_66			1760		7997.0		11519	
MCL_C_79	2017-08-22	21	1830	1820	8096.2	8083.1	12238	12190
MCL_C_80			1830		8093.0		12257	
MCL_C_81			1820		8060.2		12063	
MCL_1_67	2017-08-28	28	1750	1760	7979.2	7994.3	11424	11530
MCL_1_68			1750		7939.5		11330	
MCL_1_69			1770		8064.2		11833	
MCL_C_82	2017-08-29	28	1800	1800	8161.2	8142.0	12289	12240
MCL_C_83			1800		8179.1		12331	
MCL_C_84			1810		8085.8		12114	

212 Shake Table Test up to Collapse on a Roof Substructure of a Dutch Terraced House

Test results for flexural and compression strength for the bedding mortar specimen for the calcium silicate blocks (MS) after 10 days, 20 days and 28 days:

Specimen	Date of test	Age of specimen [days]	Density [kg/m ³]		Compressive strength [MPa]		Flexural strength [MPa]		
			Individual values	Average	Individual values	Average	Individual values	Average	
MS_1_73	2017-08-10	10	1570	1570	4.25	4.10	3.9	2.05	2.2
MS_1_74			1570		4.05	4.35		2.10	
MS_1_75			1580		2.15	4.55		2.45	
MS_2_88	2017-08-10	10	1570	1570	4.20	4.05	4.1	2.00	2.1
MS_2_89			1570		4.35	4.30		2.10	
MS_2_90			1570		3.95	3.85		2.15	
MS_C_103	2017-08-11	10	1560	1570	4.05	4.10	3.7	2.05	2.0
MS_C_104			1570		3.40	3.95		2.00	
MS_C_105			1570		4.50	1.90		2.05	
MS_1_76	2017-08-21	21	1560	1550	4.50	4.55	4.6	2.05	2.0
MS_1_77			1550		4.65	4.45		2.00	
MS_1_78			1550		4.90	4.75		1.95	
MS_2_91	2017-08-21	21	1580	1570	4.95	3.90	4.9	2.45	2.5
MS_2_92			1570		5.20	5.74		2.45	
MS_2_93			1570		5.15	4.65		2.45	
MS_C_106	2017-08-22	21	1570	1570	6.00	6.10	5.9	2.90	2.8
MS_C_107			1570		6.10	5.90		2.80	
MS_C_108			1560		5.90	5.45		2.55	
MS_1_79	2017-08-28	28	1570	1570	5.05	4.65	4.4	2.00	2.2
MS_1_80			1570		4.05	4.85		2.25	
MS_1_81			1560		4.90	3.15		2.40	
MS_2_94	2017-08-28	28	1580	1580	3.00	2.05	3.0	3.00	2.8
MS_2_95			1580		3.70	3.75		2.70	
MS_2_96			1590		2.90	2.30		2.65	
MS_C_109	2017-08-29	28	1550	1560	1.30	5.90	4.8	2.45	2.6
MS_C_110			1560		5.55	5.15		2.30	
MS_C_111			1570		5.60	5.55		2.95	

Test results for the test for flexural and compression strength for the bedding mortar specimen for the clay bricks (MCL) after 10 days, 20 days and 28 days:

Specimen	Date of test	Age of specimen [days]	Density [kg/m ³]		Compressive strength [MPa]		Flexural strength [MPa]	
			Individual values	Average	Individual values	Average	Individual values	Average
MCL_1_61	2017-08-10	10	1810	1830	5.30	5.00	1.40	1.4
MCL_1_62			1840		5.70	5.70	1.10	
MCL_1_61			1830		5.80	5.80	1.55	
MCL_C_76	2017-08-11	10	1840	1850	5.90	5.90	1.35	1.4
MCL_C_77			1850		5.70	5.85	1.40	
MCL_C_78			1860		1.90	6.25	1.30	
MCL_1_64	2017-08-21	21	1760	1760	7.80	7.35	2.85	2.7
MCL_1_65			1770		7.95	7.65	2.55	
MCL_1_66			1760		7.85	7.55	2.80	
MCL_C_79	2017-08-22	21	1830	1820	8.30	8.00	3.20	3.3
MCL_C_80			1830		8.40	8.35	3.20	
MCL_C_81			1820		7.85	8.30	3.45	
MCL_1_67	2017-08-28	28	1750	1760	4.10	7.35	3.75	3.7
MCL_1_68			1750		8.00	2.25	3.25	
MCL_1_69			1770		7.80	8.15	4.00	
MCL_C_82	2017-08-29	28	1800	1800	8.10	8.35	3.50	3.5
MCL_C_83			1800		8.25	8.35	3.45	
MCL_C_84			1810		8.15	7.90	3.40	

ANNEX VI

Additional information on masonry blocks characterisation tests

Characteristics of the two types of blocks selected for the tests:

Specimen	Mass [kg]	Length (L1) [mm]			Width (L2) [mm]			Height (H) [mm]		
		L1 (top)	L1 (down)	Average	L2 (top)	L2 (down)	Average	H1 (left)	H2 (right)	Average
BS_0	2.952	212.72	212.65	212.69	103.36	103.87	103.62	70.67	70.89	70.78
BS_1	2.978	212.65	213.03	212.84	103.37	103.40	103.39	70.84	70.99	70.92
BS_2	2.968	212.86	212.75	212.81	103.39	103.89	103.64	70.82	70.56	70.69
BS_3	2.926	213.21	212.99	213.10	102.95	103.43	103.19	70.88	71.23	71.06
BS_4	2.915	213.05	212.82	212.94	102.99	103.13	103.06	71.08	71.28	71.18
BS_5	2.761	212.71	212.61	212.66	102.08	102.16	102.12	70.82	70.98	70.90
BS_6	2.967	212.73	212.62	212.68	103.46	103.66	103.56	71.00	71.17	71.09
BS_7	2.961	212.82	212.79	212.81	103.27	103.51	103.39	70.21	70.87	70.54
BS_8	3.008	212.69	212.86	212.78	104.25	103.51	103.88	70.32	70.23	70.28
BS_9	2.964	212.71	212.68	212.70	103.70	103.76	103.73	71.12	71.01	71.07
BS_10	2.943	213.26	212.88	213.07	103.35	103.58	103.47	70.57	70.76	70.57
BCL_0	1.698	213.31	211.20	212.26	99.65	100.57	100.11	50.53	45.00	47.77
BCL_1	1.708	209.97	209.83	209.90	101.27	101.56	101.42	50.21	50.32	50.27
BCL_2	1.699	209.47	210.15	209.81	101.26	101.58	101.42	50.39	50.47	50.43
BCL_3	1.638	210.95	208.80	209.88	99.01	100.11	99.56	49.86	50.03	49.95
BCL_4	1.686	213.17	211.72	212.45	100.53	99.54	100.04	50.31	50.18	50.25
BCL_5	1.735	213.83	213.17	213.50	101.61	102.73	102.17	50.27	50.12	50.20
BCL_6	1.686	213.06	211.80	212.43	100.40	99.75	100.08	50.78	50.89	50.84
BCL_7	1.711	209.91	209.86	209.89	100.80	101.96	101.38	49.76	49.71	49.74
BCL_8	1.675	213.72	211.16	212.44	98.97	99.60	99.29	49.94	49.86	49.90
BCL_9	1.669	215.89	211.88	213.89	98.37	98.54	98.46	50.03	50.15	50.09
BCL_10	1.678	212.92	210.41	211.67	99.70	100.54	100.12	49.76	49.87	49.82

218 *Shake Table Test up to Collapse on a Roof Substructure of a Dutch Terraced House*

Determination of bulk density for calcium silicate blocks:

Specimen	Length (L1)	Width (L2)	Height (H)	Mass	Bulk density
	[m]	[m]	[m]	[kg]	[kg/m ³]
BS_0	0.21269	0.10362	0.07078	2.952	1892.41
BS_1	0.21284	0.10339	0.07092	2.978	1908.20
BS_2	0.21281	0.10364	0.07069	2.968	1903.65
BS_3	0.21310	0.10319	0.07106	2.926	1872.53
BS_4	0.21294	0.10306	0.07118	2.915	1866.09
BS_5	0.21266	0.10212	0.07090	2.761	1793.18
BS_6	0.21268	0.10356	0.07109	2.967	1894.92
BS_7	0.21281	0.10339	0.07054	2.961	1907.80
BS_8	0.21278	0.10388	0.07028	3.008	1936.35
BS_9	0.21270	0.10373	0.07107	2.964	1890.25
BS_10	0.21307	0.10347	0.07057	2.943	1891.62

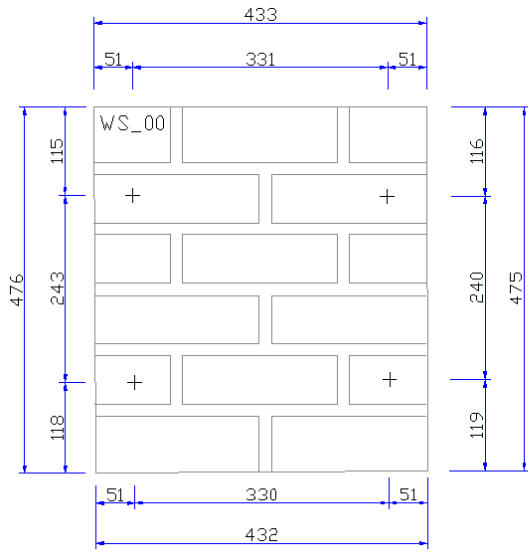
Determination of bulk density for clay blocks:

Specimen	Length (L1)	Width (L2)	Height (H)	Mass	Bulk density
	[m]	[m]	[m]	[kg]	[kg/m ³]
BCL_0	0.21226	0.10011	0.04777	1.698	1672.77
BCL_1	0.20990	0.10142	0.05027	1.708	1596.04
BCL_2	0.20981	0.10142	0.05043	1.699	1583.27
BCL_3	0.20988	0.09956	0.04995	1.638	1569.36
BCL_4	0.21245	0.10004	0.05025	1.686	1578.67
BCL_5	0.21350	0.10217	0.05020	1.735	1584.44
BCL_6	0.21243	0.10008	0.05084	1.686	1559.87
BCL_7	0.20989	0.10138	0.04974	1.711	1616.59
BCL_8	0.21244	0.09929	0.04990	1.675	1591.37
BCL_9	0.21389	0.09846	0.05009	1.669	1582.18
BCL_10	0.21167	0.10012	0.04982	1.678	1589.31

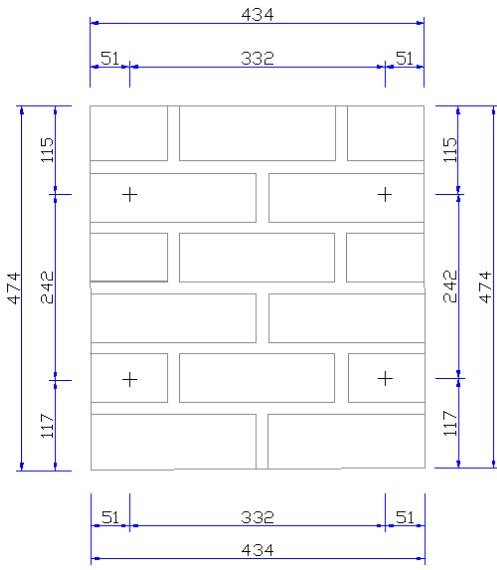
ANNEX VII

Geometry, instrumentation layout and additional information on *wallettes* and *triplets* for material characterisation tests

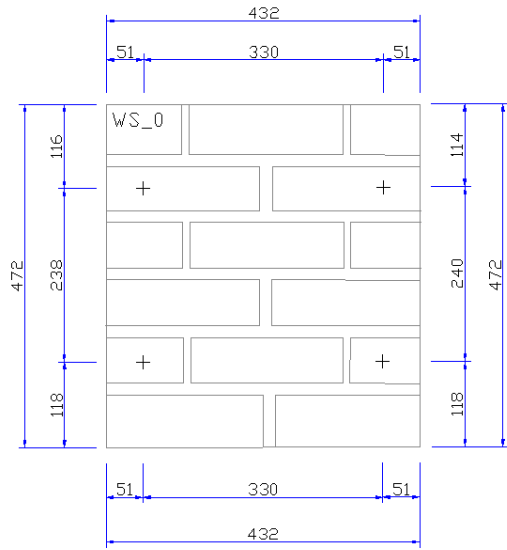
Geometry and instrumentation layout in calcium silicate *wallettes* for compressive strength tests:



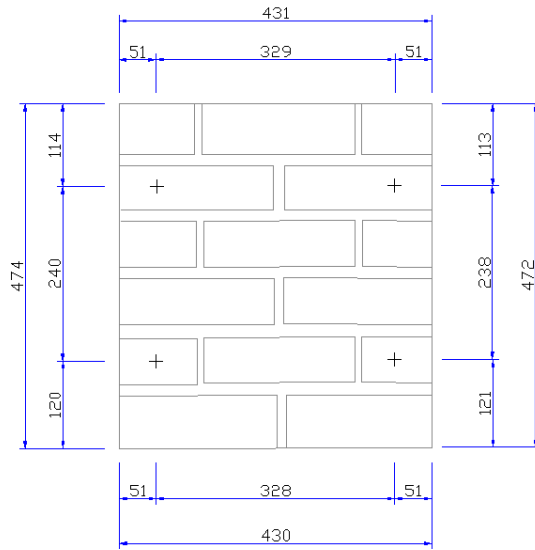
Wallette WS_00 – front side



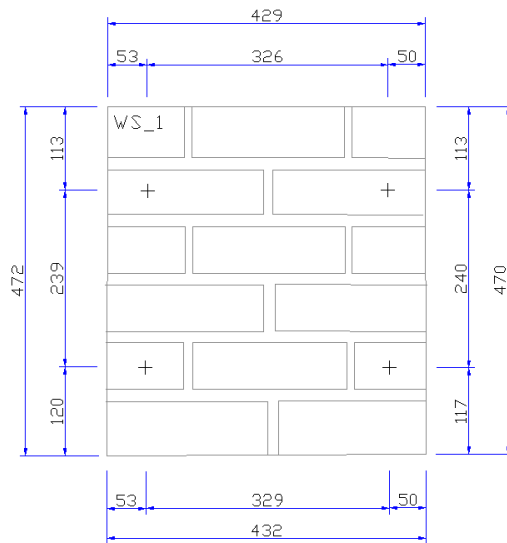
Wallette WS_00 – back side



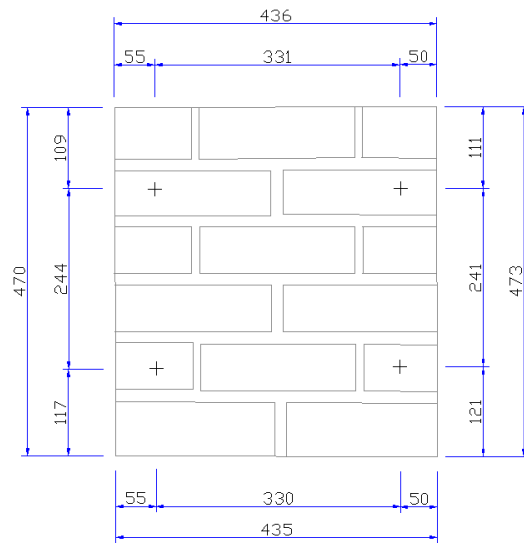
Wallette WS_0 – front side



Wallette WS_0 – back side

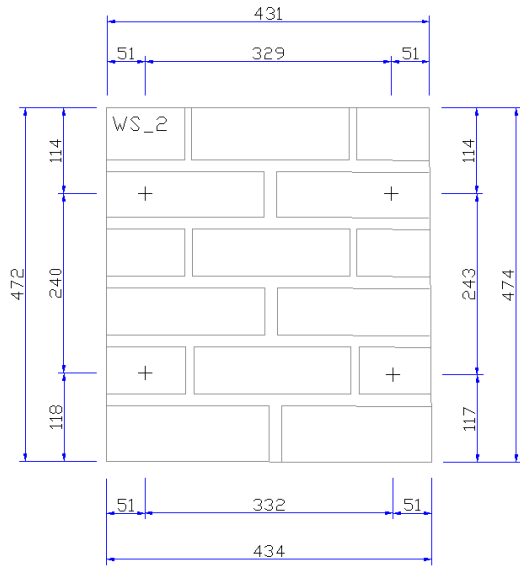


Wallette WS_1 – front side

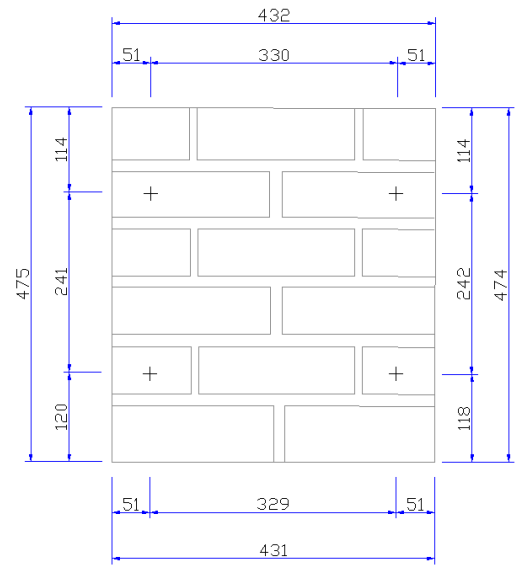


Wallette WS_1 – back side

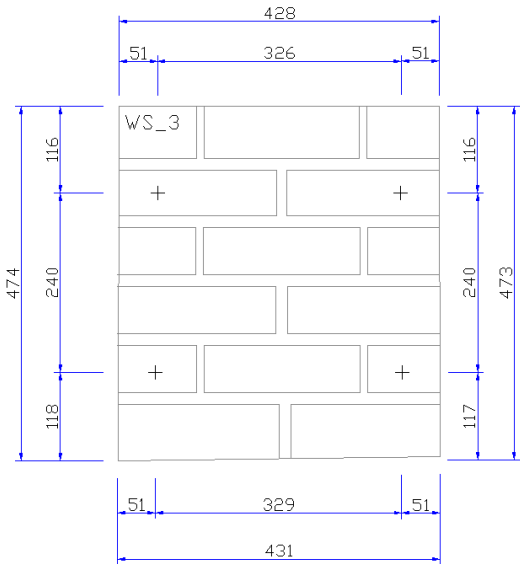
222 Shake Table Test up to Collapse on a Roof Substructure of a Dutch Terraced House



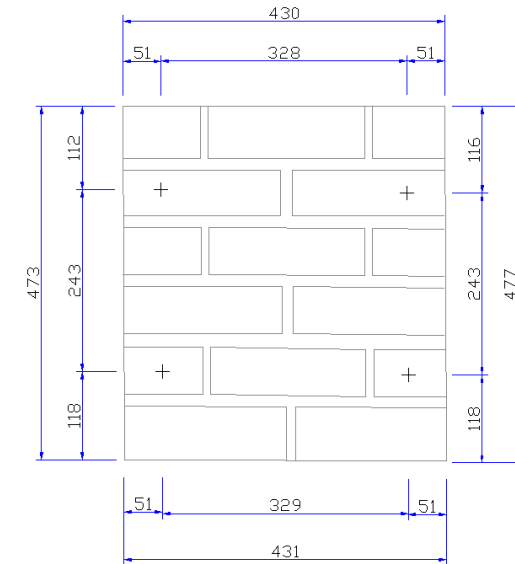
Walette WS_2 – front side



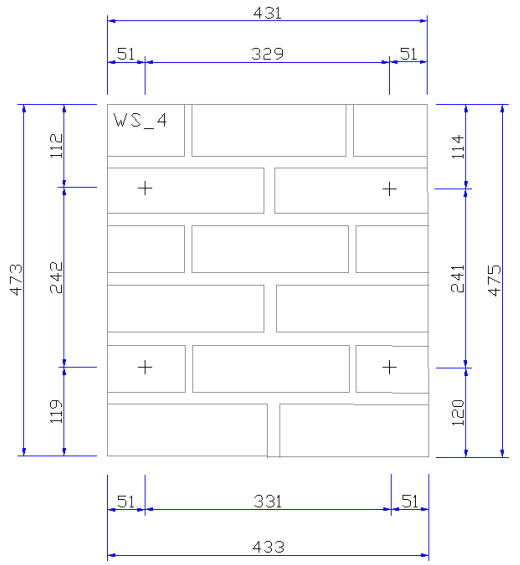
Walette WS_2 – back side



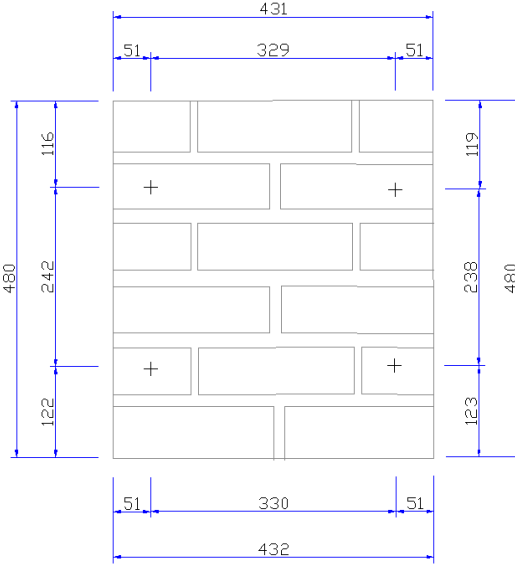
Walette WS_3 – front side



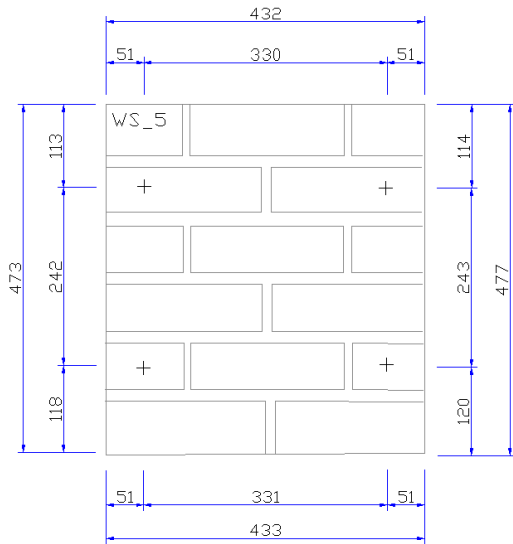
Walette WS_3 – back side



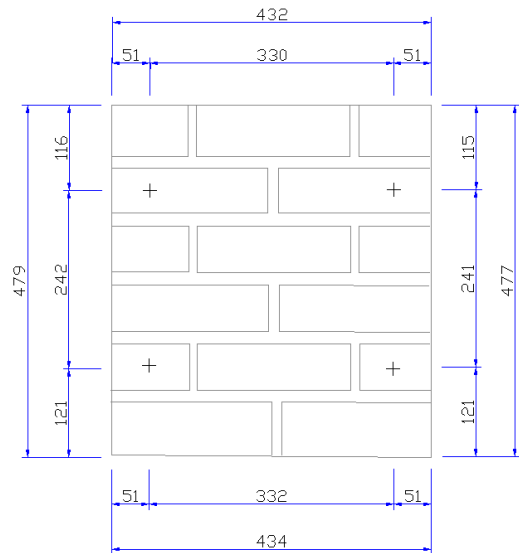
Walette WS_4 – front side



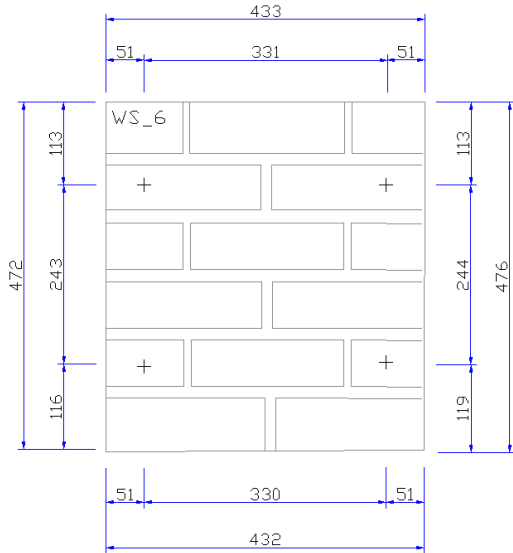
Walette WS_4 – back side



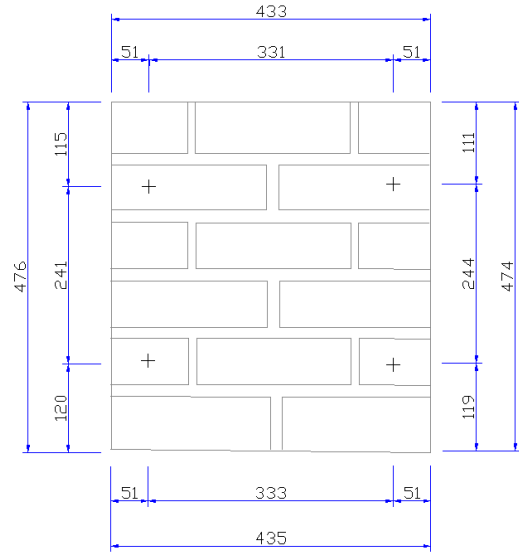
Wallette WS_5 – front side



Wallette WS_5 – back side



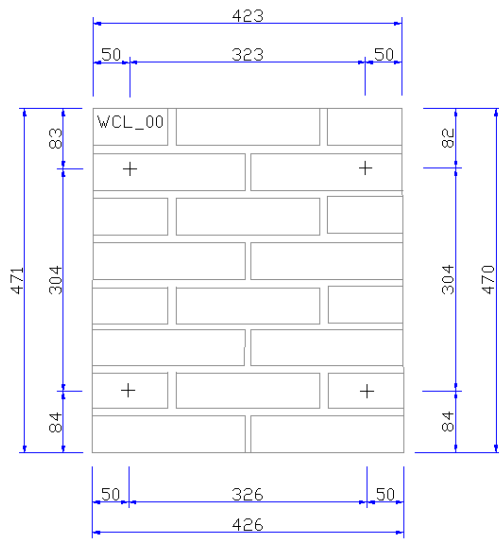
Wallette WS_6 – front side



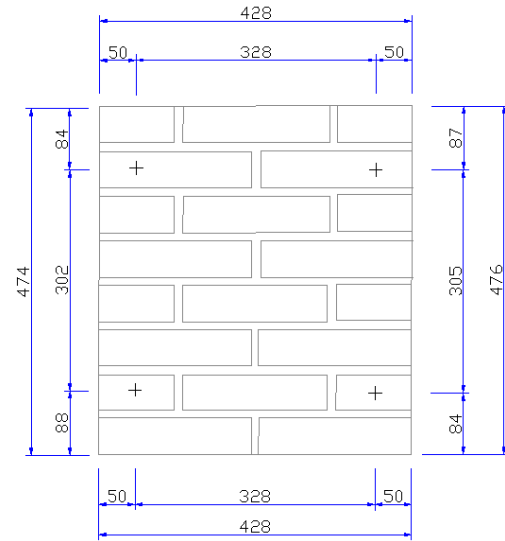
Wallette WS_6 – back side

224 Shake Table Test up to Collapse on a Roof Substructure of a Dutch Terraced House

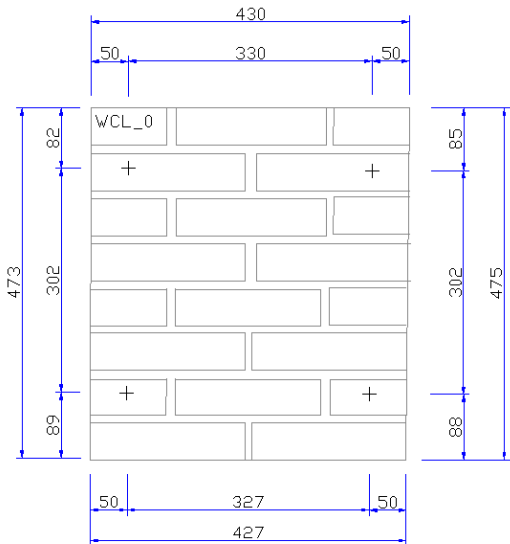
Geometry and instrumentation layout in clay *wallettes* for compressive strength tests:



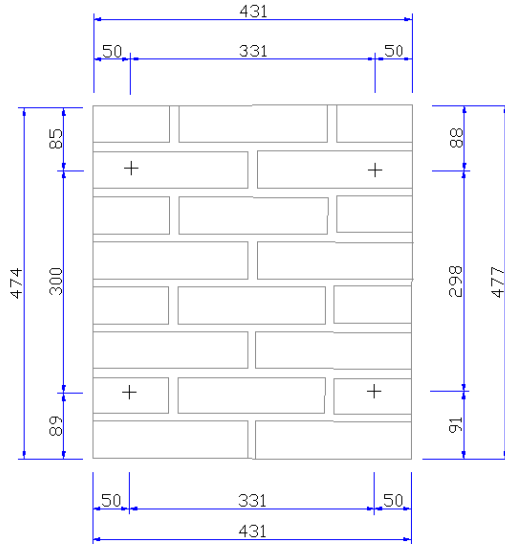
Wallette WCL_00 – front side



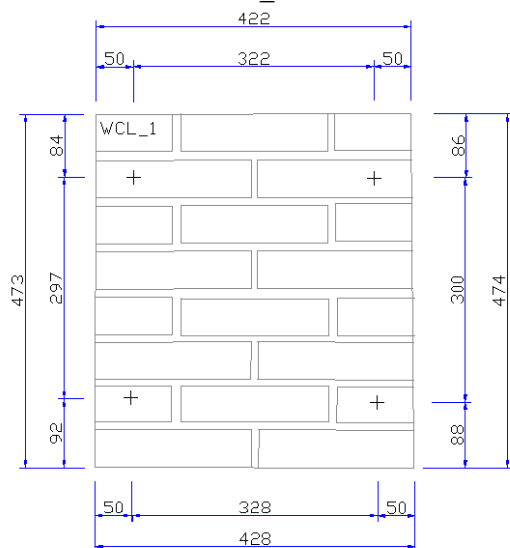
Wallette WCL_00 – back side



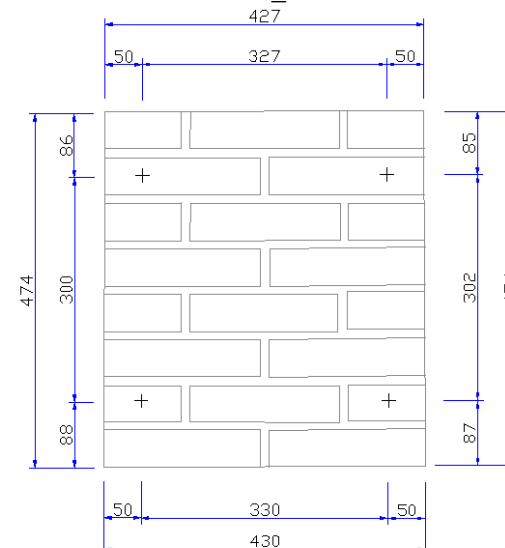
Wallette WCL_0 – front side



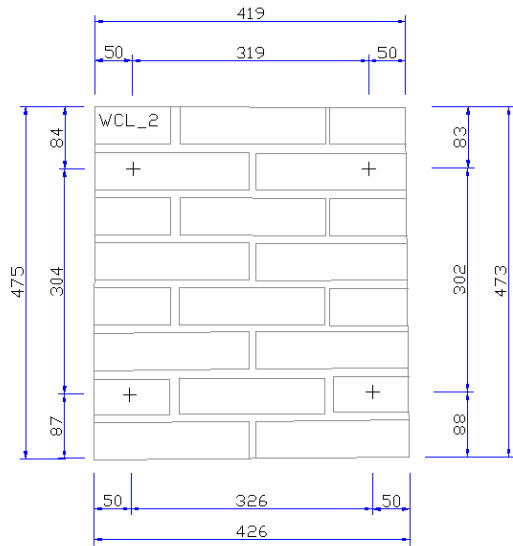
Wallette WCL_0 – back side



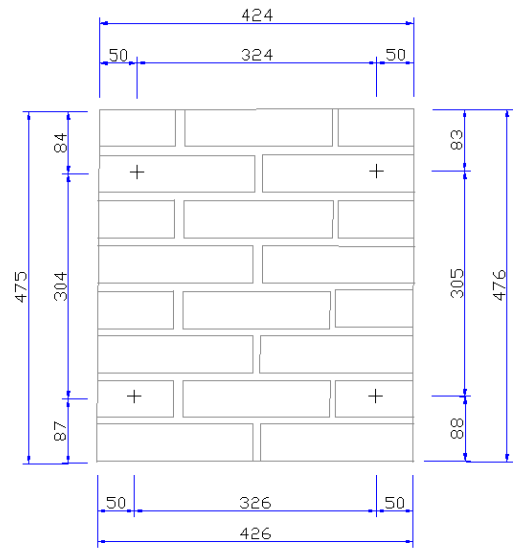
Wallette WCL_1 – front side



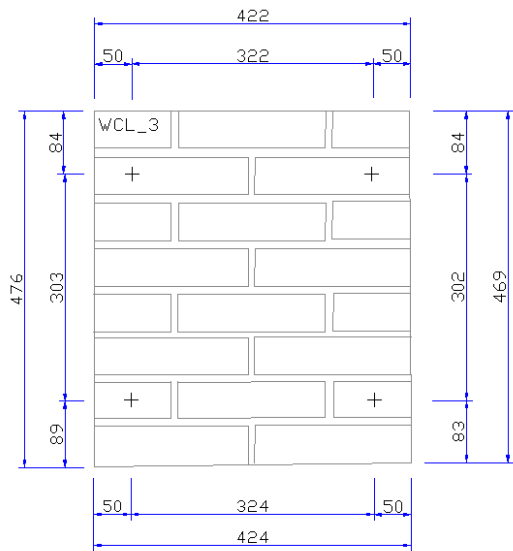
Wallette WCL_1 – back side



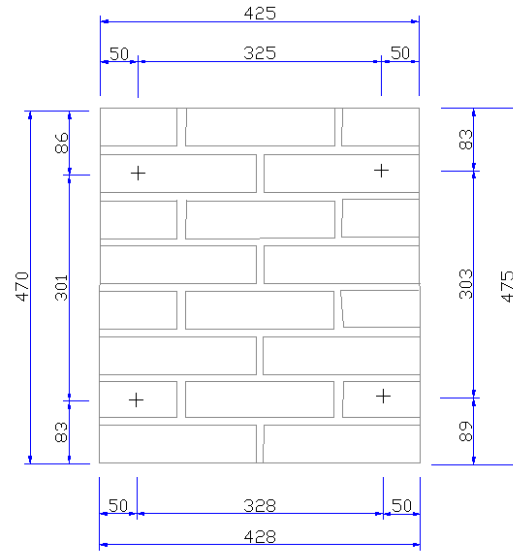
Wallette WCL_2 – front side



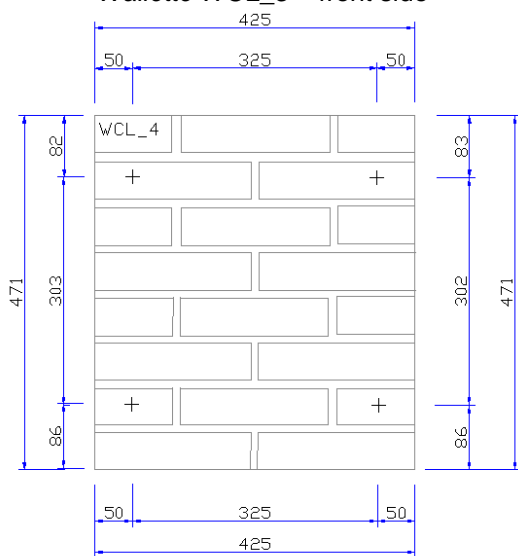
Wallette WCL_2 – back side



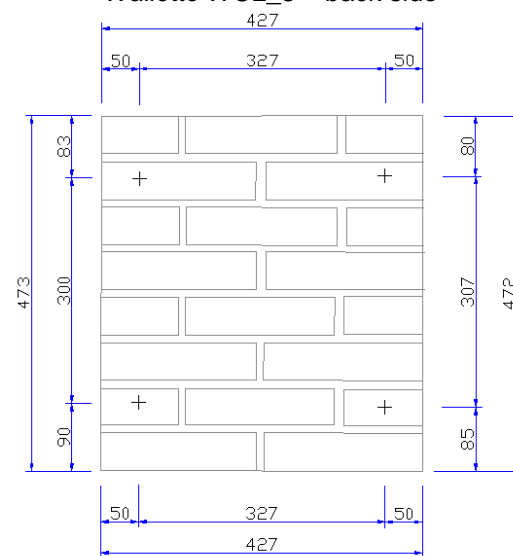
Wallette WCL_3 – front side



Wallette WCL_3 – back side

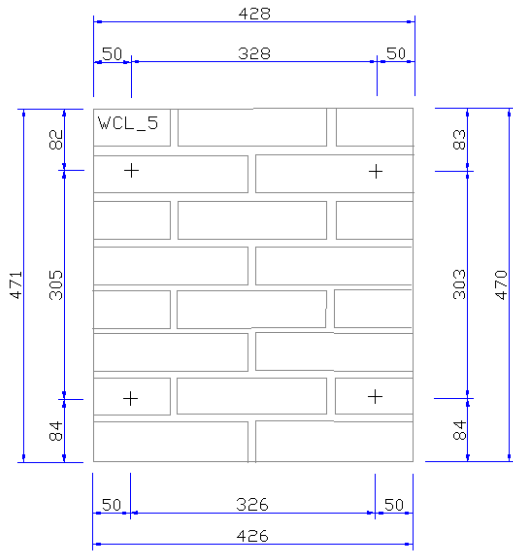


Wallette WCL_4 – front side

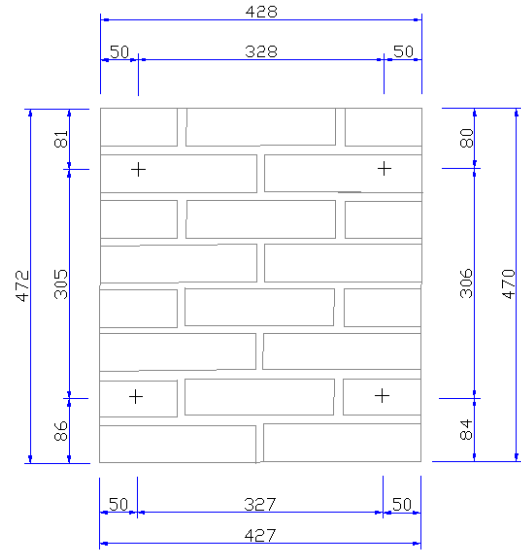


Wallette WCL_4 – back side

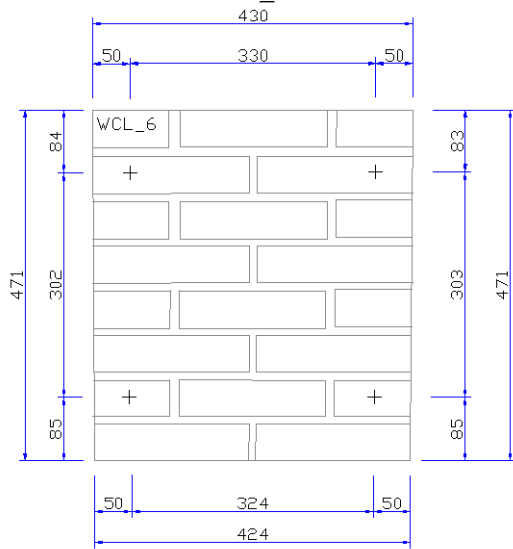
226 *Shake Table Test up to Collapse on a Roof Substructure of a Dutch Terraced House*



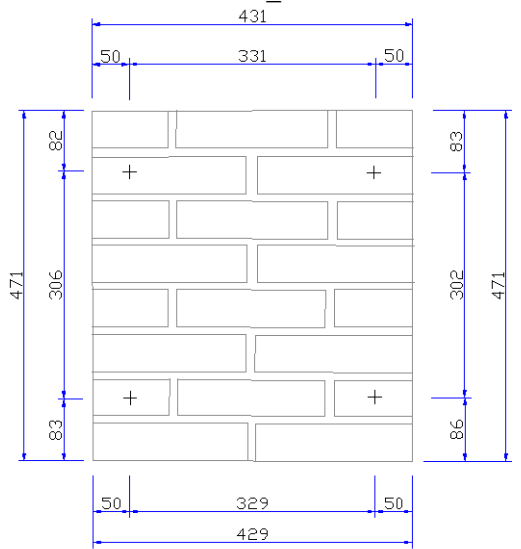
Wallette WCL_5 – front side



Wallette WCL_5 – back side



Wallette WCL_6 – front side



Wallette WCL_6 – back side

Dimensions and masses of the two types of wallettes constructed for the compression strength tests:

Specimen	Length [mm]			Average	Width [mm]			Average	Height [mm]			Mass [kg]
	Front	Up	Down		Left	Top	Bottom		Left	Right	Average	
WS_00	Front	437	434	436	Left	102.07	102.49	102.26	475	476	476	38.018
	Back	438	434		Right	102.09	102.38					
WS_0	Front	432	436	434	Left	103.22	102.94	103.20	474	474	474	38.081
	Back	432	434		Right	102.90	103.75					
WS_1	Front	435	437	435	Left	102.95	102.36	102.47	474	473	474	37.762
	Back	435	434		Right	102.07	102.48					
WS_2	Front	433	435	434	Left	102.91	102.94	102.80	473	474	474	38.374
	Back	434	433		Right	102.26	103.10					
WS_3	Front	431	434	433	Left	102.30	103.00	102.43	476	474	475	37.736
	Back	431	434		Right	102.80	101.60					
WS_4	Front	431	436	433	Left	101.59	102.77	102.68	477	476	477	38.208
	Back	431	434		Right	102.56	103.81					
WS_5	Front	435	436	435	Left	101.90	102.08	102.53	477	477	477	37.962
	Back	433	434		Right	103.21	102.93					
WS_6	Front	434	435	435	Left	103.42	101.84	102.73	474	477	476	38.306
	Back	434	435		Right	103.32	102.32					
WCL_00	Front	423	429	426	Left	101.23	101.75	101.20	476	475	476	37.818
	Back	423	430		Right	99.76	102.07					
WCL_0	Front	432	430	431	Left	99.15	102.27	101.46	476	476	476	37.891
	Back	432	430		Right	101.62	102.81					
WCL_1	Front	427	432	430	Left	101.29	101.55	101.86	475	475	474	37.577
	Back	428	431		Right	102.58	102.01					
WCL_2	Front	428	429	429	Left	98.98	101.30	100.79	475	475	474	37.808
	Back	430	429		Right	100.41	102.46					
WCL_3	Front	427	432	430	Left	99.21	100.53	99.97	476	474	475	37.985
	Back	428	432		Right	98.66	101.48					
WCL_4	Front	427	430	430	Left	99.10	100.13	100.10	474	474	477	37.550
	Back	430	431		Right	100.32	100.85					
WCL_5	Front	427	430	429	Left	100.08	100.57	100.32	472	472	477	37.749
	Back	428	430		Right	100.16	100.46					
WCL_6	Front	428	429	429	Left	100.87	101.17	100.80	473	471	476	37.458
	Back	430	428		Right	101.00	100.16					

230 Shake Table Test up to Collapse on a Roof Substructure of a Dutch Terraced House

Dimensions and masses of the two types of wallettes built for the bond strength tests:

Specimen	Height [mm]			Width [mm]			Length [mm]			Thickness of bed joint [mm]				Mass [kg]
	Left	Right	Average	Top	Bottom	Average	Front	Back	Average	Bed joint 1		Bed joint 2		
										Front	Back	Front	Back	
BWS_0	234	235	235	102.02	102.88	102.45	212	212	212	11.04	8.99	12.71	14.96	9.354
										9.58	8.99	14.26	12.90	
BWS_1	235	236	236	102.35	102.00	102.18	213	213	213	10.87	11.07	10.32	10.98	9.298
										12.99	13.36	13.79	13.61	
BWS_2	236	237	237	102.15	102.84	102.50	211	212	212	10.03	12.25	10.84	11.97	9.319
										13.44	12.80	13.14	12.88	
BWS_3	237	236	237	103.35	103.20	103.28	211	211	211	12.63	11.63	14.85	13.76	9.324
										12.06	11.90	13.75	12.67	
BWS_4	235	236	236	102.42	102.88	102.65	212	212	212	11.76	12.70	11.82	11.50	9.330
										11.73	11.08	14.31	14.10	
BWS_5	232	233	233	102.91	101.50	102.21	212	213	213	13.31	11.21	14.06	13.42	9.320
										13.30	12.15	14.61	13.39	
BWS_6	237	237	237	103.68	102.26	102.97	211	211	211	13.34	13.05	13.09	13.02	9.318
										11.77	12.50	14.75	13.22	
BWS_7	238	238	238	102.76	102.07	102.42	212	211	212	10.82	11.39	16.77	15.50	9.415
										10.45	11.45	15.78	15.63	
BWS_8	236	236	236	103.33	103.21	103.27	211	212	212	10.03	8.98	14.60	17.03	9.528
										10.82	9.22	14.51	15.88	
BWS_9	236	236	236	103.04	101.66	102.35	212	213	213	8.97	11.00	14.98	14.68	9.201
										9.98	11.01	15.18	14.89	
BWS_10	235	235	235	102.47	101.25	101.86	213	213	213	8.68	9.61	13.77	16.33	9.203
										10.81	9.60	13.85	16.69	
BWS_11	235	235	235	101.88	100.42	101.15	212	212	212	11.41	12.27	14.16	14.58	9.198
										8.91	12.83	13.24	15.13	
BWCL_0	167.42	167.45	167.44	100.33	101.61	100.97	209	210	210	10.68	9.80	10.63	6.91	6.455
										9.88	9.82	9.58	8.26	
BWCL_1	170.24	161.74	165.99	100.07	100.89	100.48	207	210	209	13.91	12.24	11.30	11.37	6.443
										12.98	13.79	11.21	11.57	
BWCL_2	170.02	171.49	170.76	100.18	100.84	100.51	206	209	208	13.51	13.54	12.70	10.78	6.495
										11.03	13.95	11.46	12.87	
BWCL_3	173.86	170.71	172.29	100.45	100.75	100.60	208	210	209	12.26	10.97	14.05	12.75	6.492
										11.11	11.77	12.08	13.43	
BWCL_4	174.52	171.02	172.77	100.70	100.17	100.44	204	207	206	13.82	12.06	14.45	13.84	6.505
										13.68	11.27	13.29	14.80	
BWCL_5	175.27	172.98	174.13	100.16	100.06	100.11	204	209	207	16.36	10.38	13.44	13.96	6.526
										13.64	12.06	13.93	14.11	
BWCL_6	175.82	176.46	176.14	101.99	100.40	101.20	208	209	209	14.38	14.05	14.20	13.41	6.708
										13.48	14.83	16.34	13.33	
BWCL_7	175.71	175.49	175.60	101.58	101.28	101.43	208	209	209	12.51	12.45	16.35	13.61	6.676
										12.97	13.75	16.67	13.15	
BWCL_8	176.65	175.47	176.06	100.55	100.20	100.38	207	207	207	15.80	12.44	16.70	13.51	6.647
										14.27	13.55	15.50	14.97	
BWCL_9	174.80	176.22	175.51	101.29	101.57	101.43	208	209	209	13.52	12.65	15.26	14.55	6.661
										13.60	14.64	17.96	12.50	
BWCL_10	173.23	173.09	173.16	100.45	99.40	99.93	206	208	207	14.12	11.41	13.99	10.48	6.618
										13.74	12.50	14.12	10.55	
BWCL_11	173.11	173.51	173.31	100.79	100.76	100.78	206	209	208	13.75	14.10	13.71	11.49	6.629
										15.12	10.15	13.29	11.69	

Determination of bulk density for calcium silicate walleτες and triplets:

Specimen	Length	Width	Height	Mass	Bulk density
	[m]	[m]	[m]	[kg]	[kg/m ³]
WS_00	0.43400	0.10320	0.47400	38.081	1793.74
Ws_0	0.43600	0.10226	0.47600	38.018	1791.39
WS_1	0.43500	0.10247	0.47400	37.762	1787.27
WS_2	0.43400	0.10280	0.47400	38.374	1814.58
WS_3	0.43300	0.10243	0.47500	37.736	1791.21
WS_4	0.43300	0.10268	0.47700	38.208	1801.62
WS_5	0.43500	0.10253	0.47700	37.962	1784.39
WS_6	0.43500	0.10273	0.47600	38.306	1800.83
Average					1795.63
BWS_0	0.21200	0.10245	0.23500	9.354	1832.66
BWS_1	0.21300	0.10218	0.23600	9.298	1810.22
BWS_2	0.21200	0.10250	0.23700	9.319	1809.51
BWS_3	0.21100	0.10328	0.23700	9.324	1805.32
BWS_4	0.21200	0.10265	0.23600	9.330	1816.66
BWS_5	0.21300	0.10221	0.23300	9.320	1837.33
BWS_6	0.21100	0.10297	0.23700	9.318	1809.59
BWS_7	0.21200	0.10242	0.23800	9.415	1821.89
BWS_8	0.21200	0.10327	0.23600	9.528	1844.08
BWS_9	0.21300	0.10235	0.23600	9.201	1788.36
BWS_10	0.21300	0.10186	0.23500	9.203	1805.00
BWS_11	0.21200	0.10115	0.23500	9.198	1825.26
Average					1817.16

Determination of bulk density for clay bricks walleτες and triplets:

Specimen	Length	Width	Height	Mass	Bulk density
	[m]	[m]	[m]	[kg]	[kg/m ³]
WCL_00	0.43100	0.10146	0.47600	37.891	1820.36
WCL_0	0.42600	0.10120	0.47600	37.818	1842.90
WCL_1	0.43000	0.10186	0.47400	37.577	1809.97
WCL_2	0.42900	0.10079	0.47400	37.808	1844.72
WCL_3	0.43000	0.09997	0.47500	37.985	1860.29
WCL_4	0.43000	0.10010	0.47700	37.55	1828.90
WCL_5	0.42900	0.10032	0.47700	37.749	1838.83
WCL_6	0.42900	0.10080	0.47600	37.458	1819.78
Average					1833.22
BWCL_0	0.21000	0.10097	0.16744	6.455	1818.13
BWCL_1	0.20900	0.10048	0.16599	6.443	1848.33
BWCL_2	0.20800	0.10051	0.17076	6.495	1819.37
BWCL_3	0.20900	0.10060	0.17229	6.492	1792.15
BWCL_4	0.20600	0.10044	0.17277	6.505	1819.72
BWCL_5	0.20700	0.10011	0.17413	6.526	1808.53
BWCL_6	0.20900	0.10120	0.17614	6.708	1800.56
BWCL_7	0.20900	0.10143	0.17560	6.676	1793.41
BWCL_8	0.20700	0.10038	0.17606	6.647	1816.97
BWCL_9	0.20900	0.10143	0.17551	6.661	1790.30
BWCL_10	0.20700	0.09993	0.17316	6.618	1847.62
BWCL_11	0.20800	0.10078	0.17331	6.629	1824.68
Average					1814.98

ANNEX VIII

Collapse mechanisms in material characterisation tests

Failure mechanisms of calcium silicate walleteres for compressive strength tests:



Walette WS_00 – front side



Walette WS_00 – lateral side



Walette WS_0 – front side



Walette WS_0 – lateral side



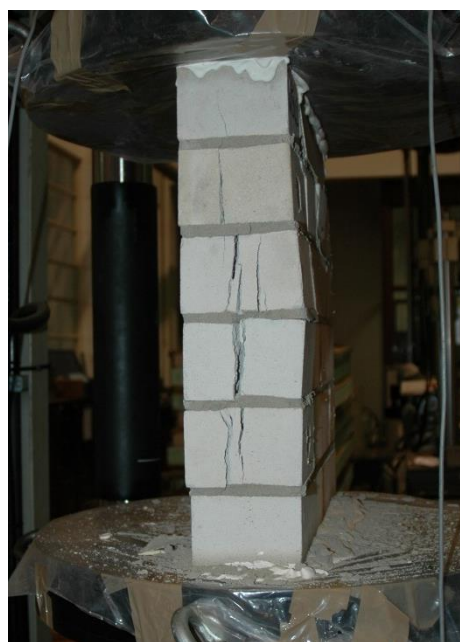
Walette WS_1 – front side



Walette WS_1 – lateral side



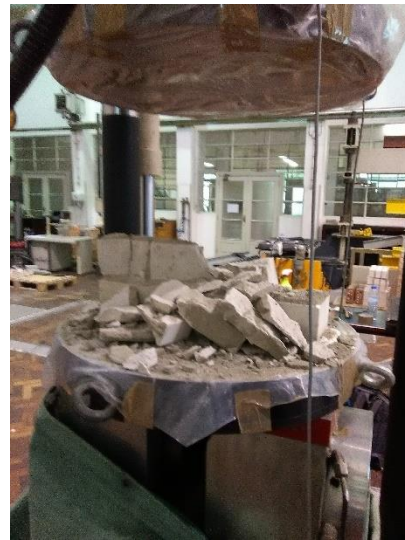
Walette WS_2 – front side



Walette WS_2 – lateral side



Wallette WS_3 – front side



Wallette WS_3 – lateral side



Wallette WS_4 – front side



Wallette WS_4 – lateral side



Wallette WS_5 – front side



Wallette WS_5 – lateral side



Walette WS_6 – front side



Walette WS_6 – lateral side

Failure mechanisms of clay *wallettes* for compressive strength tests:



Wallette WCL_00 – front side



Wallette WCL_00 – lateral side



Wallette WCL_0 – front side



Wallette WCL_0 – lateral side



Walette WCL_1 – front side



Walette WCL_1 – lateral side



Walette WCL_2 – front side



Walette WCL_2 – lateral side



Wallette WCL_3 – front side



Wallette WCL_3 – lateral side



Wallette WCL_4 – front side



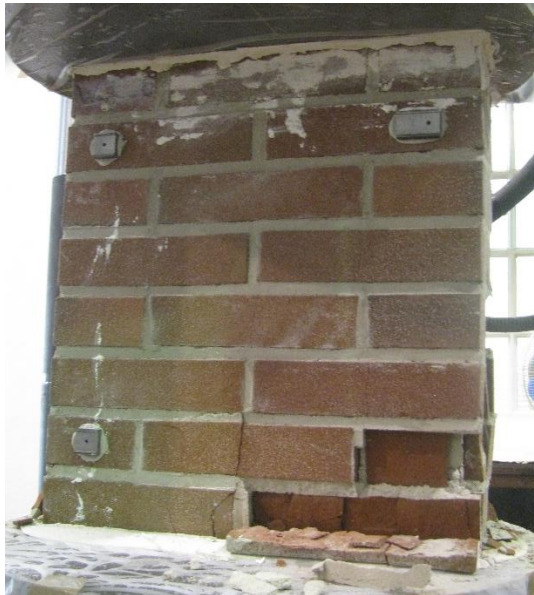
Wallette WCL_4 – lateral side



Walette WCL_5 – front side



Walette WCL_5 – lateral side



Walette WCL_6 – front side



Walette WCL_6 – lateral side

Failure mechanisms of calcium silicate triplets for bond wrench tests:



Triplet BWS_0



Triplet BWS_1



Triplet BWS_2



Triplet BWS_3



Triplet BWS_4



Triplet BWS_5

Triplet BWS_6

Triplet BWS_7



Triplet BWS_8



Triplet BWS_9



Triplet BWS_10



Triplet BWS_11

Failure mechanisms of clay triplets for bond wrench tests:



Triplet BWCL_0



Triplet BWCL_1



Triplet BWCL_2



Triplet BWCL_3



Triplet BWCL_4



Triplet BWCL_5



Triplet BWCL_6



Triplet BWCL_7



Triplet BWCL_8



Triplet BWCL_9



Triplet BWCL_10



Triplet BWCL_11



Research Report
